FORMATION OF HYDROTHERMAL SULPHIDE DEPOSITS ON THE NIUA VOLCANO, TOFUA ARC

by © Ben Robert Peterkin

Submitted to the School of Graduate Studies
in partial fulfillment of the requirements
for the degree of

Master of Science (M.Sc.) Thesis

Department of Earth Sciences

Memorial University of Newfoundland

January 2021

St. John's, Newfoundland and Labrador

Abstract

The Niua South hydrothermal vent field is an intraoceanic arc volcano-hosted hydrothermal system at the northern terminus of the Tofua-Kermadec arc. The vent field is hosted within a 500-m wide volcanic crater on the eastern flank of the southern summit of Niua volcano and contains several hydrothermal mounds that host clusters of active, high-temperature (up to 325°C) chimneys and abundant inactive spires. This thesis presents results from the first detailed exploration and sampling of this vent field, including descriptions of the mineralogy and geochemistry of the hydrothermal deposits. Two distinct mineralogical suites were identified from 33 sulphide-sulphate chimney and talus samples: a high-temperature (≥300°C), Cu-rich suite and a lower-temperature (<300°C), Ba-Zn-rich suite. The high-temperature, chalcopyrite-dominated mineralization contains elevated Bi, Te, Se, and Sn relative to the low-temperature suite, which is dominated by barite, sphalerite, galena and sulphosalts, and contains relatively higher As, Sb, Ag, Cd, and Sr concentrations. The hydrothermal mounds and associated chimneys in the central and eastern regions of the crater are associated with relatively lower temperature fluids and a higher degree of subsurface fluid mixing. In contrast, an isolated hydrothermal mound in the northern end of the crater has more focused, high-temperature venting with visible boiling at the orifice on one high-temperature vent. The enrichment of mantle incompatible elements (Ba, Pb, As, and Sb) in the hydrothermal deposits is consistent with a more felsic substrate at Niua relative to typical mid-ocean ridge settings. The composition and morphology of the hydrothermal deposits at Niua South are similar to the seawater-dominated hydrothermal system at the northwest caldera vent field at

Brothers volcano. The presence of primary bornite and euhedral hematite associated with chalcopyrite suggests that oxidizing magmatic fluids may be contributing to the hydrothermal output.

High-resolution bathymetry and visual surveys obtained by autonomous underwater vehicle and remotely-operated vehicle, respectively, provide enough detail of the seafloor to accurately identify the extent of hydrothermal deposits on the seafloor. This thesis also summarizes results of radioisotope age determinations and volumes of hydrothermal deposits within the Niua South crater. The deposit consists of three main groupings of active chimneys and mounds, with the bulk of the deposited material located in the central part of the crater. The oldest sample age indicates that venting within the crater has occurred over at least the last ~3,000 years. Volume calculations for hydrothermal material, based on the high-resolution bathymetry indicate 50,600 ± 5,060 m^3 of sulphide-sulphate material has accumulated on the seafloor within the crater. Using a bulk density estimate of the average composition of material of 2.65 ± 0.24 t/m^3, the crater contains an estimated 134,000 ± 21,700 t of deposit material. Based on the maximum age of the deposit, sulphide-rich material for the Niua South has a maximum mass accumulation rate of 47 ± 8 t/yr, comparable to other sites along mid-ocean ridges where data are available.

General Summary

Niua is a submarine volcano near Tonga, in the southwest Pacific Ocean. A volcanic crater on the side hosts a field of “black smokers”, where hot, metal-rich water (up to 325°C) discharges from the seafloor and cools to form chimney-like spires composed of minerals rich in valuable metals such as copper, zinc, silver, and gold. Based on the analysis of 33 samples, the deposits can be divided into two types: barium-zinc-dominant and copper-dominant. These compositions reflect the temperatures at which the deposits formed, which is controlled by the amount of mixing between the hot fluids and cold seawater. We also used radioactive isotopes to determine the ages of the deposits. In conjunction with size estimates that were based on high-resolution mapping of the crater, the rate at which these deposits formed was calculated. Results from this study provide insights into geological controls and rates of formation of submarine ore deposits.

Acknowledgements

Firstly, I would like to thank my supervisor, Dr. John Jamieson, whose constant support allowed for me to keep moving forward, especially in times where the task at hand felt overwhelming or impossible. I feel that he has taught me a great deal about how to conduct good science, and throughout the course of this project I have learned a lot about myself as a scientist and a person in general. I only wish that I had been as confident in the beginning as I have now become.

To Sven Petersen who dedicated much of his valuable time in getting me started with this project, during my visit to GEOMAR, in Kiel, Germany, and Melissa Anderson who provided a great deal of assistance with sample photography. Even after additional camera lessons from John, I feel I have not and perhaps will never truly understand or retain any of this knowledge. Additional thanks go to Dr. Stephen Piercey for his insightful input regarding thin section observations.

Finally, to the JJ Crew: Dennis Sánchez Mora and Euri Papanicolaou, who made office life at Memorial University a constant joy throughout these last 3 years. Our many discussions of SMS deposits over coffee helped me grasp certain concepts and gain new perspectives. Thank you for allowing me the space and time to rant about the Toronto Blue Jays or King Gizzard and the Lizard Wizard. The JJ Crew Office Techno Party playlist will be one that I listen to for years to come.

This thesis is dedicated to the memory of Brian Peterkin. I would like to think he would be very proud of this accomplishment.

Table of Contents

List of Tables

List of Figures

1. Introduction and Overview

1.1. Background

Seafloor massive sulphide (SMS) deposits form at sites of high-temperature hydrothermal fluid venting on the ocean floor. Here, metal-rich fluids discharge from the seafloor and precipitate minerals, which accumulate as seafloor and subseafloor deposits. Active hydrothermal systems are present in every marine tectonic boundary setting, including mid-ocean ridges and volcanic arc and back-arc settings (Hannington et al., 2005). The deposits themselves can host valuable metals such as Cu, Zn, Au, and Ag, and they are currently being considered as economically-viable mining targets (Hannington et al., 2010). In particular, arc-related hydrothermal systems have attracted significant interest due to the potential high grades of base and precious metals of economic interest, especially when compared to mid-ocean ridge deposits (de Ronde et al., 2005; Halbach et al., 1993; Glasby et al., 2008; Iizasa et al., 2019). These high grades result from the compositional range of generally more felsic host rock compositions, and from the contribution of magmatic volatiles (de Ronde et al., 2014; Yang & Scott, 2006).

The Niua volcano, a submarine intraoceanic arc volcano near Tonga, in the southwest Pacific Ocean, contains a crater on the flank of the southern summit with several actively forming SMS deposits. In 2016, scientists aboard the research vessel R/V *Falkor* undertook an expedition to the Niua volcano, where the entire crater was imaged with video and still cameras, and rock and fluid samples were collected using the remotely-operated vehicle (ROV) *ROPOS*.

The purpose of this research project is to document the geological characteristics of the Niua hydrothermal system, with a focus on assessing spatial and temporal variabilities in sulphide-sulphate deposit composition within a self-contained, crater-hosted hydrothermal vent field. Mass accumulation rates are determined based on the volumes and ages of hydrothermal chimneys and mound material. The results of this study yield a greater understanding of the chemical mass balance of hydrothermal systems with respect to metals and sulphur contained in hydrothermal fluids, and the overall efficiency of sulphide deposition at the seafloor (Hannington et al., 2010).

1.1.1 Regional geology and tectonic setting

The Tofua (sometimes also referred to as Tonga)-Kermadec arc system extends ~2,500 km along a NNE-SSW trend between the North Island of New Zealand and the Tonga archipelago (de Ronde et al., 2003; Fig. 1.1). The arc system represents a convergent margin of steeply dipping westward subduction of the Pacific plate under the Indo-Australian plate. The Tofua-Kermadec arc system is bisected by the Louisville Ridge, a submarine volcanic chain located east of the oceanic trench that is being actively subducted at an oblique angle to the trench (Dupont and Herzer, 1985). The intersection of the Louisville Ridge and the subduction zone serves as the boundary between the Kermadec arc to the south, and the Tofua arc to the north. A significant portion of the Louisville Ridge is assumed to have already been subducted underneath the Tofua arc (Dupont and Herzer, 1985). Along its 1,200 km length, the Kermadec arc contains 30 volcanic centers in the form of caldera or cone volcanoes (de Ronde et al., 2012).

Volcanoes are variably composed of basalt to rhyodacite (de Ronde et al., 2012). The relatively shallow depths of the volcanic centers and high magmatic volatile content of the arc magmas result in explosive eruption styles and volatile-rich hydrothermal systems (Embley et al., 2008).

The Lau Basin is an actively rifting back-arc basin situated between the Tofua arc and the Lau Ridge (Fig. 1.1). It was formed by initial rifting of the volcanic arc and subsequent back-arc spreading in the north Central Lau Basin, beginning around 6.0 Ma (Parson and Hawkins, 1994). This separated the Lau Ridge (the remnant volcanic arc) from the Tonga Ridge (the remnant forearc basin) (Dupont and Herzer, 1985). Rifting propagated southward in an intermittent, step-wise fashion, forming the Central Lau Spreading Center (CLSC), Intermediate Lau Spreading Center (ILSC), Eastern Lau Spreading Center (ELSC), and Valu Fa Ridge (VFR) respectively (Parson and Hawkins, 1994; Ewart et al., 1998). Back-arc spreading within the Lau Basin is likely responsible for the clockwise rotation (~ 17°) of the Tonga Ridge (Sager et al., 1994). Formation of the Tofua arc, the active volcanic arc along the western margin of the Tonga Ridge, began after rifting was already established ~ 3.0 Ma (Dupont and Herzer, 1985; Clift and Vroon, 1996).

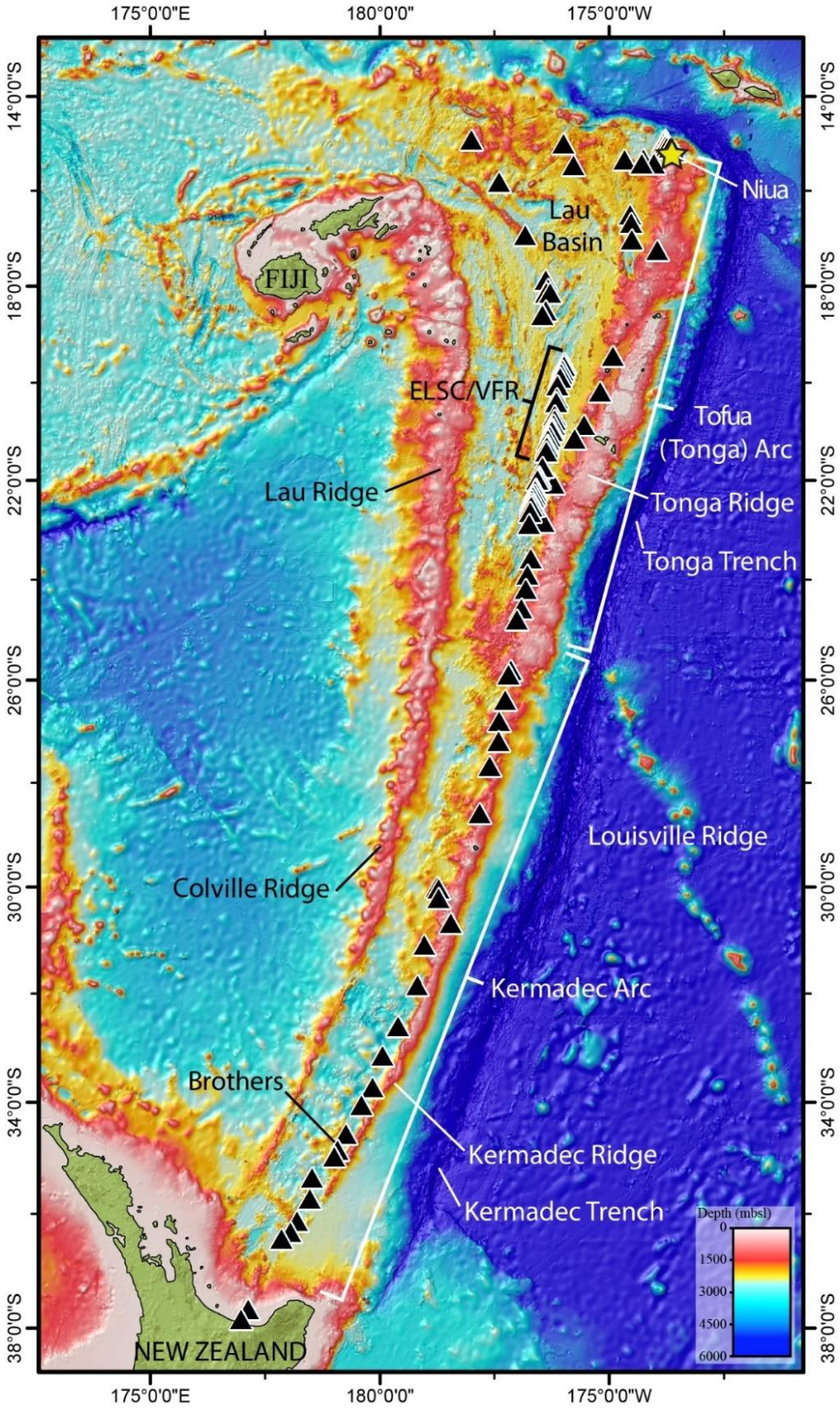
175°0'0"E
180°0'0"
175°0'0"W
14°0'0"S
18°0'0"S
22°0'0"S
26°0'0"S
30°0'0"S
34°0'0"S
38°0'0"S
Niua
Lau
Basin
FIJI
ELSC/VFR
Tofua
(Tonga) Arc
Lau Ridge
Tonga Ridge
Tonga Trench
Louisville Ridge
Colville Ridge
Kermadec Arc
Brothers
Kermadec Ridge
Kermadec Trench
NEW ZEALAND
Depth (mbsl)
0
1500
3000
4500
6000

Figure 1.1. Map of the Tofua-Kermadec arc, southwest Pacific Ocean. The yellow star near the northeast corner marks the location of Niua volcano. Black triangles represent 99 sites of confirmed or inferred (from water column surveys) active hydrothermal venting along the volcanic arc and within the back-arc basin (data from Beaulieu et al., 2013). ELSC = Eastern Lau Spreading Center, VFR = Valu Fa Ridge. Bathymetric data is from the Global Multi-Resolution Topography dataset (Ryan et al., 2009).

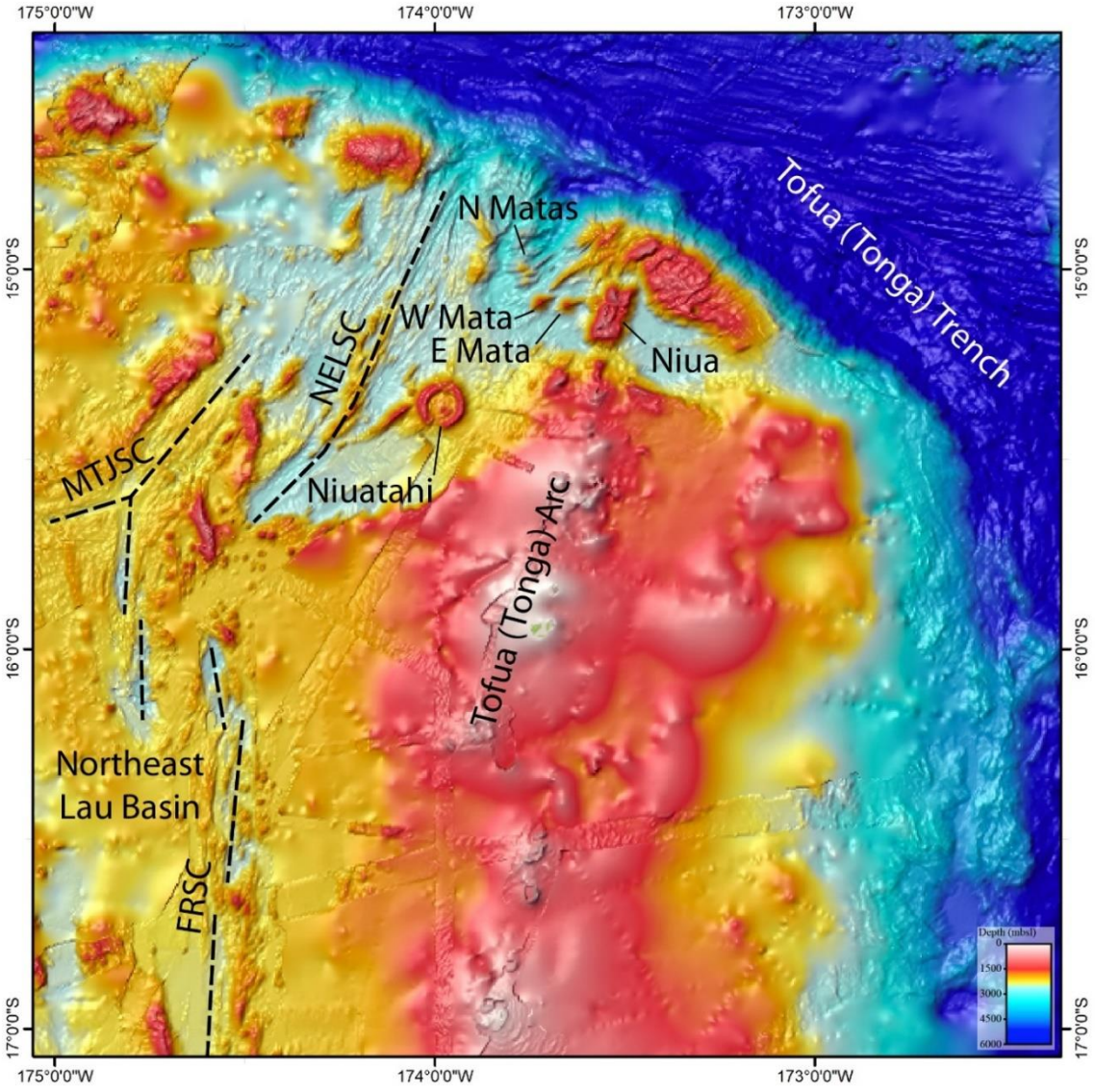

Figure 1.2. Regional bathymetric map of the northeast Lau Basin and northern extent of the Tofua (Tonga) arc. Niua volcano is situated near the northern Tofua arc terminus. Dashed lines show back-arc basin spreading centers. NELSC = Northeast Lau Spreading Center, MTJSC = Mangatolu Triple Junction Spreading Center, FRSC = Fonualei Rift Spreading Center.

Niua volcano is situated along the north-northeast trending Tofua arc (Fig. 1.2). The submarine volcano consists of two volcanic centers: Niua North and Niua South, both of which have confirmed hydrothermally-active vent fields that are ~ 10 km apart from each other (Fig. 1.3). The vent field at Niua North is characterized by a small pit (< 25 m wide) located along the western flanks of the northern summit of the volcano (~ 750 meters below sea level; mbsl) that is vigorously emitting sulphur smoke and droplets of liquid CO_2 (Resing et al., 2012). A 500 m wide crater defines the Niua South hydrothermal site that is situated at a maximum depth of 1190 mbsl.

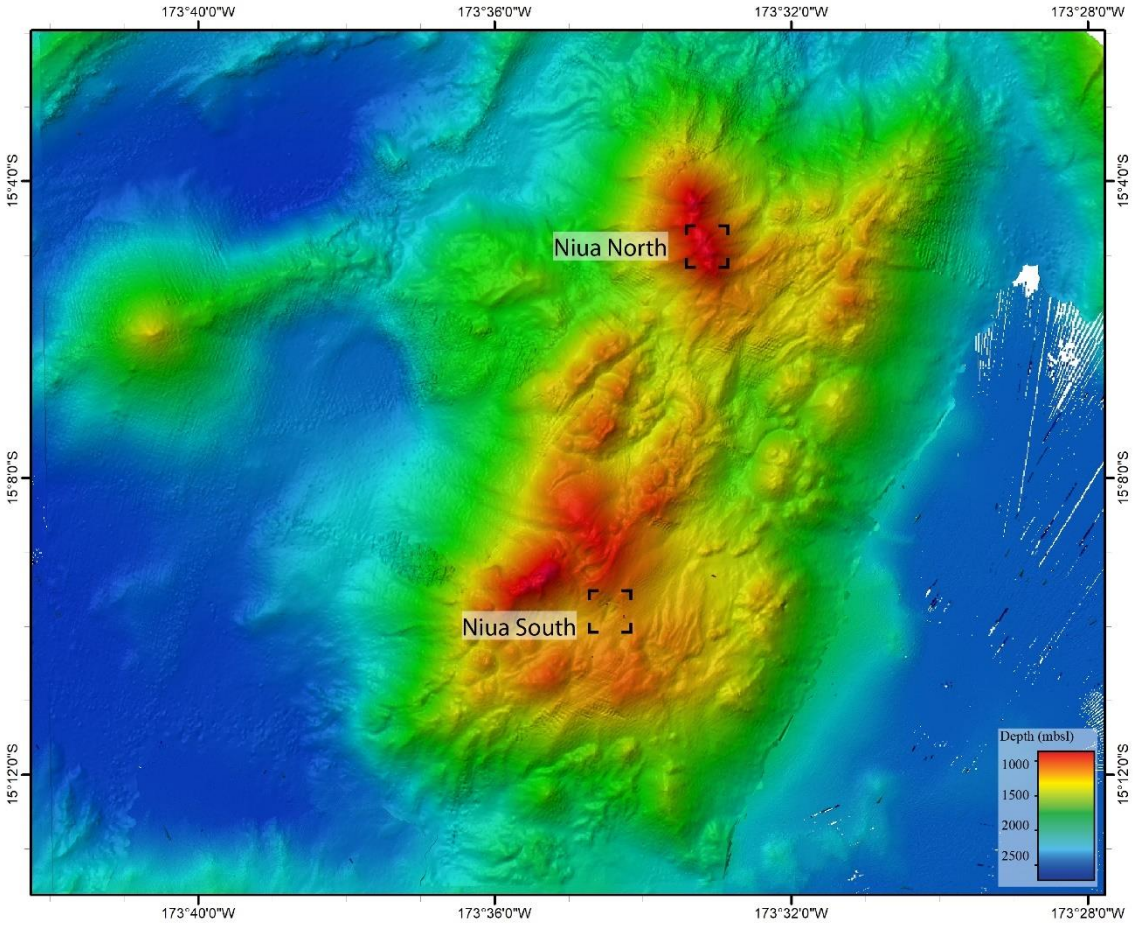

Figure 1.3. Bathymetric map of Niua volcano. The volcano is characterized by two volcanic summits, Niua North and Niua South. The volcano and surrounding area were mapped using the R/V *Falkor's* EM302 multibeam echosounder at a resolution of 25 m. The black corners mark the locations of the Niua North hydrothermal field and Niua South crater and hydrothermal field.

In arc-related environments, the influence of the subducting slab affects the types of lavas that erupt onto the seafloor (Pearce and Peate, 1995; Stern, 2002). At convergent plate margins, intraoceanic arcs form from the subduction of oceanic crust underneath adjacent oceanic crust (Embley et al., 2008). Due to the influence of the subducting slab, mature volcanic arc calderas can contain silicic lavas that result in explosive eruptions of dacitic and rhyolitic pyroclastic rocks (Fiske et al., 2001; Smith et al., 2003). As products of partial melting, arc magmas evolve with the addition of volatiles (primarily H_2O) to the mantle wedge from the dehydrated subducting slab and associated sediments (e.g., Pearce, 1983; Pearce and Peate, 1995). Primitive arc magmas are dominated by basaltic and tholeiitic lavas but become more andesitic and calc-alkaline with crustal thickening and increases in the extent of magma fractionation (Tatsumi and Eggins, 1995). As a result of the variability in arc magma composition, hydrothermal systems in arc settings are characteristically different from those hosted on typical mid-ocean ridges (de Ronde et al., 2001; Fouquet et al., 1993; Hannington et al., 2005). For example, circulating hydrothermal fluids in arc environments can contain high concentrations of alkali elements and trace elements such as Pb, As, Sb, and Ba as a result of the more felsic melt compositions (Hannington et al., 2005; Evans et al., 2017). In particular, Ba and Pb are mainly sourced from the breakdown of feldspars (Hannington et al., 1995; Barrie and Hannington, 1999). Arc-hosted hydrothermal systems also often contain a higher

concentration of magmatic volatiles (i.e. CO_2, SO_2) in the hydrothermal fluids, relative to mid-ocean ridge-hosted systems (de Ronde et al., 2014). It has been suggested that these magmatic volatiles may be important for transporting metals from the magma reservoir in some arc and back-arc submarine hydrothermal systems (Yang and Scott, 2006). Preliminary analysis of volcanic rocks collected from Niua point to a dacitic to felsic composition of eruptive melts at Niua (Rubin 2018; Pers. Comm.).

1.1.2 History of exploration along the Tofua-Kermadec arc

Evidence of hydrothermal sulphide mineralization along the Kermadec arc was first discovered in 1996, after samples of gold-bearing massive sulphide were recovered by dredge from within the calderas of the Brothers and Rumble II West volcanoes (Wright et al., 1998). In 1999, 13 submarine stratovolcanoes were systematically surveyed for hydrothermal activity along the southern arc front during the NZAPLUME (New Zealand American PLUme Mapping Expedition) cruise (de Ronde et al., 2001). This marked the first instance in which an intraoceanic arc was systematically surveyed (de Ronde et al., 2007). The hydrothermal vent fields of Brothers and Healy were identified as the most active, based on the thickness and distribution of their hydrothermal plumes (de Ronde et al., 2001). Since then, Brothers volcano has seen numerous studies detailing the mineralogy and paragenesis of recovered sulphide samples (Wright et al., 1998; de Ronde et al., 2003, 2005; Berkenbosch et al., 2012), as well as the dating of sulphide chimneys (de Ronde et al., 2005, 2011) and a specific focus on the contribution of magmatic fluids to these hydrothermal systems (de Ronde et al., 2005, 2011; Berkenbosch et al., 2012,

2015). In 2018, drill core was recovered from several sites within the Brothers caldera using the drilling vessel JOIDES Resolution during the International Ocean Discovery Program Expedition 376 Brothers Arc Flux (de Ronde et al., 2019). The extensive interest that the Brothers volcano has received over the last decade makes it the most well-documented submarine arc hydrothermal system in the world.

Exploration along the Tofua arc segment is limited relative to that of the Kermadec. In early 2008, researchers on board the R/V *Southern Surveyor* were the first to discover hydrothermal activity at Niua volcano, using conductivity, temperature, depth (CTD) casts (Resing et al., 2012). In November of 2008, scientists onboard the R/V *Thompson* undertook an expedition to the northeast Lau Basin to conduct water-column plume surveys, while simultaneously collecting high-resolution bathymetric data (Merle et al., 2008). During the expedition, the Niua South crater was found to contain active hydrothermal vents using CTD tow-yo water column surveys (Merle et al., 2008). These discoveries sparked a greater interest in further exploration of these areas. In November of 2011, during expedition KM1129a onboard the R/V *Kilo Moana*, high-resolution (1 m) multibeam echosounder sonar mapping of the entire Niua volcano was conducted using the autonomous underwater vehicle (AUV) *ABYSS* (Resing et al., 2012). In September of 2012, the R/V *Roger Revelle*, equipped with the ROV *QUEST 4000*, visited Niua South. On two separate dives, eight rock samples (4 volcanic host rock and 4 massive sulphide samples) were collected (Fig. 1.4). In 2012, a technical report was prepared for Nautilus Minerals Inc., a seafloor mineral exploration company, in which average metal concentrations for sulphide deposits at Niua were determined to be 8.1% Cu, 15.3% Zn,

13.7 g/t Au, and 313 g/t Ag, based on three chimney grab samples obtained using a commercial ROV (Jankowski, 2012).

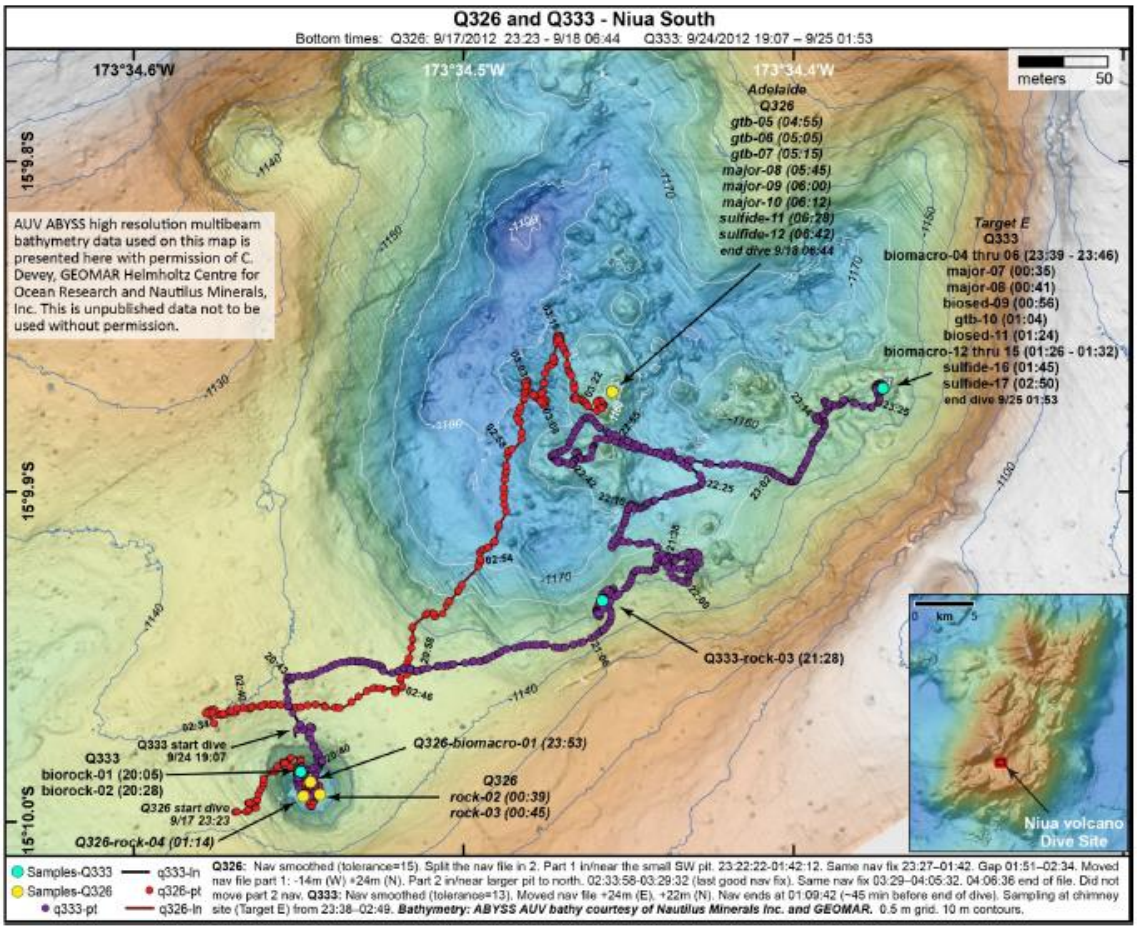

Figure 1.4. High-resolution multibeam bathymetric map of Niua South (provided by GEOMAR and Nautilus Minerals Inc.) illustrating the dive-tracks of two separate dives of ROV QUEST 4000, during the R/V *Roger Revelle* expedition (Q326 in red and Q333 in purple). Sampling locations (all types) are marked by the blue and yellow circles (Resing et al., 2012).

1.1.3 Expedition of the R/V *Falkor*

In 2016, research scientists aboard the R/V *Falkor* visited the Niua volcano during a dedicated two-week cruise to study the crater. The primary objective of the research cruise was to systematically photograph and video survey the 500-m diameter crater floor at sub-cm resolution. Using a custom-built camera system mounted onto the ROV *ROPOS*, photogrammetric surveys were conducted within the crater (Fig. 1.5). This process uses overlapping photographs to construct a 3-D digital model of the hydrothermal vent field. An ultra-high definition ("4K") video camera, also attached to ROPOS, was also used to document each dive throughout the two-week period. This high-resolution visual dataset provides a unique opportunity to correlate patterns, textures and features identified from previously collected high-resolution acoustic AUV bathymetric data to specific geological features identified from ROV imagery. During the cruise, a geological map of the major volcanic and hydrothermal features within the study site was also produced.

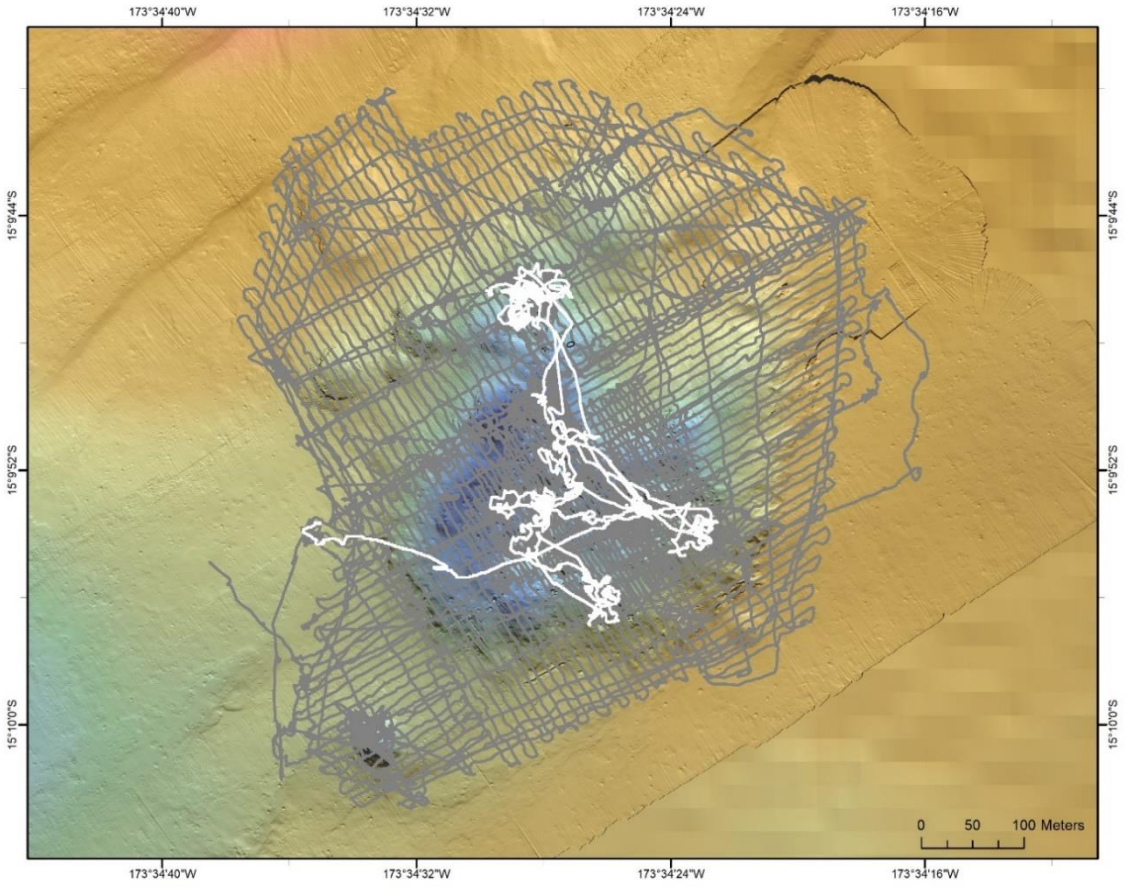

Figure 1.5. High-resolution (50 cm) bathymetric map of the Niua South study site (the bottom right section of the map displays 25 m ship bathymetry). The map shows the three systematic ROV bottom photogrammetry dive tracks (grey) and sampling dive tracks (white). The high-resolution AUV bathymetry was provided by Nautilus Minerals Inc. and was collected during the R/V *Roger Revelle* expedition to the Lau Basin in 2012 using the GEOMAR AUV *Abyss*.

The expedition consisted of six separate ROV dives, including three survey dives (D1916, D1917, and D1921) dedicated to systematically photographing the entire crater (Fig. 1.5) and three dedicated sampling dives (D1918, D1919, and D1920; Figs. 1.6 to 1.8, respectively). Thirty-six rock and sediment samples were collected. Approximately 150 hours of video was recorded over the two-week period, with the three photo survey dives

accounting for ~75% of the ROV dive time. Just over 900 photographs were captured throughout the five dives.

During the first sampling dive (D1918), 13 rock samples were collected (Fig. 1.6), as well as 21 fluid and biology samples. The dive focused on two main active chimney complexes within a 50-m radius, in the northern part of the crater. The samples collected provide a wide range of active and inactive sulphide-sulphate chimney pieces. Several samples were collected from the tip and proximal area of an active two-phase (i.e., boiling) chimney (Gartman et al., 2018). Maximum fluid temperature of 325°C was recorded at both active chimney complexes, using a high-temperature probe.

The second sampling dive (D1919) focused on central sites within the crater, covering an area of roughly 100 m^2 (Fig. 1.7). Six samples were collected from active and inactive chimney complexes. Fifteen fluid and biology samples were also collected.

The final sampling dive (D1920) took place in the central region of the crater but covered a much greater area than the previous dive (Fig. 1.8). This dive yielded the most rock samples with a total of 16. These rock samples reflect the greatest variation, spatially and compositionally of all dives. Five fluid and biology samples were also collected. Although most samples are composed of sulphide and sulphate material, five of the samples are fragments of volcanic pumice. As with the previous dive, the ROV again returned to the northern area, but did not collect additional samples there.

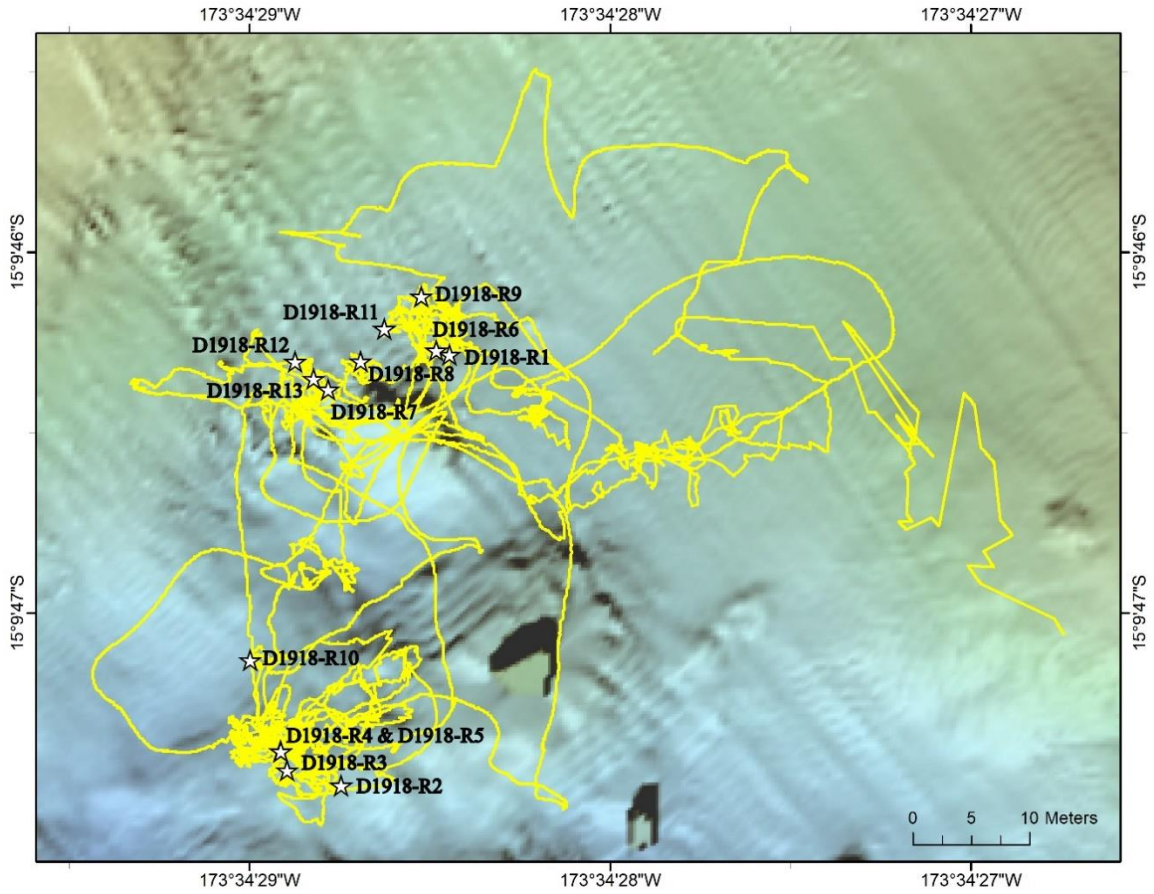

Figure 1.6. High-resolution (50 cm) bathymetric map of the northern area of the Niua South crater. The map shows the dive track for D1918, and the locations of the 13 rock samples collected, denoted by white stars.

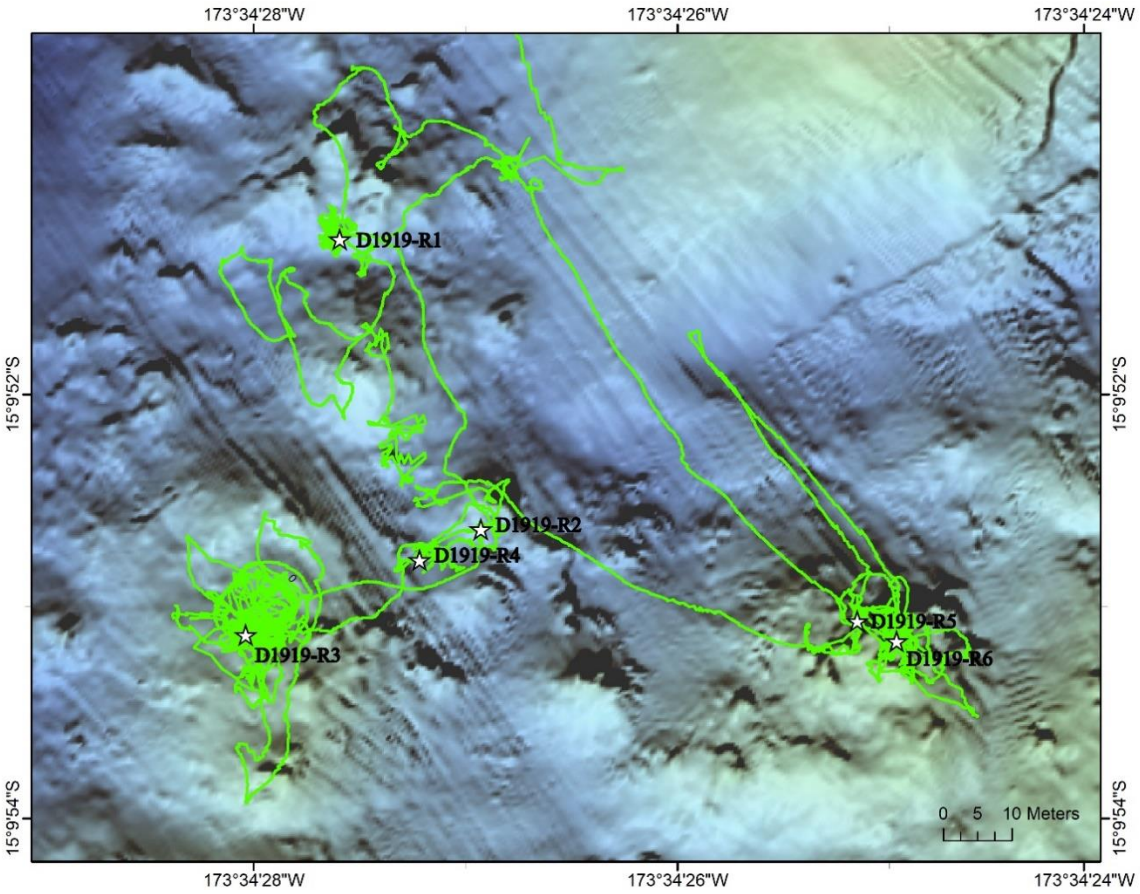

Figure 1.7. High-resolution (50 cm) bathymetric map of the central and eastern areas of the Niua South crater. The map shows the dive track for the second sampling dive, D1919, and the locations of the six rock samples collected, denoted by white stars.

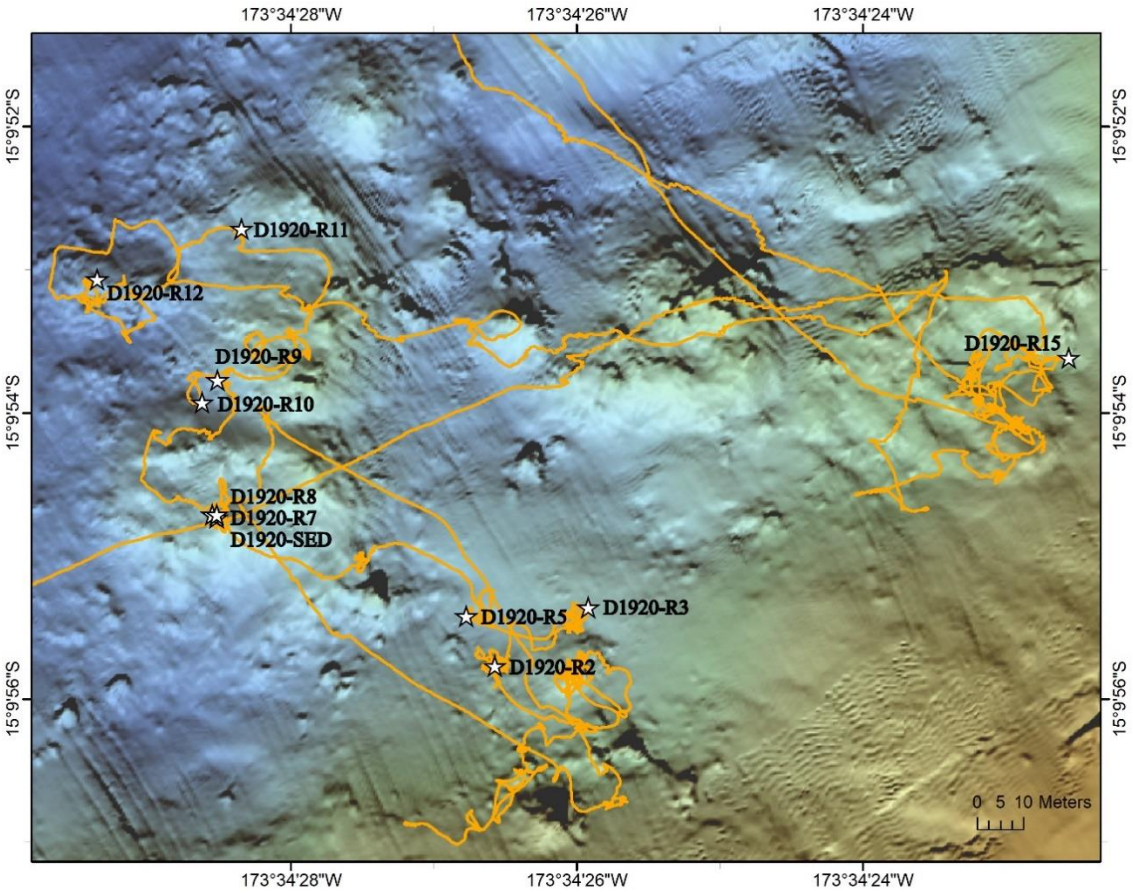

Figure 1.8. High-resolution (50 cm) bathymetric map of the central, eastern, and southern area of the Niua South crater. The map shows the dive track for third and final sampling dive, D1920, and the locations of the 11 rock samples collected, denoted by white stars.

1.2. Methods

1.2.1 Data collection

Data for this study were collected during the two-week *Virtual Vents* research expedition in early 2016. In May 2016, preliminary laboratory analyses were conducted at GEOMAR Helmholtz Centre for Ocean Research Kiel, Germany. Here, most of the rock

samples collected during the cruise were described, photographed, and finally cut into thin section slabs before being sent to Memorial University of Newfoundland (MUN).

1.2.2 Petrography

Of the 30 rock samples collected, 50 subsample slabs were cut using a diamond-bladed rock saw and made into standard 1×2” polished thin sections (30 microns). Most of the rock samples are quite porous and were therefore also impregnated with epoxy during this process to prevent the samples from breaking during cutting and polishing. Each thin section was cut with the intent of matching with geochemical subsamples. Select samples contain multiple thin sections because of the significant variation in sulphide and sulphate mineralogy that can occur over short distances within these samples (e.g., sulphide chimney exterior and interior can be only centimeters apart but be composed of completely different minerals). The mineralogy and textures of each sample were examined and described using both a stereo-microscope and petrographic microscope under both transmitted and reflected light.

1.2.3 SEM-EDX

For mineral identification purposes, specific mineral phases were further analyzed using a FEI MLA 650F scanning electron microscope (SEM) with an energy dispersive x-ray (EDX) detector. Mineral identification and semi-quantitative trace element composition analyses were completed primarily on polished thin sections, with some additional examination using corresponding epoxy-mounted slabs. High-resolution images were

captured using both electron backscatter and secondary electron detection settings. Semi-quantitative elemental analyses were performed between 15-20 kV under high vacuum, with a working distance of 12 mm.

1.2.4 Whole-rock Geochemistry

Representative portions for each subsample were analyzed for their major and trace element concentrations. Subsamples were powdered at Memorial University using a tungsten carbide ring and puck mill. Geochemical analyses were carried out at Activation Laboratories Inc. in Ancaster, Ontario. Two separate methods were employed to quantify bulk elemental abundances: (1) instrumental neutron activation analysis (INAA), and (2) inductively coupled plasma mass spectrometry (ICP-MS), following sample preparation by sodium peroxide fusion. Concentrations of Ag, As, Au, Ba, Br, Ce, Co, Cr, Cs, Eu, Fe, Hf, Ir, La, Lu, Na, Nd, Ni, Sb, Sc, Se, Sm, Ta, Tb, Th, U, W, Yb, and Zn were measured by INAA, while Al, B, Be, Bi, Ca, Cd, Cu, Dy, Er, Ga, Gd, Ge, Ho, In, K, Li, Mg, Mn, Mo, Nb, Pb, Pr, Rb, S, Si, Sn, Sr, Te, Ti, Tl, Tm, V, and Y were measured by ICP-MS. In some cases, one method is preferred over the other, based on several element specific factors. For example, select elements such as As, Bi, Sb, Se, Te, and Tl are considered volatile elements that can be lost during fusion processes. The INAA method is a solid source method without any loss of elements due to volatilization, thus it is the favoured method for these elements. Also, with mass spectrometry, it is easier to overwhelm the detectors for elements like Ba, which is a major component of many of the samples, thus INAA is the more reliable choice.

1.2.5 Geochronology using the ^{226}Ra/Ba method

The use of ^{226}Ra decay as a geochronometer allows for the dating of barite-rich hydrothermal samples that are between 200 – 20,000 years old (Ditchburn et al., 2012; Jamieson et al., 2013). Barite preferentially concentrates Ra through element substitution, due to the similar ionic charge and radii to Ba. Following the decay chain of ^{238}U to stable ^{206}Pb, the intermediate daughter product ^{226}Ra decays (half-life of 1600 years) from its parent isotope ^{230}Th and accumulates in basaltic crust, where Ba is also present (Jamieson et al., 2013). Both Ra and Ba are leached from the crust during hydrothermal alteration and mobilized to the seafloor via hydrothermal fluids. However, the parent isotope ^{230}Th is not mobilized by the fluids because of its low solubility, and thus ^{226}Ra becomes separated and unsupported by its parent isotope (Ditchburn et al., 2012). The ratio of the amount of ^{226}Ra to Ba (N) in a sample and an initial value of ^{226}Ra/Ba (N_0), which represents the ratio at the time the sample formed, is used to determine an age (t, in years) for the given sample, using the following equation:

$$t = \frac{\ln\left({}^{N_0}/_{N}\right) \times\ 1600 \text{ years}}{\ln 2} \qquad \text{(Equation 1)}$$

The initial ^{226}Ra/Ba values cannot be measured directly; however, samples collected from active "zero-age" vents are used as a proxy for initial ratios for older samples, assuming there is no spatial variability of Ra or Ba concentrations in the hydrothermal fluids within the vent field, nor are there temporal changes in these concentrations on the order of thousands of years (de Ronde et al., 2005; Jamieson et al., 2013). The ^{226}Ra/Ba method is

applicable to a wide range of tectonic settings where barite is hosted in SMS deposits (Jamieson et al., 2013). The Ba-rich felsic host rocks at Niua South account for the high abundance of barite within hydrothermal chimneys, making this dating method ideal for these samples.

Twenty-nine hydrothermal samples from Niua South were chosen for dating by gamma spectrometry, based on barite content, and spatial diversity within the crater. Samples that contained less than 1 wt.% Ba were excluded, as the low Ba content and associated low Ra activity would be below the analytical uncertainty thresholds required for precise-enough age calculations (e.g., ±~200 years). Selected hydrothermal sample powders were weighed and placed in 8 mL polypropylene sample tubes and sealed with rubber septa and epoxy to prevent the escape of the intermediate gaseous decay product ^{222}Rn. It is important to seal the samples and prevent escape of Rn gas because both ^{226}Ra and ^{235}U emit gamma radiation at an energy level of 186 keV, and this potential spectral interference makes measurement of ^{226}Ra at this energy level unreliable. Therefore, the activity of ^{214}Pb and/or ^{214}Bi, both short-lived daughter isotope of ^{226}Ra via decay of intermediate daughters ^{222}Rn and ^{218}Po, and significant emitters of gamma rays, can instead be used as a proxy for activity of ^{226}Ra as long as all daughter isotopes are in secular equilibrium with the ^{226}Ra parent, which requires that ^{222}Rn cannot escape (Jamieson et al., 2013). The sealed tubes were set aside for 21 days, representing five half-lives of ^{222}Rn ($t_{1/2}$ of 3.8 days), the time required for ^{222}Rn, ^{214}Pb and ^{214}Bi to attain secular equilibrium with ^{226}Ra. Activity values for ^{214}Pb and ^{214}Bi are consistently nearly

equal (R^2 = 0.99), thus the average values of the activities for these two isotopes were used as a proxy of ^{226}Ra.

Of the 29 hydrothermal samples used for Ra dating, 16 samples (including zero-age samples) also contain detectable ^{228}Ac, which is a short-lived daughter product and can be used as a proxy for ^{228}Ra. The ^{228}Ra/^{226}Ra activity ratio can be used to date very young chimneys (i.e. 3 to 35 years; Ditchburn et al., 2012). Radium-228 has a much shorter half-life (5.75 years) than ^{226}Ra, and the activity ratio ^{228}Ra/^{226}Ra decreases with time to the point where older rock samples no longer contain detectable ^{228}Ra after ~7 half-lives.

Gamma spectrometry analyses of the powdered samples was conducted using a CANBERRA high-purity Ge well detector and DSA-1000 Digital Signal Analyser. Data acquisitions were managed using Genie 2000 Basic Spectrometry Software, where count times for each sample ran for 24 hours. Gamma spectra were calibrated using BL-5 natural uranium ore, with a certified ^{226}Ra activity of 857 ± 38 Bq/g.

1.2.6 SMS deposit volume analysis

Jamieson et al. (2014) previously employed a method to calculate volumes of SMS deposits at the Endeavour segment, Juan de Fuca Ridge, by manually identifying sulphide edifices using high-resolution (<2m) bathymetry and outlining their sulphide footprints. Using GIS software, a horizontal cut-off was assigned for each footprint, marking the boundary of exposed sulphide material from the underlying volcanic or sedimentary substrate, which allows for an estimated volume of exposed sulphide material to be determined. Where hydrothermal mounds occur on a slope, a horizontal mid-point was

assigned such that hydrothermal material present below the horizontal cut-off was balanced by the incorporation of non-hydrothermal material in the volume estimation. A modified GIS-based approach was also implemented for Niua South. Using 50 cm resolution bathymetry of the crater coupled with the aid of complete video and photomosaic coverage of the entire crater floor, an estimate of the volume of surface and minor subsurface hydrothermal material was made. Subsequently, the combination of volume and density estimates of the deposits (i.e., tonnage) and their ages were then used to determine the rate at which they form on the seafloor. In this study, we interpolated a lower surface boundary of sulphide material using the surrounding bathymetry.

1.3. Thesis Objectives

Apart from Brothers volcano, arc-hosted hydrothermal systems have not been the subject of intensive study, especially in comparison to the numerous studies of mid-ocean ridge hosted hydrothermal systems such as Endeavour, TAG or EPR 9°N. The extensive mapping, visual surveys and sampling of the Niua South volcano provide an exceptional opportunity for a holistic geological characterization of an arc volcano-hosted hydrothermal system.

The Niua South hydrothermal system is also unique in that its spatial extent is confined to the interior of a 500 m diameter volcanic crater. The spatial constraints imposed by the crater have provided a unique opportunity for a comprehensive visual (video and still camera) survey of the crater, something that has never before been accomplished at any hydrothermal vent field on the seafloor. This allows for a complete inventory and

quantification of active hydrothermal venting and deposition within the vent field. The combined visual data sets, deposit volumes derived from high-resolution bathymetry, and rock and fluid sampling provide a unique opportunity to constrain deposit growth rates and chemical mass balance within the hydrothermal system.

The primary aim of this project was to characterize the geological setting, morphology, and composition of the Niua South hydrothermal vent field. This information will increase our understanding of the geological characteristics of arc volcano hosted hydrothermal systems in general. The second aim of this project was to produce a chemical mass balance of the Niua South hydrothermal system, including growth rates and depositional efficiency of hydrothermally-mobilized metals and sulphur.

1.4. Thesis Organization

This thesis consists of four chapters. Chapter 1 introduces the thesis, including study area and methodologies.

In Chapter 2, results and analysis of hydrothermal sulphide mineralogy and geochemistry of the Niua South crater are presented. This serves as the first detailed documentation of seafloor hydrothermal deposits at this location. The aim of the study was to determine the composition of hydrothermal sulphide chimneys based on petrographic observations of 30 sulphide samples, coupled with multi-element geochemical analyses. These results are compared to other studied deposits within the same arc and back-arc system.

Chapter 3 presents an investigation of the ages, volumes, and rates of hydrothermal sulphide accumulation within the Niua South crater. This is the first use of the ^{226}Ra/Ba dating method on hydrothermal deposits from Niua South. The combination of 50 cm resolution bathymetric maps and full video and photomosaic coverage of the crater floor allowed for an accurate discrimination of hydrothermal sulphide material from host rock. Using 3-D geological modelling software, the total maximum volume of hydrothermal sulphide material on the seafloor was calculated. The combination of samples ages, and volume estimation were used to determine mass accumulation rates of hydrothermal sulphide material.

Chapter 4 summarizes the main conclusions of this thesis and recommendations for future work.

Finally, the appendices contain: (A) detailed descriptions of each thin section with sample descriptions relevant to Chapter 2; (B) results of geochemical analyses for all elements analyzed by INAA and ICP-MS; (C) quality control data for standard reference materials related to geochemical analysis; and (D) visual porosity estimates based on hand samples and thin sections.

Repetition of details (e.g., background geology, methods) in the different chapters reflects the intent of Chapters 2 and 3 to each be submitted as standalone submissions to peer-reviewed journals.

1.5. References

Barrie, C. T., & Hannington, M. D. (1999). Classification of volcanic-associated massive sulfide deposits based on host-rock composition. *Volcanic-Associated Massive Sulfide Deposits; Processes and Examples in Modern and Ancient Settings*, *8*, p. 1–11.

Beaulieu, S. E., Baker, E. T., German, C. R., & Maffei, A. (2013). An authoritative global database for active submarine hydrothermal vent fields. *Geochemistry, Geophysics, Geosystems*, *14*(11), p. 4892–4905. https://doi.org/10.1002/2013GC004998.

Berkenbosch, H. A., de Ronde, C. E. J., Gemmell, J. B., McNeill, A. W., & Goemann, K. (2012). Mineralogy and Formation of Black Smoker Chimneys from Brothers Submarine Volcano, Kermadec Arc. *Economic Geology*, *107*(8), p. 1613–1633. https://doi.org/10.2113/econgeo.107.8.1613.

Berkenbosch, H. A., de Ronde, C. E. J., Paul, B. T., & Gemmell, J. B. (2015). Characteristics of Cu isotopes from chalcopyrite-rich black smoker chimneys at Brothers volcano, Kermadec arc, and Niuatahi volcano, Lau basin. *Mineralium Deposita*, *50*, p. 811–824. https://doi.org/10.1007/s00126-014-0571-y.

Clift, P. D., & Vroon, P. Z. (1996). Isotopic evolution of the Tonga arc during Lau Basin rifting; evidence from the volcaniclastic record. *Journal of Petrology*, *37*(5), p. 1153–1173. https://doi.org/10.1093/petrology/37.5.1153.

de Ronde, C.E.J., Humphris, S.E., Hoefig, T.W., Reyes, A.G., IODP Expedition 376 Scientists (2019). Critical role of caldera collapse in the formation of seafloor mineralization: The case of Brothers volcano. *Geology*, 47 (8), p. 762-766

de Ronde, C. E. J., Baker, E. T., Massoth, G. J., Lupton, J. E., Wright, I. C., Feely, R. A., & Greene, R. R. (2001). Intra-oceanic subduction-related hydrothermal venting, Kermadec volcanic arc, New Zealand. *Earth and Planetary Science Letters*, *193*, p. 359–369. https://doi.org/10.1016/S0012-821X(01)00534-9.

de Ronde, C. E. J., Faure, K., Bray, C. J., Chappell, D. A., & Wright, I. C. (2003). Hydrothermal fluids associated with seafloor mineralization at two southern Kermadec arc volcanoes, offshore New Zealand. *Mineralium Deposita*, *38*, p. 217–233. https://doi.org/10.1007/s00126-002-0305-4.

de Ronde, C. E. J., Hannington, M. D., Stoffers, P., Wright, I. C., Ditchburn, R. G., Reyes, A. G., et al. (2005). Evolution of a submarine magmatic-hydrothermal system: Brothers volcano, southern Kermadec Arc, New Zealand. *Economic Geology*, *100*(6), p. 1097–1133. https://doi.org/10.2113/gsecongeo.100.6.1097.

de Ronde, C. E. J., Baker, E. T., Massoth, G. J., Lupton, J. E., Wright, I. C., Sparks, R. J., et al. (2007). Submarine hydrothermal activity along the mid-Kermadec Arc, New Zealand: Large-scale effects on venting. *Geochemistry, Geophysics, Geosystems*, *8*(7), p. 1–27. https://doi.org/10.1029/2006GC001495.

de Ronde, C. E. J., Massoth, G. J., Butterfield, D. A., Christenson, B. W., Ishibashi, J., Ditchburn, R. G., et al. (2011). Submarine hydrothermal activity and gold-rich mineralization at Brothers Volcano, Kermadec Arc, New Zealand. *Mineralium Deposita*, *46*(5), p. 541–584. https://doi.org/10.1007/s00126-011-0345-8.

de Ronde, C. E. J., Butterfield, D. A., & Leybourne, M. I. (2012). Metallogenesis and Mineralization of Intraoceanic Arcs I: Kermadec - Introduction. *Economic Geology*, *107*(8), p. 1521–1525.

de Ronde, C. E. J., Hein, J. R., & Butterfield, D. A. (2014). Metallogenesis and mineralization of intraoceanic arcs II: The Aeolian, Izu-Bonin, Mariana, and Kermadec arcs, and the Manus backarc basin-introduction. *Economic Geology*, *109*(8), p. 2073–2077. https://doi.org/10.2113/econgeo.109.8.2073.

Ditchburn, R. G., de Ronde, C. E. J., & Barry, B. J. (2012). Radiometric dating of volcanogenic massive sulfides and associated iron oxide crusts with an emphasis on 226Ra/Ba and 228Ra/226Ra in volcanic and hydrothermal processes at intraoceanic Arcs. *Economic Geology*, *107*(8), p. 1635–1648. https://doi.org/10.2113/econgeo.107.8.1635.

Dupont, J., & Herzer, R. H. (1985). Effect of Subduction of the Louisville Ridge on the Structure and Morphology of the Tonga Arc. *Geology and Offshore Resources of Pacific Island Arcs-Tonga Region, Circum-Pacific Council for Energy and Mineral Resources Earth Science Series v. 2*, *2*, p. 323–332.

Embley, R. W., de Ronde, C. E. J., & Ishibashi, J. (2008). Introduction to special section on Active Magmatic, Tectonic, and Hydrothermal Processes at Intraoceanic Arc Submarine Volcanoes. *Journal of Geophysical Research: Solid Earth*, *113*(8), p. 8–13. https://doi.org/10.1029/2008JB005871.

Evans, G. N., Tivey, M. K., Seewald, J. S., & Wheat, C. G. (2017). Influences of the Tonga Subduction Zone on seafloor massive sulfide deposits along the Eastern Lau Spreading Center and Valu Fa Ridge. *Geochimica et Cosmochimica Acta*, *215*, p. 214–246. https://doi.org/10.1016/j.gca.2017.08.010.

Ewart, A., Collerson, K. D., Regelous, M., Wendt, J. I., & Niu, Y. (1998). Geochemical Evolution within the Tonga – Kermadec – Lau Arc – Back-arc Systems : the Role of Varying Mantle Wedge Composition in Space and Time, *39*(3), p. 331–368.

Fiske, R. S., Naka, J., Iizasa, K., Yuasa, M., & Klaus, A. (2001). Submarine silicic caldera at the front of the Izu-Bonin arc , Japan : Voluminous seafloor eruptions of rhyolite pumice. *GSA Bulletin*, *113*(7), p. 813–824.

Fouquet, Y., Von Stackelberg, U., Charlou, J. L., Erzinger, J., Herzig, P. M., Muhe, R., & Wiedicke, M. (1993). Metallogenesis in back-arc environments: The Lau basin example. *Economic Geology*, *88*(8), p. 2154–2181. https://doi.org/10.2113/gsecongeo.88.8.2154

Gartman, A., Hannington, M. D., Jamieson, J. W., Peterkin, B., Garbe-Schönberg, D., Findlay, A. J., et al. (2018). Boiling-induced formation of colloidal gold in black smoker hydrothermal fluids. Geology, 46(1), p. 1–4. https://doi.org/https://doi.org/10.1130/G39492.1.

Glasby, G. P., Iizasa, K., Hannington, M. D., Kubota, H., & Notsu, K. (2008). Mineralogy and composition of Kuroko deposits from northeastern Honshu and their possible modern analogues from the Izu-Ogasawara (Bonin) Arc south of Japan: Implications for mode of formation. *Ore Geology Reviews*, *34*(4), p. 547–560. https://doi.org/10.1016/j.oregeorev.2008.09.005.

Halbach, P., Pracejus, B., & Marten, A. (1993). Geology and mineralogy of massive sulfide ores from the central Okinawa trough, Japan. *Economic Geology*, *88*(8), p. 2210–2225. https://doi.org/10.2113/gsecongeo.88.8.2210.

Hannington, M. D., Jonasson, I. R., Herzig, P. M., & Petersen, S. (1995). Physical and chemical processes of seafloor mineralization at mid-ocean ridges, American Geophysical Union. p. 115–157. https://doi.org/10.1029/GM091p0115.

Hannington, M. D., de Ronde, C. E. J., & Petersen, S. (2005). Sea-Floor Tectonics and Submarine Hydrothermal Systems. *Economic Geology*, *100*, p. 111–141.

Hannington, M. D., Jamieson, J. W., Monecke, T., & Petersen, S. (2010). Modern Sea-Floor Massive Sulfides and Base Metal Resources: Toward an Estimate of Global Sea-Floor Massive Sulfide Potential. *Society of Economic Geologists Special Publication*, *15*, p. 111–141.

Iizasa, K., Asada, A., Mizuno, K., Katase, F., Lee, S., Kojima, M., & Ogawa, N. (2019). Native gold and gold-rich sulfide deposits in a submarine basaltic caldera, Higashi-Aogashima hydrothermal field, Izu-Ogasawara frontal arc, Japan. *Mineralium Deposita*, *54*, p. 117–132. https://doi.org/10.1007/s00126-018-0808-2.

Jamieson, J. W., Hannington, M. D., Clague, D. A., Kelley, D. S., Delaney, J. R., Holden, J. F., et al. (2013). Sulfide geochronology along the Endeavour Segment of the Juan de Fuca Ridge. *Geochemistry, Geophysics, Geosystems*, *14*(7), p. 2084–2099. https://doi.org/10.1002/ggge.20133.

Jamieson, J. W., Clague, D. A., & Hannington, M. D. (2014). Hydrothermal sulfide accumulation along the Endeavour Segment, Juan de Fuca Ridge. *Earth and Planetary Science Letters*, *395*, p. 136–148. https://doi.org/10.1016/j.epsl.2014.03.035.

Jankowski, P. (2012). *NI 43-101 Technical Report 2011 PNG, Tonga, Fiji, Solomon Islands, New Zealand, Vanuatu and the ISA*.

Merle, S. G., Embley, R. W., Lupton, J. E., Baker, E. T., Resing, J. A., & Lilley, M. (2008). *Northeast Lau Basin, R/V Thompson Expedition TN227*.

Parson, L. M., & Hawkins, J. W. (1994). Two-stage ridge propagation and the geological history of the Lau backarc basin. *Proceedings of the Ocean Drilling Program, Scientific Results*, *135*(1990), p. 819–828. https://doi.org/10.2973/odp.proc.sr.135.153.1994.

Pearce, J. A. (1983). Role of the Sub-continental Lithosphere in Magma Genesis at Active Continental Margins. In C. J. Hawkesworth & M. J. Norry (Eds.), *Continental basalts and mantle xenoliths* (pp. 230–249). Nantwich, Cheshire, England: Shiva Publication Ltd.

Pearce, J. A., & Peate, D. W. (1995). Tectonic implications of the composition of volcanic arc magmas. *Ann. Rev. Earth Planet. Sci*, *23*, p. 251–285.

Resing, J. A., Embley, R. W., & Merle, S. G. (2012). *Submarine Ring of Fire-2012 (SRoF-12) Northeast Lau Basin: R/V Roger Revelle Expedition RR1211, Cruise Report Sept 9-25, 2012, Suva-Samoa*.

Ryan, W. B. F., Carbotte, S. M., Coplan, J. O., O'Hara, S., Melkonian, A., Arko, R., et al. (2009). Global multi-resolution topography synthesis. *Geochemistry, Geophysics, Geosystems*, *10*(3). https://doi.org/10.1029/2008GC002332

Sager, W., Chris, J. M., & Abrahamsen, N. (1994). Paleomagnetic Constraints on Tonga Arc Tectonic Rotation from Sediments Drilled at Sites 840 and 841. *Proceedings of the Ocean Drilling Program, Scientific Results*, p. 763–783. https://doi.org/10.2973/odp.proc.sr.135.119.1994.

Smith, I. E. M., Worthington, T. J., Stewart, R. B., Price, R. C., & Gamble, J. A. (2003). Felsic volcanism in the Kermadec arc, SW Pacific: crustal recycling in an oceanic setting. *Geological Society of London Special Publication*, *219*, p. 99–118.

Stern, R. J. (2002). Subduction zones. *Reviews of Geophysics*, *40*(4), p. 1395–1406. https://doi.org/10.1007/978-90-481-8702-7_149.

Tatsumi, Y., & Eggins, S. (1995). *Subduction Zone Magmatism*. Cambridge, Massachusetts: Blackwell Science.

Wright, I. C., de Ronde, C. E. J., Faure, K., & Gamble, J. A. (1998). Discovery of hydrothermal sulfide mineralization from southern Kermadec arc volcanoes (SW Pacific). *Earth and Planetary Science Letters*, *164*, p. 335–343.

Yang, K., & Scott, S. D. (2006). Magmatic fluids as a source of metals in seafloor hydrothermal systems. *Back Arc Spreading Systems: Geological, Biological, Chemical and Physical Interactions: Geophysical Monograph*, *166*, p. 163–184.

2. Mineralogy and Geochemistry of Hydrothermal Deposits from the Niua Volcano, Tofua Arc

2.1. Introduction

Seafloor hydrothermal systems are known to occur in all submarine tectonic settings, including mid-ocean ridges and volcanic arc and back-arcs (Hannington et al., 2005). Along intraoceanic arcs, where oceanic crust of one tectonic plate is subducting beneath that of an adjacent plate, the influence of subducted sediments and volatiles released from the hydrated subducting slab on the overlying mantle and crust affects the types of lavas that erupt onto the seafloor (Pearce and Peate, 1995; Stern, 2002). The volatiles released from these subducting processes serve as important transporting agents for trace elements that are typically enriched in arc lavas (Yang and Scott, 1996). As a result, hydrothermal fluids and associated seafloor mineral deposits along intraoceanic arcs are compositionally different from those hosted on typical mid-ocean ridges (de Ronde et al., 2001; Fouquet et al., 1993; Hannington et al., 2005). In many cases, the composition of hydrothermal fluids in arc-related settings reflect a more felsic composition, derived from the leaching of felsic host rocks. Furthermore, arc-related fluids can also be affected by magmatic volatile contributions or subseafloor phase separation, the latter of which is more likely to occur at shallower depths of arc volcano summits, relative to mid-ocean ridges (Monecke et al., 2014). In particular, arc-related hydrothermal systems have garnered significant interest due to the potential high grades of major and trace elements of economic interest (i.e. Zn, Pb, Ag, and Au), especially when compared to mid-ocean

ridge deposits (Hannington et al., 2010). So far, studies of subduction-related hydrothermal systems have focused largely on back-arc settings (Fouquet et al., 1993, 2018; Yang and Scott, 2002; Koschinsky et al., 2002; Ishibashi et al., 2006; Ferrini et al., 2008; Mottl et al., 2011; Yeats et al., 2014; Johns et al., 2014; Wohlgemuth-Ueberwasser et al., 2015; Evans et al., 2017; Seewald et al., 2019). Furthermore, our understanding of hydrothermal systems located on arc volcanoes is largely limited to studies from the Brothers arc volcano on the Kermadec Arc (Baker et al., 2012; Berkenbosch et al., 2012; de Ronde et al., 2003, 2005, 2011, 2019; Embley et al., 2012; Wright et al., 1998).

The Niua volcano, a 1,500 m high, dual-summit submarine intraoceanic arc volcano, situated near Tonga on the northern extent of the Tofua Arc, southwest Pacific Ocean, contains a volcanic crater on the flank of the southern summit that hosts the active Niua South hydrothermal vent field. Hydrothermal venting within this crater has resulted in the accumulation of hydrothermal sulphide material forming chimneys and mound deposits. In 2016, scientists aboard the R/V *Falkor* visited the Niua South vent field during the *Virtual Vents* cruise (Kwasnitschka, 2016) sponsored by the Schmidt Ocean Institute. During this cruise, the entire ~500 m diameter crater was visually surveyed, and rock and fluid samples were collected using the remotely-operated vehicle (ROV) *ROPOS*. In this chapter, the formation of the Niua South deposit is documented through the analysis of high-resolution bathymetry and ROV video. The composition of the deposit is investigated through petrographic and geochemical analyses of a suite of 33 chimney and talus samples collected from the deposit. The overall goal of this study is to understand the formation of seafloor hydrothermal deposits hosted on arc volcanoes, including their

controls on metal endowment and resource potential. The composition and style of hydrothermal deposition at Niua South is compared to other arc- and back-arc-hosted hydrothermal systems along the Tofua-Kermadec arc and back-arc.

2.2. Geological Setting

Niua volcano is situated near the northern terminus of the Tofua arc (Resing et al., 2012). The Tofua-Kermadec arc system extends ~2,500 km along a south-southwest trend from Tonga to the North Island of New Zealand and represents a convergent margin of westward subduction of the Pacific plate under the Indo-Australian plate (Fig. 1.1). Twenty-three sites of either confirmed or inferred (from water column plume surveys) active hydrothermal systems have been identified along the northern Tofua arc, three of which are known to host hydrothermal sulphide deposits (Niua South, Volcano 18, and Volcano 19; Beaulieu et al., 2013; Lee et al., 2015; Monecke et al., 2016; Stoffers et al., 2006). South of the Tofua arc, the 1,200 km Kermadec arc hosts 29 submarine volcanic centers, but only three sites are known to host significant hydrothermal sulphide deposits (Brothers volcano, Rumble II West volcano, and Clark volcano). However, 19 other sites along the Kermadec arc front and rear-arc have confirmed or inferred active venting (Beaulieu et al., 2013; Monecke et al., 2016). With the exception of Brothers volcano, only limited exploration (if any, beyond water column plume surveys) has taken place at many of the other sites (de Ronde et al., 2007).

The Lau Basin is an actively forming back-arc basin situated between the Tofua arc and the Lau Ridge (Fig. 1.1). The majority of sites with either confirmed or inferred hydrothermal venting within this region are largely confined to the main back-arc spreading centers (i.e., Central Lau Spreading Center (CLSC), Intermediate Lau Spreading Center (ILSC), Eastern Lau Spreading Center (ELSC), and Valu Fa Ridge (VFR)) that extend from 18°S to 23°S. Several volcanoes are located in the northeast region of the Lau Basin, including Niuatahi, West Mata, East Mata, and the North Mata group (Taha, Ua, Tolu, Fa, Nima, Ono, and Fitu), which is located ~50 km west of Niua (Fig. 1.2). Five of the North Mata volcanoes are hydrothermally active (exceptions are Nima and Taha; Baker et al., 2019). For the active sites, high-temperature venting (based on plume characteristics) is confirmed at all but two sites (East Mata and Fa; Baker et al., 2019).

Niua volcano consists of two coalesced volcanic centers: Niua North and Niua South (Fig. 1.3). The two volcanic summits are ~9 km apart from each other, and hydrothermal venting has been confirmed on both centers. Data from limited sampling of volcanic rocks near and within the hydrothermal vent sites indicate that the magma composition of the volcano is dominantly rhyolitic (Resing et al., 2012; Haase et al., 2018); however, more mafic to intermediate composition lavas have been sampled from along the northern and western flanks of the volcano (Haase et al., 2018). Hydrothermal venting at Niua North occurs within a small (<25 m wide) depression located at 750 mbsl on the western flank of the northern summit of the volcano. Venting is characterized by vigorous emission of native sulphur and droplets of liquid CO_2 (Resing et al., 2012). At Niua

South, hydrothermal activity occurs within a 500-m wide crater, at an average depth of 1,180 mbsl (Fig. 2.1).

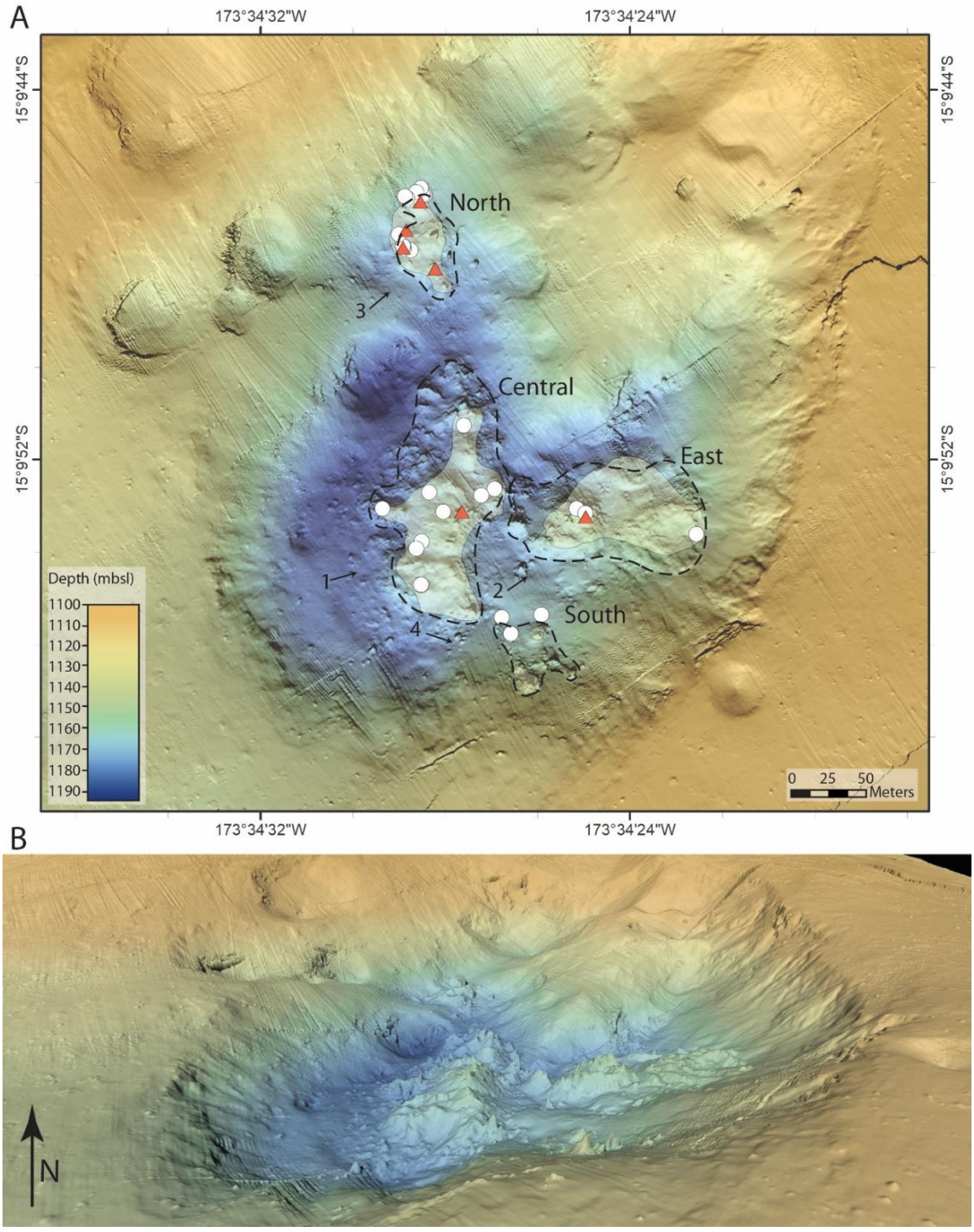

Figure 2.1. High-resolution (50 cm) bathymetric map of the Niua South study site. (a) Rock sampling locations are denoted by white circles. Black dashed lines mark the boundaries of hydrothermal mound material present in each of the four hydrothermal regions within the crater. Yellow shaded areas outline diffuse venting and were determined by visual observations of ROV video surveys. Red triangles represent the locations of high-temperature (300–325°C) chimneys. Numbers (1-4) and arrows indicate the location and viewing direction of the four oblique views in Figure 2.2. The high-resolution AUV bathymetry was provided by Nautilus Minerals Inc., mapped during the R/V *Kilo Moana* expedition to the Lau Basin in 2011. (b) Oblique view of the crater highlights hydrothermal mounds and chimneys within the crater.

2.3. Methods

The *Virtual Vents* expedition consisted of six separate dives using ROV ROPOS. Three dives were specifically dedicated to conducting still photo and video surveys of the entire crater, and three dives were dedicated for rock, fluid, and biological sampling (Fig. 1.5). Thirty sulphide-sulphate hydrothermal samples were collected. Samples were collected with a goal of obtaining the most diverse representation of the composition of the deposits. Thirty-three subsamples were selected for thin section petrographic analysis with matching powdered subsamples for multi-element geochemical analyses. Three additional powdered subsamples do not have accompanying thin sections. Thin sections were cut to be representative of the samples that were collected. Thin sections were analyzed with a petrographic microscope under both transmitted and reflected light (Appendix A). Scanning electron microscope (SEM) and X-ray diffraction (XRD) analyses were used for further mineral phase identification. Scanning electron microscope analysis was carried out on a FEI MLA 650F scanning electron microscope energy dispersive x-ray (SEM-EDX) detector. High-resolution images were captured using both

electron backscatter and secondary electron detection settings. Elemental analyses were performed between 15-20 kV under high vacuum, with a working distance of 12 mm. X-ray diffraction analysis was carried out on a Rigaku Ultima-IV instrument equipped with a Cu source, monochromator and scintillation detector operating at 40 kV and 44 mA. Analyses were completed with continuous sampling for Cu Kα 2θ ranging from 5°-100° in steps of 0.02°.

Subsamples were powdered using a tungsten carbide vessel in a shatter box. Bulk geochemical analyses for each powdered subsample were conducted at ActLabs, in Ontario, Canada, by instrumental neutron activation analysis (INAA) for Ag, As, Au, Ba, Br, Ce, Co, Cr, Cs, Eu, Fe, Hf, Ir, La, Lu, Na, Nd, Ni, Sb, Sc, Se, Sm, Ta, Tb, Th, U, W, Yb, and Zn, and inductively coupled plasma mass spectrometry (ICP-MS) with a Na_2O_2 fusion preparation for Al, B, Be, Bi, Ca, Cd, Cu, Dy, Er, Ga, Gd, Ge, Ho, In, K, Li, Mg, Mn, Mo, Nb, Pb, Pr, Rb, S, Si, Sn, Sr, Te, Ti, Tl, Tm, V, and Y (Appendix B). For the INAA method, results are all within 6% of certified values for the GXR-1 standard reference material (Appendix C). For ICP-MS, accuracy estimates are all within 6% using three repeat measurements of the OREAS 922 standard reference material. On average, the precision is 3% based on three repeat measurements of OREAS 922 and three repeat measurements of the OREAS 622 standard reference material (Appendix C). These uncertainties increase for reported concentrations that are within an order of magnitude of their respective detection limits.

2.4. Hydrothermal Chimney and Mound Morphology

The hydrothermal vent field at Niua South is located within a circular depression on the flank of the volcano (Fig 2.1). The crater floor reaches a maximum depth of ~1,190 m below sea level on the western edge, and, on average the volcanic floor (i.e., excluding the hydrothermal mounds) is approximately 1,180 m deep. The boundary walls along the western side of the crater reach heights of up to 50 m, whereas the more steeply dipping eastern walls vary from 40 to 80 m high. The location of the crater, relative to the volcano summit (~2 km SE with a depth difference of ~546 m), is unusual, as hydrothermal activity associated with arc volcanoes along the Tofua-Kermadec arc is typically focused within large (>1–2 km wide) summit calderas (de Ronde et al., 2005; Kim et al., 2006; Stoffers et al., 2006; Leybourne et al., 2012a, 2012b). The Gondou hydrothermal vent field, within the actively-rifting Okinawa Trough, is, like Niua South, situated along the flank of a caldera volcano (Minami and Ohara, 2017), suggesting that the occurrence of hydrothermal venting on the flank of the volcano is not restricted to the Tofua-Kermadec arc.

The floor of the Niua South crater consists of several individual or clusters of hydrothermal mounds that form on a substrate of felsic pumice fragments (Fig. 2.1a). Individual hydrothermal mounds contained within the crater can reach heights of 25 m, but more typically rise 10 to 15 m above the crater floor (Fig. 2.1b, Fig 2.2). Basal dimensions of the mounds vary between 15 and 20 m. Where several hydrothermal mounds coalesce, the hydrothermal structures can be up to 60 m long, and can form irregular-shaped, elongate crests. Mounds in the central and eastern regions of the crater

are overall much larger than those in the northern and southern regions (Fig. 2.2). Hydrothermal mounds are typically topped with chimney complexes that contain multiple isolated or coalescing chimney spires that reach heights of up to ~5 m above the mounds. Chimney complexes also form along the flanks of the mounds.

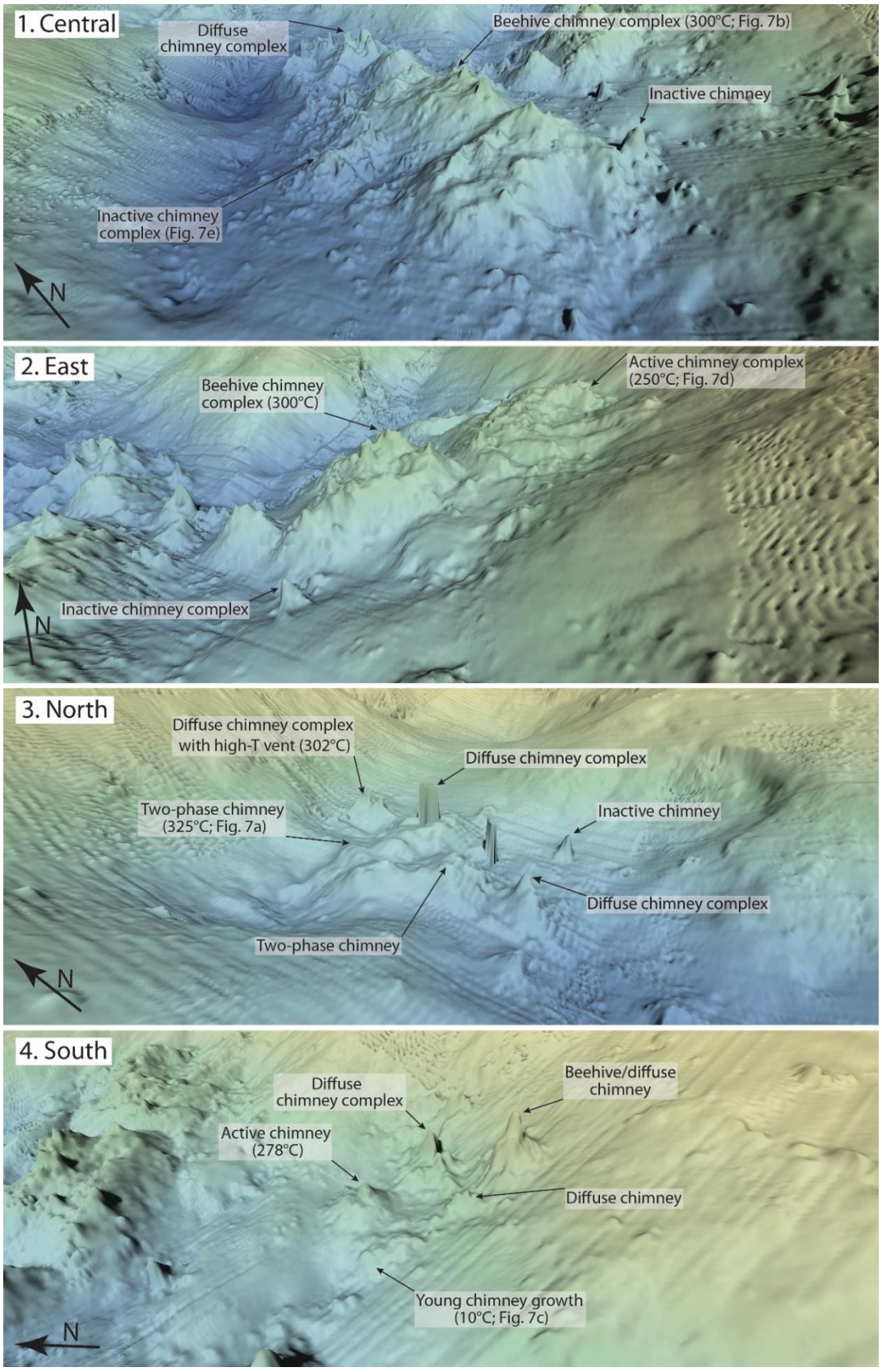
1. Central
Diffuse chimney complex
Beehive chimney complex (300°C; Fig. 7b)
Inactive chimney
Inactive chimney complex (Fig. 7e)
N
2. East
Active chimney complex (250°C; Fig. 7d)
Beehive chimney complex (300°C)
Inactive chimney complex
N
3. North
Diffuse chimney complex with high-T vent (302°C)
Diffuse chimney complex
Two-phase chimney (325°C; Fig. 7a)
Inactive chimney
Diffuse chimney complex
Two-phase chimney
N
4. South
Beehive/diffuse chimney
Diffuse chimney complex
Active chimney (278°C)
Diffuse chimney
Young chimney growth (10°C; Fig. 7c)
N

Figure 2.2. Oblique views for four separate regions of the crater: central, east, north, and south. The number for each region corresponds to the numbered arrows in Figure 2.1.

The actively venting chimneys are generally the tallest standing structures (relative to inactive chimneys) and can display hydrothermal flow regimes that range from focused, black or white smoke to clear, diffuse venting. Three active chimneys, located at an average depth of 1164 mbsl in the northern region, are emitting a two-phase hydrothermal fluid, noted by visible boiling within the first few centimetres of the vent orifice (Fig. 2.3a; Gartman et al., 2018). The maximum fluid temperature recorded at one of these vents, 325°C, is the highest venting temperature recorded at Niua South, and corresponds to the temperature of the seawater two-phase boundary at that depth (Bischoff and Rosenbauer, 1984). Beehive structures are common at the peaks of active spires and their steep cone-shaped tops often emit black smoke (Fig. 2.3b). A range of temperatures (250–302°C) were recorded from these types of active chimneys. Areas of clear, lower temperature (≤250°C) diffuse venting, identified by the presence of shimmering fluid, have been identified on the flanks and bases of both chimneys and mounds, and are often associated with young chimney growth (Fig. 2.3c). Typical vent fauna includes *Ifremeria nautilei* and *Alviniconcha* sp. gastropod snails, bythograeid and *Paralomis sp.* crabs, polynoid scaleworms and alvinocarid shrimp (Kwasnitschka et al., 2016). White bacterial mats often coat the outer surfaces or occur within horizontal cracks in active chimneys (Fig. 2.3b-d). Active venting is occurring at ~70% of the major chimney complexes within the crater, while the remaining 30% are inactive. Nine of the active chimneys are venting high-T fluid (≥300°C), either confirmed by direct temperature measurements or inferred by the presence of focused emission of black smoke or boiling. Overall, roughly

25 lower-temperature venting chimney complexes were identified, with many more sites of diffuse venting. Inactive chimneys located adjacent to active vents are generally tall, free-standing, intact structures. In contrast, spires within inactive chimney complexes are typically shorter than active spires with many showing evidence of partial collapse. Inactive chimneys and mounds do not host bacterial mats and the density of animals on their outer surfaces is significantly lower (Fig. 2.3e). The abundance of chimney debris on the flanks of the hydrothermal mounds suggests that the collapse of spires is a common occurrence (Fig. 2.3e), and the accumulation of chimney debris can be an important component of mound accretion (Hannington et al., 1995).

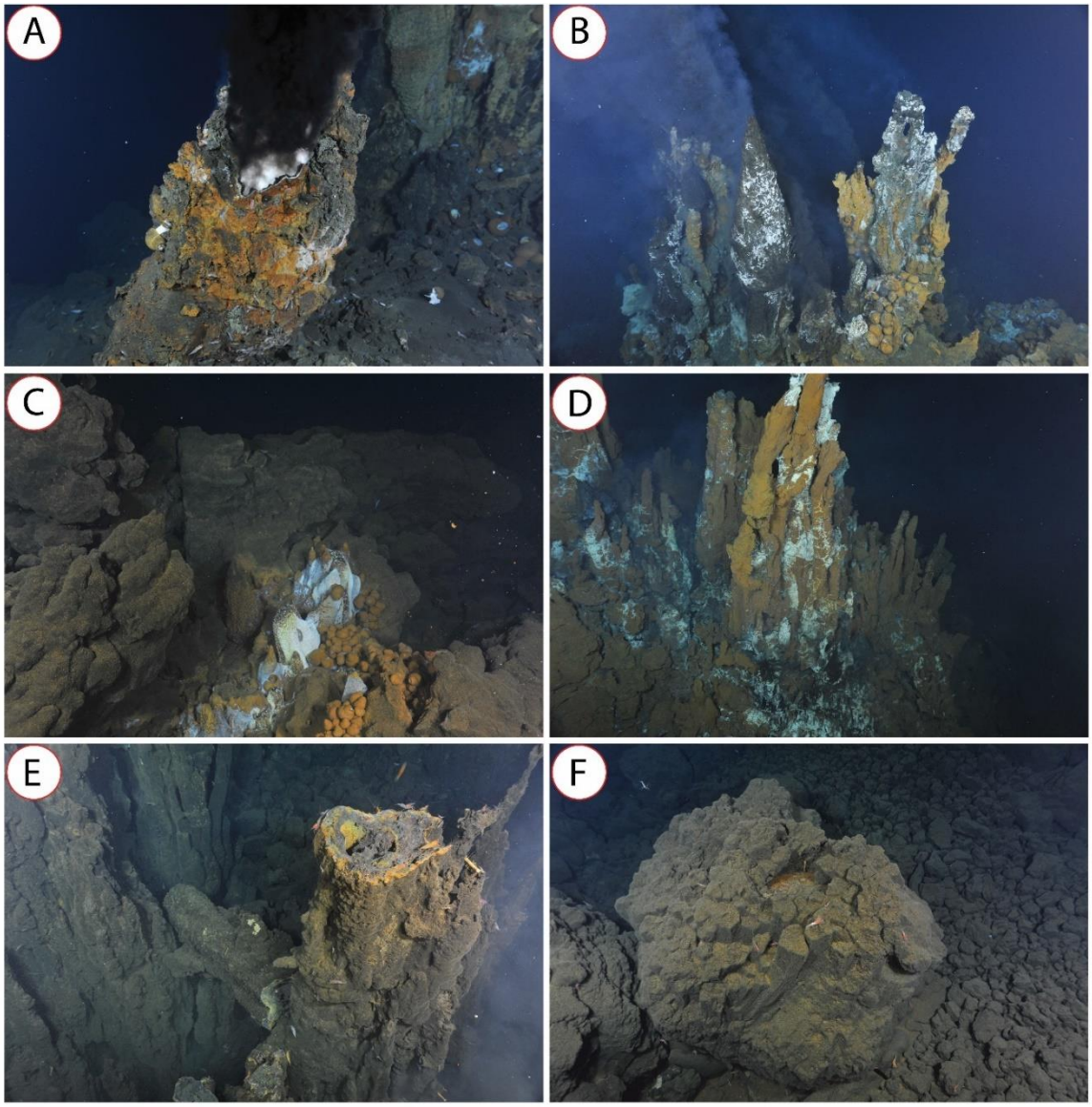

Figure 2.3. Hydrothermal chimneys and volcaniclastic rocks observed at Niua South. (a) Focused, two-phase, black smoker chimney in the northern region. Boiling fluids (T_{Max} of 325°C) can be seen within a few centimetres of the vent orifice. The width of the vent orifice is ~20 cm. (b) Active chimney complex venting black and grey smoke. Several chimneys on the left side are topped with ~1 m tall beehive structures. Select spires within the chimney complex are no longer active. (c) Isolated area of young chimney growth amongst chimney talus. Fluids venting at this site were clear and diffuse. The small diffuse vent at the back is ~20 cm wide. (d) Chimney complex largely exhibiting diffuse venting out of the base and sides of chimneys. White bacterial mats coat the tips and cracks of these chimneys. The central collection of active spires is ~80 cm wide at the base. (e) Toppled-over inactive chimney on the flanks of a large inactive chimney complex. The width of the exposed chimney trunk is ~70 cm. (f) Large block of dacite

displaying columnar jointing on a base of fragmented felsic material. The block is ~1 m wide.

2.5. **Hydrothermal Deposit Mineralogy**

Hydrothermal chimneys and talus samples within the Niua South crater are composed of sulphide and sulphate minerals that commonly occur at other arc- and back-arc-hosted vent fields, including barite, chalcopyrite, sphalerite, pyrite, marcasite, anhydrite, and minor phases such as tetrahedrite-tennantite, Pb-As sulphosalts, Pb-As-Sb sulphosalts, bornite, digenite, covellite, and hematite (Berkenbosch et al., 2012; de Ronde et al., 2003; Evans et al., 2017; Fouquet et al., 1993; Iizasa et al., 2019; Ikehata et al., 2015; Kim et al., 2006; Yeats et al., 2014). Hydrothermal samples at Niua South are assigned to three mineral suites based on the relative abundances of barite, sphalerite, and chalcopyrite (Fig. 2.4). A barite-rich suite consists of a mineral assemblage dominated by barite and sphalerite with some pyrite/marcasite and minor (1–5% average modal abundance) galena, chalcopyrite, and sulphosalts (Fig. 2.4a). Trace amounts (<1%) of Pb-As sulphosalts and Pb-As-Sb sulphosalts occur within this assemblage. Secondary Cu-sulphide phases are rare in this assemblage; however, disseminated covellite is present in some of the samples. A sphalerite-rich suite contains a more diverse mineral assemblage, but is still primarily dominated by barite (45%; Fig. 2.4b). Relative proportions of chalcopyrite and sphalerite are near equal (~20%), with chalcopyrite commonly lining the interior fluid conduits of chimneys and growth of sphalerite concentrated along the chimney exterior walls. Sulphosalts within this suite are predominantly tennantite-

tetrahedrite, with lesser Pb-As and Pb-As-Sb sulphosalts. Lastly, a chalcopyrite-rich suite is dominated by chalcopyrite or anhydrite, while the combined abundances of barite, pyrite, marcasite, and sphalerite average less than 20% (Fig. 2.4c). Replacement of chalcopyrite by secondary Cu-sulphide phases (i.e., bornite, digenite, and covellite) is common within the chalcopyrite-rich assemblage; however, their modal abundances are too low to be illustrated in Figure 2.4. One active chimney sample dominated by anhydrite (~ 95%) is included in the chalcopyrite-rich suite despite a minor abundance of chalcopyrite (~5%). A maximum fluid temperature of 300°C was recorded at this chimney.

These three mineral assemblages are commonly found at many seafloor hydrothermal deposits, and reflect changes in temperature and pH associated with differing degrees of hydrothermal fluid-seawater mixing (Hannington et al., 1995; Gartman et al., 2019). The association between these mineral assemblages and temperatures of formation have now been well established within seafloor hydrothermal systems (Fouquet et al., 1988; Rona et al., 1993; Hannington et al., 1995; Tivey, 1995). Therefore, at Niua South the barite-rich suite is associated with a low-temperature assemblage (<~200°C), the sphalerite-rich suite represents an intermediate-temperature assemblage (~200–300°C), and the chalcopyrite-rich suite represents a high-temperature assemblage (>~300°C).

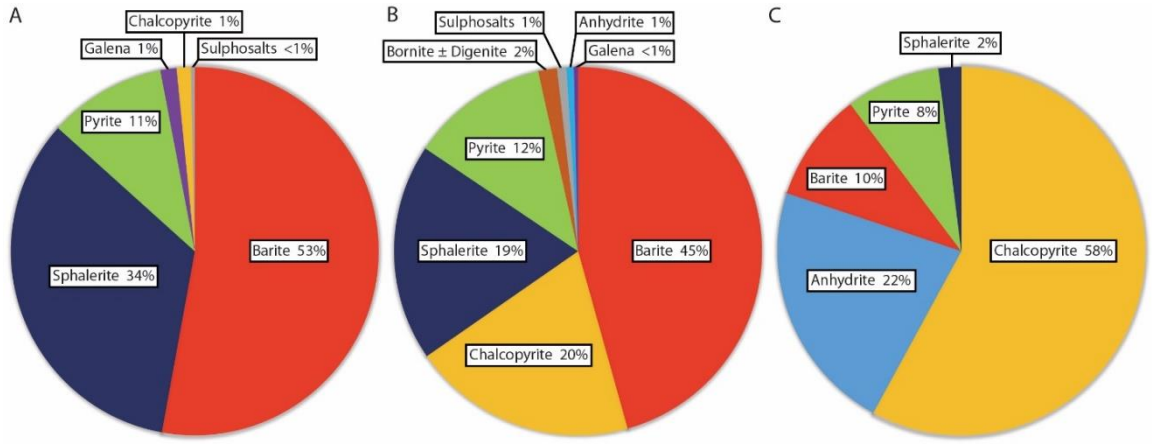

Figure 2.4. Relative proportions of mineral phases, based on thin section observations, and subdivided into low-, intermediate-, and high-temperature sample suites. The three mineral assemblages consist of different associations of minerals governed largely by changes in temperature, pH, and Eh, associated with the mixing of hot hydrothermal fluid with cold seawater. Minerals found in trace abundance (<1%) from all sample suites (e.g., covellite, hematite, amorphous silica, gold, Bi-tellurides) are not significant enough to be plotted.

2.5.1 Barite and anhydrite

Of the 33 hydrothermal samples collected from within the crater, barite is the most commonly occurring mineral phase, and half of the samples are composed of at least 50% barite. Barite occurs with a variety of crystal habits, including euhedral to subhedral bladed and tabular crystals, acicular crystals, and plumose crystals. Both bladed and acicular forms often occur as radiating clusters. Crystal sizes reach up to 50 mm, with smaller crystals typically occurring near the exterior of the chimney samples, whereas coarser-grained crystals are found within interior pore spaces of the sample groundmass, where growth is largely uninhibited by other mineral phases (Fig. 2.5a). Acicular barite occurs exclusively at the exterior of chimney samples. Plumose barite occurs in the interior groundmass of sphalerite- and barite-dominated samples, or near the exterior of

chalcopyrite-rich samples. Plumose texture in barite typically consists of fine-grained branching, bladed barite that is mantled by pyrite blebs and subsequently overgrown by massive sphalerite (Fig. 2.5b). Chalcopyrite and other high-temperature (>300°C) sulphide minerals are commonly overgrowing or mantling plumose barite, rather than sphalerite, in samples where chalcopyrite is the dominant mineral in the sample (Fig. 2.5d). While it is uncommon, relict plumose texture has been observed in massive sphalerite, where the inner barite crystals have been psuedomorphed by the surrounding sphalerite (Fig. 2.5e). In these cases, characteristic blebs of pyrite mark the former boundaries of barite crystals. Evidence of barite crystal resorption also includes outlines of coarse-grained barite crystals that are visible in massive chalcopyrite overgrowths (Fig. 2.5f). Results of SEM analysis indicates that in this case, relict barite crystals are now infilled by amorphous silica. Barite is generally absent in thick chalcopyrite inner conduit linings.

The presence of anhydrite is limited to five samples that were collected exclusively from the walls and tips of high-temperature black smoker chimneys. Overall, these samples consist predominantly of anhydrite and chalcopyrite, with minor to trace pyrite, marcasite, and sphalerite. Anhydrite occurs mainly as anhedral to subhedral bladed and tabular crystals that range from 25 μm to 1 mm. The smallest crystals tend to occur in compact clusters with very little associated pore space (Fig. 2.5g). Anhydrite is virtually absent from all inactive chimney samples.

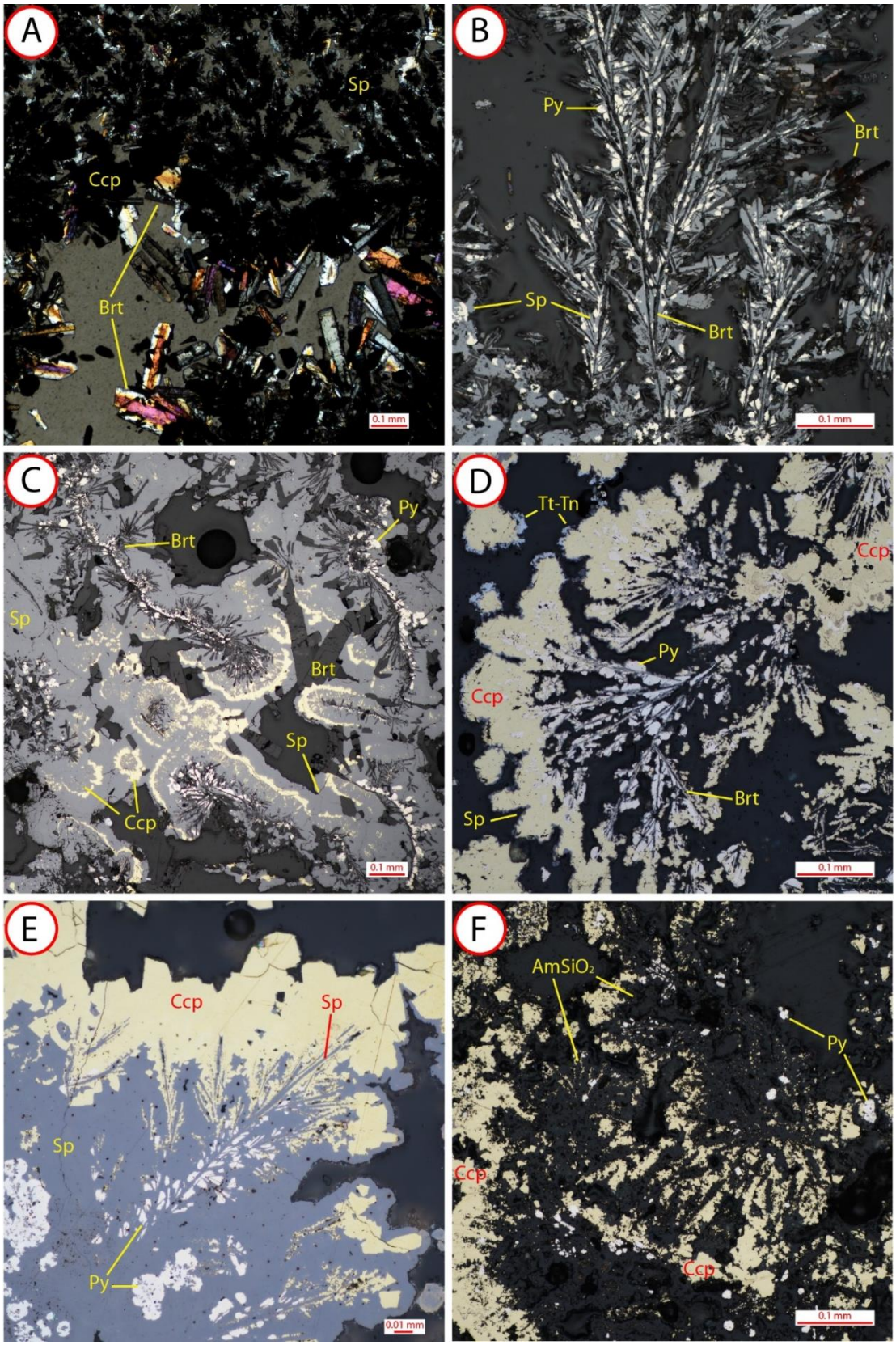
A
Sp
Ccp
Brt
0.1 mm
B
Py
Brt
Sp
Brt
0.1 mm
C
Py
Brt
Sp
Brt
Sp
Ccp
0.1 mm
D
Tt-Tn
Ccp
Py
Ccp
Brt
Sp
0.1 mm
E
Ccp
Sp
Sp
Py
0.01 mm
F
AmSiO2
Py
Ccp
Ccp
0.1 mm

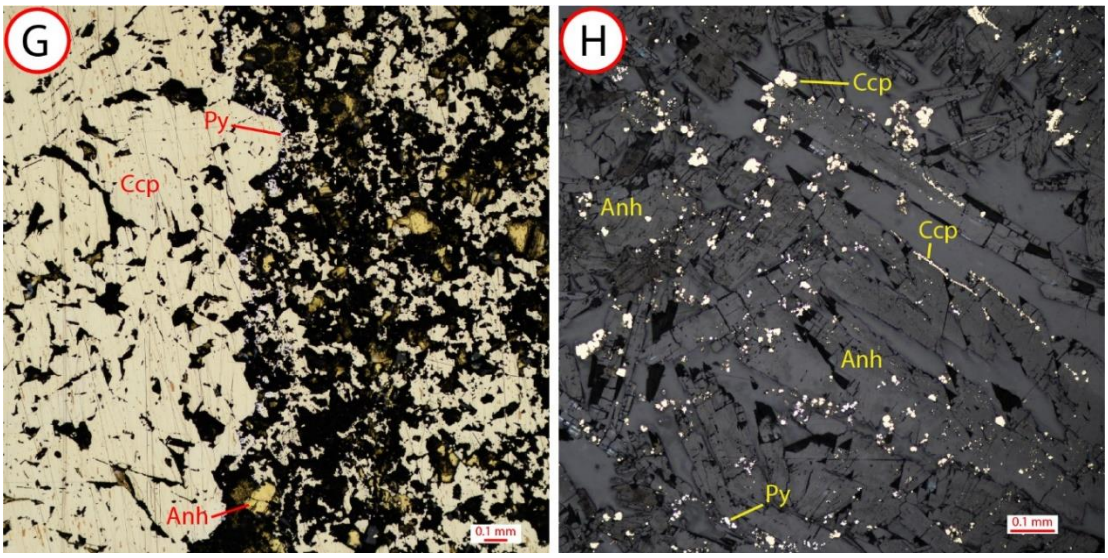

Figure 2.5. Photomicrographs of common textures observed in barite and anhydrite. All photos are captured under reflected light, except for (g), which was taken using a combination of reflected and transmitted light. (a) Coarse-grained bladed barite is exclusive to infilling of open pore spaces. Barite within the interior groundmass is largely overgrown by later sulphide minerals and is comparatively fine-grained. (b) Plumose texture, with pyrite blebs mantle thin branching blades of barite and are later overgrown by sphalerite. (c) Slightly elongate, and irregular plumose texture with the same characteristic mineralization style as the previous image. Chalcopyrite has overgrown some of the massive sphalerite and also forms intergrowths. Chalcopyrite disease in sphalerite increases in intensity away from the inner barite. Late sphalerite overgrows pre-existing sulphide minerals. (d) Plumose texture with abundant pyrite mantling, and subsequent overgrowths of chalcopyrite. Small patches of remnant sphalerite within massive chalcopyrite suggests that extensive replacement of sphalerite has occurred. (e) Relict plumose texture in which the inner barite has been overgrown and pseudomorphed by sphalerite. Intact blebs of pyrite outline the boundaries of relict barite crystals. (f) Pseudomorphed barite with massive chalcopyrite overgrowth. The defined boundaries of chalcopyrite overgrowths have the appearance of a bladed crystal habit, but now contain amorphous silica. (g) Anhydrite is largely overgrown by massive chalcopyrite and is no longer present within the chalcopyrite vent lining (left). (h) Dense growth of bladed anhydrite with sparse sulphide mineral overgrowth. A thin mantle of chalcopyrite is also present. Mineral abbreviations are based on Kretz (1983).

2.5.2 Chalcopyrite and tetrahedrite-tennantite

Chalcopyrite commonly forms as overgrowths of pyrite, barite, and sphalerite in areas of focused, high-temperature fluid flow (Fig. 2.6a) and as up to 5 cm thick massive layers along the lining of interior open fluid conduits (Fig. 2.6b). In some cases, chalcopyrite is overgrown by late-stage, low-temperature sulphide minerals (i.e., sphalerite, galena, Pb-As sulphosalts, Pb-As-Sb sulphosalts) and barite. Chalcopyrite is also commonly found in sphalerite as "chalcopyrite disease", where chalcopyrite occurs as disseminated replacement within and along the edges of sphalerite grains (Fig. 2.6c; Barton Jr. & Bethke, 1987; Eldridge et al., 1983). Chalcopyrite is also intergrown with sphalerite, as interlocking irregular-shaped crystals of both mineral phases (Fig. 2.6d). Within selected samples, chalcopyrite occurs as alternating bands with sphalerite along with occasional intergrowths of blebby pyrite (Fig. 2.6e). Chalcopyrite also forms exsolution lamellae in some bornite (Fig. 2.6f), which may indicate contemporaneous growth of bornite-digenite and chalcopyrite from an intermediate solid solution (Li et al., 2018). The northern region of the crater contains the greatest average abundance of chalcopyrite, with several samples containing up to 70% modal abundance. Chalcopyrite-dominated samples in the remainder of the crater are not as common.

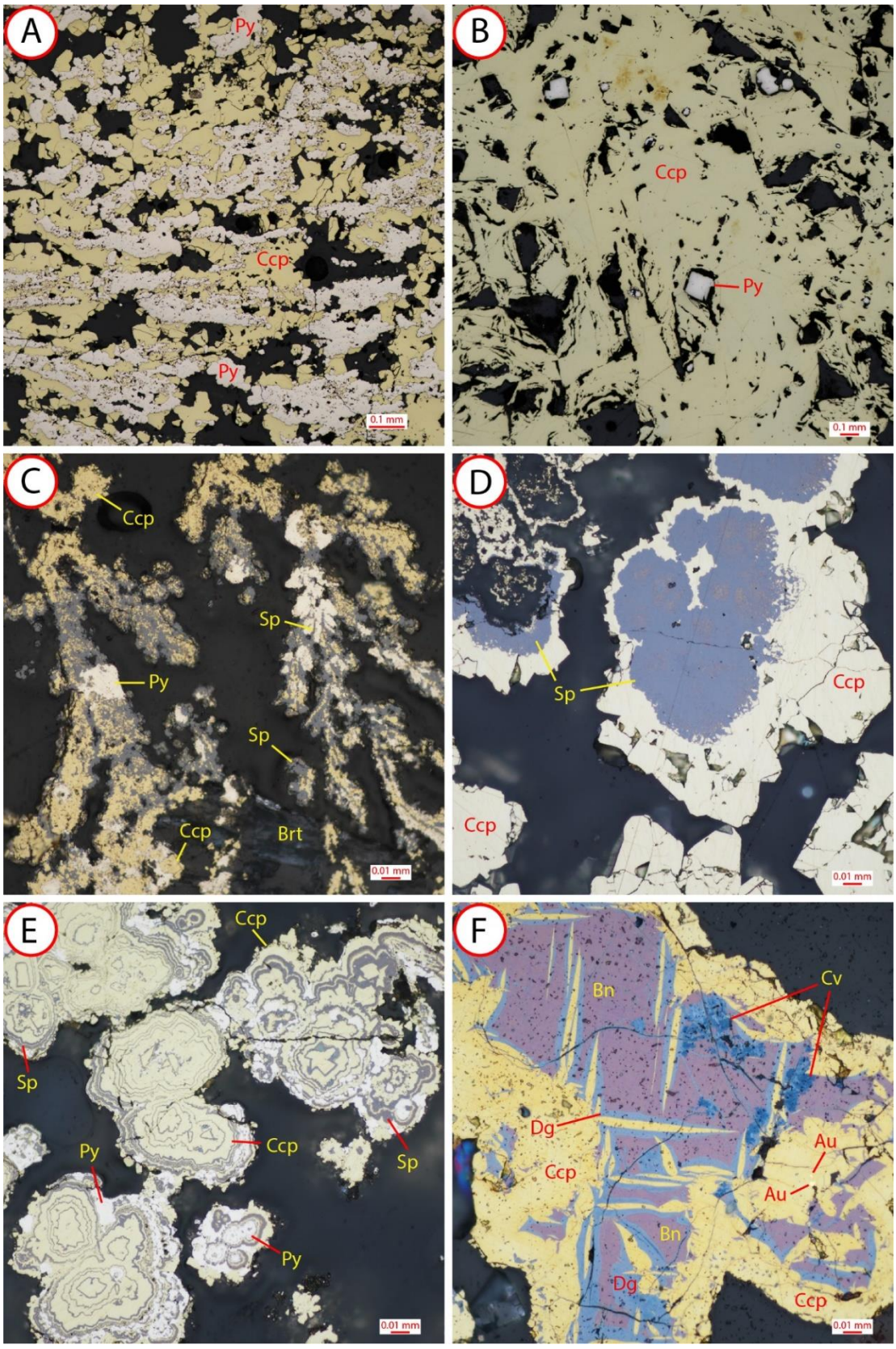
A
Py
Ccp
Py
0.1 mm
B
Ccp
Py
0.1 mm
C
Ccp
Sp
Py
Sp
Ccp
Brt
0.01 mm
D
Sp
Ccp
Ccp
0.01 mm
E
Ccp
Sp
Py
Ccp
Sp
Py
0.01 mm
F
Bn
Cv
Dg
Au
Ccp
Au
Bn
Dg
Ccp
0.01 mm

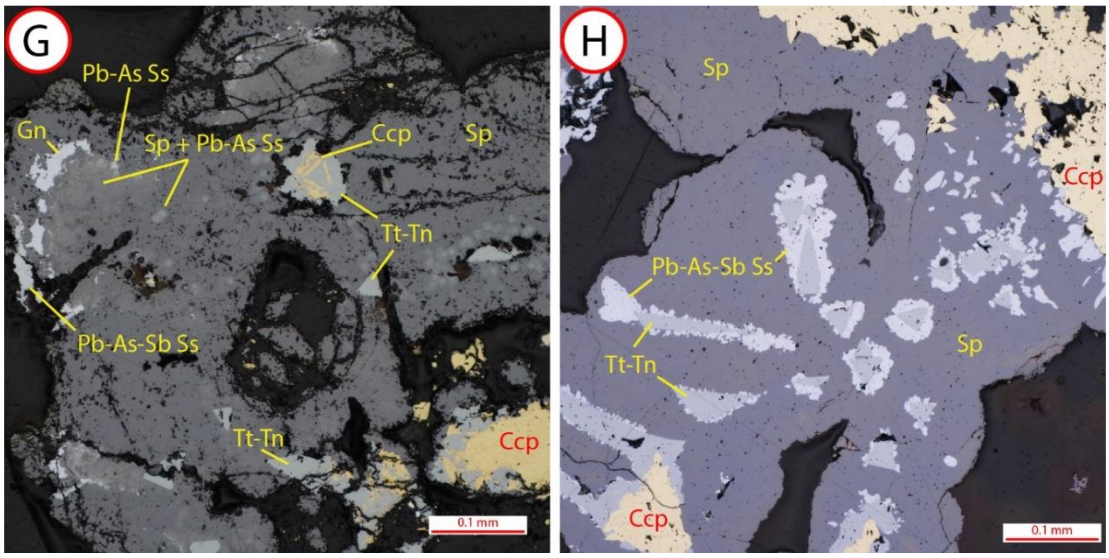

Figure 2.6. Photomicrographs of common textures of chalcopyrite and tetrahedrite-tennantite. All photos are captured under reflected light. (a) Chalcopyrite overgrowth of massive pyrite. Pyrite has a laminated appearance, possibly reflecting the sequential mineralization of pyrite within the chimney exterior during early-stage growth. (b) Massive chalcopyrite lining, with late euhedral pyrite within pore spaces. (c) Dendritic, fine-grained intergrowth of chalcopyrite and sphalerite. Pyrite is occasionally incorporated in the texture. (d) Massive chalcopyrite overgrowth of sphalerite. The two phases are also intergrown in some places, reflecting fluid temperatures of ~300°C, where both phases can form. It also appears as fine, disseminated patches occurring within the sphalerite grain interiors due to chalcopyrite disease. (e) Episodic precipitation of chalcopyrite and sphalerite forming alternating bands. Blebs of pyrite are occasionally intergrown within the texture. (f) Exsolution texture with primary digenite and bornite rimming chalcopyrite, formed from contemporaneous growth from a solid solution. Covellite seems to have formed as a replacement mineral based on its presence along cracks or near open space. (g) Minor abundance of Pb-As and Pb-As-Sb sulphosalts, and galena within massive sphalerite. Transitional co-precipitation appears to be occurring towards the interior sphalerite where faint patches of Pb-As sulphosalts are also observed. Angular grains of tetrahedrite-tennantite were observed in complex intergrowths with chalcopyrite. Lead-As and Pb-As-Sb sulphosalts of such small dimensions are difficult to distinguish by simple microscopy and have been verified by scanning electron microscopy. (h) Tetrahedrite-tennantite replaces chalcopyrite along its grain boundaries. Massive sphalerite and minor Pb-As-Sb sulphosalts subsequently overgrow chalcopyrite and tetrahedrite-tennantite.

Tetrahedrite-tennantite solid solution is an accessory mineral phase in chimney samples and is always associated with chalcopyrite. It forms anhedral to subhedral triangular-

shaped crystals (Fig. 2.6g). Tetrahedrite-tennantite often forms irregular intergrowths with chalcopyrite (Fig. 2.6g and 2.6h); it also occurs as small inclusions within chalcopyrite and is intergrown with galena and sphalerite.

2.5.3 Sphalerite

Sphalerite is generally massive and associated with barite, pyrite (Fig. 2.7a), and minor galena (Fig. 2.7b). Massive sphalerite is generally Fe-poor, based on its yellow-brown appearance under transmitted light (Fig. 2.7c). Dendritic sphalerite is common near the exterior of chimney samples, where barite and sphalerite are the dominant mineral phases. Branching sphalerite dendrites almost always envelop pyrite blebs; however, they are notably devoid of an inner barite nucleus from which they grow (Fig. 2.7d). In some samples, sphalerite occurs intimately with Fe-oxides (Fig. 2.7e). This texture in sphalerite occurs in barite- and sphalerite-dominated samples, where chalcopyrite is generally absent. Oxidation of sphalerite cores result in a corroded appearance, while the grain edges are generally free of this effect (Fig. 2.7e). Alternating bands of sphalerite within colloform pyrite masses and blebs also occur (Fig. 2.7f). In rare cases, these colloform textures appear fractured, with sphalerite precipitated along these fractures. Throughout most samples, massive sphalerite appears to be partially replaced by other sulphide minerals. Irregular, transitional boundaries between sphalerite and other minerals are suggestive of intergrowths or replacement (Fig. 2.6d, Fig. 2.7). In contrast, where sphalerite overgrows chalcopyrite or other high-temperature minerals, distinct boundaries always separate the two phases. Distinct boundaries also occur adjacent to the pore spaces

of massive chalcopyrite-dominated vent linings (Fig. 2.7h). Other low-temperature phases, such as galena, are mostly present in sphalerite grains as inclusions or as late overgrowths (Fig. 2.7i). Chalcopyrite disease in sphalerite occurs most commonly in sulphide-sulphate samples that contain a transitional stage between pre-existing sphalerite-dominated mineralization and higher temperature chalcopyrite-dominated mineralization.

2.5.4 Galena and Pb-bearing sulphosalts

Disseminated galena commonly occurs in sphalerite-rich samples (Fig. 2.7a and 2.7b). Often the occurrence of galena is fine-grained and forms inclusions in the surrounding sphalerite (Fig. 2.6g) and can mantle or overgrow high-temperature sulphides such as chalcopyrite (Fig. 2.7h). Under cross-polarized light, petrographic observations of some galena-like mineral grains exhibit distinct anisotropic behaviour that is more typical of Pb-As-Sb sulphosalts (Fig. 2.7i and 2.7j). Scanning electron microscope analyses indicate significant amounts of As (between 13.5–21 atom %) or Sb (~1–3.5 atom %) within these anisotropic grains, consistent with Pb-As and Pb-As-Sb sulphosalts. Stoichiometrically, elemental ratios of Pb:As:S align most closely with that of tsugaruite ($Pb_4As_2S_7$) (e.g., Shimizu et al. (1998)). However, petrographically, the Pb-As-Sb sulphosalt more closely matches jordanite ($Pb_{14}(As,Sb)_6S_{23}$), which is grey-white with a lesser ‘greenish-tint’, and forms massive grains with stronger anisotropism than tsugaruite (Shimizu et al., 1998; Ikehata et al., 2015). Jordanite and other Pb-sulphosalt phases have been documented in hydrothermal deposits at other back-arc spreading centers (Herzig et al., 1993; Fouquet et

al., 1993; Ikehata et al., 2015) and within the interior of chalcopyrite-sulphate chimneys from the northwest caldera vent field at Brothers volcano (Berkenbosch et al., 2012). At Niua South, these sulphosalts occur within late-stage, low-temperature mineral assemblages (i.e., with sphalerite, galena, and barite).

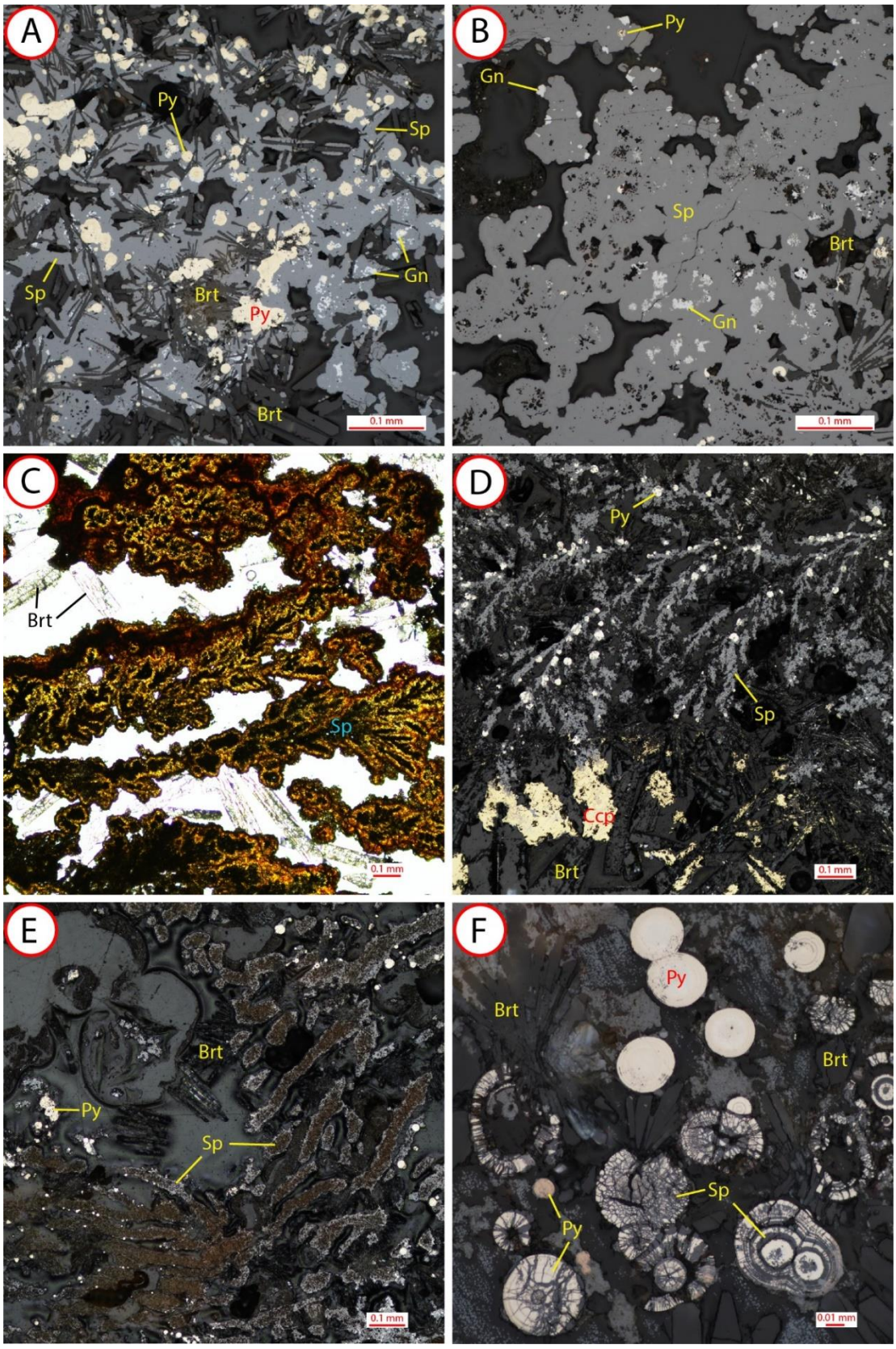
A
Py
Sp
Sp
Brt
Py
Gn
Brt
0.1 mm
B
Py
Gn
Sp
Brt
Gn
0.1 mm
C
Brt
Sp
0.1 mm
D
Py
Sp
Ccp
Brt
0.1 mm
E
Brt
Py
Sp
0.1 mm
F
Py
Brt
Brt
Sp
Py
0.01 mm

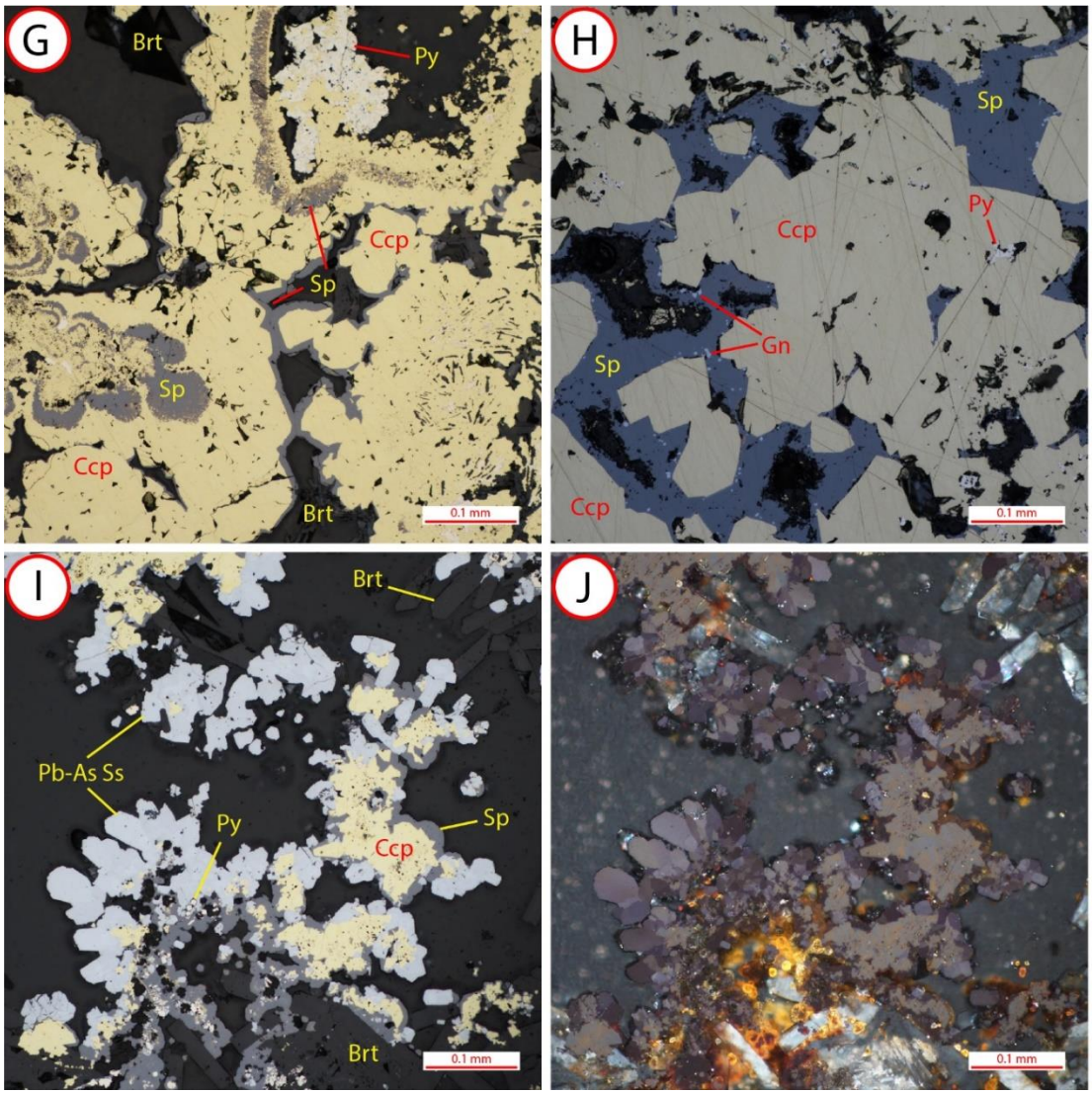

Figure 2.7. Photomicrographs of common textures observed in sphalerite, galena, and Pb-bearing sulphosalts. All photos are captured under reflected light unless otherwise specified. (a) Massive sphalerite overgrowths of barite and blebby pyrite, with disseminated intergrown galena. (b) Massive sphalerite with disseminated intergrown galena. Some replacement of galena may have occurred along grain edges. (c) Dendritic sphalerite zoning with Fe-rich centres, and Fe-poor exteriors. Photomicrograph is taken using plane polarized transmitted light. (d) Dendritic sphalerite containing small pyrite blebs. Chalcopyrite replacement occurs towards the bottom of the photograph. (e) "Tiger-stripe" texture in sphalerite, occasionally occurring near the exterior of chimney samples. The pitted, fuzzy orange appearance within the centre of massive sphalerite shows replacement by Fe-oxides. (f) Primary alternating bands of sphalerite within colloform pyrite. Later infilling of sphalerite occurs within highly fractured forms. Preserved colloform pyrite is visible at the top. Thin section contains residual carbon coating,

evident in two slightly darker pyrite blebs (bottom left). (g) Two stages of sphalerite growth associated with chalcopyrite. Early sphalerite is co-precipitated with chalcopyrite, forming bands, followed by outward growth of chalcopyrite. The presence of bands of sphalerite suggests that minor repeating physicochemical changes within the chimney wall has allowed both sphalerite and chalcopyrite to form in this manner. Late sphalerite occurs as thin overgrowths along the edges of chalcopyrite within pore spaces. Late barite is also present. (h) Similar late-stage sphalerite forming along the edges of subhedral chalcopyrite within pore spaces. Tiny inclusions of galena are often intergrown with sphalerite. (i) Coarse-grained subhedral Pb-As sulphosalts overgrowing sphalerite and chalcopyrite, representing late-stage growth with relatively uninhibited crystal growth. (j) Same image as (i), but taken under cross-polarized light, which highlights the strong anisotropy observed in Pb-As sulphosalts.

2.5.5 Pyrite and marcasite

Pyrite is present in most samples, generally in minor abundance (1–5%), but in some cases constitutes as much as 40% modal abundance. Pyrite occurs in a variety of textures, including massive, blebby, colloform, euhedral, and framboidal. The most common textures are massive and blebby pyrite (Fig. 2.7a), which, in many cases, exhibits colloform banding (Fig. 2.7f, Fig. 2.8a). Massive pyrite and marcasite locally occur as semi-laminated crusts that form along chimney exteriors and also form separate growth zones within the interiors of chimneys (Fig. 2.8b). Colloform masses also form in the outer rind of some chimney samples. Colloform textures appear most often in barite- and sphalerite-dominated samples but can be present with thin chalcopyrite overgrowths. It is common for colloform pyrite and/or marcasite to overgrow the outer walls of the chimneys, forming marked boundaries of separate stages of lateral chimney growth (Fig. 2.8b). Framboidal pyrite is present in only one sample where framboids are compact and resemble blebby pyrite (Fig. 2.8c). Towards more chalcopyrite-dominated areas, such as interior conduit linings, pyrite occurs mostly as disseminated, late-stage euhedral crystals

that form within pore spaces of massive chalcopyrite (Fig. 2.6b, Fig. 2.8d). Ovoid rings composed of pyrite ± marcasite are common in barite- and sphalerite-dominated samples, and contain barite, sphalerite, chalcopyrite, pyrite, and covellite inside their structure (Fig. 2.8e). In studies of other vent fields, similar rings have been previously interpreted as preserving the morphological form of vent organisms (Jones et al., 2008; Berkenbosch et al., 2012).

Marcasite is intimately associated with pyrite throughout many of the samples. However, unlike pyrite, it is absent in chalcopyrite-rich zones. In two samples, pyrite and marcasite together account for at least 50% of the modal abundance. Marcasite is generally present as intergrowths with massive pyrite (Fig. 2.8f and 2.8g). In rare cases marcasite and pyrite form alternating phases in bands or zones (Fig. 2.8h). Precipitation of marcasite, instead of pyrite, in seafloor hydrothermal deposits has been interpreted to indicate precipitation at a lower pH (<5) (Murowchick and Barnes, 1986; Schoonen and Barnes, 1991).

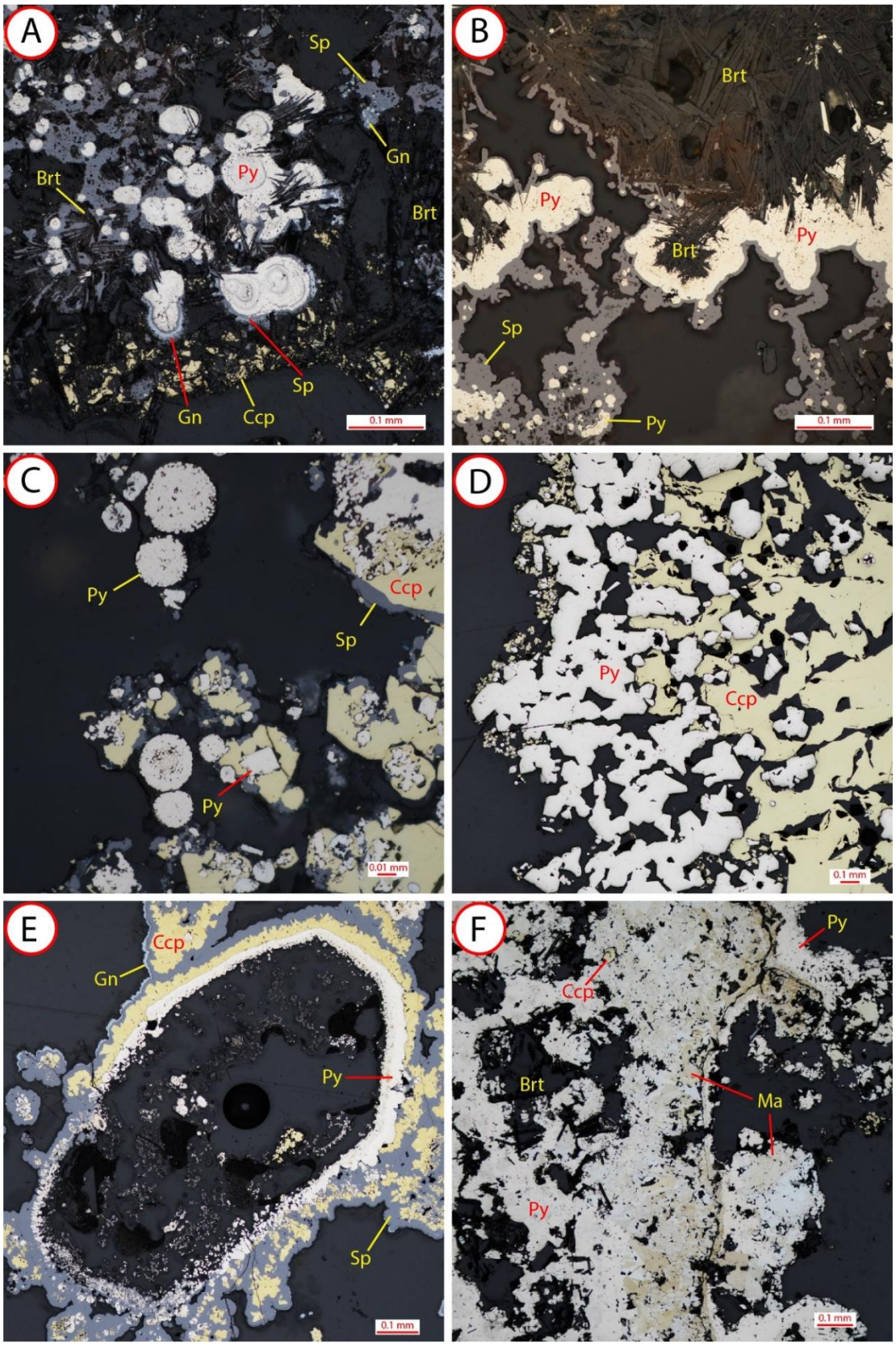
A
Sp
Gn
Py
Brt
Brt
Sp
Gn
Ccp
0.1 mm
B
Brt
Py
Py
Brt
Sp
Py
0.1 mm
C
Py
Ccp
Sp
Py
0.01 mm
D
Py
Ccp
0.1 mm
E
Ccp
Gn
Py
Sp
0.1 mm
F
Py
Ccp
Brt
Ma
Py
0.1 mm

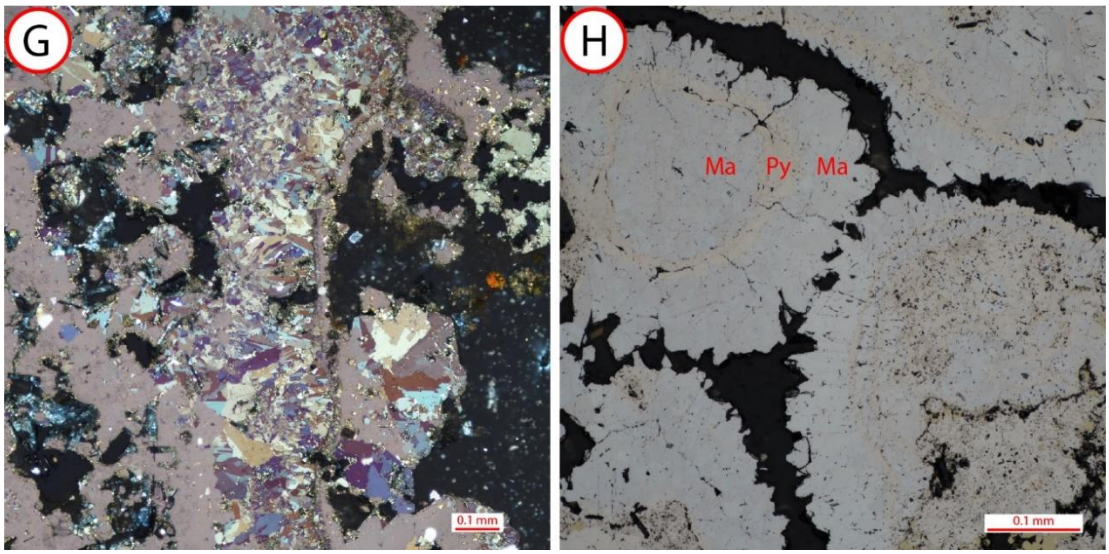

Figure 2.8. Photomicrographs of common textures and growth relationships observed in pyrite and marcasite. All photos are captured under reflected light. (a) Colloform masses and blebs of pyrite overgrowing pre-existing barite are commonly observed within several barite- and sphalerite-dominated samples. (b) Massive pyrite wall with marcasite overgrowing fine-grained bladed and acicular barite (above) and overgrown by sphalerite (below). The wall represents an overgrown exterior crust of pyrite and marcasite. This wall separates two sulphide growth zones within the sample. (c) Rare framboidal pyrite. (d) Euhedral pyrite along the inner chalcopyrite lining of an inactive vent. Pyrite is also present within pore spaces of massive chalcopyrite. (e) Example of an ovoid pyrite ring, which is often overgrown by or contains other sulphide minerals within its structure. (f) Alternating precipitation of pyrite and marcasite. Marcasite can be distinguished from pyrite by strong bireflectance. (g) Previous photomicrograph taken under cross-polarized light (XPL). Marcasite also exhibits strong pleochroism under XPL. (h) Rare alternating growth of marcasite and pyrite.

2.5.6 Bornite, secondary Cu-sulphides, and hematite

Bornite is present in five samples from the north, central, and eastern regions of the crater. The occurrence of exsolution lamellae of chalcopyrite within bornite suggest that the growth of primary bornite and chalcopyrite occurred simultaneously, originating from a Cu-Fe-S solid solution (Fig. 2.6f, Fig. 2.9a and 2.9b). Digenite commonly overgrows

and replaces bornite and is frequently rimming chalcopyrite lamellae (Fig. 2.6f, Fig. 2.9a and 2.9b). Late covellite replaces bornite and chalcopyrite, often forming along interior cracks (Fig. 2.9a and 2.9d-f). In some cases, later chalcopyrite overgrows and replaces bornite (Fig. 2.6f, Fig. 2.9a and 2.9b). Tetrahedrite-tennantite also occur where bornite is present (Fig. 2.9a and Fig. 2.9b and 2.9e). In one sample, a transitional replacement from chalcopyrite to bornite-digenite occurs along a transect from the chalcopyrite-dominated interior to the anhydrite-dominated exterior of an active hydrothermal chimney (Fig. 2.9e). These replacement products are secondary and are distinct from primary exsolution. Exclusive to this active chimney are disseminated, fine-grained masses of euhedral, bladed hematite. These small (<15 μm), scattered clusters occur within the interstices of massive chalcopyrite grains (Fig. 2.9f).

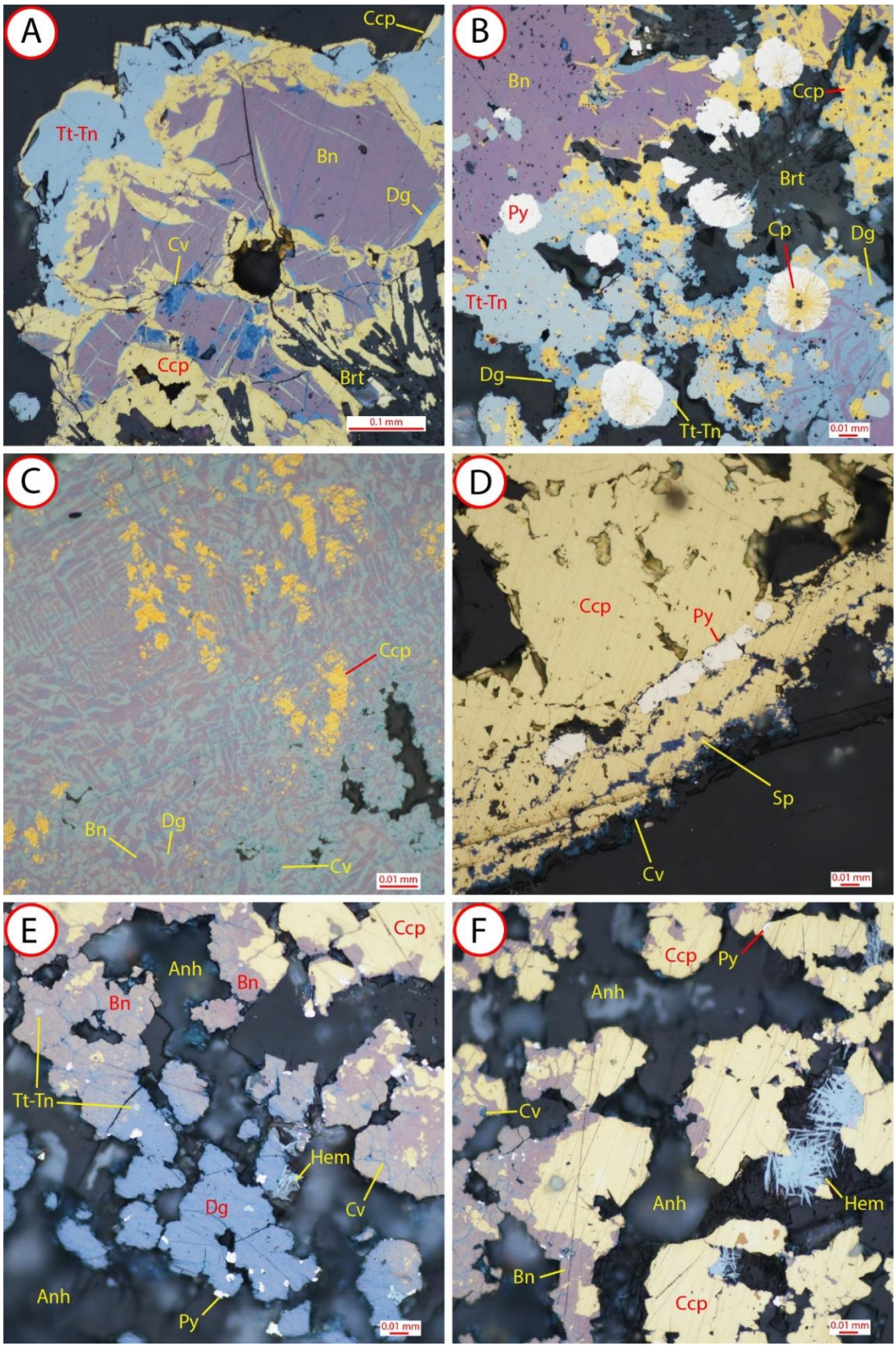
A
Ccp
Tt-Tn
Bn
Dg
Cv
Ccp
Brt
0.1 mm
B
Bn
Ccp
Brt
Py
Cp
Dg
Tt-Tn
Dg
Tt-Tn
0.01 mm
C
Ccp
Bn
Dg
Cv
0.01 mm
D
Ccp
Py
Sp
Cv
0.01 mm
E
Ccp
Anh
Bn
Bn
Tt-Tn
Hem
Dg
Cv
Anh
Py
0.01 mm
F
Ccp
Py
Anh
Cv
Anh
Hem
Bn
Ccp
0.01 mm

Figure 2.9. Photomicrographs of bornite, secondary Cu-sulphide phases, and hematite. All photos are captured under reflected light. (a) Complex growth and replacement of Cu-sulphide phases, showing simultaneous growth of bornite and chalcopyrite forming exsolution lamellae. Secondary replacement by digenite and covellite occurs primarily along the edges of bornite, but also extends into cracks and exsolution lamellae. Tetrahedrite-tennantite is seen intergrown with chalcopyrite. (b) Complex growth of Cu-sulphide phases. Digenite is replacing chalcopyrite. Chalcopyrite is also present as infill within fractured pyrite blebs. (c) Fine intergrowths of bornite, digenite and chalcopyrite. Bornite and digenite form discrete exsolution lamellae, while chalcopyrite occurs as tiny droplets. (d) Exterior replacement of massive chalcopyrite by covellite. Replacement occurs along grain edges and within fractures. (e) Extensive secondary replacement of massive chalcopyrite by bornite, and subsequent replacement by digenite and covellite. Initial replacement by bornite occurs along the edges of massive chalcopyrite and progressively moves inward. (f) Secondary replacement of chalcopyrite by bornite. Digenite and covellite forms along fractures within bornite. Rare primary hematite is present within pore spaces adjacent to chalcopyrite.

2.5.7 Gold, bismuth, and tellurium containing particles

Inclusions of native gold were previously identified within one active chimney sample and associated vent fluid (T_{Max} = 250°C) from the eastern region of the crater, and were spatially associated with chalcopyrite and barite (Gartman et al., 2018). Further native gold particles have been identified from the same sample within at least four separate minerals, including chalcopyrite, barite, tetrahedrite-tennantite, and sphalerite (Fig. 2.6f, Fig. 2.10a-d). Detected particles range in size from ≤1 to 5 µm. Most of the grains are anhedral with some exhibiting rounded or oblong forms (Fig. 2.6f; Fig. 2.10a-d), similar to those reported by Gartman et al. (2018). Several subangular to subrounded grains are inclusions within the chalcopyrite lining of the sampled boiling chimney (T_{Max} = 325°C), and range in size from ~0.4 to 13 µm. Energy dispersive x-ray spectroscopy (EDS) analysis revealed that two of these inclusions are primarily Bi, and five are primarily Te, and the remaining grains (>20) showing energy peaks for both Bi and Te. In addition,

three particles contain peaks for Au and Te. Five Bi-rich particles are found in another chimney sample and show association with Cl, suggesting a bismuth oxychloride.

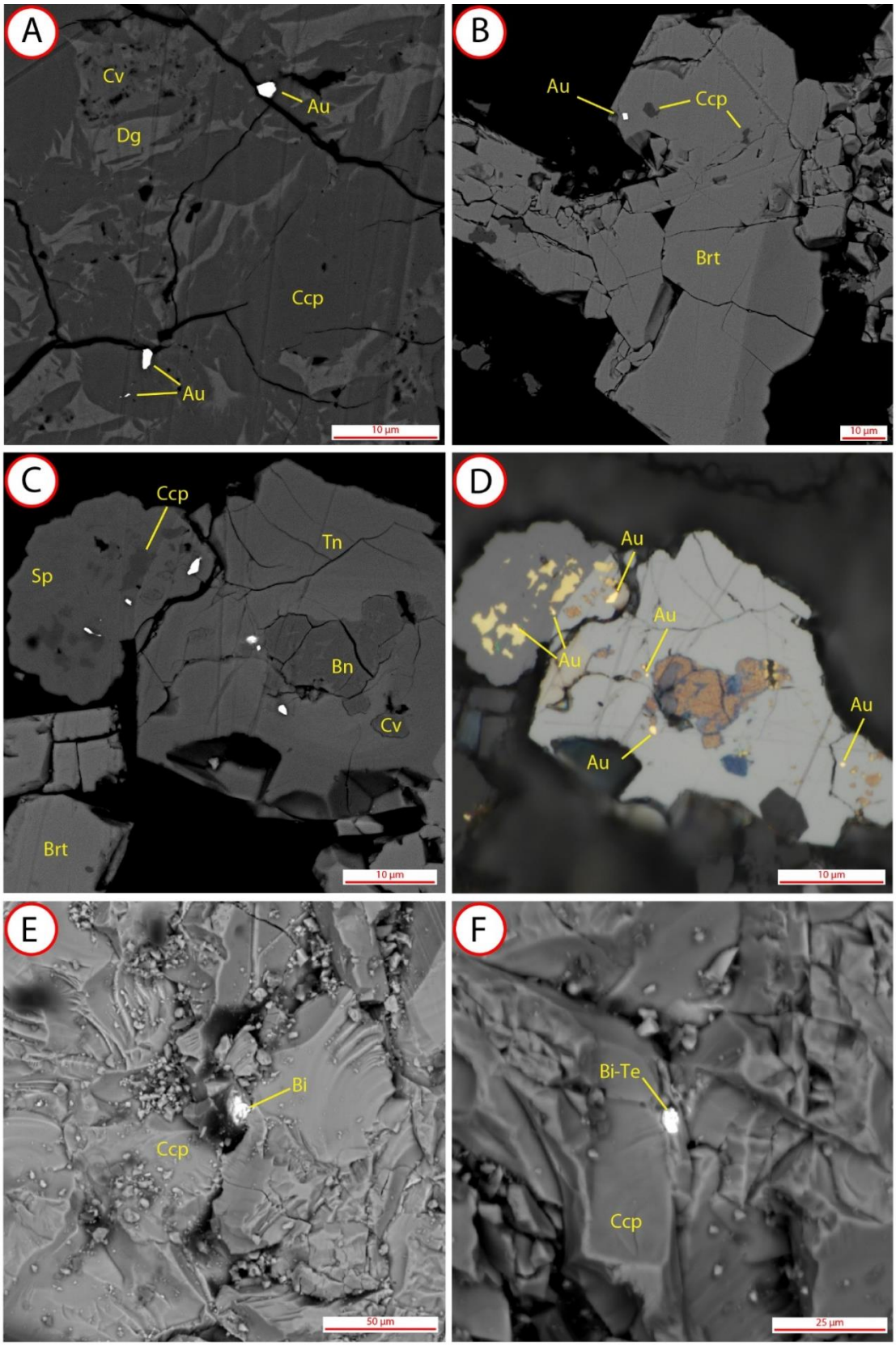
A
Cv
Au
Dg
Ccp
Au
10 µm
B
Au
Ccp
Brt
10 µm
C
Ccp
Tn
Sp
Bn
Cv
Brt
10 µm
D
Au
Au
Au
Au
Au
10 µm
E
Bi
Ccp
50 µm
F
Bi-Te
Ccp
25 µm

Figure 2.10. Backscattered electron (BSE) images and photomicrograph of native gold. All images are from the same hydrothermal sample that contains 50.6 ppm Au. (a) Grains of gold within chalcopyrite. (b) Individual anhedral gold grain hosted in barite crystal. (c) Gold grains (white) within tennantite and sphalerite. These grains display a variety of shapes and sizes. (d) Photomicrograph of previous image (reflected light), highlighting the similar appearance of gold grains and chalcopyrite blebs. (e) Bi-rich inclusion within chalcopyrite. (f) Bi-telluride grain within chalcopyrite.

Table 2.1: Whole-rock geochemistry for hydrothermal sulphide samples.

Analyte Symbol	Fe	Cu	Zn	Pb	Au	Ag	S	Si	Ba	Ca
Unit	%	%	%	%	ppb	ppm	%	%	%	%
Detection Limit	0.01	0.0002	0.001	0.00008	2	2	0.01	0.01	0.002	0.01
Analysis Method	INAA	FUS-MS	INAA	FUS-MS	INAA	INAA	FUS-MS	FUS-MS	INAA	FUS-MS
IGSN										
IEMMR0001	29.4	26.4	0.603	0.0858	3530	25	35.7	0.05	1.87	0.05
IEMMR0002	27.9	33.1	0.036	0.00577	1720	10	34.6	0.04	bdl	0.05
IEMMR0003	27.8	33.4	0.077	0.0164	672	bdl	33.7	0.23	0.392	0.88
IEMMR0004	20.2	20.7	0.941	0.14	5590	32	32.7	0.09	1.56	7.55
IEMMR0005	14.3	10.6	0.173	0.0681	4380	21	30.7	0.02	0.409	15.6
IEMMR0006	7.59	3.63	6.39	0.976	22900	210	15.4	1.02	16.2	0.11
IEMMR0007	21.8	16.4	1.44	0.254	14500	97	29.7	0.22	7.17	0.06
IEMMR0008	16.5	14	4.31	0.602	15200	115	26.2	0.2	7.14	3.21
IEMMR0009	34.1	28.4	0.046	0.0492	9880	37	36	0.22	0.464	0.04
IEMMR000A	9.4	1.07	25.9	2.58	6080	264	28.3	0.13	9.86	0.05
IEMMR000B	20.8	18.1	1.75	0.238	16500	138	26.6	0.21	8.31	0.13
IEMMR000C	9	2.74	11.6	1.02	9020	175	18.6	0.05	14.7	0.1
IEMMR000D	8.4	3.17	10.2	0.649	24500	376	17.1	0.06	14.9	0.18
IEMMR000E	3.11	0.0541	29.5	1.94	11800	647	18.4	0.85	22.1	0.12
IEMMR000F-1	2.28	0.646	18.8	1.53	14800	316	11.8	3.97	27	0.12
IEMMR000F-2	1.26	0.032	37.3	3.25	444	177	20.4	2.35	15.6	0.05
IEMMR000F-3	3.36	0.228	32.1	2.81	12200	556	20	bdl	19.9	0.1
IEMMR000G-1	5.28	0.91	15.6	1.55	8190	471	16.1	bdl	26.4	0.15
IEMMR000G-2	6.29	1.82	21.4	1.67	12400	299	16.9	0.22	24.2	0.41
IEMMR000G-3	7.39	2.44	14.7	1.03	11800	242	17.5	0.17	22.8	2.82
IEMMR000G-4	12.4	5.7	15.8	0.502	25700	328	21.9	0.08	20.7	0.09
IEMMR000H	1.22	0.153	19.9	3.86	6550	322	15.2	0.56	19.4	0.1
IEMMR000I	6.92	2.37	9.9	1.39	26900	389	14.3	2.48	26.2	0.12
IEMMR000J-1	5.32	1.19	16.9	1.79	11400	307	18.6	bdl	18.1	0.17
IEMMR000J-2	3.27	3.32	0.095	0.0133	3640	4	27.2	0.03	0.458	25.5
IEMMR000L	1.95	0.702	7.86	1.42	13700	266	7.76	0.74	38.3	0.12
IEMMR000M	4.27	0.648	32.1	0.991	25900	415	18.8	1.2	19.9	0.09
IEMMR000O	11.5	10.3	0.045	0.0222	15100	22	13.8	0.04	26.8	0.08
IEMMR000Q	5.76	1.68	9.23	0.416	25000	229	16.9	4.04	8.06	0.08
IEMMR000R	7.32	1.57	17	1.98	16700	296	28	0.03	3.88	0.09
IEMMR000S	27.8	6.98	3.69	0.151	9090	117	35.2	0.1	11.5	0.12
IEMMR000T	8.73	3.14	6.48	1.52	16000	316	17.6	1.14	9.16	0.18
IEMMR000U	38.5	1.52	0.176	0.0848	6020	33	43.3	0.15	8.52	0.09
IEMMR000V	4.98	0.815	28.7	0.2	16100	125	24.2	0.01	13.3	0.08
IEMMR000W	3.59	1.32	6.32	1.37	9890	201	12.2	0.57	11.7	0.19
IEMMR000Z	8.5	21.9	0.426	0.0741	50600	124	17.6	bdl	15.5	1.77

bdl = below detection level

Table 2.1 (cont.):

Analyte Symbol	As	Bi	Cd	Co	Sb	Se	Sn	Sr	Te
Unit	ppm	ppm	ppm	ppm	ppm	ppm	ppm	ppm	ppm
Detection Limit	1	2	2	0.1	0.1	0.5	0.5	3	6
Analysis Method	INAA	FUS-MS	FUS-MS	INAA	INAA	INAA	FUS-MS	FUS-MS	FUS-MS
IGSN									
IEMMR0001	904	48	15	208	81	1400	15.7	394	60
IEMMR0002	66	23	bdl	159	9	2680	9.5	21	29
IEMMR0003	122	8	3	18.5	15	2630	29.2	220	7
IEMMR0004	643	75	28	111	111	474	7.9	1410	66
IEMMR0005	711	73	6	173	60	120	3.8	1750	80
IEMMR0006	4200	bdl	344	161	890	bdl	1.5	3250	bdl
IEMMR0007	1720	45	69	219	235	bdl	bdl	1820	11
IEMMR0008	2640	62	141	137	560	70	4.4	2230	40
IEMMR0009	1410	93	bdl	249	61	220	8.3	97	22
IEMMR000A	3280	5	936	111	1800	bdl	bdl	3080	bdl
IEMMR000B	1260	9	72	143	346	29	3.1	3660	bdl
IEMMR000C	2160	3	384	145	872	bdl	1.2	5040	bdl
IEMMR000D	2150	bdl	560	129	934	bdl	1.4	4620	bdl
IEMMR000E	5890	bdl	723	78.9	1890	bdl	1.2	3150	bdl
IEMMR000F-1	2350	bdl	489	63.9	1060	bdl	1.4	3330	bdl
IEMMR000F-2	6850	bdl	620	14.4	1950	bdl	1.2	2240	bdl
IEMMR000F-3	4000	bdl	758	89.9	2220	bdl	1.6	2790	bdl
IEMMR000G-1	4900	bdl	573	201	1430	bdl	1	4160	bdl
IEMMR000G-2	5290	bdl	511	127	1490	bdl	1.3	3610	bdl
IEMMR000G-3	3010	bdl	386	152	948	bdl	1.2	3860	bdl
IEMMR000G-4	2220	bdl	367	172	886	bdl	1.8	3490	bdl
IEMMR000H	4120	bdl	694	98	1840	bdl	bdl	3420	bdl
IEMMR000I	6640	bdl	357	229	1660	bdl	0.9	4620	bdl
IEMMR000J-1	5570	bdl	570	189	1380	bdl	bdl	5410	bdl
IEMMR000J-2	120	41	2	44.5	25	32	bdl	2690	21
IEMMR000L	3900	bdl	343	54.8	1060	bdl	1.9	3020	bdl
IEMMR000M	2310	bdl	1190	48	1190	bdl	2.8	2460	bdl
IEMMR000O	276	bdl	bdl	120	50	bdl	1.6	2760	bdl
IEMMR000Q	750	bdl	845	280	604	bdl	3	1880	bdl
IEMMR000R	1340	9	1400	38.2	1620	bdl	1.9	1360	10
IEMMR000S	2300	22	137	200	193	63	2.6	1860	15
IEMMR000T	7290	bdl	330	106	2290	bdl	0.7	4000	bdl
IEMMR000U	4580	6	5	121	54	bdl	1.2	1730	bdl
IEMMR000V	664	2	956	28.7	1060	bdl	1.4	1300	bdl
IEMMR000W	4430	bdl	415	133	1260	bdl	0.7	4580	bdl
IEMMR000Z	6180	bdl	16	9.7	741	bdl	bdl	4630	bdl

bdl = below detection level

2.5.8 Geochemistry

Table 2.1 contains an abbreviated list of the elemental composition of 36 hydrothermal samples from Niua South. This shortened list showcases elements that commonly show notable trends within arc-related hydrothermal deposits; a full list of element composition is shown in Appendix B. Enrichments in Ba, Sr, Zn, Pb, As, Sb, Cd, and Ag are generally accompanied by relative depletions in Cu, Fe, Bi, Sn, Se, and Te. As observed in the sample mineralogy, these trends are temperature-dependant, and are largely linked to the formation of chalcopyrite or sphalerite and barite. Other elements such as Ca, Co, In, Ni, Mn, Mo, Si, and Au do not share significant correlations with major sulphide and sulphate mineral forming elements.

From their bulk geochemical composition, hydrothermal samples from Niua South can be classified as either Ba-Zn-dominated or Cu-dominated samples. Spatially, Cu-rich samples (>10 wt.% Cu) are largely restricted to the northwest section of the crater, whereas Ba-Zn-rich (>10 wt.% Zn) samples are more abundant in the central region of the crater. These two geochemical classifications are comparable to the mineralogical assemblages assigned to the samples (Fig. 2.4), where the high-temperature assemblage represents the Cu-rich suite. Collectively, the low-temperature and intermediate-temperature assemblages are geochemically similar and represent the Ba-Zn-rich suite. Predictably, barite and sphalerite are the dominate minerals found in the Ba-Zn-rich suite. Barium concentrations average 13.7 wt.% ± 9.6 wt.% (sd) for all samples (n=36), with only six samples containing less than 1 wt.% Ba. Samples with the lowest concentrations of Ba are dominated by chalcopyrite or anhydrite. Barium is closely correlated with Sr (*r*

= 0.60; Fig. 2.11), reflecting the common substitution of Sr for Ba within the barite lattice (Hannington et al., 1995; Jamieson et al., 2016). A weak negative correlation exists between Ba and Ca (r = -0.37), which has been reported as strongly negative at other hydrothermal vent sites like the Endeavour Segment, Juan de Fuca Ridge (Hannington et al., 1995; Jamieson et al., 2016). Significant abundances of Ca are found only in active chimney samples, where concentrations range from ~7 wt.% to 25.5 wt.%. These samples are notably Ba-poor, (i.e., generally containing less than 1 wt.%).

Other mineral phases that commonly occur in the Ba-Zn-rich suite include galena, and Pb-As and Pb-As-Sb sulphosalts. Trace elements such as Cd, Sb, Pb, and Ag all show strong positive correlations (r = >0.60) with Zn in this suite. Cadmium commonly substitutes into the sphalerite lattice for Zn (Zhang, 1987; Huston et al., 1995; Cook et al., 2009), whereas Sb, Pb, and Ag are present in galena and sulphosalts associated with sphalerite. Arsenic and Sb, which are typically enriched in felsic-hosted seafloor hydrothermal deposits, are variably enriched throughout the Ba-Zn suite (Hannington et al., 2005; Monecke et al., 2016), with As having a strong positive correlation with both Sb and Pb (r = 0.73 and r = 0.60, respectively) and a moderate positive correlation with Ag (r = 0.56). Abundances of Sb and As are also attributed to minor growth of tetrahedrite-tennantite and As- or Sb-rich galena. Lead shares the strongest correlation with Sb (r = 0.88).

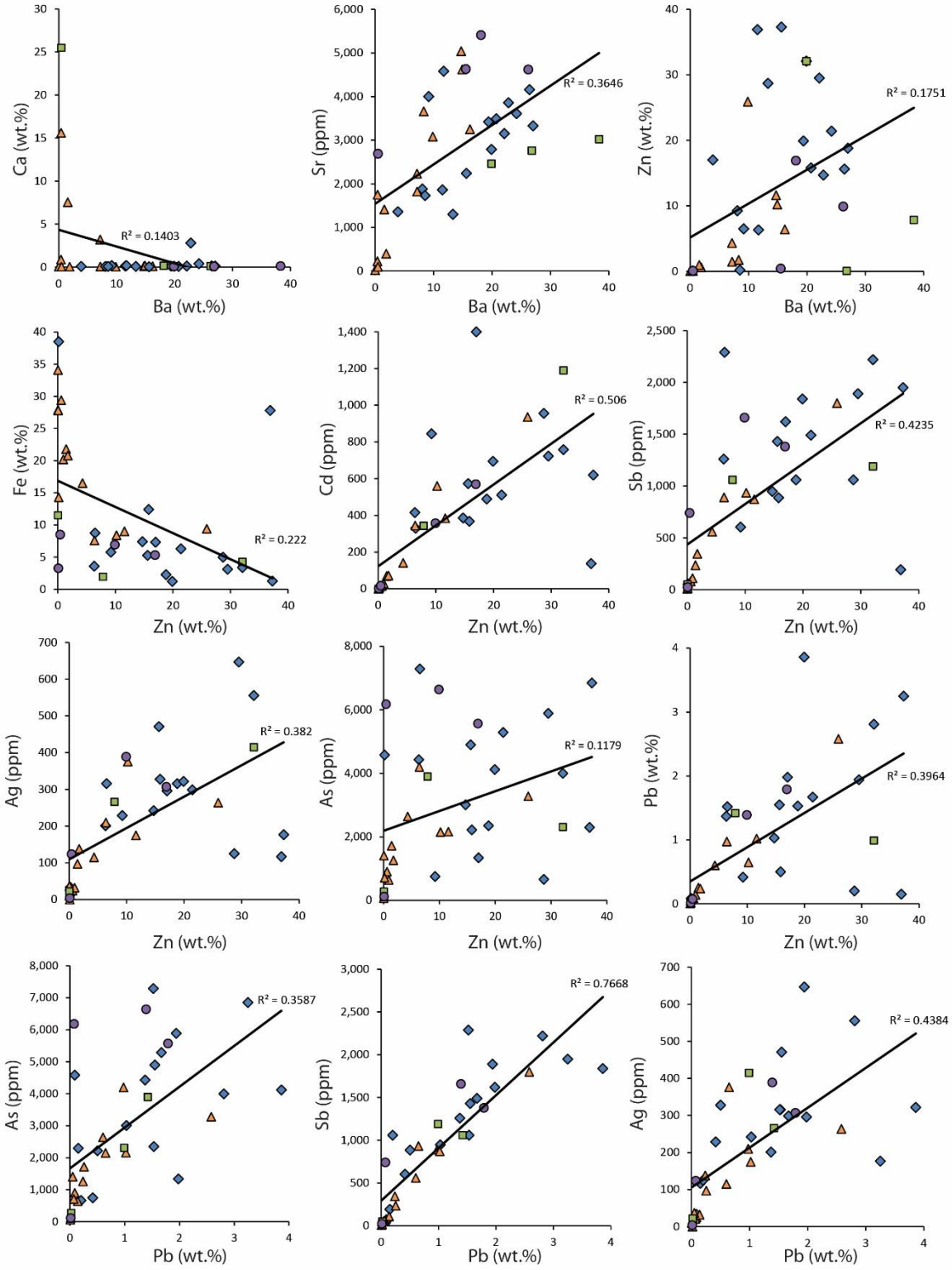
Ca (wt.%)
Ba (wt.%)
R² = 0.1403
Sr (ppm)
Ba (wt.%)
R² = 0.3646
Zn (wt.%)
Ba (wt.%)
R² = 0.1751
Fe (wt.%)
Zn (wt.%)
R² = 0.222
Cd (ppm)
Zn (wt.%)
R² = 0.506
Sb (ppm)
Zn (wt.%)
R² = 0.4235
Ag (ppm)
Zn (wt.%)
R² = 0.382
As (ppm)
Zn (wt.%)
R² = 0.1179
Pb (wt.%)
Zn (wt.%)
R² = 0.3964
As (ppm)
Pb (wt.%)
R² = 0.3587
Sb (ppm)
Pb (wt.%)
R² = 0.7668
Ag (ppm)
Pb (wt.%)
R² = 0.4384

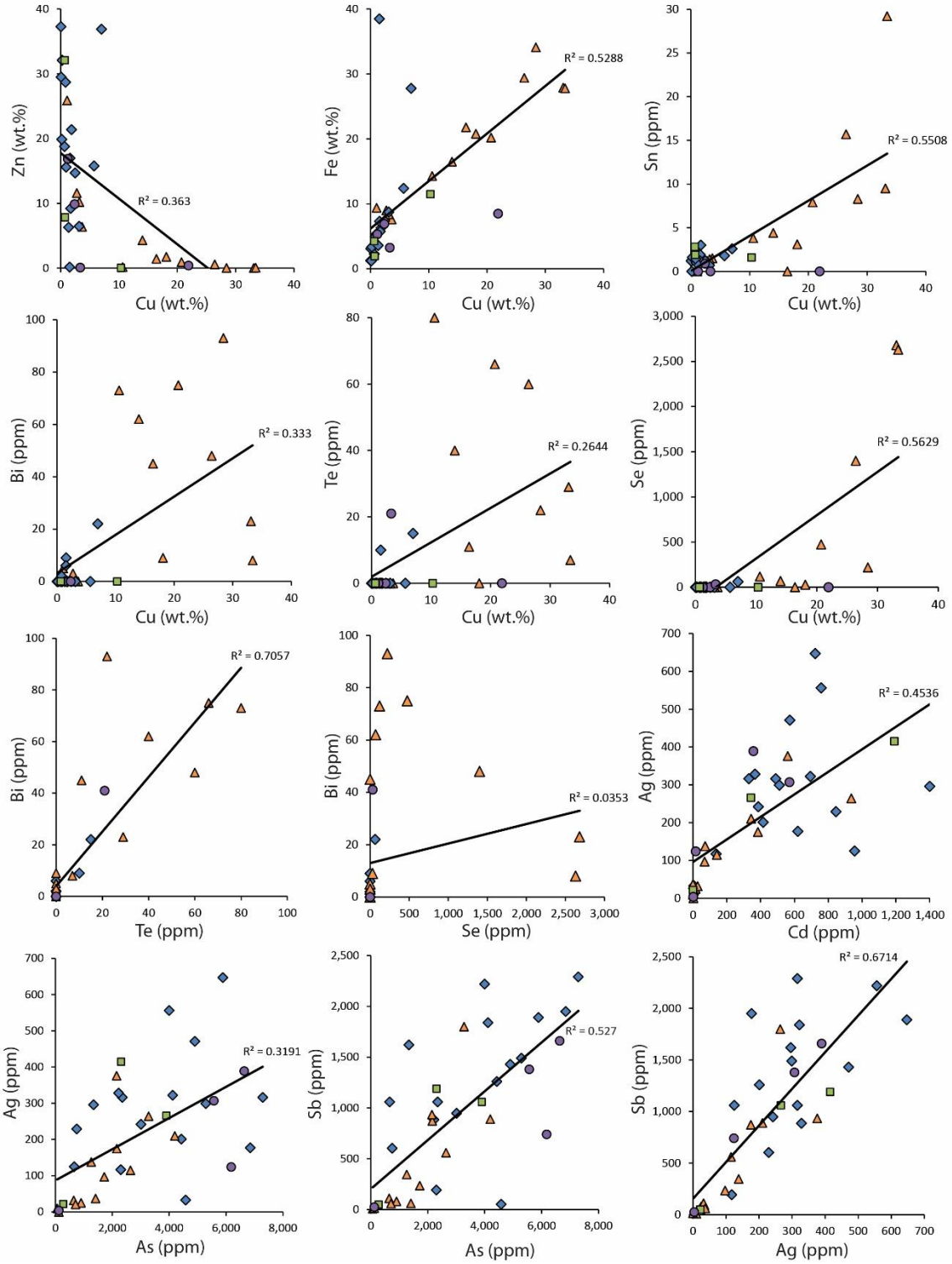
Zn (wt.%)
Cu (wt.%)
R² = 0.363
Fe (wt.%)
Cu (wt.%)
R² = 0.5288
Sn (ppm)
Cu (wt.%)
R² = 0.5508
Bi (ppm)
Cu (wt.%)
R² = 0.333
Te (ppm)
Cu (wt.%)
R² = 0.2644
Se (ppm)
Cu (wt.%)
R² = 0.5629
Bi (ppm)
Te (ppm)
R² = 0.7057
Bi (ppm)
Se (ppm)
R² = 0.0353
Ag (ppm)
Cd (ppm)
R² = 0.4536
Ag (ppm)
As (ppm)
R² = 0.3191
Sb (ppm)
As (ppm)
R² = 0.527
Sb (ppm)
Ag (ppm)
R² = 0.6714

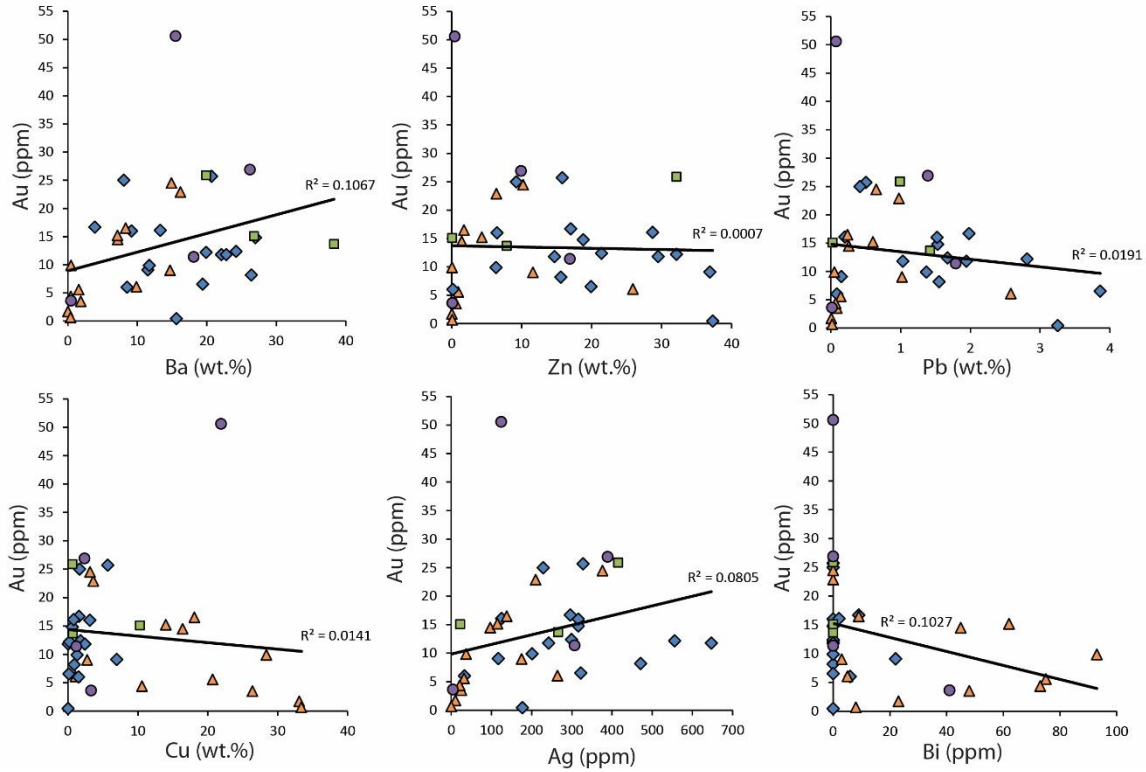

Figure 2.11. Bivariate plots of select elements versus major sulphide and sulphate forming elements (Ba, Zn, Pb, and Cu) and trace elements. N= 36. Sample points are colour-coded based on their location within the vent field; orange triangles = north, blue diamonds = central, purple circles = east, and green squares = south.

Precious metal (Au and Ag) abundances are elevated at Niua South relative to deposit samples from mid-ocean ridges (Hannington et al., 2005, 2010). Gold content averages 13.5 ppm ± 9.7 ppm (sd) for all samples (n=36) and reaches a maximum of 50.6 ppm in a chalcopyrite-bornite-rich sample collected from an active chimney at the base of the east crater wall (Fig. 2.4a and Fig.2.4b, Fig. 2.10, Fig. 2.11). Gold shows no significant correlations with any other abundant elements (Fig. 2.11), suggesting that Au does not preferentially form with any other mineral phase. However, it does share a moderate positive correlation with Sr (r = 0.43) and a weak positive correlation with Ba (r = 0.33). Silver content averages 214 ppm ± 163.7 ppm (sd) for all samples (n=36) with the highest

content reaching 647 ppm within a Ba-Zn-rich talus sample from the northern portion of the central mound (Fig. 2.4a). The strong positive correlations of Ag with Sb, Cd, Pb, and Zn ($r = 0.82$, $r = 0.67$, $r = 0.66$, $r = 0.62$), and moderate positive correlation with As ($r = 0.56$) suggests that the majority of Ag resides within inclusions in sphalerite, galena, tetrahedrite-tennantite, Pb-As sulphosalts, and Pb-As-Sb sulphosalts (Fig. 2.11). Silver peaks were present in SEM-EDS analysis of all these minerals. The association of Ag with Zn and Cd may be primarily due to its presence in galena, which is commonly found with sphalerite. Strong correlations of Ag and Sb are likely a result of Ag substitution in tetrahedrite-tennantite (Sack and Loucks, 1985). Barium and Sr share a strong and moderate positive correlation with Ag, respectively ($r = 0.63$, $r = 0.54$).

Chalcopyrite is the dominant mineral found in Cu-rich samples. However other Cu-bearing sulphide minerals contribute minor (1–5 wt.%) and trace (<1 wt.%) abundances of Cu, including bornite, tetrahedrite-tennantite, digenite, and covellite. The trace elements most strongly correlated with the Cu-rich suite are Se and Sn ($r = 0.75$, $r = 0.74$, respectively), which commonly substitute into the chalcopyrite lattice (Maslennikov et al., 2009). Bismuth and Te strongly correlate with each other ($r = 0.84$) and show moderate positive correlations with Cu ($r = 0.58$, $r = 0.51$, respectively). Bismuth and Te both have an affinity for intermediate- to high-temperature hydrothermal conditions, and are typically enriched in chalcopyrite (Monecke et al., 2016). Tellurium can also substitute for S in the chalcopyrite lattice (Butler and Nesbitt, 1999). Of the Bi-rich grains observed in massive chalcopyrite using the SEM, most, but not all, contain Te. Selenium also shows a peak within the Bi-rich grain with the highest concentration of Te. These

observations support the presence of a discrete Bi-telluride phase. The very strong correlation between Bi and Te, but not Se (r = 0.19, r = 0.33), suggests tellurobismuthite (Bi_2Te_3) or tetradymite (Bi_2Te_2S) as two potential phases.

2.6. Discussion

2.6.1 Mineral paragenesis

The mineralogy of chimney and talus samples collected from Niua is similar to other styles of hydrothermal mineralization observed at other arc-hosted sites, most notably at the northwest caldera of Brothers volcano along the southern Kermadec arc (de Ronde et al., 2003, 2005; Berkenbosch et al., 2012). Growth of focused, black smoker chimneys at Niua can be divided into three separate stages that may be gradational between one another and or concurrent depending on the location within the chimney wall (Fig. 2.12). Furthermore, these mineral assemblages may undergo constant dissolution and reprecipitation as part of zone refining during chimney growth (Haymon, 1983; Rona et al., 1993; Tivey, 1995; Wohlgemuth-Ueberwasser et al., 2015).

2.6.1.1 Early-stage

In the early stages of chimney growth, sulphate (barite and anhydrite) and minor growth of low-temperature sulphide minerals (marcasite and/or pyrite) dominate the thin walls of early chimney structures, similar to that described by Tivey & McDuff (1990). Barite and

anhydrite can both form at low temperatures, with barite forming at temperatures of <100°C (Jamieson et al., 2016) and anhydrite at ~150°C (Bischoff and Seyfried, 1978). Early sulphate and sulphide phases are typically fine-grained (Fig. 2.5b, Fig. 2.7a, Fig. 2.8b), reflecting the rapid precipitation of minerals from high degrees of seawater mixing (Herzig and Hannington, 1995). Early crusts of marcasite and pyrite form on the exterior surfaces of some chimneys, similar to reports from other vent fields (Juniper et al., 1992; Hannington et al., 1995). Colloform texture, observed primarily in pyrite (Fig. 2.7a and 2.7f, Fig. 2.8a-c), appears to be the result of rapid precipitation, much like other textures observed in early-stage sulphide formation (Maslennikov et al., 2009). With progressive thickening of the chimney walls by sulphide minerals, the interior of the chimney becomes increasingly insulated, allowing for the precipitation of sphalerite and galena (Fig. 2.7a-b). Barite and sphalerite dominate much of the low-temperature assemblage and are characteristic of many of the sulphide-sulphate talus samples collected along the flanks of active and inactive chimney complexes within the crater (Fig. 2.5a-b, Fig. 2.7a-c, and 2.7e). These samples correspond to either diffuse chimneys or the outer walls of focused, black smoker chimneys.

The primary textures observed in sphalerite are largely controlled by the rate at which sphalerite precipitates or the mode in which sphalerite is replaced by other phases. Dendritic texture, also observed in barite and anhydrite, is the result of rapid crystallization from a highly supersaturated fluid (Fig. 2.7c-e; Fouquet et al., 1993; Jamieson et al., 2016). This suggests that a rapid influx of seawater increases the thermal gradient within the chimney structure allowing for dendritic sphalerite to form in the near

exterior around pre-existing sulphides. The presence of Fe-oxide within dendritic sphalerite suggests that the influence of oxygen from seawater mixing causes this replacement (Fig. 2.7e). Furthermore, de Ronde et al. (2011) suggest that this texture is indicative of rapid quenching of hydrothermal fluid, in which seawater mixing controls cooling. Lastly, alternating circular bands of sphalerite found to occur within chalcopyrite and colloform pyrite may be caused by repeating, rapid shifts in physicochemical gradients within chimney walls that affect mineral precipitation (Fig. 2.6e, Fig. 2.7f, Fig. 2.8a) and are consistent with similar observations from Brothers volcano (Berkenbosch et al., 2012).

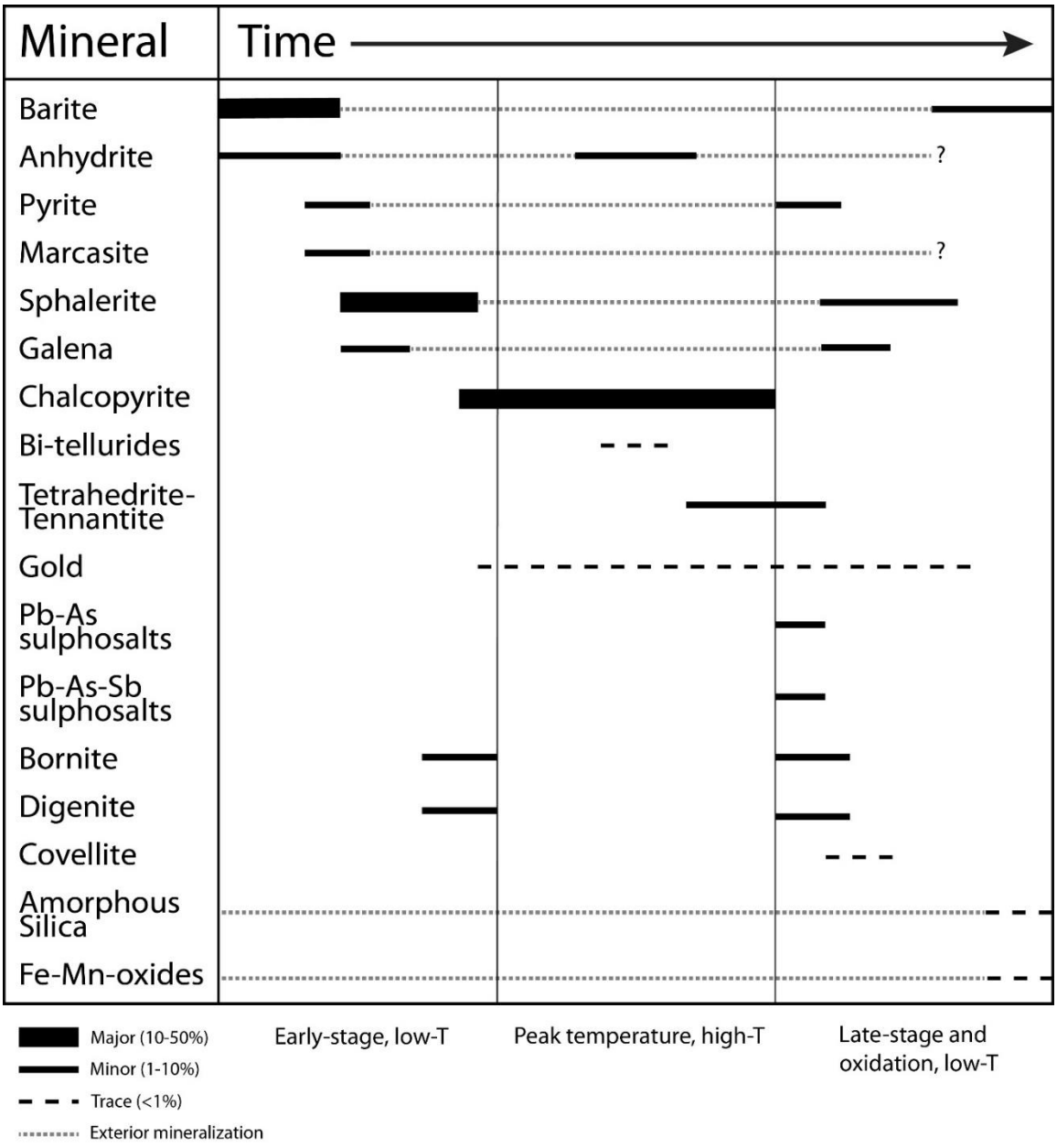

Figure 2.12. Paragenetic diagram that encompasses all stages of mineralization observed at the Niua South hydrothermal field. The style and thickness of each bar corresponds to the relative abundance for that mineral. The full evolution of mineral formation applies to high-temperature (~325°C) vent interiors. The duration of each stage of mineralization is not equal. Dotted lines (grey) indicate the mineralization occurring at the vent exterior.

2.6.1.2 Peak-temperature stage

Chimneys that become further insulated by prolonged growth and thickening of the chimney walls will begin to precipitate chalcopyrite within the interior (Fig. 2.5e and 2.5g, Fig. 2.6b, Fig. 2.7h, Fig. 2.8d). Conduits are characterized by inner chalcopyrite linings of up to several centimetres thick. Only three chimneys are currently active at this peak temperature stage at Niua, but chalcopyrite-rich talus samples suggest that more are likely to have been active in the past. Extensive interior precipitation of chalcopyrite characterizes this peak temperature formation stage, where maximum fluid temperatures of 325°C were recorded at one of the two-phase chimneys (Fig. 2.7a). Chalcopyrite can extensively replace and overprint pre-existing phases, and remineralization occurs throughout the chimney wall, where the early-stage sulphide minerals reprecipitate towards the exterior of the chimney (Fig. 2.5d-f, Fig. 2.6c-e, Fig. 2.7d, and 2.7g-h). With increasing temperatures and reducing conditions, barite can be resorbed from its solid phase into the hydrothermal fluid and be remobilized (Fig. 2.5e-f; Eldridge et al., 1983; Ditchburn and de Ronde, 2017). Anhydrite is often present in the tips of active chimneys immediately adjacent to inner chalcopyrite linings (Fig. 2.5g). As opposed to early-stage formation of fine-grained anhydrite, growth here can produce coarse, unoriented crystals that appear to provide enough interstitial space for subsequent sulphide minerals to grow (Fig. 2.5h). Primary bornite and digenite are largely associated with chalcopyrite, and form exsolution lamellae (Fig. 2.6f, Fig. 2.9a-c), a product of simultaneous growth of both phases from a solid solution. Precipitation of tetrahedrite-tennantite also occurs largely on the rims of or as intergrowths with chalcopyrite (Fig. 2.6e and 2.6f, Fig. 2.9a

and 2.9b). Inclusions of gold and Bi-tellurides are found within chalcopyrite (Fig. 2.6f, Fig. 2.10a and 2.10e and 2.10f), and some gold inclusions are found in tetrahedrite-tennantite (Fig. 2.10c and 2.10d).

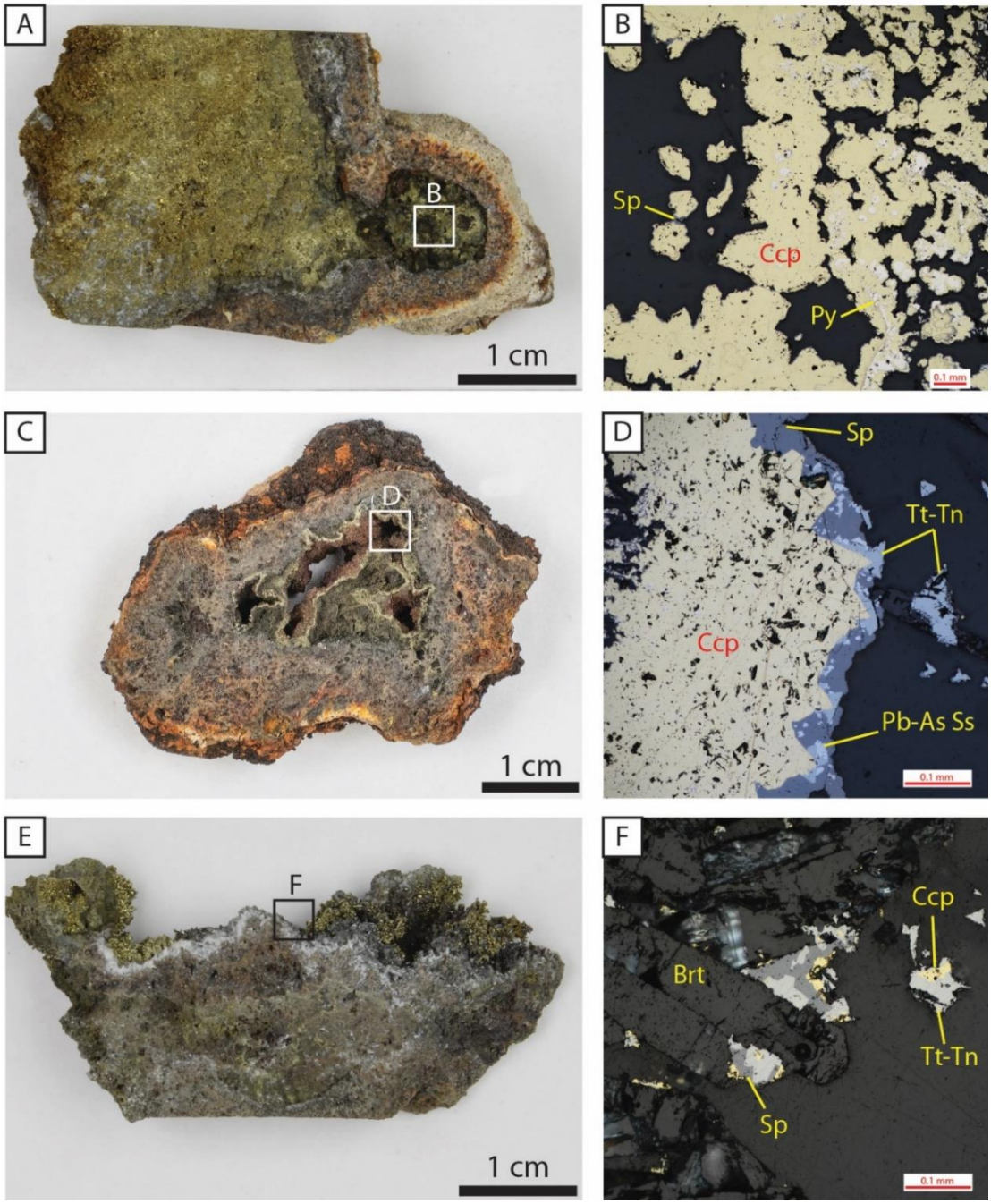

Figure 2.13. Late-stage precipitation of intermediate (e.g., tetrahedrite-tennantite) and low-temperature sulphides (e.g., sphalerite, sulphosalts, galena) within vent orifices and linings. The sulphide minerals overgrow, to varying degrees, the massive chalcopyrite formed during peak temperatures. (a-b) Little to no late-stage sulphide overgrowth within an active chimney sample. (c-d) Significant overgrowth of late-stage sulphide minerals within an inactive talus sample. (e-f) Overgrowth of sphalerite, chalcopyrite, and tetrahedrite-tennantite on a thick layer of late coarse-grained barite found along the inner vent lining, indicating the resurgence of hydrothermal activity within a single active chimney in the central region.

2.6.1.3 Late-stage

Late-stage mineral precipitation occurs during the waning stages of formerly high-temperature fluid flow. Primary late-stage mineralization includes sphalerite, galena, Pb-As sulphosalts, Pb-As-Sb sulphosalts, pyrite ± marcasite, and barite, and secondary phases such as bornite, digenite, and covellite. Growth of these secondary minerals occurs along the edges of massive chalcopyrite and tetrahedrite-tennantite (Fig. 2.13a-d). Fine-grained Pb-As and Pb-As-Sb sulphosalts or galena nucleate on these grain boundaries and are subsequently overgrown by sphalerite (Fig. 2.6h). In some cases, these conduits or pores become completely infilled by late sulphide mineralization (Fig. 2.7h). Late-stage barite growth occurs within open pore spaces and vugs, generally after all other sulphide mineralization (Fig. 2.5a, Fig. 2.7i). However, sphalerite overgrowth of barite has been observed in select samples, perhaps indicating a localized resurgence of hydrothermal activity. While barite may be remobilized within the peak-temperature stage, the extremely low solubility of barite at ambient seawater temperatures allows for its preservation in chimneys long after the hydrothermal system becomes inactive (Hannington et al., 1995; Jamieson et al., 2016). In contrast, the absence of anhydrite within inactive chimneys is consistent with anhydrite dissolution at ambient seawater

temperatures due to its retrograde solubility (Blount and Dickson, 1969). The occurrence of gold inclusions in sphalerite and barite also spans into the late-stage evolution of chimneys. Formation of amorphous silica is considered the last phase of primary mineralization (Fig. 2.5f).

2.6.2 Spatial variability in hydrothermal deposit composition

The prevalence of late-stage, low-temperature mineralization within the hydrothermal samples collected at Niua South gives evidence to suggest that the crater may contain individual chimneys that are experiencing a localized waning of hydrothermal activity and that peak venting temperatures are short-lived. An active chimney sample collected from the central region best highlights this waning, while also showing evidence of a subsequent resurgence of activity (Fig. 2.13e and 2.13f). The chimney was diffusely venting at the time of collection and is composed of a mineral assemblage that spans the entire paragenetic sequence. The late, low-temperature mineral assemblage of coarse-grained barite, sphalerite, and galena formed after a period of peak-temperature chalcopyrite mineralization, indicating that the active chimney was no longer maintaining the hydrothermal fluid temperatures it once had within its central conduit. However, subsequent banded overgrowths of sphalerite and chalcopyrite ± tetrahedrite-tennantite show that the temporary period of waning within the diffuse spire has been followed by a resurgence of activity (Fig. 2.13). While this could just be a localized occurrence, fluid temperatures of 300°C recorded from an adjacent chimney spire are consistent with precipitation of chalcopyrite. Active samples from the high-temperature northern region

do not exhibit significant overgrowth of chalcopyrite by late-stage barite, sphalerite or galena as observed in active chimney samples from the other regions. Overall, almost every inactive chimney or talus sample displays instances of this late-stage mineral assemblage. It should be noted that, although many of the collected samples show evidence of hydrothermal waning, this should not be taken as an indication that the overall hydrothermal system is necessarily waning. Venting within hydrothermal vent fields can be spatially dynamic, and fields typically contain a higher number of inactive vents, relative to active vents (Jamieson et al., 2014; Minami and Ohara, 2017; Seewald et al., 2019). The focusing of high-temperature venting at the northern end of the crater may simply be a result of the migration of focused hydrothermal upflow to this area over time.

The distinct differences in mineral assemblages between separate regions of the crater suggests that subsurface fluid temperatures are also distinct from one region to another. Hydrothermal samples collected from the northern region of the crater are almost all dominated by chalcopyrite, reflecting a state of peak-temperature activity within the hydrothermal system (Fig. 2.14). All 13 samples from the norther region were collected from two main active chimney complexes within 50-m of each other, one of which is venting boiling hydrothermal fluids (~325°C), and the other venting high-temperature hydrothermal fluids (~302°C). The venting of a boiling fluid suggests that negligible conductive cooling or shallow subsurface mixing of the vent fluid with local seawater is occurring below the two-phase vent (Bischoff and Rosenbauer, 1984). Sulphide-sulphate talus at the base of these active chimneys also contain the chalcopyrite-dominated, high-temperature mineral assemblages. Of the 13 samples, only 3 samples contain less than

15% modal abundance of chalcopyrite, and these samples have a corresponding mineralogical composition typical of the intermediate-temperature mineral suite. In contrast, chimney and talus samples from the central, eastern, and southern regions contain lower modal abundances of chalcopyrite, with 12 samples containing less than 5% chalcopyrite and 7 other samples contain between 5 – 20% chalcopyrite (Fig. 2.14). The central, eastern, and southern regions consist of four main active chimney complexes that are characterized by more diffuse venting and beehive-topped active spires, relative to the high-flux, open conduit vents in the northern region. One bornite-rich chimney complex in the eastern region shows an anomalous modal abundance of bornite of ~ 15% and gold content (50.6 ppm; Fig. 2.11, Fig. 2.14). The same correlation of mineral assemblages and associated temperatures are inferred for past venting, as recorded in the mineralogy of talus material throughout the crater. A combination of higher temperature fluid venting and dominance of high-temperature mineral assemblages define the chimney and talus material in the north, relative to the other hydrothermally-active parts of the crater. This indicates that (1) high-temperature subsurface fluid flow is concentrated in the northern part of the crater, or, alternately, (2) there is greater conductive cooling, or higher degrees of subsurface infiltration of cold seawater that is mixing with ascending hydrothermal fluid in the central, eastern, and southern regions that results in the venting of lower temperature fluids in the more southern parts of the crater.

Overall, active chimney complexes and underlying talus mounds in the central, eastern, and southern regions of the crater contain a higher proportion of lower temperature,

diffuse venting, relative to the more focused venting in the north. Based on observations from ROV video and data from the high-resolution bathymetry, hydrothermal mounds in the central and eastern regions are also larger than those in the north and may facilitate an increase in shallow seawater influx due to the potential of increased permeability of hydrothermal deposits. Based on surface observations in the AUV bathymetry or ROV video, there is no obvious fault control on permeability. Given the similar salinities and redox state of fluids collected from the various active vents at Niua (Gartman et al., 2019), it is likely that the entire field is fed by a single source fluid, and thus the difference in venting temperature between the northern vents and the central and eastern vents is due to a higher degree of subseafloor permeability and seawater infiltration in the central and eastern parts of the crater.

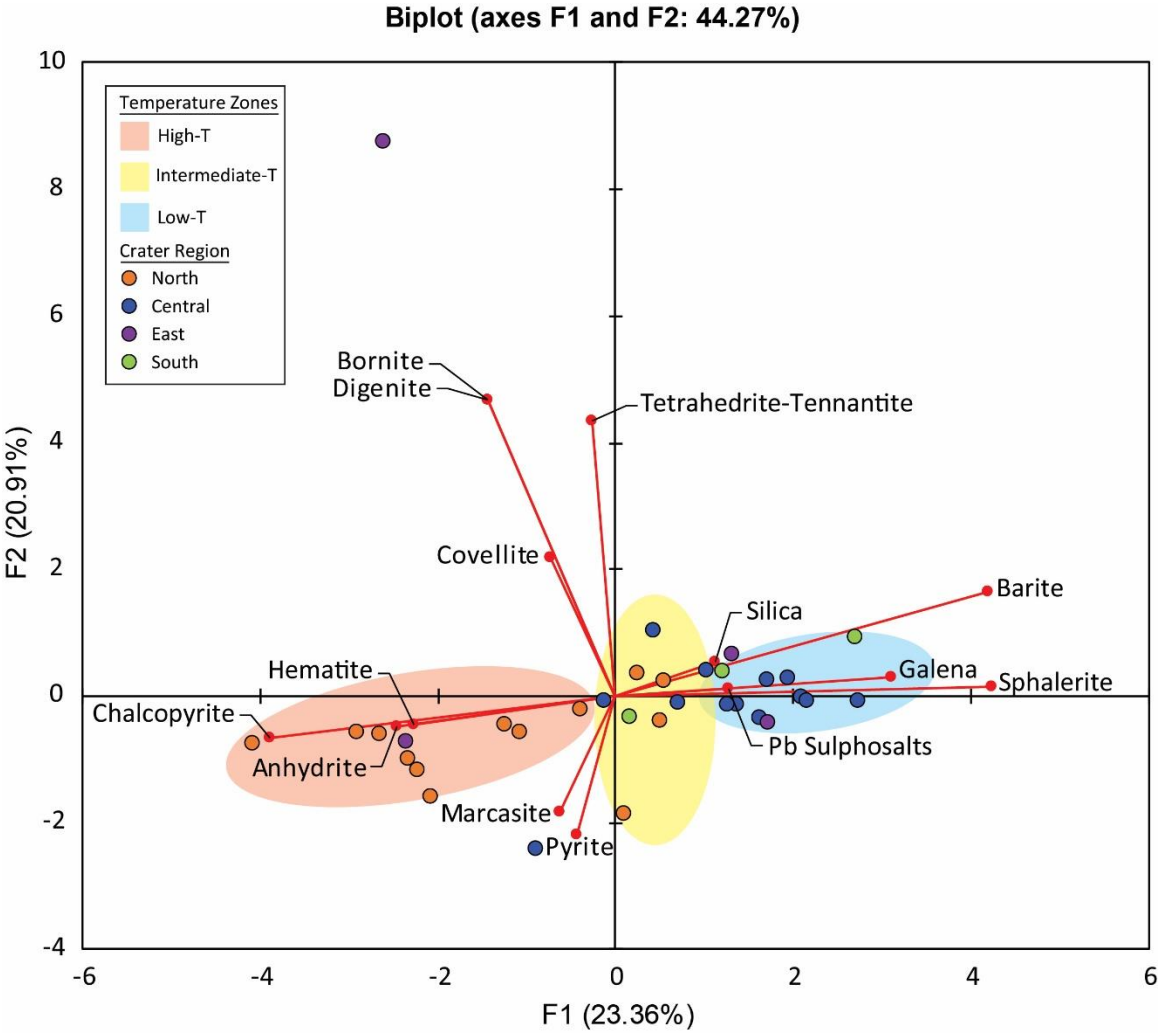

Figure 2.14. Principal component analysis of mineral modal abundances from sample thin sections. Sample points are colour-coded based on their location within the vent field; N=33. Colour-shaded areas group samples based of temperature, consistent with temperature-based subdivisions of samples classified in Figure 2.4.

2.6.3 Comparisons of hydrothermal deposits along the Tofua-Kermadec arc and back-arc

Volcanic arc and back-arc-related seafloor hydrothermal activity and associated sulphide deposition constitute roughly 40% of all known hydrothermal sites worldwide, with back-

arc basins hosting almost twice as many (and generally larger) sulphide deposits than volcanic arcs (Hannington et al., 2010). There are also key distinctions in the composition of hydrothermal deposits at back-arcs compared to volcanic arcs. Average bulk compositions of deposits found in intraoceanic back-arc basins show lower abundances in Cu, Zn, Pb, Au, Ag, Sb, Te, and Tl compared to intraoceanic arcs deposits like Niua, but are still relatively enriched in all but Cu with respect to mid-ocean ridges (Hannington et al., 2010; Monecke et al., 2016). The enrichment of elements such as Pb, As, Sb, and Ba in felsic-hosted deposits in arc and back-arc systems reflects the relative abundance of these elements in the host rocks (Hannington et al., 2005; Keith et al., 2016; Evans et al., 2017). Prolonged development of intraoceanic back-arc basins eventually leads to mature back-arc spreading centers, where the evolution to more basaltic oceanic crust produces hydrothermal deposits comparable to those found at mid-ocean ridges (Herzig et al., 1993; Fouquet et al., 1993).

Within the Lau Basin, the hydrothermal vent fields situated along the main mature back-arc spreading centers (i.e., CLSC, ILSC, ELSC, and VFR) become increasingly closer to the Tofua arc front from north to south. Along the ELSC and VFR, changes in crustal lithology from north to south correlate with increases in mantle-incompatible element abundances in both fluid and hydrothermal deposit samples (Evans et al., 2017). A grouping of six vent fields along these back-arc spreading ridges (from north to south) Kilo Moana, TowCam, Tahi Moana, ABE, Tu'i Malila, and Mariner are hosted in rocks that transition from back-arc basin basalts in the north to a combination of andesitic,

dacitic, and rhyolitic host-rocks further south. This transition corresponds to increases in Ba, Pb, As, and Sb in hydrothermal deposit samples (Evans et al., 2017).

Relative enrichments of Pb, As, and Sb in SMS deposit samples at Niua South are consistent with similar geochemical trends reported in the hydrothermal deposit samples by Evans et al. (2017) (Fig. 2.15). While average Ba content at Niua is elevated relative to the distal back-arc sites (i.e., Kilo Moana, TowCam, Tahi Moana, and ABE), it is not as high as that of the Tu'i Malila vent field, which is positioned within the back-arc, but relatively close to the Tofua arc. Even with the omission of barite-rich flanges from this dataset (3 samples; 40–49 wt.% Ba), samples at Tu'i Malila still have anomalously elevated barite content compared to Niua South.

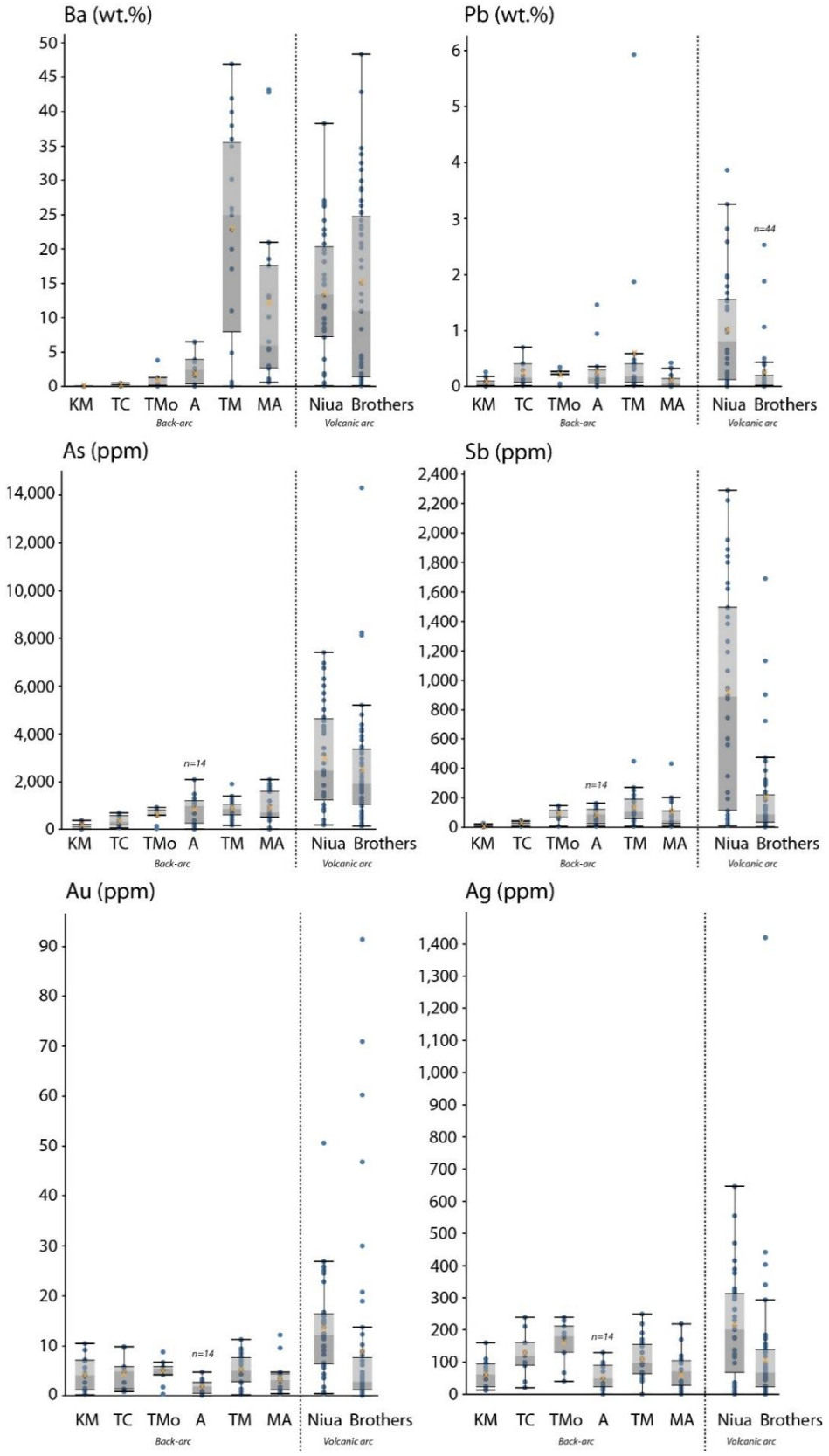
Ba (wt.%)
Pb (wt.%)
As (ppm)
Sb (ppm)
Au (ppm)
Ag (ppm)
KM TC TMo A TM MA Niua Brothers
Back-arc
Volcanic arc
n=14
n=44

Figure 2.15. Compilation of compositions of hydrothermal deposits from the ELSC (from Evans et al., 2017), Brothers volcano (de Ronde et al., 2005), and Niua South (this study). Hydrothermal sites (X-axis) transition left to right from back-arc settings to progressively more arc-influenced. This transition is associated with changes in crustal lithology, from basaltic to more felsic host rock composition. Eighteen samples characterized as active or relict flanges, and squat terraces were omitted from the Evans et al., (2017) dataset comparison. This was done to more accurately compare to the hydrothermal chimney and talus samples collected from Niua South. Additionally, an average element content was used for 27 geochemical subsamples reported by de Ronde et al., (2005) from a single sphalerite chimney. All samples used from Brothers caldera are from the northwest caldera hydrothermal field. Location abbreviations: KM = Kilo Moana (n=16), TC = TowCam (n=10), TMo = Tahi Moana (n=9), A = ABE (n=15), TM = Tu'i Malila (n=21), MA = Mariner (n=18). For data for the first 6 hydrothermal sites, see supplementary data from Evans et al. (2017). For data from Niua (n=36), see Table 2.1. For data from Brothers (n=57), see supplementary data from de Ronde et al. (2005) and de Ronde et al., (2011). Plot whiskers extend to data within 1.5 times the interquartile range. Small orange x's mark the average value for each dataset.

In general, average Pb content for the ELSC sites increases from north to south, except for Mariner, which has a lower average Pb content than all other sites. Again, the Tu'i Malila vent field has an anomalously high abundance of Pb for one sample, owing to the frequent presence of galena (Evans et al., 2017). Average Pb content is highest at Niua South. Ewart et al. (1998) have attributed past and present subduction of the Louisville Ridge-Seamount Chain along the Tofua arc as sources of Pb within arc lavas. It is unknown if this process has contributed Pb to arc lavas at Niua, but this is a possible source for the relative enrichments of Pb within the crater deposits. Average elemental content of Pb, As, and Sb shows depletions at the northwest caldera site at Brothers, relative to Niua South. Brothers lacks any contribution of Pb from subduction of the seamount chain. However, the subduction of the basaltic-dominated Hikurangi Plateau beneath the southern Kermadec arc may also be contributing to an enrichment of Pb, As, and Sb in more felsic arc lava compositions (de Ronde et al., 2007; Timm et al., 2014).

Average As and Sb content increase from north to south along the ELSC and is highest at Brothers and Niua, with the exception of Sb at Mariner. Arsenic content at Brothers is slightly lower than Niua, whereas Sb is significantly higher. At Niua, As and Sb form multiple discrete sulphosalt mineral phases, in which these elements are a major component, whereas Evans et al. (2017) only report these trace metals as components of other sulphide minerals (i.e. As in pyrite, marcasite, sphalerite, and some chalcopyrite and wurtzite; Sb in sphalerite, and some wurtzite and chalcopyrite), but rarely within discrete phases. The Mariner vent field, where trace amounts of tennantite were reported, is again a prominent exception. Vent fluids analyzed at Mariner are notably lower pH than both Niua and the remaining ELSC sites and are hypothesized to have localized input of magmatic volatiles (Mottl et al., 2011). In the context of other hydrothermal deposits along the Tonga-Kermadec arc and back-arc sites, Niua South shows consistent geochemical enrichments that are considered to be associated with its position directly on the volcanic arc, similar to Brothers. These trends are also consistent with the progressive geochemical trends that correlate with distance from the arc for seawater-dominated hydrothermal systems within the back arc (i.e., excluding Mariner).

2.6.4 Precipitation of Au in arc volcano-hosted hydrothermal systems

Average Au content in Niua South and Brothers samples are high compared to the ELSC back-arc sites, which show a high degree of variability in concentrations of both Au and Ag (de Ronde et al., 2005, 2011; Evans et al., 2017). The highest Au concentration are recorded from Brothers samples, but average Au content is highest at Niua South. At

Brothers volcano, high Au contents (up to 91 ppm) are linked to a magmatic suite of elements including Bi, Te, and Se, and the mechanism of gold enrichment was suggested to be scavenging by liquid bismuth (Berkenbosch et al., 2012), as is suggested for other Au-Bi rich systems (e.g., Törmänen & Koski, 2005). At Niua, the proposed mechanism of gold enrichment is boiling of high-temperature fluids, which induces the formation of gold colloids that are transported within ascending fluids (Gartman et al., 2018). The association of gold particles with both low- and high temperature mineral assemblages highlights the capacity of gold to be deposited across a wide range of fluid temperature conditions within the chimneys. This is evidenced in both focused and diffuse flow fluids (Gartman et al., 2018), as well as in the wall of a diffusely venting chimney, as observed in this study. In all cases where particles do not occur as discrete phases, they occur as inclusions within chalcopyrite and barite.

In contrast to conductive cooling and oxidation related deposition of Au from solution (e.g., Fuchs et al., 2019) it is not clear that either colloidal transport, or liquid Bi scavenging, would result in specific major mineralogical associations of Au. Gold colloids could leave solution at multiple locations in the fluid-flow path based on colloid destabilization, and although melts of Bi or Au-Bi would solidify below either 271 or 274°C, respectively, Au-Bi minerals may occur in higher temperature assemblages as the liquid elements have been suggested to become trapped within mineral grains and solidify later (Törmänen and Koski, 2005). Although both mechanisms may therefore result in variable major mineral associations, Au enriched through liquid-Bi scavenging should be spatially associated with Bi and may include Au-Bi minerals, which are not observed at

Niua, and although Au and Bi are both individually enriched at Niua, their geochemical correlation is not significant (Table 2.1, Fig. 2.11). Therefore, the mechanism for gold enrichment is still unclear.

2.6.5 Evidence for magmatic contributions

Circulating hydrothermal fluids in volcanic arc and back-arc hydrothermal systems have been suggested to carry a magmatic signature. Evidence for a magmatic signature include (1) elevated concentrations of magmatic volatiles (e.g., CO_2) and 'magmatophile' elements (e.g., Se, Te, or Bi) in hydrothermal fluids relative to mid-ocean ridges (Berkenbosch et al., 2012; de Ronde et al., 2005, 2011; Evans et al., 2017; Leybourne et al., 2012b; Lupton et al., 2008; Wohlgemuth-Ueberwasser et al., 2015); (2) analyses of copper and sulphur isotopes in sulphide and gangue minerals within seafloor hydrothermal deposits (Berkenbosch et al., 2015; de Ronde et al., 2005; McDermott et al., 2015); and (3) high metal concentrations in melt and fluid inclusion data from select minerals in seafloor host rocks and hydrothermal deposits, respectively (Yang and Scott, 1996, 2002; de Ronde et al., 2005). Ultimately, magmatic volatiles may be important for transporting metals directly from the magma reservoir to ascending hydrothermal fluids (Yang and Scott, 2006). Most of the studies investigating magmatic input into hydrothermal systems have either focused on direct or indirect analysis of the compositions of hydrothermal fluids or fluid inclusions, as opposed to the associated mineral deposits.

At Brothers volcano, there are two closely-spaced, but distinct hydrothermal systems: a hydrothermal system located on the northwest caldera wall that is interpreted to be seawater-dominated, and is characterized by typical sulphide-rich chimneys; and a hydrothermal system at the summit of a resurgent dacitic cone, located ~2.5 km to the SE, that is characterized by an advanced argillic alteration assemblage including native sulphur, low-pH fluids, and is interpreted to be influenced by direct magmatic degassing (de Ronde et al., 2005). Berkenbosch et al. (2012) suggest that the occurrences of enargite, tennantite, specular hematite, and Bi-tellurides in chimney samples at the seawater-dominated northwest caldera site is evidence of input of magmatic volatiles. Secondary bornite and other Cu-sulphide phases (i.e., digenite and covellite), and euhedral hematite were also observed in Cu-rich chimneys sampled from the northwest caldera. This mineral assemblage is attributed to late oxidizing fluids associated with an increase in the inward advection of seawater through the chimney walls, signifying the waning stages of active chimney growth (de Ronde et al., 2011). Bornite also occurs with enargite, alunite, and anhydrite under high-sulphidation conditions in some subaerial magmatic-hydrothermal systems (de Ronde et al., 2005, 2011).

Similar to Brothers, the Niua volcanic complex also hosts two discrete, highly contrasting hydrothermal systems: one dominated by magmatic fluids at Niua North, and the other by more typical seawater-dominated fluids at Niua South (Resing et al., 2012). The resurgent cone site at Brothers volcano is characterized by upwelling fluids that are low-temperature (≤122°C) and diffuse, and are also relatively metal-poor and gas- and sulphur-rich (de Ronde et al., 2011). At Niua North, individual vents are mostly

composed of low-lying mounds of native sulphur and bacterial mats, and are associated with liquid CO_2 and molten sulphur, and therefore comparable to the widespread expulsion of magmatic gases at central cone at Brothers (Resing et al., 2012). These observations suggest that there is a component of magmatic CO_2 added directly to the hydrothermal system below Niua North (Lupton et al., 2008). In contrast, the northwest caldera of Brothers volcano hosts focused, high-temperature (≤300°C) chimneys, that are relatively metal-rich and gas-poor (de Ronde et al., 2011), similar to Niua South. Bornite, hematite, and Bi-tellurides form within chalcopyrite-rich chimneys at both sites, but their origins appear to be different. Three of the four samples collected from the 325°C boiling chimney in the northern region of the Niua South crater contain notable occurrences of chalcopyrite with bornite, digenite, and covellite (Fig. 2.6f, Fig. 2.9a and 2.9d-f), and euhedral hematite (Fig. 2.9e and 2.9f). The bornite and euhedral hematite within these samples are interpreted to be primary and could be a result of more oxidized magmatic fluids (de Ronde et al., 2011). More oxidized fluids could result from mixing with local cold seawater. However, this mechanism is unlikely to occur within the northern region of the Niua South crater, as these vents are dominated by the high-temperature mineral suite (e.g., chalcopyrite, anhydrite, and pyrite; >300°C) and boiling fluids (~325°C) that have not been cooled by either mixing or conductive cooling. Furthermore, if bornite and hematite formed simply from changes in redox state due to mixing, their occurrence would be more widespread in other hydrothermal systems. However, sulphur isotope compositions of fluids from Niua South do not show any evidence of magmatic SO_2 disproportionation, suggesting that there is currently not a significant magmatic contribution to the hydrothermal fluids (Gartman et al., 2019; McDermott et al., 2015).

It thus remains unclear as to the source of the more oxidizing mineral assemblage associated with the high-temperature vents in the northern region of the crater. It is possible that there is enough of a magmatic contribution to cause a noticeable increase in the redox state of the fluid and associated mineral deposits, but not enough for this contribution to be detectable by S-isotope fractionations associated with SO_2 disproportionation. Further investigations of the abundances and partitioning of magmatic-associated elements such as Bi, Te, and Se may provide important insights into the possible contribution of magmatic volatiles to the Niua South hydrothermal system.

2.7. Conclusions

Hydrothermal deposits at the Niua South crater provide a record of arc-volcano hosted hydrothermal circulation and mineral deposition. Active chimneys forming within the Niua South crater are venting at fluid temperatures between 250–325°C. A variety of hydrothermal flow regimes are present in the active chimneys, from high-temperature, focused, two-phase chimneys, to low-temperature diffuse chimneys. Chimney and talus samples collected within the crater are either Cu- or Ba-Zn-rich and are largely composed of chalcopyrite + anhydrite + pyrite/marcasite ± secondary Cu-sulphide phases, and barite + sphalerite + pyrite/marcasite + galena ± chalcopyrite, respectively. Overall, the samples from Niua South follow a paragenetic growth sequence consisting of three stages. The early-stage of chimney growth is defined by the initial formation of barite or anhydrite, followed by pyrite/marcasite and sphalerite. Peak temperature formation occurring within

some active chimneys is chalcopyrite-dominated but is also accompanied by local primary bornite and digenite forming complex intergrowths and exsolution. The late stages of chimney growth are identified by overgrowths of inner chalcopyrite linings within the interior of active of inactive chimneys, by a low-temperature mineral assemblage. This stage is characterized by an abundance of sphalerite and barite with other minor phases including galena, sulphosalts, secondary Cu-sulphides, and native gold. Trace elements abundances are variably enriched within the samples but can be associated with either Cu- or Ba-Zn-rich mineralization. Higher abundances of As, Sb, Ag, Cd, and Sr are found in low-temperature Ba-Zn-rich samples, while Bi, Te, Se, and Sn are commonly elevated in high-temperature Cu-rich samples. Gold is variably enriched throughout the samples and is found within high- and low-temperature active chimneys and inactive sulphide-sulphate talus.

Back-arc vent fields within the Lau Basin show general increases in the abundance of Ba, Pb, As, and Sb with closer proximity to the Tofua-Kermadec volcanic arc, and, as a volcanic arc, Niua South is consistent with this trend. The enrichment of such elements reflects the more felsic nature of host rocks present in arc volcano-hosted hydrothermal systems. Additionally, average bulk compositions of deposits found in intraoceanic arc deposits show enrichments in Cu, Zn, Au, Ag, Te, and Tl compared to intraoceanic back-arc deposits. In comparison, mid-ocean ridge deposits are characteristically depleted in all of these elements, with the exception of Cu (Hannington et al., 2010; Monecke et al., 2016). This is largely owed to the mafic composition of typical mid-ocean ridge lavas.

Primary associations of bornite, digenite, and euhedral hematite within active high-temperature chimneys suggest a possible contribution of more oxidizing vent fluids at Niua South, similar to Brothers volcano, and elements attributed to magmatic origins, such as Bi, Te, Au, and Se, that are enriched in these chimneys point to possible past magmatic contributions to the vent fluid. However, current venting fluids appear to be seawater-dominated.

Prior to this study, much of our understanding of arc volcano-hosted hydrothermal systems was from the results of multiple studies of Brothers volcano. This study provides an important contribution to our understanding of the diversity in morphology, geological setting and composition of seafloor hydrothermal deposits hosted on arc volcanoes by highlighting the similarities and differences between the hydrothermal systems at Brothers and Niua South.

2.8. References

Baker, E. T., Walker, S. L., Embley, R. W., & de Ronde, C. E. J. (2012). High-Resolution Hydrothermal Mapping of Brothers Caldera, Kermadec Arc. Economic Geology, 107, p. 1583–1593.

Baker, E. T., Walker, S. L., Massoth, G. J., & Resing, J. A. (2019). The NE Lau Basin: Widespread and Abundant Hydrothermal Venting in the Back-Arc Region Behind a Superfast Subduction Zone. Frontiers in Marine Science, 6(July), p. 1–15. https://doi.org/10.3389/fmars.2019.00382.

Barton Jr., P. B., & Bethke, P. M. (1987). Chalcopyrite disease in sphalerite: Pathology and epidemiology. American Mineralogist, 72, p. 451–467.

Beaulieu, Stace E; Szafrański, Kamil M (2020): InterRidge Global Database of Active Submarine Hydrothermal Vent Fields Version 3.4. PANGAEA, https://doi.org/10.1594/PANGAEA.917894

Beaulieu, S. E., Baker, E. T., German, C. R., & Maffei, A. (2013). An authoritative global database for active submarine hydrothermal vent fields. Geochemistry, Geophysics, Geosystems, 14(11), p. 4892–4905. https://doi.org/10.1002/2013GC004998.

Berkenbosch, H. A., de Ronde, C. E. J., Gemmell, J. B., McNeill, A. W., & Goemann, K. (2012). Mineralogy and Formation of Black Smoker Chimneys from Brothers Submarine Volcano, Kermadec Arc. Economic Geology, 107(8), p. 1613–1633. https://doi.org/10.2113/econgeo.107.8.1613.

Bischoff, J. L., & Rosenbauer, R. J. (1984). The critical point and two-phase boundary of seawater, 200-500C. Earth and Planetary Science Letters, 68, p. 172–180.

Bischoff, J. L., & Seyfried, W. E. (1978). Hydrothermal chemistry of seawater from 25° to 350°C. American Journal of Science, 278, p. 838–860.

Blount, C. W., & Dickson, F. W. (1969). The solubility of anhydrite (CaSO4) in NaCl-H2O from 100 to 450°C and 1 to 1000 bars. Geochimica et Cosmochimica Acta, 33, p. 227–245. https://doi.org/10.1016/0016-7037(69)90140-9.

Butler, I. B., & Nesbitt, R. W. (1999). Trace element distributions in the chalcopyrite wall of a black smoker chimney: insights from laser ablation inductively coupled plasma mass spectrometry (LA–ICP–MS). Earth and Planetary Science Letters, 167, p. 335–345.

Cook, N. J., Ciobanu, C. L., Pring, A., Skinner, W., Shimizu, M., Danyushevsky, L., et al. (2009). Trace and minor elements in sphalerite: A LA-ICPMS study. Geochimica et Cosmochimica Acta, 73, p. 4761–4791. https://doi.org/10.1016/j.gca.2009.05.045.

de Ronde, C. E. J., Baker, E. T., Massoth, G. J., Lupton, J. E., Wright, I. C., Feely, R. A., & Greene, R. R. (2001). Intra-oceanic subduction-related hydrothermal venting, Kermadec volcanic arc, New Zealand. Earth and Planetary Science Letters, 193, p. 359–369. https://doi.org/10.1016/S0012-821X(01)00534-9.

de Ronde, C. E. J., Faure, K., Bray, C. J., Chappell, D. A., & Wright, I. C. (2003). Hydrothermal fluids associated with seafloor mineralization at two southern Kermadec arc volcanoes, offshore New Zealand. Mineralium Deposita, 38, p. 217–233. https://doi.org/10.1007/s00126-002-0305-4.

de Ronde, C. E. J., Hannington, M. D., Stoffers, P., Wright, I. C., Ditchburn, R. G., Reyes, A. G., et al. (2005). Evolution of a submarine magmatic-hydrothermal system: Brothers volcano, southern Kermadec Arc, New Zealand. Economic Geology, 100(6), p. 1097–1133. https://doi.org/10.2113/gsecongeo.100.6.1097.

de Ronde, C. E. J., Baker, E. T., Massoth, G. J., Lupton, J. E., Wright, I. C., Sparks, R. J., et al. (2007). Submarine hydrothermal activity along the mid-Kermadec Arc, New Zealand: Large-scale effects on venting. Geochemistry, Geophysics, Geosystems, 8(7), p. 1–27. https://doi.org/10.1029/2006GC001495.

de Ronde, C. E. J., Massoth, G. J., Butterfield, D. A., Christenson, B. W., Ishibashi, J., Ditchburn, R. G., et al. (2011). Submarine hydrothermal activity and gold-rich mineralization at Brothers Volcano, Kermadec Arc, New Zealand. Mineralium Deposita, 46(5), p. 541–584. https://doi.org/10.1007/s00126-011-0345-8.

de Ronde, C. E. J., Humphris, S. E., Höfig, T. W., & Scientists, E. 376. (2019). Expedition 376 Preliminary Report: Brothers Arc Flux. International Ocean Discovery Program. https://doi.org/https://doi.org/10.14379/iodp.pr.376.2018.

Ditchburn, R. G., & de Ronde, C. E. J. (2017). Evidence for Remobilization of Barite Affecting Radiometric Dating Using 228 Ra, 228 Th, and 226 Ra/Ba Values: Implications for the Evolution of Sea-Floor Volcanogenic Massive Sulfides. Economic Geology, 112, p. 1231–1245. https://doi.org/10.5382/econgeo.2017.4508.

Dupont, J., & Herzer, R. H. (1985). Effect of Subduction of the Louisville Ridge on the Structure and Morphology of the Tonga Arc. Geology and Offshore Resources of Pacific Island Arcs-Tonga Region, Circum-Pacific Council for Energy and Mineral Resources Earth Science Series v. 2, 2, p. 323–332.

Eldridge, C. S., Barton Jr., P. B., & Ohmoto, H. (1983). Mineral textures and their bearing on formation of the Kuroko Orebodies. Economic Geology, 5, p. 241–281.

Embley, R. W., de Ronde, C. E. J., Merle, S. G., Davy, B., & Caratori Tontini, F. (2012). Detailed morphology and structure of an active submarine arc caldera: Brothers Volcano, Kermadec Arc. Economic Geology, 107, p. 1557–1570. https://doi.org/10.2113/econgeo.107.8.1557.

Evans, G. N., Tivey, M. K., Seewald, J. S., & Wheat, C. G. (2017). Influences of the Tonga Subduction Zone on seafloor massive sulfide deposits along the Eastern Lau Spreading Center and Valu Fa Ridge. Geochimica et Cosmochimica Acta, 215, p. 214–246. https://doi.org/10.1016/j.gca.2017.08.010.

Ewart, A., Collerson, K. D., Regelous, M., Wendt, J. I., & Niu, Y. (1998). Geochemical Evolution within the Tonga – Kermadec – Lau Arc – Back-arc Systems : the Role of Varying Mantle Wedge Composition in Space and Time, 39(3), p. 331–368.

Ferrini, V. L., Tivey, M. K., Carbotte, S. M., Martinez, F., & Roman, C. (2008). Variable morphologic expression of volcanic, tectonic, and hydrothermal processes at six hydrothermal vent fields in the Lau back-arc basin. Geochemistry, Geophysics, Geosystems. https://doi.org/10.1029/2008GC002047.

Fouquet, Y., Auclair, G., Cambon, P., & Etoubleau, J. (1988). Geological setting and mineralogical and geochemical investigations on sulfide deposits near 13°N on the East Pacific Rise. Marine Geology, 84, p. 145–178. https://doi.org/10.1016/0025-3227(88)90098-9.

Fouquet, Y., Von Stackelberg, U., Charlou, J. L., Erzinger, J., Herzig, P. M., Muhe, R., & Wiedicke, M. (1993). Metallogenesis in back-arc environments: The Lau basin example. Economic Geology, 88(8), p. 2154–2181. https://doi.org/10.2113/gsecongeo.88.8.2154.

Fouquet, Y., Pelleter, E., Konn, C., Chazot, G., Dupré, S., Alix, A. S., et al. (2018). Volcanic and hydrothermal processes in submarine calderas: The Kulo Lasi example (SW Pacific). Ore Geology Reviews, 99. https://doi.org/10.1016/j.oregeorev.2018.06.006.

Fuchs, S., Hannington, M. D., & Petersen, S. (2019). Divining gold in seafloor polymetallic massive sulfide systems. Mineralium Deposita, 54, p. 789–820. https://doi.org/10.1007/s00126-019-00895-3.

Gartman, A., Hannington, M. D., Jamieson, J. W., Peterkin, B., Garbe-Schönberg, D., Findlay, A. J., et al. (2018). Boiling-induced formation of colloidal gold in black smoker hydrothermal fluids. Geology, 46(1), p. 1–4. https://doi.org/https://doi.org/10.1130/G39492.1.

Gartman, A., Findlay, A. J., Hannington, M. D., Garbe-Schönberg, D., Jamieson, J. W., & Kwasnitschka, T. (2019). The role of nanoparticles in mediating element deposition and transport at hydrothermal vents. Geochimica et Cosmochimica Acta, 261, p. 113–131. https://doi.org/10.1016/j.gca.2019.06.045.

Graham, I. J., Reyes, A. G., Wright, I. C., Peckett, K. M., Smith, I. E. M., & Arculus, R. J. (2008). Structure and petrology of newly discovered volcanic centers in the northern Kermadec-southern Tofua arc, South Pacific Ocean. Journal of Geophysical Research: Solid Earth, 113(8). https://doi.org/10.1029/2007JB005453.

Haase, K. M., Beier, C., Bach, W., Kleint, C., Anderson, M., Buttner, H., et al. (2018). RV Sonne Cruise Report Tonga Rift Cruise No. SO263.

Hannington, M. D., Jonasson, I. R., Herzig, P. M., & Petersen, S. (1995). Physical and chemical processes of seafloor mineralization at mid-ocean ridges, American Geophysical Union. p. 115–157. https://doi.org/10.1029/GM091p0115.

Hannington, M. D., de Ronde, C. E. J., & Petersen, S. (2005). Sea-Floor Tectonics and Submarine Hydrothermal Systems. Economic Geology, 100, p. 111–141.

Hannington, M. D., Jamieson, J. W., Monecke, T., & Petersen, S. (2010). Modern Sea-Floor Massive Sulfides and Base Metal Resources: Toward an Estimate of Global Sea-Floor Massive Sulfide Potential. Society of Economic Geologists Special Publication, 15, p. 111–141.

Haymon, R. M. (1983). Growth history of hydrothermal black smoker chimneys. Nature, 301, p. 695–698.

Herzig, P. M., & Hannington, M. D. (1995). Polymetallic massive sulfides at the modem seafloor A review. Ore Geology Reviews, 10(10), p. 95–115.

Herzig, P. M., Hannington, M. D., Fouquet, Y., von Stackelberg, U., & Petersen, S. (1993). Gold-rich polymetallic sulfides from the Lau back arc and implications for the geochemistry of gold in sea-floor hydrothermal systems of the Southwest Pacific. Economic Geology, 88(8), p. 2182–2209. https://doi.org/10.2113/gsecongeo.88.8.2182.

Huston, D. L., Sie, S. H., Suter, G. F., Cooke, D. R., & Both, R. A. (1995). Trace elements in sulfide minerals from eastern Australian volcanic-hosted massive sulfide deposits: Part I. Proton microprobe analyses of pyrite, chalcopyrite, and sphalerite, and Part II. Selenium levels in pyrite: comparison with δ34S values and implic. Economic Geology, 90, p. 1167–1196. https://doi.org/10.2113/gsecongeo.90.5.1167.

Iizasa, K., Asada, A., Mizuno, K., Katase, F., Lee, S., Kojima, M., & Ogawa, N. (2019). Native gold and gold-rich sulfide deposits in a submarine basaltic caldera, Higashi-Aogashima hydrothermal field, Izu-Ogasawara frontal arc, Japan. Mineralium Deposita, 54, p. 117–132. https://doi.org/10.1007/s00126-018-0808-2.

Ikehata, K., Suzuki, R., Shimada, K., Ishibashi, J., & Urabe, T. (2015). Mineralogical and Geochemical Characteristics of Hydrothermal Minerals Collected from Hydrothermal Vent Fields in the Southern Mariana Spreading Center. https://doi.org/10.1007/978-4-431-54865-2_22.

Ishibashi, J.-I., Lupton, J. E., Yamaguchi, T., Querellou, J., Nunoura, T., & Takai, K. (2006). Expedition reveals changes in Lau Basin hydrothermal system. Eos, 87(2), p. 13–17. https://doi.org/10.1029/2006EO020001.

Jamieson, J. W., Clague, D. A., & Hannington, M. D. (2014). Hydrothermal sulfide accumulation along the Endeavour Segment, Juan de Fuca Ridge. Earth and Planetary Science Letters, 395, p. 136–148. https://doi.org/10.1016/j.epsl.2014.03.035.

Jamieson, J. W., Hannington, M. D., Tivey, M. K., Hansteen, T., Williamson, N. M. B., Stewart, M., et al. (2016). Precipitation and growth of barite within hydrothermal vent deposits from the Endeavour Segment, Juan de Fuca Ridge. Geochimica et Cosmochimica Acta, 173. https://doi.org/10.1016/j.gca.2015.10.021.

Jankowski, P. (2012). NI 43-101 Technical Report 2011 PNG, Tonga, Fiji, Solomon Islands, New Zealand, Vanuatu and the ISA.

Johns, S. M., Ditchburn, R. G., Barry, B. J., & Yeats, C. J. (2014). Episodic subseafloor hydrothermal activity within the eastern Manus back-arc basin determined by uranium-series disequilibrium in barite. Economic Geology, 109(8), p. 2227–2241. https://doi.org/10.2113/econgeo.109.8.2227.

Jones, B., de Ronde, C. E. J., & Renaut, R. W. (2008). Mineralized microbes from Giggenbach submarine volcano, 113(November 2007), p. 1–13. https://doi.org/10.1029/2007JB005482.

Juniper, S. K., Jonasson, I. R., Tunnicliffe, V., & Southward, A. J. (1992). Influence of a tube-building polychaete on hydrothermal chimney mineralization. Geology, 20(10), p. 895–898. https://doi.org/10.1130/0091-7613(1992)020<0895:IOATBP>2.3.CO;2.

Keith, M., Häckel, F., Haase, K. M., Schwarz-Schampera, U., & Klemd, R. (2016). Trace element systematics of pyrite from submarine hydrothermal vents. Ore Geology Reviews, 72. https://doi.org/10.1016/j.oregeorev.2015.07.012.

Kim, J., Lee, I., Halbach, P., Lee, K.-Y., Ko, Y.-T., & Kim, K.-H. (2006). Formation of hydrothermal vents in the North Fiji Basin: Sulfur and lead isotope constraints. Chemical Geology, 233, p. 257–275. https://doi.org/10.1016/j.chemgeo.2006.03.011.

Koschinsky, A., Seifert, R., Halbach, P., Bau, M., Brasse, S., De Carvalho, L. M., & Fonseca, N. M. (2002). Geochemistry of diffuse low-temperature hydrothermal fluids in the North Fiji Basin. Geochimica et Cosmochimica Acta, 66(8), p. 1409–1427. https://doi.org/10.1016/S0016-7037(01)00855-9.

Kretz, R. (1983). Symbols for rock-forming minerals, 68, p. 277–279.

Kwasnitschka, T. (2016). Virtual Vents : The changing face of hydrothermalism revealed. https://doi.org/10.7284/906663.

Lee, S., Kim, S. J., Ju, S. J., Pak, S. J., Son, S. K., Yang, J., & Han, S. (2015). Mercury accumulation in hydrothermal vent mollusks from the southern Tonga Arc, southwestern Pacific Ocean. Chemosphere, 127, p. 246–253. https://doi.org/10.1016/j.chemosphere.2015.01.006.

Leybourne, M. I., de Ronde, C. E. J., Wysoczanski, R. J., Walker, S. L., Timm, C., Gibson, H. L., et al. (2012). Geology, hydrothermal activity, and sea-floor massive sulfide mineralization at the rumble II west mafic caldera. Economic Geology, 107(8). https://doi.org/10.2113/econgeo.107.8.1649.

Leybourne, M. I., Schwarz-Schampera, U., de Ronde, C. E. J., Baker, E. T., Faure, K., Walker, S. L., et al. (2012). Submarine magmatic-hydrothermal systems at the monowai volcanic center, Kermadec Arc. Economic Geology, 107(8), p. 1669–1694. https://doi.org/10.2113/econgeo.107.8.1669.

Li, K., Brugger, J. L., & Pring, A. (2018). Exsolution of chalcopyrite from bornite-digenite solid solution: an example of a fluid-driven back-replacement reaction. Mineralium Deposita, 53, p. 903–908. https://doi.org/10.1007/s00126-018-0820-6.

Lupton, J. E., Lilley, M., Butterfield, D. A., Evans, L., Embley, R. W., Massoth, G., et al. (2008). Venting of a separate CO2-rich gas phase from submarine arc volcanoes: Examples from the Mariana and Tonga-Kermadec arcs. Journal of Geophysical Research: Solid Earth, 113(8). https://doi.org/10.1029/2007JB005467.

Maslennikov, V. V., Maslennikova, S. P., Large, R. R., & Danyushevsky, L. V. (2009). Silurian Yaman-Kasy volcanic-hosted massive sulfide deposit (southern Urals, Russia) using laser ablation-inductively coupled plasma mass spectrometry (LA-ICPMS. Economic Geology, p. 1111–1141.

McDermott, J.M., Ono, S., Tivey, M.K., Seewald, J.S., Shanks, III, W.C., and Solow, A.R. (2015). Identification of sulfur sources and isotopic equilibria in submarine hot-springs using multiple sulfur isotopes. Geochimica et Cosmochimica Acta, v. 150, p. 169-187.

Merle, S. G., Embley, R. W., Lupton, J. E., Baker, E. T., Resing, J. A., & Lilley, M. (2008). Northeast Lau Basin, R/V Thompson Expedition TN227.

Minami, H., & Ohara, Y. (2017). The Gondou hydrothermal field in the Ryukyu Arc: A huge hydrothermal system on the flank of a caldera volcano. Geochemistry, Geophysics, Geosystems, 18(9), p. 3489–3516. https://doi.org/10.1002/2017GC006868.

Monecke, T., Petersen, S., & Hannington, M. D. (2014). Constraints on water depth of massive sulfide formation: Evidence from modern seafloor hydrothermal systems in arc-related settings. Economic Geology. https://doi.org/10.2113/econgeo.109.8.2079.

Monecke, T., Petersen, S., Hannington, M. D., Grant, H., & Samson, I. (2016). The minor element endowment of modern sea-floor massive sulfide deposits and comparison with deposits hosted in ancient volcanic successions. Reviews in Economic Geology, 18, p. 245–306.

Mottl, M. J., Seewald, J. S., Wheat, C. G., Tivey, M. K., Michael, P. J., Proskurowski, G., et al. (2011). Chemistry of hot springs along the Eastern Lau Spreading Center. Geochimica et Cosmochimica Acta, 75(4), p. 1013–1038. https://doi.org/10.1016/j.gca.2010.12.008

Murowchick, J. B., & Barnes, H. L. (1986). Marcasite precipitation from hydrothermal solutions. Geochimica et Cosmochimica Acta, 50(12), p. 2615–2629. https://doi.org/10.1016/0016-7037(86)90214-0.

Pearce, J. A., & Peate, D. W. (1995). Tectonic implications of the composition of volcanic arc magmas. Ann. Rev. Earth Planet. Sci, 23, p. 251–285.

Resing, J. A., Embley, R. W., & Merle, S. G. (2012). Submarine Ring of Fire-2012 (SRoF-12) Northeast Lau Basin: R/V Roger Revelle Expedition RR1211, Cruise Report Sept 9-25, 2012, Suva-Samoa.

Rona, P. A., Hannington, M. D., Raman, C. V., Thompson, G., Tivey, M. K., Humphris, S. E., et al. (1993). Active and relict sea-floor hydrothermal mineralization at the TAG hydrothermal field, Mid-Atlantic Ridge. Economic Geology, 88, p. 1989–2017. https://doi.org/10.2113/gsecongeo.88.8.1989.

Sack, R. O., & Loucks, R. R. (1985). Thermodynamic properties of tetrahedrite-tennanites: constraints on the interdependence of the Ag-Cu, Fe-Zn, Cu-Fe, and As-Sb exchange reactions. American Mineralogist, 70(11–12), p. 1270–1289.

Schoonen, M. A. A., & Barnes, H. L. (1991). Mechanisms of pyrite and marcasite formation from solution: III. Hydrothermal processes. Geochimica et Cosmochimica Acta, 55(12), p. 3491–3504. https://doi.org/10.1016/0016-7037(91)90050-F.

Seewald, J. S., Reeves, E. P., Bach, W., Saccocia, P. J., Craddock, P. R., Walsh, E., et al. (2019). Geochemistry of hot-springs at the SuSu Knolls hydrothermal field, Eastern Manus Basin: Advanced argillic alteration and vent fluid acidity. Geochimica et Cosmochimica Acta, 255, p. 25–48. https://doi.org/10.1016/j.gca.2019.03.034.

Shimizu, M., Miyawaki, R., Kato, A., Matsubara, S., Matsuyama, F., & Kiyota, K. (1998). Tsugaruite, Pb4As2S7, a new mineral species from the Yunosawa mine, Aomori Prefecture, Japan. Mineralogical Magazine, 62(6), p. 793–799.

Stern, R. J. (2002). Subduction zones. Reviews of Geophysics, 40(4), p. 1395–1406. https://doi.org/10.1007/978-90-481-8702-7_149.

Stoffers, P., Worthington, T. J., Schwarz-Schampera, U., Hannington, M. D., Massoth, G. J., Hekinian, R., et al. (2006). Submarine volcanoes and high-temperature hydrothermal venting on the Tonga arc, southwest Pacific. Geology, 34(6), p. 453–456. https://doi.org/10.1130/G22227.1.

Timm, C., Davy, B., Haase, K. M., Hoernle, K. A., Graham, I. J., de Ronde, C. E. J., et al. (2014). Subduction of the oceanic Hikurangi Plateau and its impact on the Kermadec arc. Nature Communications, 5, p. 1–9. https://doi.org/10.1038/ncomms5923.

Tivey, M. K. (1995). Modeling Chimney Growth and Associated Fluid Flow at Seafloor Hydrothermal Vent Sites. Geophysical Monograph, 91, p. 158–177. https://doi.org/10.1029/GM091p0158.

Tivey, M. K., & McDuff, R. E. (1990). Mineral Precipitation in the Walls of Black Smoker Chimneys: A Quantitative Model of Transport and Chemical Reaction. J. Geophys. Res., 95(B8), p. 12617–12637. https://doi.org/10.1029/JB095iB08p12617.

Törmänen, T. O., & Koski, R. A. (2005). Gold enrichment and the Bi-Au Association in Pyrrhotite-Rich Massive Sulfide Deposits, Escanaba Trough, Southern Gorda Ridge. Economic Geology, 100, p. 1135–1150. https://doi.org/10.2113/gsecongeo.100.6.1135.

Wohlgemuth-Ueberwasser, C. C., Viljoen, F., Petersen, S., & Vorster, C. (2015). Distribution and solubility limits of trace elements in hydrothermal black smoker sulfides: An in-situ LA-ICP-MS study. Geochimica et Cosmochimica Acta, 159, p. 16–41. https://doi.org/10.1016/j.gca.2015.03.020.

Wright, I. C., de Ronde, C. E. J., Faure, K., & Gamble, J. A. (1998). Discovery of hydrothermal sulfide mineralization from southern Kermadec arc volcanoes (SW Pacific). Earth and Planetary Science Letters, 164, p. 335–343.

Yang, K., & Scott, S. D. (1996). Possible contribution of a metal-rich magmatic fluid to a sea-floor hydrothermal system. Nature, 383, p. 420–423.

Yang, K., & Scott, S. D. (2002). Magmatic Degassing of Volatiles and Ore Metals into a Hydrothermal System on the Modern Sea Floor of the Eastern Manus Back-Arc Basin , Western Pacific. Economic Geology, 97, p. 1079–1100.

Yeats, C. J., Parr, J. M., Binns, R. A., Gemmell, J. B., & Scott, S. D. (2014). The SuSu Knolls Hydrothermal Field, Eastern Manus Basin, Papua New Guinea. Economic Geology, 109(8), p. 2207–2226.

Zhang, Q. (1987). Trace elements in galena and sphalerite and their geochemical significance in distinguishing the genetic types of Pb-Zn ore deposits. Chinese Journal of Geochemistry, 6(2), p. 177–190. https://doi.org/10.1007/BF02872218.

3. Mass Accumulation Rates of Hydrothermal Deposits from the Niua South Vent Field, Tofua Arc

3.1. Introduction

Despite decades of finding, sampling, and modelling the formation of seafloor hydrothermal deposits, longstanding questions still remain regarding their formation (Hannington et al., 1995, 2011). Primary among these questions is the time it takes for deposits to form and the ultimate fate of the metals that are mobilized by hydrothermal systems. Previous studies have attempted to quantify the flux of metals to the seafloor, chimney and deposit growth rates, and the percent efficiency of deposition, defined as the percentage of metals or sulphur that accumulate at the vent site versus what is expelled into the water column (Baker et al., 1993; Tivey, 1995; Elderfield and Schultz, 1996; Humphris and Cann, 2000; Hannington et al., 2011; Jamieson et al., 2014). Attempts to quantify these processes have utilized data such as radioisotope dating (Ditchburn et al., 2012; Jamieson et al., 2013) and vent fluid chemistry and discharge rates (Bischoff and Seyfried, 1978; Seyfried et al., 2003; Mottl et al., 2011; Evans et al., 2017; Seewald et al., 2019), and estimates of heat flow (Baker, 2007; Lowell et al., 2013).

In the last decade, sub-meter resolution bathymetric data has become more widely available, due to an increase in autonomous underwater vehicle (AUV) surveys, making the identification and quantification of size of hydrothermal deposits and other seafloor features much easier and more accurate (Jamieson et al., 2014; Minami and Ohara, 2017;

Murton et al., 2019). Jamieson et al. (2014) employed a method to calculate volumes of seafloor massive sulfide (SMS) deposits at the Endeavour segment, Juan de Fuca Ridge, by manually identifying sulphide edifices from bathymetric data and outlining their sulphide footprints. Using GIS software, a horizontal cut-off was assigned for the base of each footprint, marking the boundary of exposed sulphide material from the underlying oceanic crust. This allowed for the volume of exposed sulphide material delineated in the bathymetry to be calculated. These data were then combined with U-series disequilibrium dating of the deposits to calculate overall hydrothermal mass accumulation rates for surficial material at Endeavour (Jamieson et al., 2014).

The Niua South vent field is a crater-hosted deposit of sulphide- and sulphate-rich material that has accumulated in several distinct hydrothermal mounds and chimneys. The availability of high-resolution (50 cm) bathymetry, comprehensive video surveying of the entire crater, and barite-rich deposit that allow for absolute dating of the deposits using the ^{226}Ra/Ba method make the Niua South vent field the ideal setting to quantitatively evaluate the hydrothermal evolution of a vent field. The purpose of this study is to present the first age constraints on the accumulation of hydrothermal sulphide material within the Niua South crater, and combined with volume estimates, reconstruct the history of hydrothermal venting, and provide spatial and temporal constraints on the rates at which this material is accumulating on the seafloor. For this study, an improved GIS-based approach has been developed to yield a more accurate estimate of deposit volumes at Niua South and allow for the first calculations of mass accumulation rates and chemical

mass balance for an arc-hosted hydrothermal vent field.

3.2. Methods

3.2.1 Geochronology using the ^{226}Ra/Ba method

Radium-226 is a decay product within the ^{238}U decay series. This radioisotope has a half-life of 1,600 years and, due to its similar charge and ionic radius to Ba, can easily substitute in the barite lattice. The use of ^{226}Ra decay as a geochronometer allows for the dating of barite-bearing hydrothermal samples between 200 – 20,000 years old (Ditchburn et al., 2012; Jamieson et al., 2013). Radium-226 decays from ^{230}Th and accumulates in basaltic crust, where Ba is also present as a trace element in feldspars (Jamieson et al., 2013). Both are leached from the crust during hydrothermal alteration and mobilized to the seafloor via hydrothermal fluids (Jamieson et al., 2013). However, the parent isotope ^{230}Th is not mobilized by the fluids because of its low solubility, and thus ^{226}Ra becomes unsupported by its parent isotope (Ditchburn et al., 2012). The ratio of the amount of ^{226}Ra to Ba (N) and an initial value of ^{226}Ra/Ba (N_0) (i.e., the ratio N at the time of formation) is used to determine an age (t, in years) for a given sample, using the following equation:

$$t = \frac{\ln\left({}^{N_0}/_{N}\right) \times\ 1600 \text{ years}}{\ln 2} \qquad \text{(Equation 1)}$$

The initial ^{226}Ra/Ba value of a sample cannot be measured directly, as it represents the ^{226}Ra/Ba of the sample at the time of crystallization (Fig. 3.1a; de Ronde et al., 2005). Young, active "zero-age" vents are used as a proxy for initial ratios for older samples, assuming there is no spatial variability of ^{226}Ra/Ba in the hydrothermal fluids within the vent field, nor does this ratio change significantly over the lifespan of the hydrothermal system (Fig. 3.1b; de Ronde et al., 2005; Jamieson et al., 2013). The ^{226}Ra/Ba method is applicable to a wide range of tectonic settings where barite is hosted in SMS deposits, including arcs, back-arcs and sedimented systems and mid-ocean ridges that are influenced by enhanced mantle melting (Jamieson et al., 2013). The Ba-rich felsic host rocks at Niua South account for the high abundance of barite within hydrothermal chimneys, making this dating method ideal for this site.

Twenty-nine hydrothermal samples that were collected by ROV at Niua South were selected for dating. Samples were selected based on high barite content, and spatial diversity within the crater. Samples that contained less than 1 wt.% Ba were excluded, as the low Ba content and associated low Ra activity would be below detection limits required for precise-enough age calculations (Jamieson et al., 2013). Selected hydrothermal sample powders were weighed and placed in 8 mL polypropylene sample tubes and sealed with rubber septa and epoxy to prevent the escape of the intermediate gaseous decay product ^{222}Rn (Table 3.1). It is important to seal the samples and prevent escape of Rn gas because ^{226}Ra shares an overlapping gamma emission decay energy peak with ^{235}U at 186 keV, making quantification of ^{226}Ra unreliable due to the possible presence of ^{235}U. Therefore, the activity of ^{214}Pb and/or ^{214}Bi, both short-lived daughter

isotope of ^{226}Ra via decay of intermediate daughters ^{222}Rn and ^{218}Po, and significant gamma emitters, can instead be used as a proxy for activity of ^{226}Ra as long as all daughter isotopes are in secular equilibrium with the ^{226}Ra parent, which requires that system remains closed with respect to ^{222}Rn (Jamieson et al., 2013). The sealed tubes were set aside for 21 days, representing five half-lives of ^{222}Rn ($t_{1/2}$ of 3.8 days), the time required for ^{222}Rn (and therefore ^{214}Pb and ^{214}Bi) to attain secular equilibrium with ^{226}Ra. Activity values for ^{214}Pb and ^{214}Bi are consistently near-equal ($R^2 = 0.99$), thus the average values of the activities were used as a proxy of ^{226}Ra. Three of the 29 selected samples were additionally chosen as zero-age samples (Table 3.1). These samples originate from the tips of active chimneys, and best represent the most recent occurrences of mineralization.

Gamma spectrometry analysis of the powdered samples was conducted using a CANBERRA high-purity Ge well detector and DSA-1000 Digital Signal Analyser. Data acquisitions were managed using Genie 2000 Basic Spectrometry Software, where count times for each sample ran for a period of 24 hours. Gamma spectra were calibrated using BL-5 natural uranium ore, with a certified ^{226}Ra activity of 857 ± 38 Bq/g (Natural Resources Canada, 2017).

Age uncertainties are derived from a combination of analytical uncertainties such as the uncertainty of barium concentrations and Ra activity, and the uncertainty of the initial value of ^{226}Ra/Ba. Barium concentrations measured by instrumental neutron activation analysis (INAA) have a one-sigma (1σ) uncertainty (δBa) of ~5%, based on seven repeat measurements of the GXR-1 reference standard, which has an accepted concentration of

750 ppm Ba. This reference concentration is significantly higher than the 20 ppm Ba detection limit of this method. Radium-226 activity uncertainties ($\delta^{226}Ra$) are related to counting errors and the uncertainty associated with the BL-5 certified calibration reference material and have an average value of ~4% of the measured ^{226}Ra activity. The uncertainty of the ratio of the amount of decayed ^{226}Ra to Ba (δN) is determined by propagation of the uncertainties associated with measurements of Ba concentration and ^{226}Ra activity for each sample. The uncertainty of the initial ^{226}Ra/Ba value (δN_0) is derived from the mean squared weighted deviation (MSWD) of the three zero-age samples (Fig. 3.1a). The uncertainties associated with both N and N_0 can be propagated through the decay equation (Equation 1) to determine the age uncertainty, shown in the following equation:

$$\delta t = \frac{1600 \text{ years}}{\ln 2}\left(\frac{\delta Ba}{Ba} + \frac{\delta^{226}Ra}{^{226}Ra} + \frac{\delta N_0}{N_0}\right) \quad \text{(Equation 2)}$$

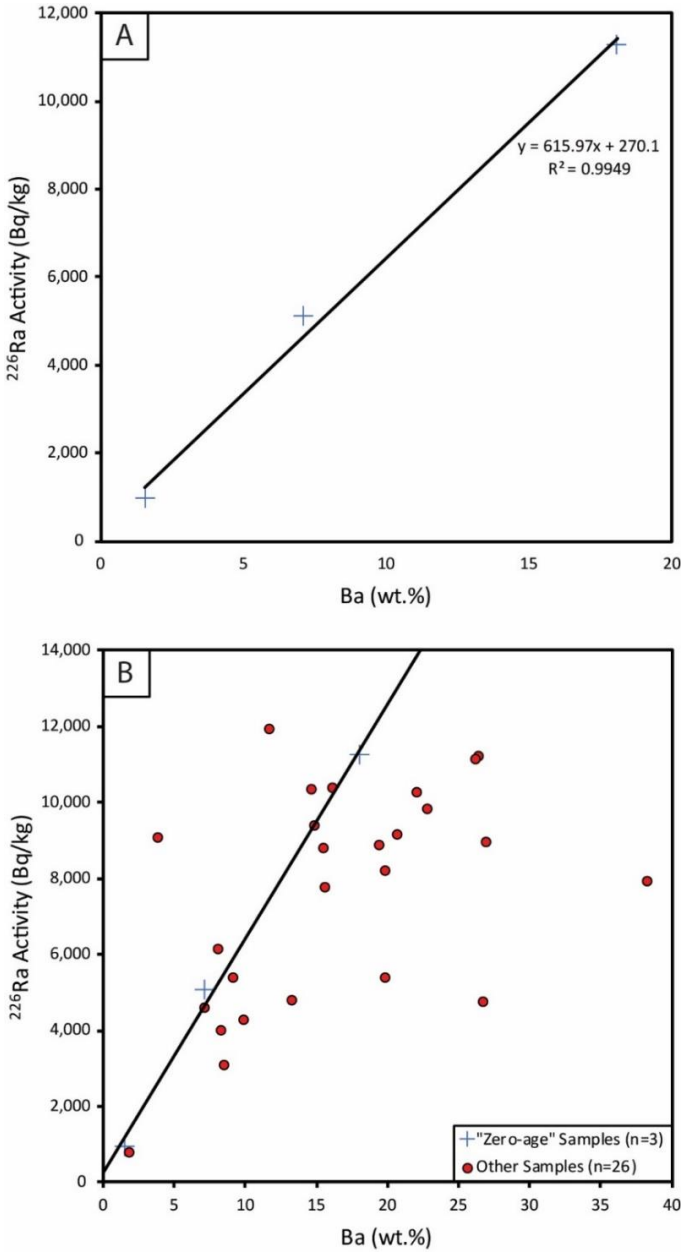

Figure 3.1. (a) ^{226}Ra activity versus Ba content of zero-age hydrothermal sulphide samples from Niua South crater. The slope of linear regression represents the initial ^{226}Ra/Ba value (N_0). The error of the initial ^{226}Ra/Ba value is the standard deviation of the slope of the linear regression. (b) ^{226}Ra activity versus Ba content of all hydrothermal sulphide samples. At the time of formation, points should plot on the zero-age regression line (black line), and as samples age, the activity of ^{226}Ra decreases whereas the Ba content remains unchanged.

3.2.2 Deposit volumes

High-resolution (50 cm) bathymetry of Niua volcano was collected by multibeam echosounder mounted on the AUV *ABYSS* during the R/V *Kilo Moana* expedition (KM1129a; Resing et al., 2012). Hydrothermal chimneys, mounds, and talus material within the Niua crater were identified by using a combination of high-resolution bathymetry and video coverage of the seafloor. These features are positive topographic features on the crater floor, and most mounds within the crater are defined by sub-rounded slope bases with steep, centralized chimney edifices. Hydrothermal mounds within the central and eastern regions of the crater are largely coalesced and make up the bulk of total sulphide formation.

The volume of each sulphide mound was calculated by tracing an initial outline of the extent of hydrothermal material on the crater floor on the bathymetric map using a combination of bathymetric features and visual ground-truthing from high-definition video obtained during sampling and surveying dives with the ROV. In most cases, the bathymetric data easily highlights major sulphide mounds and chimneys; thus, the initial outline accounts for the majority of sulphide material present within the crater. Dive videos were largely used as a means of ground-truthing and to refine the outlines to ensure they are as accurate as possible.

Once the outlines of the hydrothermal deposits were established, a GIS-based volume calculator was used to determine a total volume of sulphide material. In order to determine volumes, the sulphide outline was used to cut-out and remove the area of

contained sulphide material from the original bathymetric grid. A new surface to fill in the removed deposits was then interpolated using a function that employs inverse distance weighting (IDW). The newly created surface is shaped according to the surrounding morphology of the crater floor and used as a hypothetical lower cut-off of subseafloor material. The differences between the original deposit topographies and interpolated basal surfaces within the deposit outline were then calculated for each 50 cm x 50 cm pixel to produce a total volume of material above the seafloor. These combined methods improve on the approach taken by Jamieson et al. (2014) at Endeavour by incorporating the surrounding bathymetry to more accurately interpolate the original seafloor topography underneath the hydrothermal deposits, rather than a simple, manually assigned horizontal-basal cut-offs to determine the lower sulphide boundaries. Additionally, the higher resolution of bathymetric data (50 cm, compared to 1 m resolution at Endeavour, increases the resolution required to differentiate hydrothermal material from volcanic debris. However, in both studies, subseafloor mineralization remains largely unaccounted in the estimation process.

An uncertainty buffer of 10% was assigned to the volumes of each individual deposit to account for uncertainties associated with: 1) delineating the boundary of sulphide deposit from the combination of bathymetry and ROV imagery; 2) the interpretations of the lower surface; and 3) limitations from calculating volumes from using a 50 cm bathymetric grid.

3.2.3 Deposit density, tonnage, and mass accumulation rates

Densities of hydrothermal material were calculated using a combination of the weighted average of the density of major mineral phases (e.g., barite, chalcopyrite, sphalerite, pyrite and marcasite, and anhydrite) and the average porosity of each sample, which was visually estimated from all studied thin sections and averages ~40% ± 12% (sd) for 33 samples. With the bulk density estimate (ρ) and the total calculated volume (V), a total tonnage is calculated using Equation 3. The resulting tonnage and the minimum age of sulphide material yields a maximum mass accumulation rate (MAR), as shown in Equation 4.

$$tonnage = V \times \rho \qquad \text{(Equation 3)}$$

$$mass\ accumulation\ rate = \frac{tonnage}{age} \qquad \text{(Equation 4)}$$

Porosity and density uncertainties were estimated using their respective standard deviation values. The uncertainties for tonnage and mass accumulation rates (MAR) were determined by the propagation of uncertainties associated with porosity and density estimates and tonnage and age determinations (t), respectively. These equations are given below:

$$\delta tonnage = tonnage\left[\sqrt{\left(\frac{\delta V}{V}\right)^2 + \left(\frac{\delta \rho}{\rho}\right)^2}\right] \qquad \text{(Equation 5)}$$

$$\delta MAR = MAR\left[\sqrt{\left(\frac{\delta tonnage}{tonnage}\right)^2 + \left(\frac{\delta t}{t}\right)^2}\right] \quad \text{(Equation 6)}$$

3.3. Results

3.3.1 Temporal variability of sulphide chimneys

The abundance of barite throughout the crater-hosted deposit allowed for 29 subsamples to be dated (Table 3.1). Ages range from present (zero age) to ~2900 ± 200 years old, indicating that hydrothermal venting at Niua South has been ongoing for at least ~2900 years. There is a greater number of dated samples from the central region (n=14) versus the north and south regions (n=7; n=3, respectively), which could be related to the relative sizes of the hydrothermal mounds (Fig. 3.2). Sample ages are summarized spatially in Figure 3.2 and graphically in Figure 3.3. The ages of samples collected from the central and eastern regions fall within a relatively narrow range, with 10 samples with ages between 652 ± 180 yr and 1429 ± 180 yr (Fig. 3.2). Additionally, three samples from the northern region of chimneys and mounds fall within this age range. The large eastern region of chimneys and mounds are only represented by two samples; one sample is included within the range of 10 samples at 855 ± 180 yr and the other (from the wall of an active chimney) at less than 200 years old (Fig. 3.2).

Table 3.1. Ages of hydrothermal samples using the ^{226}Ra/Ba method

Sample ID	Crater Region	Latitude	Longitude	Ba (wt.%)	^{226}Ra Activity (Bq/kg)	Age (^{226}Ra/Ba) (years)
Active Zero-Age Samples						
D1918-R4	North	-15.16316167	-173.5746983	1.56	952 ± 32	-
D1918-R8	North	-15.16288333	-173.5746617	7.14	5089 ± 161	-
D1919-R6A	East	-15.16476833	-173.5736017	18.1	11277 ± 356	-
Active/Inactive Chimney and Talus Samples						
D1918-R1	North	-15.16285667	-173.5745683	1.87	770 ± 26	930 ± 192
D1918-R6	North	-15.16285333	-173.5745783	16.2	10387 ± 328	<200 ± 180
D1918-R7	North	-15.16288333	-173.5746617	7.17	4596 ± 146	<200 ± 181
D1918-R10	North	-15.16309167	-173.5747217	9.86	4263 ± 135	817 ± 181
D1918-R11	North	-15.16283667	-173.5746183	8.31	4018 ± 128	559 ± 181
D1918-R12	North	-15.16287500	-173.5746730	14.9	9410 ± 297	<200 ± 181
D1918-R13	North	-15.16286200	-173.5746870	14.7	10364 ± 327	<200 ± 181
D1919-R1	Central	-15.16424167	-173.5743317	22.1	10263 ± 324	652 ± 180
D1919-R2A	Central	-15.16462167	-173.5741467	27	8956 ± 283	1429 ± 180
D1919-R2B	Central	-15.16462167	-173.5741467	15.6	7769 ± 245	491 ± 181
D1919-R2C	Central	-15.16462167	-173.5741467	19.9	8199 ± 259	928 ± 180
D1919-R3 TOP	Central	-15.16476000	-173.5744550	26.4	11226 ± 354	855 ± 180
D1919-R3 TRUNK 1	Central	-15.16476000	-173.5744550	22.8	9828 ± 310	824 ± 180
D1919-R3 TRUNK 2	Central	-15.16476000	-173.5744550	20.7	9151 ± 289	766 ± 180
D1919-R4	Central	-15.16466167	-173.5742267	19.4	8896 ± 281	681 ± 180
D1919-R5	East	-15.16474167	-173.5736533	26.2	11144 ± 352	855 ± 180
D1920-R2	South	-15.16549167	-173.5740483	38.3	7939 ± 251	2514 ± 180
D1920-R3	South	-15.16537833	-173.5738667	19.9	5373 ± 170	1904 ± 181
D1920-R5	South	-15.16539500	-173.5741033	26.8	4770 ± 151	2866 ± 181
D1920-R7	Central	-15.16520333	-173.5745883	8.06	6146 ± 195	<200 ± 181
D1920-R8	Central	-15.16519833	-173.5745967	3.88	9060 ± 286	<200 ± 183
D1920-R9	Central	-15.16493667	-173.5745867	9.16	5376 ± 170	<200 ± 181
D1920-R10	Central	-15.16498000	-173.5746167	8.52	3108 ± 99	1210 ± 181
D1920-R11	Central	-15.16464333	-173.5745400	13.3	4809 ± 152	1230 ± 181
D1920-R12	Central	-15.16474167	-173.5748200	11.7	11918 ± 376	<200 ± 181
D1920-R15	East	-15.16489333	-173.5729333	15.5	8788 ± 278	<200 ± 181

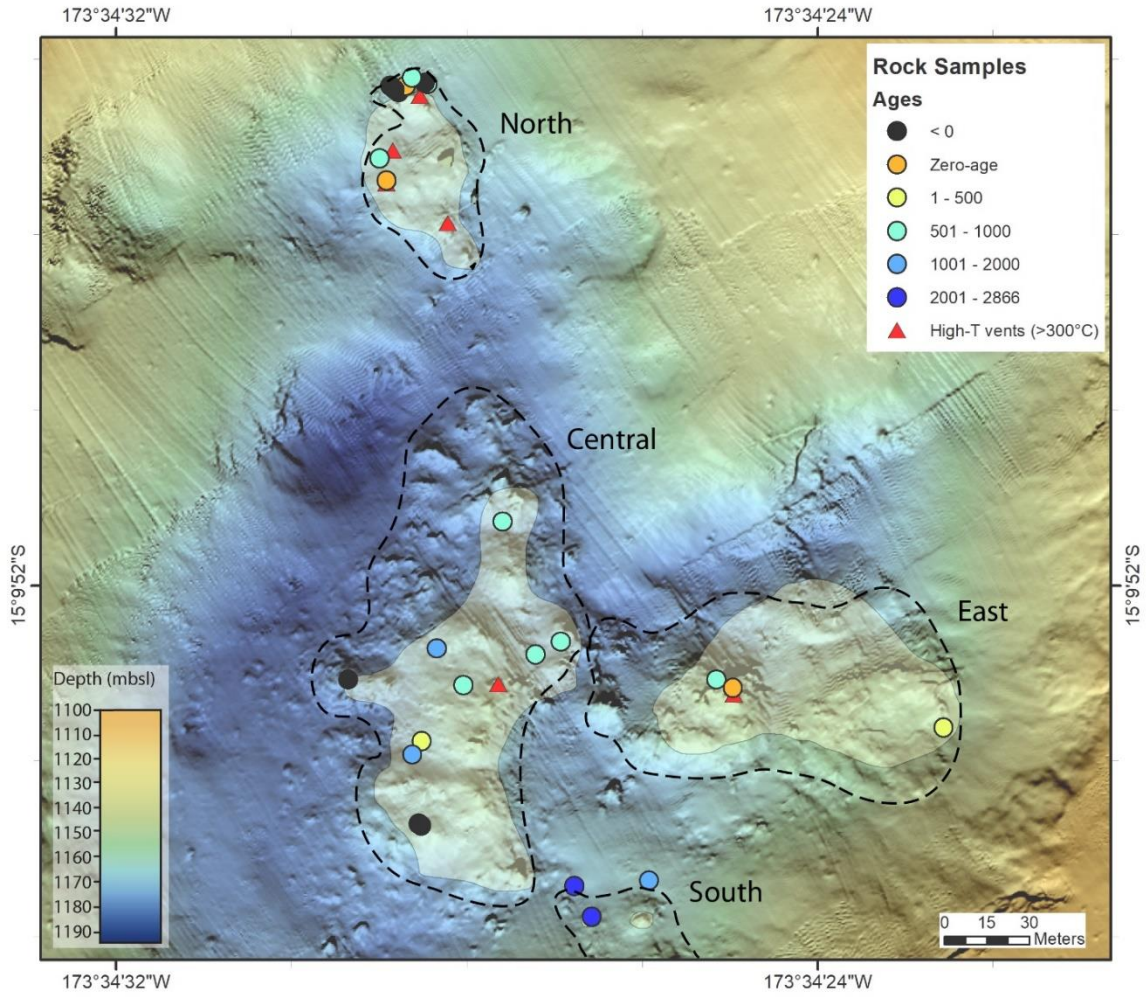

Figure 3.2. High-resolution (50 cm) bathymetric map of the Niua South study site showing the spatial distribution of dated hydrothermal samples. Black dashed lines mark the rough boundaries of hydrothermal mound material present in each of the four hydrothermal regions within the crater. Yellow shaded areas are areas of diffuse venting. Red triangles represent the locations of high-temperature (300–325°C) chimneys. Samples are coloured based on their age, with orange to yellow samples being the youngest, and more blue markers showing progressively older samples. High-temperature vents correspond with the three selected zero-age samples. The central region chimneys and mounds show a wide range of samples ages, whereas the northern samples tend to be younger on average, and the southern samples tend to be older on average. The high-resolution AUV bathymetry was provided by Nautilus Minerals Inc., mapped during the R/V *Kilo Moana* expedition to the Lau Basin in 2011.

The youngest ages within the crater are mostly found in the northern region, where three samples are too young for their ages to be resolved with this technique (i.e., <200 years) (Fig. 3.2; Table 3.1). High-temperature (325°C) venting in the north is thought to be a result of a lower degree of mixing of seawater with subseafloor hydrothermal fluids than other parts of the crater. The smaller size of hydrothermal mounds in the north are consistent with the venting in this region being relatively younger than elsewhere in the crater. The three samples from the north with resolvable ages indicate that the earliest instance of known venting in the north is from at least 1000 years ago.

Hydrothermal samples that yield calculated ages of less than 200 years (including negative ages) fall outside of the age window for this method because the ^{226}Ra/Ba of the "old" and zero age sample are too similar, and the associated uncertainties of both measurements make any calculated age meaningless (Jamieson et al., 2013).

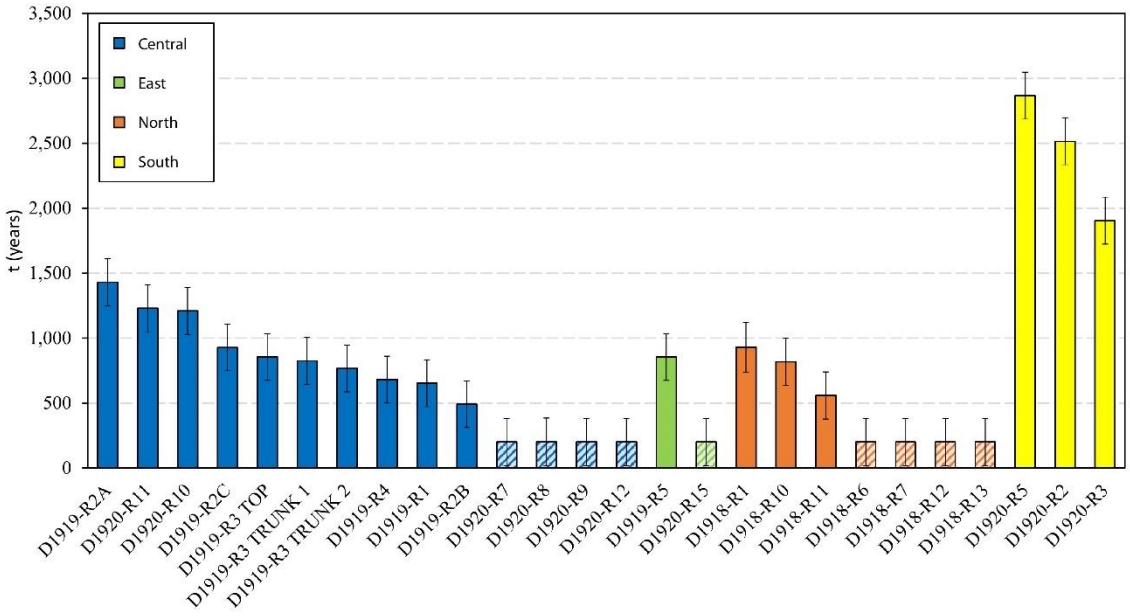

Figure 3.3. Age distribution for hydrothermal sulphide samples from the Niua South crater. Pattern filled data bars represent samples with ages of <200 years.

3.3.2 Areas and volumes of hydrothermal mound material

The total accumulation of hydrothermal material is distributed among nine groupings of coalesced hydrothermal mounds, with the coalesced central and east grouping making up the bulk of material present (Fig. 3.4). Calculated areas of hydrothermal mound material from each region are shown in Table 3.2.

Table 3.2. Mounds from the central and eastern regions form a widespread coalescence of multiple mounds that share an overlapping footprint and, for the purposes of volume calculations, are considered as a single deposit. This deposit has an area of 25,550 m^2, and a calculated volume of 48,000 ± 4,800 m^3. The base outline of the deposit extends up the walls of the crater (particularly in the east), or dips within depressions in the crater floor (mostly in the west), resulting in elevation differences of up to 44 m along the seafloor. Large elevation changes (up to ~24 m) also exist in the main southern mound and nearby isolated edifices, where they are mostly built-up along the slope of the southern crater wall. There are three large chimneys in the southern region, and observations from ROV video indicate that much of the material in between these chimneys appears to be largely surface talus. The southern deposits have a total area of 1,800 m^2, and a combined volume of 600 ± 60 m^3. In the north region of the crater, there is one main mound, which hosts vigorous hydrothermal venting, and several high-temperature (≥300°C) chimneys are present. Small inactive peripheral chimneys are also

distributed around this main mound, but no hydrothermal material is present between these chimneys and the main hydrothermal mound. In contrast to the other regions, there is a minimal elevational difference (~12 m) along the base of the main deposit. Here, deposit material has an area of 1,810 m^2, and a volume of 1,940 ± 194 m^3. Additionally, two small, distal, inactive edifices are situated along the NE crater wall, but only account for 75 ± 8 m^3 of sulphide material.

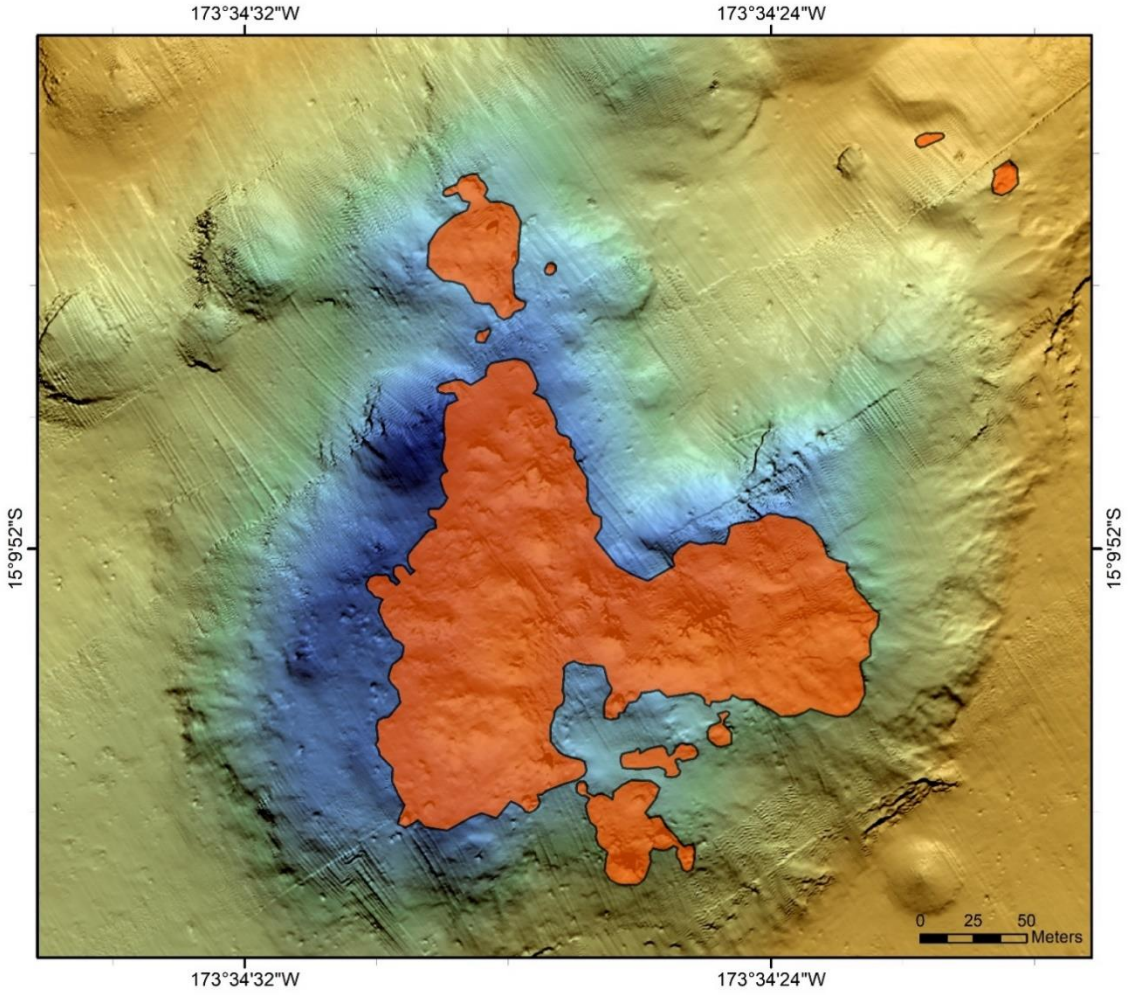

Figure 3.4. Hydrothermal sulphide mounds contained within the Niua South crater. Mounds are outlined in black, with red fill (30% transparency) representing the contained deposit material. Boundaries of sulphide material were defined using a combination of

high-resolution (50 cm) bathymetry and video surveys of the crater floor. The large central mound contains the vast majority of sulphide formation within the crater. Calculated areas of each group of mounds are summarized in Table 3.2.

Table 3.2. Calculated areas of sulphide material within the Niua South crater.

Mound Name	Crater Region	# of samples	Polygon area (m^2)	Calculated area[a] (m^2)	Unaccounted area (m^2)	Error[b] (%)
Central/East Mound	Central/East	16	25,545	20,535	5,010	19.6
North Mounds	North	1	1,814	1,648	166	9.2
South Mounds	South	3	1,761	1,022	739	42.0
Crater Wall	Northeast	0				
Total within crater			29,120	23,205	5,915	20.3

a Calculated area excludes surface area with negative differences in the volume calculation.
b Error represents the percentage of unaccounted area per polygon area.

3.3.3 Densities, tonnages, and mass accumulation rates

The bulk density estimate for sulphide material at the Niua South vent field is 2.65 ± 0.34 g/cm^3. This value is similar to dry bulk density estimates reported at Endeavour, on the Juan de Fuca Ridge (3.1 g/cm^3; Jamieson et al., 2014; Tivey et al., 1999) and Solwara 1, Eastern Manus Basin (2.24 g/cm^3; Lipton, 2012). The estimated bulk density of sulphide material results in a total tonnage of 134,100 ± 21,700 t, using Equation 3 (

Table 3.3). Hydrothermal mounds in the central and eastern regions contain ~127,000 ± 20,500 t of sulphide material, which accounts for 95% of the total deposit tonnage. Based on these results, a tonnage of ~134,000 t with a minimum age of ~2900 years yields a mass accumulation rate of ~50 t/yr.

Table 3.3. Estimated volumes, tonnages, and mass accumulation rates of hydrothermal mounds from the Niua South crater vent field.

Mound Name	# of samples	Minimum age (y)	Volume (m^3)	Estimated tonnage[a] (t)	Maximum accumulation rate (t/y)
Central/East Mound	16	1,429 ± 180	47,972 ± 4,797	127,126 ± 20,559	89 ± 18
North Mounds	1	930 ± 192	1,941 ± 194	5,144 ± 832	6 ± 1.5
South Mounds	3	2,866 ± 181	607 ± 60.7	1,609 ± 260	0.6 ± 0.1
Crater Wall	0	-	75 ± 7.5	199 ± 32	-
Total within crater		2,866 ± 181	50,595 ± 5,059	134,077 ± 21,683	47 ± 8

a Calculated from total volumes using an estimated density of 2.65 t/m^3.

3.4. Discussion

3.4.1 Comparison of age data to other arc-related hydrothermal deposits

The oldest age recorded at Niua South, 2866 ± 181 years, from the southern region of chimneys and mounds, represents the minimum age of hydrothermal venting within the volcanic crater. Furthermore, this age suggests that the Niua South crater has been volcanically dormant over the last ~3,000 years, as volcanic eruptions within the crater would have destroyed any existing hydrothermal deposits. The lack of common minerals associated with the oxidation of sulphide-rich hydrothermal deposits, such as atacamite, jarosite, and dark Mn-oxide coatings is consistent with a relatively young age of the deposits at Niua South, compared to older deposits (> 50,000 years) on the Mid-Atlantic Ridge (Hannington, 1993; Hannington et al., 1998; Jamieson et al., 2014).

In general, Niua South hydrothermal ages are consistent with previous studies along the Kermadec arc where $^{226}Ra/Ba$ or $^{228}Ra/Ba$ methods were utilized. The oldest mineralization found at Brothers volcano is in mineralized breccia samples dated at ~1,200 years old. These samples originate from the northwest caldera region, where chimney fragments were also obtained and dated at 890 years old, and at least 100 sulphide-rich chimney spires were dated at less than 40 years (de Ronde et al., 2005, 2011). Also, along the Kermadec arc, samples have been dated from the Rumble II West and Clark volcanoes. Maximum ages from Rumble II West are close to the oldest ages determined at Brothers, at ~1,500 years old (de Ronde et al., 2005). On the other hand, at ~19,000 years old, barite-rich breccia recovered from Clark volcano stands as being much older than other SMS related deposit material that has been dated along the Kermadec or Tofua arc (Ditchburn et al., 2012). Prior to this study, the only hydrothermal site dated along the Tofua arc or back-arc was at Niuatahi (Volcano "O") caldera, where a single chimney was dated at <16 years old using ^{228}Ra (Ditchburn et al., 2012).

Beyond the Kermadec-Tofua arc and back-arc, the global abundance of age data remains limited with regards to volcanic arc-related SMS deposits. The East Diamante volcano, located along the southern Mariana arc, has had several chimney samples dated at <35 years, and an older chimney sample at 880 years old (Ditchburn et al., 2012), and, in a more recent study, chimneys and mound layers were dated at 3,350 to 3,920 years old, similar to the oldest recorded sample at Niua South (Hein et al., 2014). In the eastern Manus back-arc basin, several mineralized samples originating from Pual Ridge (Nautilus Minerals Inc. deposits/prospects Solwara 6 and 7) and various vent fields of the Suzette

hydrothermal area (Nautilus Minerals Inc. deposits/prospects Solwara 1 and 5) have also been dated. Six samples from Pual Ridge indicate an age range of 39 to 850 years old, corresponding to various sections of two different chimneys (Johns et al., 2014). Twenty-eight chimney and drill core samples from the Suzette hydrothermal area yield a much older maximum age of 5,610 years old from a drill core and 4,670 years old for a chimney sample (Johns et al., 2014). In summary, the maximum ages of hydrothermal material determined at all volcanic arc and back-arc sites studied thus far are, for the most part, ~5,000 years old or less.

The age of deposits from Niua South are also comparable to some mid-ocean ridge sites (i.e. Endeavour, Juan de Fuca Ridge, ~5,850 years old; Jamieson et al., 2013). However, when compared with numerous active hydrothermal deposits along the slow-spreading Mid-Atlantic Ridge, where deposits can be > 50,000 years, arc-related deposits are overall much younger (de Ronde et al., 2005; Ditchburn et al., 2012; Hein et al., 2014; Johns et al., 2014). This is likely a direct result of the frequent volcanic eruptions that effectively destroy or bury previously formed deposits, resetting the onset of accumulation of hydrothermal material at vent sites along volcanic arcs and back-arcs, relative to deposits that form over prolonged periods of time at relatively stable, magma-starved slow- and intermediate-spreading ridges (Hannington et al., 2005).

3.4.2 Mass accumulation rates

The deposit outcrop area of Niua South is larger than some other arc and back-arc hydrothermal vent fields (e.g., Brothers, Kermadec arc (~5,000 m^2); Suiyo Seamount,

Izu-Bonin arc (~3,000 m^2); PACMANUS, Solwara 6, and Solwara 7, eastern Manus basin (~15,000 m^2 each); Izena Cauldron, Okinawa Trough (~5,000 m^2); Hannington et al., 2011, Data Repository 1). Several of these sites have consistent ranges of estimated deposit sizes between 100,000 and 300,000 t, and Niua South falls within this range. However, most of these other sites do not have accompanying age data from which accumulation rates can be calculated. The growth rate of hydrothermal deposits at Niua South of ~50 t/yr is comparable to previous studies conducted at mid-ocean ridges. Sample ages at TAG are much older in comparison at ~50,000 yr (Lalou et al., 1995). When accumulation rates are calculated over this timespan, then the 2.7 million tonne mound formed at a rate of 54 t/yr. However, it is suggested that TAG has been hydrothermally active for only ~10% of this timespan; thus, a time-adjusted accumulation rate of 360 t/yr that accounts for only active periods exceeds that of Niua South (Hannington et al., 1998; Jamieson et al., 2014). Maximum accumulation rates calculated at the Main Endeavour Field (50 t/yr) and High Rise Field (76 t/yr) within the Endeavour axial valley are directly comparable to rates calculated at Niua South (Jamieson et al., 2014). Minimum ages at these hydrothermal fields (2272 and 843 years, respectively) also fall within the range of ages of the hydrothermal samples at Niua South (Jamieson et al., 2014).

3.4.3 Volume calculation uncertainties

The extensive ground-truthing provided by video surveys of the Niua South crater allows for an evaluation of the accuracy of identification of hydrothermal deposits on the

seafloor using only the 50 cm resolution bathymetry grid. In the central region of the crater, hydrothermal chimneys and mounds are easily identified in the bathymetry against a generally horizontal crater floor. However, these features become less obvious in the steeper areas of the crater walls and additional confirmation from visual surveys is required. In rare instances, hydrothermal deposits that were visually confirmed by ROV observations were not identified at all in the bathymetric data. For example, two small isolated hydrothermal edifices on the northeast crater wall were identified visually but were not as easily discernable in the bathymetry data (Fig. 3.5b). In examples like this, GIS-based spatial analysis and visualization tools can partially aid in the identification of such features. The larger of the two edifices is discernable using slope-shaded bathymetry, where the steep-sided morphology of the edifice stands out from the sloping wall (Fig. 3.5a).

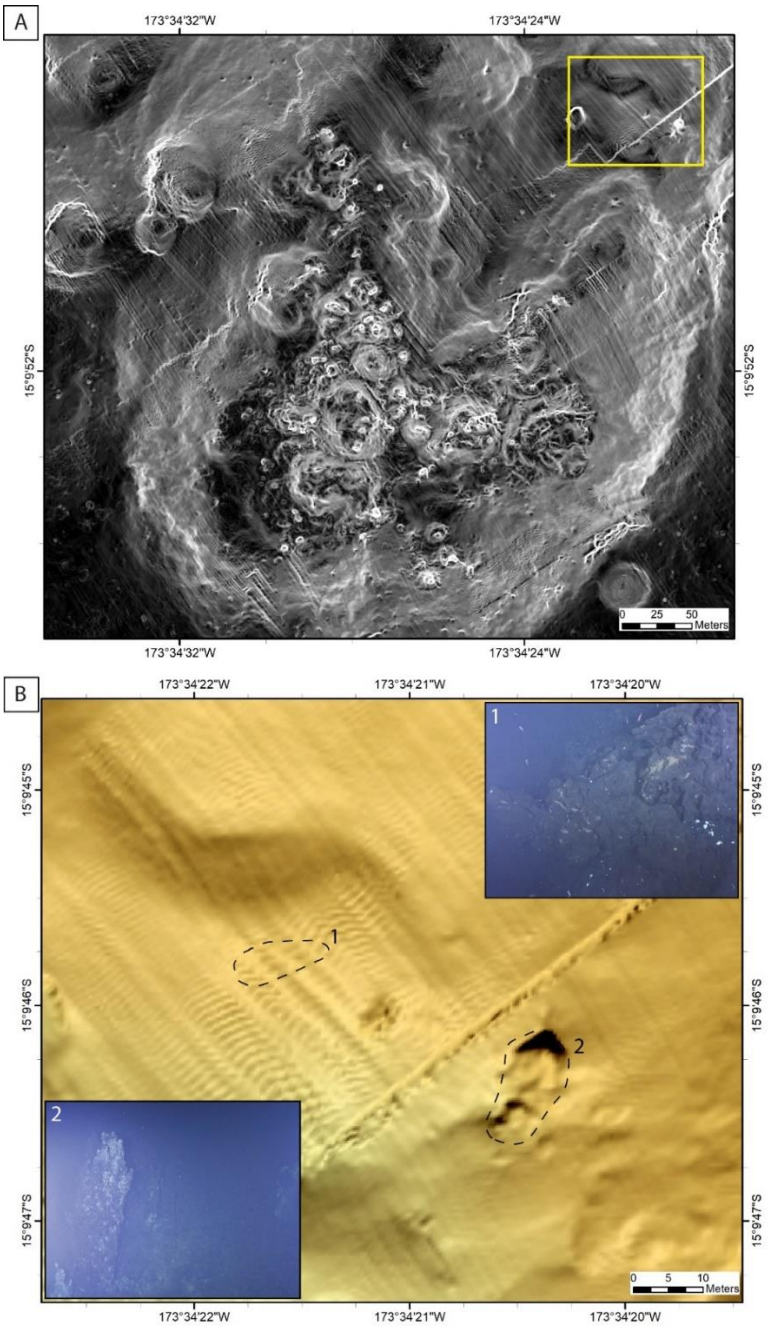

Figure 3.5. (a) Slope-shaded bathymetry of the Niua South crater. Whiter areas of the seafloor indicate higher slope angles (max = 88°). The yellow box denotes the location of Figure 3.5b. (b) High-resolution (50cm) bathymetry of the northeast region of inactive hydrothermal chimneys and mounds. Numbered images of the inactive chimneys and mounds were obtained from screen captures of ROV survey dive video. This degree of zooming shows bathymetric data artifacts that hide or interfere with seafloor features.

The process of determining deposit volumes still requires refining in order to produce the most accurate results possible. The primary source of error associated with the volume determination method used in this study results from boundary effects associated with the interpolated lower surface that is defined along the edges of the deposit outlines. In some areas, the interpolated surface ramps up abruptly from the edges of the outline before it curves and levels out towards the center of the surface, causing the interpolated surface to be elevated relative to the true height of deposit material, therefore creating "negative" volume (North Mound Profile 2 and Central/East Profile 1; Fig. 3.7). These boundary effects are most pronounced in areas with high degrees of topographic variation near the deposit boundaries, such as directly east of the central mound. These areas are highlighted in Figure 3.5b, and it is their occurrence throughout the surface that contributes the most overall error in the calculated volumes (Table 3.2). This effect is most prominent in the main central deposit outline, where an area of about 5,000 m^2 of material is unaccounted, compared to what has been visually confirmed (~20% of its total area), resulting in considerable volume of interior deposit material that is not included in the total volume. Within the southern region, ~740 m^2, or 40% of the total area is also unaccounted due to the extrapolated lower surface. However, this material is thought to be mostly sulphide-rich talus that thinly covers the surface of the crater floor in between large mounds and chimneys and therefore does not contribute significant uncertainty to the total volume estimation. The main northern mound and adjacent isolated chimneys are largely unaffected by this error (~9% of its total area), and therefore volume and tonnage estimates from this region are currently the most accurate.

Unexplained grid artifacts were also generated in the ArcGIS-generated interpolated surface during elevation void fill of the removed deposit material. These artifacts are most apparent in a hill shade map of the newly generated raster (Fig. 3.6a). Vertical profiles from north to south show that the elevation of the interpolated surface increases stepwise by ~0.75 to 1 m increments at each visible horizontal grid line; thus, the interpolated surface sits slightly more elevated than it should, reducing the resulting total volume of deposit material (Fig. 3.7). Similar vertical grid artifacts that trend from east to west are slightly visible, but vertical profiles show that they contribute just as much error to the interpolated surface (Fig. 3.7). These errors are observed only in the large central mounds and could be due to the large size and irregular shape of hydrothermal material considered in this area. Based on the shape and orientation of these artifacts, they are likely a software issue associated with the interpolation of the lower surface.

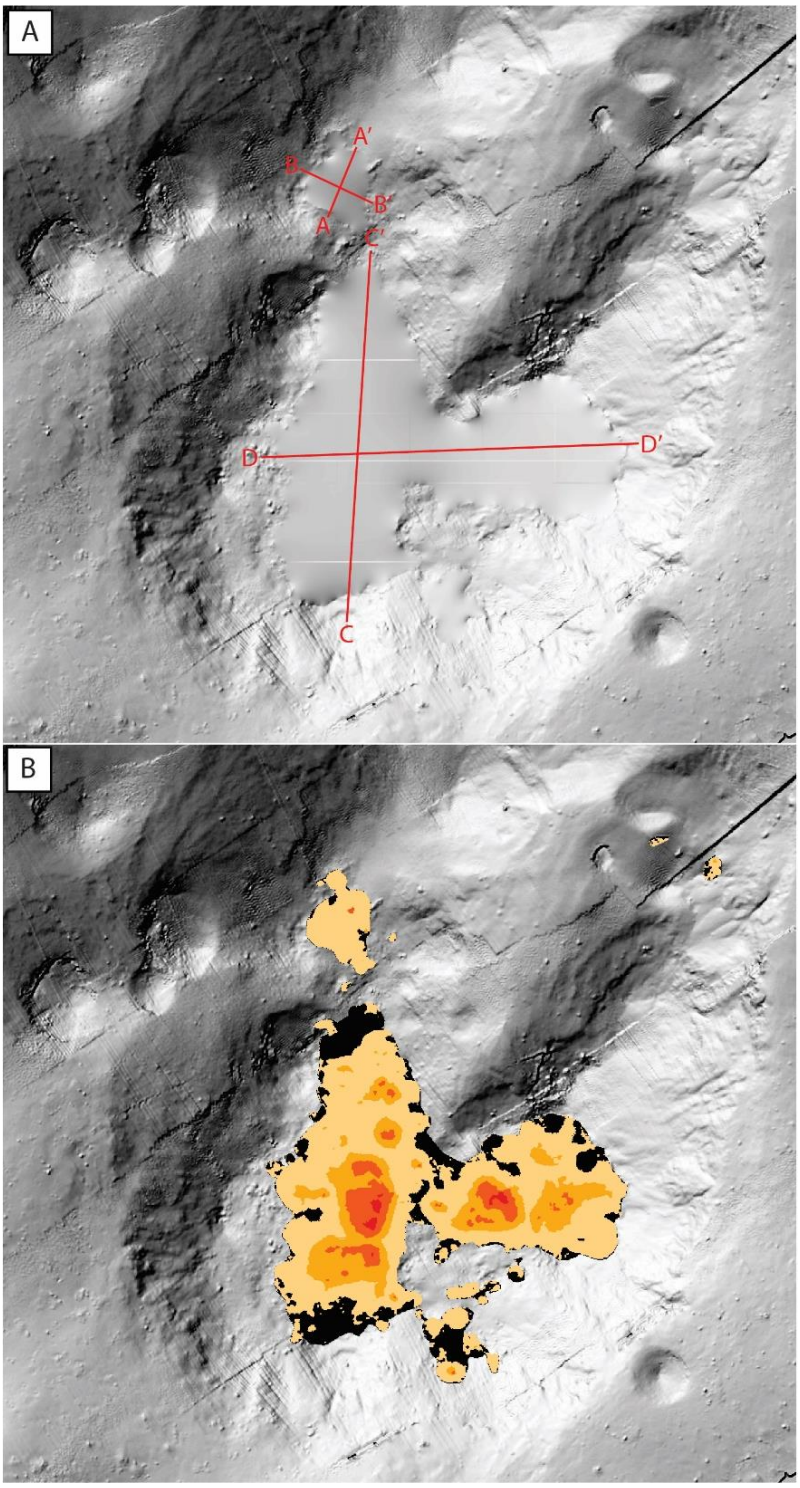

Figure 3.6. Hill shade maps generated using 50 cm bathymetric data. (a) Interpolated surface created using the GIS-based elevation void fill function. The main hydrothermal mound has small unexplained “grid-like” artifacts within the interpolated surface, which

contributes error to the surface volume calculation. Profile lines A-A', B-B', C-C', and D-D' correspond to vertical profiles illustrated in Figure 3.7. (b) Classified raster image (5 classes) produced from the subtraction of the removed deposit material raster, and surface interpreted using the elevation void fill function in ArcGIS. Coloured areas show positive differences (i.e., areas where the interpolated surface is lower than that of the true surface) between the two raster datasets, where the black areas represent negative differences (i.e., areas where the interpolated surface is higher than that of the true surface). The final surface volume calculation does not include the areas of negative difference values, as a planar height of $h = 0$, excludes any negative difference values.

The Niua South crater vent field poses an interesting problem pertaining to how tonnage estimates are accurately determined for seafloor massive sulphides. The process of defining an area of surface material is a relatively simple task, and has been used in previous studies (Moss et al., 2001; Jamieson et al., 2014). However, it is important to note that, in all the examples of tonnages and accumulation rates presented above (including Niua South), the tonnages and associated accumulation rates apply only to the accumulation of surface material, and do not include the accumulation of sulphide material that precipitates in the subseafloor, and therefore the overall accumulation rates of metals and sulphur mobilized by this hydrothermal system. The relative proportion of subsurface to surface accumulation in seafloor hydrothermal deposits is poorly constrained and likely controlled by the permeability and degree of fracturing within the local substrate and therefore highly variable (Jamieson et al., 2014). It is therefore difficult to use these tonnages to provide insights into rates of formation of land-based volcanogenic massive sulphide deposits (the ancient equivalents of SMS deposits that are preserved in abducted oceanic crust) for which estimates of the proportion of subsurface to surface sulphide mineralization range from 30 to 40% (Hannington et al., 1998).

Tonnage estimates that include both surface and subsurface mineralization are only possible when supported by data from seafloor drilling or potentially modeling of geophysical data (e.g., Middle Valley, Juan de Fuca Ridge; TAG, Mid-Atlantic Ridge; PACMANUS and Solwara 1, eastern Manus basin; Hannington et al., 1998; Zierenberg et al., 1998; Lipton, 2012; Monecke et al., 2016). The most detailed estimates of subseafloor mineralization is from the Solwara 1 deposit, in which 2.5 Mt of sulphide-rich material was calculated over an area of ~90,000 m^2 (Lipton, 2012). The relative proportion of surface material to subsurface mineralization could be greater than 50% (Lipton, 2012). While the true volume of subsurface sulphide material at Niua South is unknown, it is reasonable to assume that the volumes calculated in this study provide a minimum volume of total sulphide material, despite all GIS-based uncertainties.

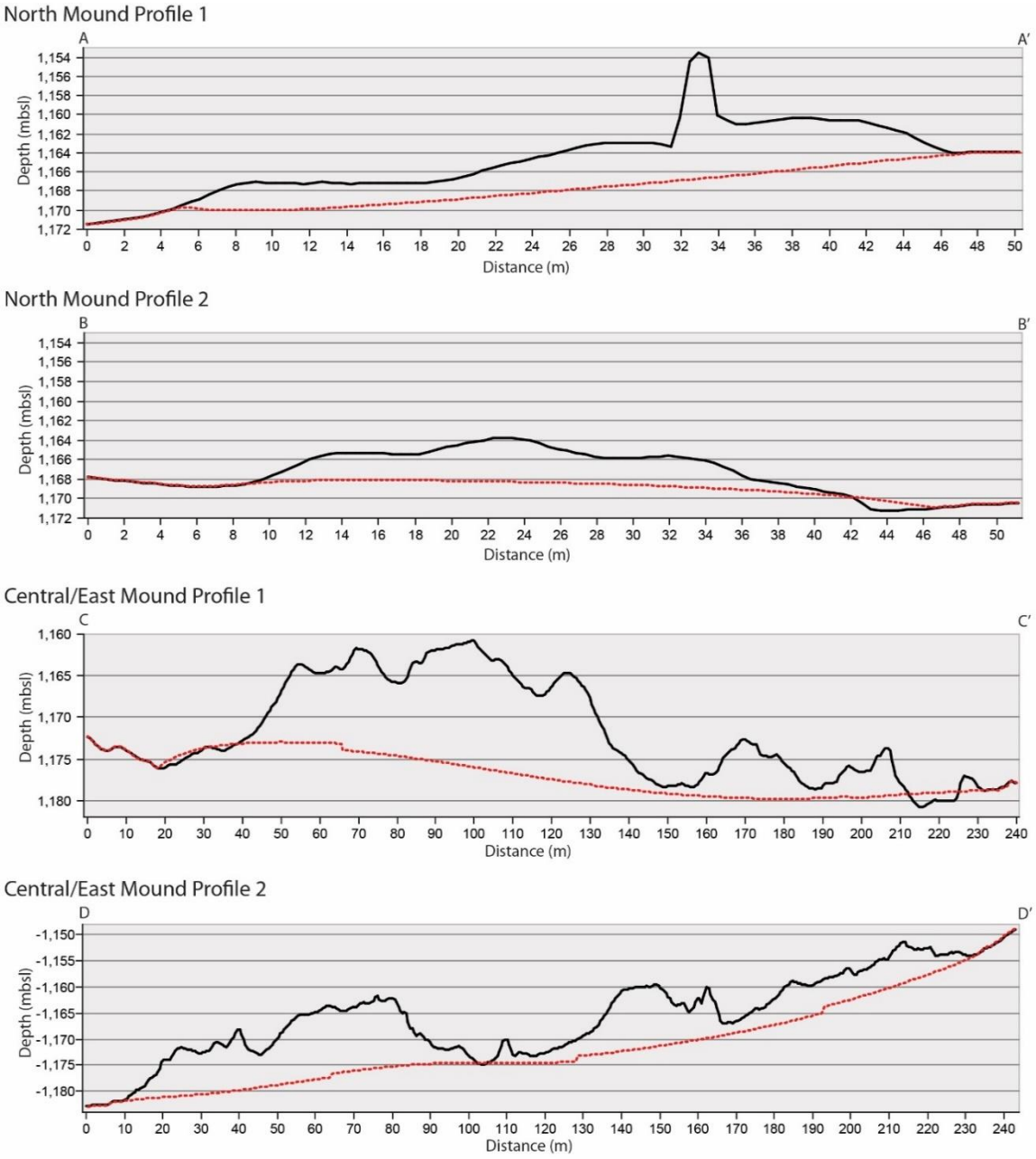

Figure 3.7. Vertical profiles of both bathymetric surfaces (solid black lines) and interpolated surfaces (dashed red lines) for the north and central/east hydrothermal mounds. There are no vertical exaggerations applied to the bathymetric surfaces.

3.5. Conclusions

This study provides the first reports of age and mass accumulation rate data for the Niua South vent field. The vent deposit is ~2900 years old and accumulating at a rate of ~50 t/yr. Results of this study demonstrate that the maximum accumulation rates of sulphide-sulphate deposits at the Niua South crater vent field are comparable to other hydrothermal deposits in mid-ocean ridges where data are available. However, these types of data are still relatively absent for other arc-related deposits. This study marks the first time that mass accumulation rates have been determined for a single, well-constrained hydrothermal system. The availability of both sub-meter AUV-based mapping and age determinations are extremely rare for seafloor hydrothermal systems. However, increasing use of AUVs for high-resolution mapping and improved dating techniques will allow for more systems to be investigated in a similar way to Niua South, thus increasing our understanding of deposit formation rates.

The findings from this study highlight the difficulty with determining total sulphide accumulation at vent sites in the absence of drilling. While drilling at Niua South could help to accurately estimate subsurface mineralization, seafloor drilling is technically challenging and expensive, and unlikely to be performed at a site as small as Niua South. Instead, future work should involve the estimation of fluid fluxes within active chimneys to understand the chemical mass balance of the hydrothermal system, as fluid chemistry has already been collected for previous studies resulting from the R/V *Falkor* expedition. This could ultimately result in the first accurate determination of the depositional efficiency of a well-constrained hydrothermal system.

3.6. References

Baker, E. T. (2007). Hydrothermal cooling of midocean ridge axes: Do measured and modeled heat fluxes agree? Earth and Planetary Science Letters, 263, p. 140–150. https://doi.org/10.1016/j.epsl.2007.09.010.

Baker, E. T., Massoth, G. J., Walker, S. L., & Embley, R. W. (1993). A method for quantitatively estimating diffuse and discrete hydrothermal discharge. Earth and Planetary Science Letters, 118, p. 235–249. https://doi.org/10.1016/0012-821X(93)90170-E.

Bischoff, J. L., & Seyfried, W. E. (1978). Hydrothermal chemistry of seawater from 25° to 350°C. American Journal of Science, 278, p. 838–860.

de Ronde, C. E. J., Hannington, M. D., Stoffers, P., Wright, I. C., Ditchburn, R. G., Reyes, A. G., et al. (2005). Evolution of a submarine magmatic-hydrothermal system: Brothers volcano, southern Kermadec Arc, New Zealand. Economic Geology, 100(6), p. 1097–1133. https://doi.org/10.2113/gsecongeo.100.6.1097.

de Ronde, C. E. J., Massoth, G. J., Butterfield, D. A., Christenson, B. W., Ishibashi, J., Ditchburn, R. G., et al. (2011). Submarine hydrothermal activity and gold-rich mineralization at Brothers Volcano, Kermadec Arc, New Zealand. Mineralium Deposita, 46(5), p. 541–584. https://doi.org/10.1007/s00126-011-0345-8.

Ditchburn, R. G., de Ronde, C. E. J., & Barry, B. J. (2012). Radiometric dating of volcanogenic massive sulfides and associated iron oxide crusts with an emphasis on 226Ra/Ba and 228Ra/226Ra in volcanic and hydrothermal processes at intraoceanic Arcs. Economic Geology, 107(8), p. 1635–1648. https://doi.org/10.2113/econgeo.107.8.1635.

Elderfield, H., & Schultz, A. (1996). Mid-ocean ridge hydrothermal fluxes and the chemical composition of the ocean. Annual Review of Earth & Planetary Sciences, 24, p. 191–224. https://doi.org/10.1146/annurev.earth.24.1.191.

Evans, G. N., Tivey, M. K., Seewald, J. S., & Wheat, C. G. (2017). Influences of the Tonga Subduction Zone on seafloor massive sulfide deposits along the Eastern Lau Spreading Center and Valu Fa Ridge. Geochimica et Cosmochimica Acta, 215, p. 214–246. https://doi.org/10.1016/j.gca.2017.08.010.

Hannington, M. D. (1993). The formation of atacamite during weathering of sulfides on the modern seafloor. The Canadian Mineralogist, 31(4), p. 945–956.

Hannington, M. D., Jonasson, I. R., Herzig, P. M., & Petersen, S. (1995). Physical and chemical processes of seafloor mineralization at mid-ocean ridges, American Geophysical Union. p. 115–157. https://doi.org/10.1029/GM091p0115.

Hannington, M. D., Galley, A. G., Herzig, P. M., & Petersen, S. (1998). Comparison of the TAG mound and stockwork complex with Cyprus-type massive sulphide

deposits. Proceedings of the Ocean Drilling Program, Scientific Results, 158, p. 389–415.

Hannington, M. D., Jamieson, J. W., Monecke, T., Petersen, S., & Beaulieu, S. (2011). The abundance of seafloor massive sulfide deposits. Geology, 39(12), p. 1155–1158. https://doi.org/10.1130/G32468.1.

Hein, J. R., de Ronde, C. E. J., Koski, R. A., Ditchburn, R. G., Mizell, K., Tamura, Y., et al. (2014). Layered hydrothermal barite-sulfide mound field, East Diamante caldera, Mariana volcanic arc. Economic Geology, 109, p. 2179–2206. https://doi.org/10.2113/econgeo.109.8.2179.

Humphris, S. E., & Cann, J. R. (2000). Constraints on the energy and chemical balances of the modern TAG and ancient Cyprus seafloor sulfide deposits. Journal of Geophysical Research, 105(No. B12), p. 28,477-28,488.

Jamieson, J. W., Hannington, M. D., Clague, D. A., Kelley, D. S., Delaney, J. R., Holden, J. F., et al. (2013). Sulfide geochronology along the Endeavour Segment of the Juan de Fuca Ridge. Geochemistry, Geophysics, Geosystems, 14(7), p. 2084–2099. https://doi.org/10.1002/ggge.20133.

Jamieson, J. W., Clague, D. A., & Hannington, M. D. (2014). Hydrothermal sulfide accumulation along the Endeavour Segment, Juan de Fuca Ridge. Earth and Planetary Science Letters, 395, p. 136–148. https://doi.org/10.1016/j.epsl.2014.03.035.

Johns, S. M., Ditchburn, R. G., Barry, B. J., & Yeats, C. J. (2014). Episodic subseafloor hydrothermal activity within the eastern Manus back-arc basin determined by uranium-series disequilibrium in barite. Economic Geology, 109(8), p. 2227–2241. https://doi.org/10.2113/econgeo.109.8.2227.

Lalou, C., J. L. Reyss, E. Brichet, P. A. Rona, and G. Thompson. (1995). Hydrothermal activity on a 10(5)-year scale at a slow-spreading ridge, TAG hydrothermal field, mid-Atlantic Ridge 26-degrees-N. *Journal of Geophysical Research*, 100, p. 17,855–17,862

Lipton, I. (2012). Mineral Resource Estimate, Solwara Project, Bismarck Sea, PNG.

Lowell, R. P., Farough, A., Hoover, J., & Cummings, K. (2013). Characteristics of magma-driven hydrothermal systems at oceanic spreading centers. Geochemistry, Geophysics, Geosystems, 14(6), p. 1756–1770. https://doi.org/10.1002/ggge.20109.

Minami, H., & Ohara, Y. (2017). The Gondou hydrothermal field in the Ryukyu Arc: A huge hydrothermal system on the flank of a caldera volcano. Geochemistry, Geophysics, Geosystems, 18(9), p. 3489–3516. https://doi.org/10.1002/2017GC006868.

Monecke, T., Petersen, S., Hannington, M. D., Grant, H., & Samson, I. (2016). The minor element endowment of modern sea-floor massive sulfide deposits and comparison

with deposits hosted in ancient volcanic successions. Reviews in Economic Geology, 18, p. 245–306.

Moss, R., Scott, S. D., & Binns, R. A. (2001). Gold content of eastern Manus Basin volcanic rocks: Implications for enrichment in associated hydrothermal precipitates. Economic Geology, 96, p. 91–107. https://doi.org/10.2113/gsecongeo.96.1.91.

Mottl, M. J., Seewald, J. S., Wheat, C. G., Tivey, M. K., Michael, P. J., Proskurowski, G., et al. (2011). Chemistry of hot springs along the Eastern Lau Spreading Center. Geochimica et Cosmochimica Acta, 75(4), p. 1013–1038. https://doi.org/10.1016/j.gca.2010.12.008.

Murton, B. J., Lehrmann, B., Dutrieux, A. M., Martins, S., de la Iglesia, A., Stobbs, I. J., et al. (2019). Geological fate of seafloor massive sulphides at the TAG hydrothermal field (Mid-Atlantic Ridge). Ore Geology Reviews, 107, p. 903–925. https://doi.org/10.1016/j.oregeorev.2019.03.005.

Resing, J. A., Embley, R. W., & Merle, S. G. (2012). Submarine Ring of Fire-2012 (SRoF-12) Northeast Lau Basin: R/V Roger Revelle Expedition RR1211, Cruise Report Sept 9-25, 2012, Suva-Samoa.

Seewald, J. S., Reeves, E. P., Bach, W., Saccocia, P. J., Craddock, P. R., Walsh, E., et al. (2019). Geochemistry of hot-springs at the SuSu Knolls hydrothermal field, Eastern Manus Basin: Advanced argillic alteration and vent fluid acidity. Geochimica et Cosmochimica Acta, 255, p. 25–48. https://doi.org/10.1016/j.gca.2019.03.034.

Seyfried, W. E., Seewald, J. S., Berndt, M. E., Ding, K., & Foustoukos, D. I. (2003). Chemistry of hydrothermal vent fluids from the Main Endeavour Field, northern Juan de Fuca Ridge: Geochemical controls in the aftermath of June 1999 seismic events. Journal of Geophysical Research: Solid Earth, 108(B9), p. 1–23. https://doi.org/10.1029/2002jb001957.

Tivey, M. K. (1995). Modeling Chimney Growth and Associated Fluid Flow at Seafloor Hydrothermal Vent Sites. Geophysical Monograph, 91, p. 158–177. https://doi.org/10.1029/GM091p0158.

Tivey, M. K., Stakes, D. S., Cook, T. L., Hannington, M. D., & Petersen, S. (1999). A model for growth of steep-sided vent structures on the Endeavour Segment of the Juan de Fuca Ridge: Results of a petrologic and geochemical study. Journal of Geophysical Research, 104883(10), p. 859–22.

Zierenberg, R. A., Fouquet, Y., Miller, D. J., Bahr, J. M., Baker, P. A., Bjerkgård, T., et al. (1998). The deep structure of a sea-floor hydrothermal deposit. Nature, 392(6675), p. 485–488. https://doi.org/10.1038/33126.

4. Summary

Seafloor massive sulphide deposits have become an important focus of discussion in the context of future mining endeavours. However, the resource potential for seafloor massive sulfide (SMS) deposits is still relatively unconstrained and rapidly evolving, as research expeditions are still frequently discovering new sites of hydrothermal or volcanic activity on the seafloor, developing new ideas, or expanding upon decades of research that countless scientists have gathered from well-known sites. While significant scientific contributions have been made to submarine volcanic-arc hydrothermal systems and associated deposits, these systems remain relatively unexplored in comparison to more commonly studied mid-ocean ridge systems. This thesis marks the first significant introduction to the Niua South volcano and presents a detailed characterization of hydrothermal venting at the crater hosted deposit.

4.1. Findings

Chapter 2 highlights the mineralogy and geochemistry of hydrothermal deposits from Niua South, which are similar to other known volcanic arc hosted deposits. At the broadest scale, individual mineral phases identified in chimney and talus samples are consistent with what is commonly observed from other sites situated in arc and back-arc settings. While many of these phases can also be common in mid-ocean ridge (MOR) deposits (e.g., chalcopyrite, pyrite, sphalerite, and barite), the exclusive presence of unique phases from each respective setting is what largely differentiates their overall

mineralogy (i.e., pyrrhotite is common in MOR, while galena or sulphosalts are more common in arc-related settings). In the case of Niua South, the 36 samples collected for this study can be geochemically separated into either Cu- or Ba-Zn-rich sample types that are mainly composed of chalcopyrite + anhydrite + pyrite/marcasite ± secondary Cu-sulphide phases, and barite + sphalerite + pyrite/marcasite + galena ± chalcopyrite, respectively. In general, elevated levels of As, Sb, Ag, Cd, and Sr are found in low-temperature Ba-Zn-rich hydrothermal samples at Niua South, while Bi, Te, Se, and Sn tend to be more abundant in high-temperature Cu-rich samples. In particular, Au is variably enriched throughout all samples and is found within both high- and low-temperature active chimneys and inactive talus material. The geochemical contents of the hydrothermal samples are distinct from not just mid-ocean ridge deposits, but also back-arc basin deposits (the latter of which can be mineralogically very similar to Niua South). However, back-arc vent fields within the Lau Basin have increasing concentrations of Ba, Pb, As, and Sb with increasing proximity to the Tofua-Kermadec volcanic arc. Niua South is consistent with a volcanic arc signature akin to that of Brothers volcano and shows enrichments in all four of these elements compared to back-arc sites. Present venting at Niua South appears to be seawater-dominated, like the NW caldera vent field at Brothers; however, possible past magmatic contributions are supported by the presence of elements that are attributed to magmatic volatiles (e.g., Bi, Te, Au, and Se) and minerals such as bornite and hematite that indicate more oxidizing fluids.

Results of Chapter 3 show that the maximum rates of sulphide-sulphate accumulation at the Niua South crater vent field are comparable to other hydrothermal deposits found

along mid-ocean ridges (where data is available). A maximum accumulation rate of ~50 ± 9 t/yr was calculated based on a maximum sample age of ~2,900 ± 200 yr. A total volume of 50,600 ± 5,060 m^3 of hydrothermal material was determined for the crater deposits. Assuming a bulk density estimate of average sulphide-sulphate material of 2.65 ± 0.24 t/m^3, the deposit is estimated to be comprised of ~127,000 ± 20,500 t of hydrothermal material. These findings highlight that total sulphide accumulation is difficult to accurately determine without the addition of supporting data (i.e., drilling or seismic data).

4.2. Future Research

The addition of the Niua South dataset to the global database of SMS deposits serves as an important contribution to the characterization of intraoceanic hydrothermal systems. The Brothers volcano is the best studied arc hydrothermal system along the Kermadec-Tofua arc, but this thesis has contributed towards Niua South being one of the few other hydrothermal sites along the arc that have been subjected to specific focused exploration and sampling. There is still a dearth of hydrothermal accumulation and age data to support these types of deposits on a global level. The increasing use of AUVs in high-resolution seafloor mapping is the first step to allowing for detailed analysis of newly discovered sites, and more accurate investigations into known hydrothermal sites, and Niua South is a rare case where both sub-meter bathymetry and age data are both available.

With the support of future expeditions to Niua South, it has the potential to become one of the best studied hydrothermal systems in the world. However, there is an abundance of future work that can be done without the need to return to the site in the near future. Firstly, an analysis of host-rock compositions present within crater could give some additional context for the abundances of trace elements in hydrothermal fluids and deposits. The estimation of fluid fluxes within active chimneys would be a unique contribution to the understanding the chemical mass balance of the hydrothermal system. Supporting fluid chemistry data is available from other studies that resulted from the 2016 R/V *Falkor* expedition. A measure of the depositional efficiency would significantly elevate our understanding of SMS deposit formation on a global level, and its level of accuracy would be unprecedented.

5. Appendices

APPENDIX A – Petrographic descriptions of hydrothermal sulphide samples from Niua South crater

The following are detailed thin-section descriptions of all samples used in this study.

D1918 – R1:

Site Description

This was the first sulphide sample collected on the *Falkor* expedition to Niua South. It was taken from the base of a large sulphide chimney mound. The mound slope is littered with an abundance of large sulphide talus blocks that resemble broken-up pieces of extinct chimneys. Diffuse venting appeared to be occurring in some small, white-coated chimneys adjacent to the sulphide mound, however from the ROV video, it is not obvious if the sulphide mound is active.

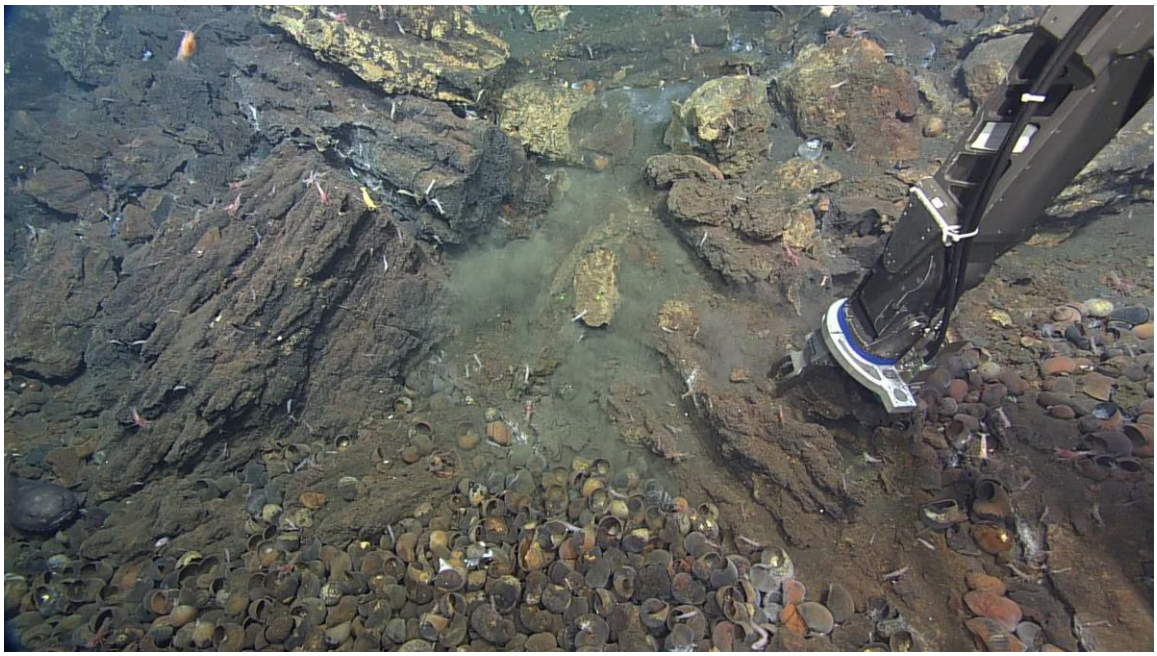

The ROV arm grabbing sample D1918-R1 from the base of a large sulphide mound.

Hand Sample Description

The sample contains a wide (1 x 3 cm) central vent lined with a dense chalcopyrite-rich layer with relatively low porosity. The piece may represent the top, or upper section of an extinct chimney, which has had much of the inner conduit clogged with subsequent sulphide mineralization as venting ceased. The groundmass changes from brassy yellow

to a dark grey towards the sample exterior, indicating a decrease in chalcopyrite and an increase in pyrite and marcasite ± sphalerite. Towards the exterior, the porosity greatly increases. It is also covered in a brown-grey thin outer crust of Fe oxidation.

a. **b.**

Hand sample of D1918-R1. a) Shows an infilled major vent conduit. b) Shows a cut cross-section of the vent conduit with a thick chalcopyrite lining, highlighting that it is only partially infilled.

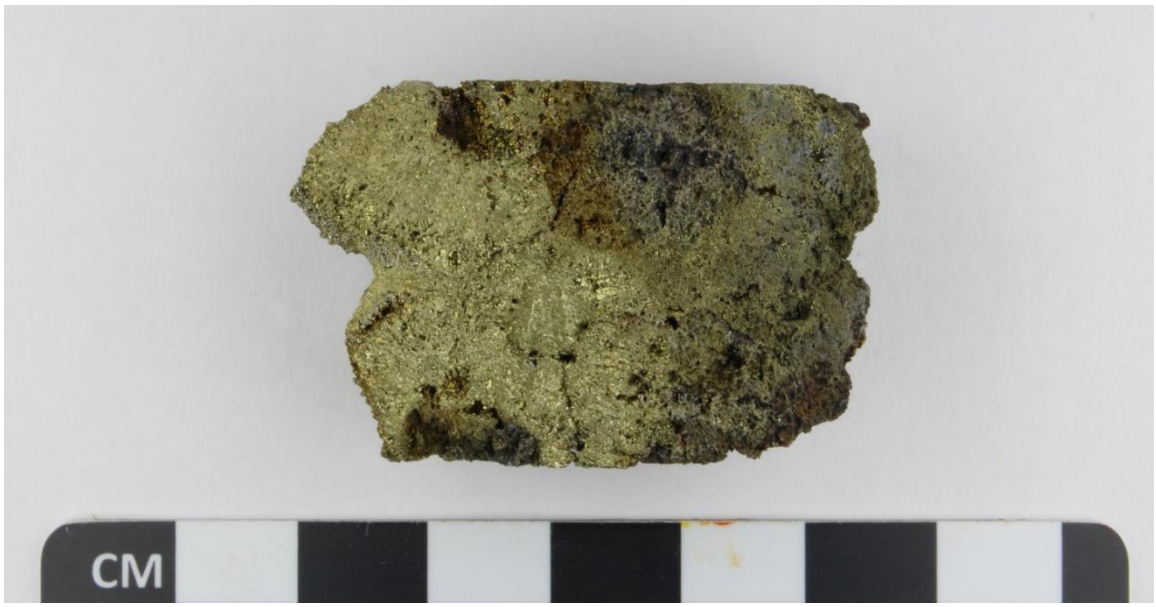

Thin section slab for D1918-R1. This is located at the inner chalcopyrite lining as it transitions towards the exterior.

Mineral Abundances and Occurrences

Chalcopyrite – 85% (vent lining), 55% (interior and exterior)

Pyrite – 15% (vent lining), 28% (interior and exterior)

Marcasite – 10% (interior and exterior)

Barite – 5% (interior and exterior)

Sphalerite – 2% (interior and exterior)

Pb-As Sulphosalt – < 1% (interior and exterior)

Bornite – < 1% (interior and exterior)

Covellite – << 1% (interior and exterior)

The dense interior lining is chalcopyrite-dominated, but also contains disseminated euhedral pyrite within the massive chalcopyrite. Coarse-grained masses of euhedral and subhedral pyrite occur along the edges of the inner vent orifice. Towards the exterior zone the abundance and density of massive chalcopyrite decreases and subhedral pyrite and marcasite increases. Here, pyrite and marcasite are commonly found in anhedral to euhedral clusters and are overgrown by chalcopyrite. Barite occurs as bladed and radiating acicular crystals in localized clusters within pore spaces and has an increased abundance towards the exterior wall. Select clusters of plumose barite have no sulphide overgrowth. Sphalerite rims chalcopyrite in localized pore spaces. Tiny inclusions of Pb-As sulphosalts are found within sphalerite. Trace amounts of primary bornite occur roughly along the boundaries of the two zones. Disseminated replacement by covellite accompanies this growth. Bornite in this sample only, exhibits extreme anisotropism and may instead be idaite (a similar Cu-Fe-S phase).

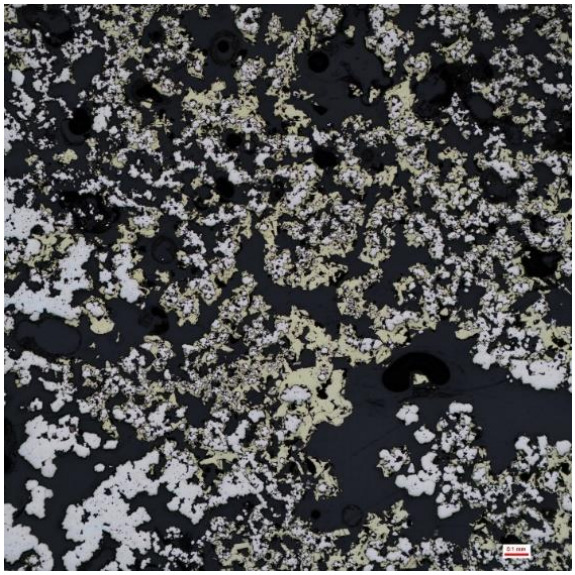

a.

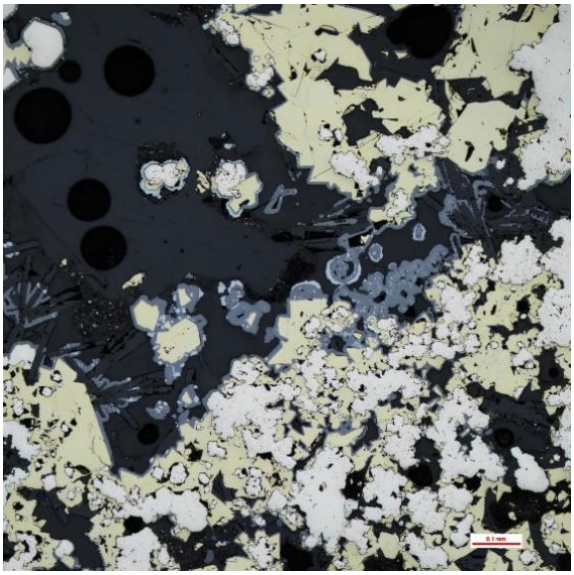

b.

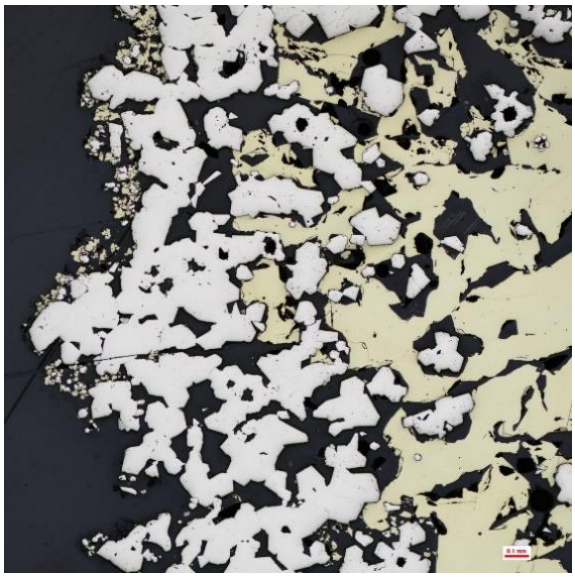

c.

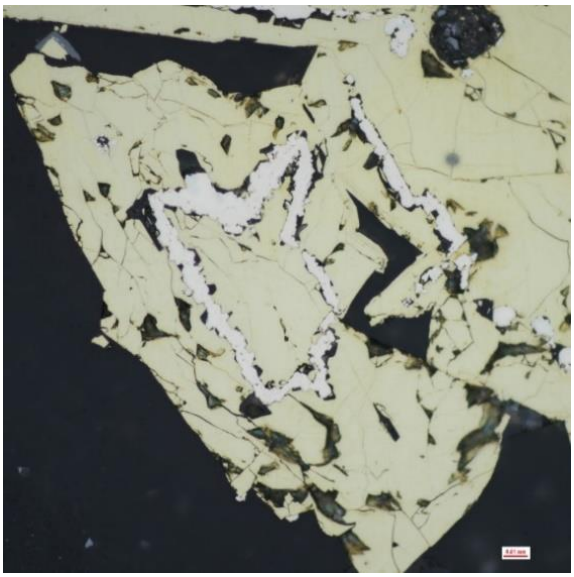

d.

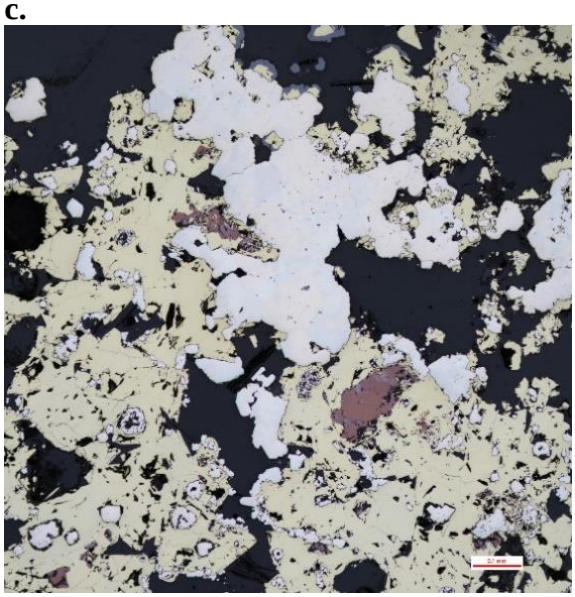

e.

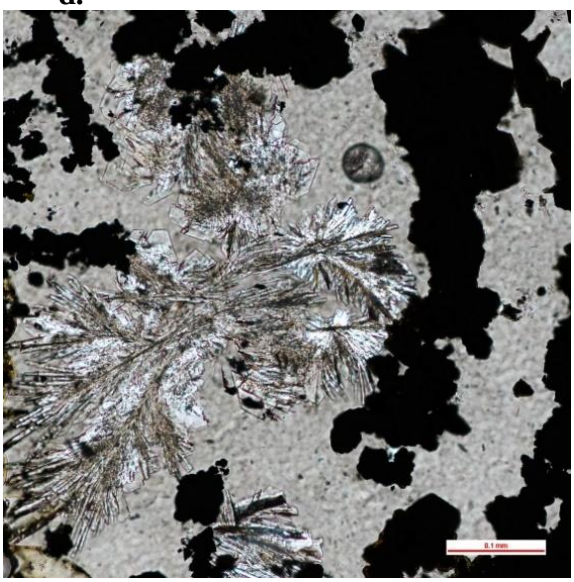

f.

Photomicrographs of sample D1918-R1. All photos are taken under reflected light, except for f, which was taken under transmitted light. a) Chalcopyrite with massive pyrite ± marcasite. Increased abundance of pyrite and marcasite as you move away from the central chalcopyrite vent lining. b) Chalcopyrite overgrowing subhedral pyrite, mantled by late-stage sphalerite and galena. Barite and late-stage marcasite rims can be found in localized pores. c) Late-stage euhedral pyrite grown on massive chalcopyrite. Typical along the central vent lining. d) Rare, laminated growths of pyrite within chalcopyrite, suggestive of alternating stages of sulphide growth. e) Localized bornite with unusual strong bireflectance and anisotropy is accompanied by covellite replacement. f) Plumose barite exhibiting little to no sulphide overgrowth.

D1918 – R2:

Site Description

This sample consists of separate pieces of sulphide material collected on the flanks of an active boiling chimney. They were located adjacent to a tall-standing, active chimney complex with diffusely venting beehive structures and several inactive spires. It was scooped up using the bucket attachment, which simultaneously collected snails for biological study.

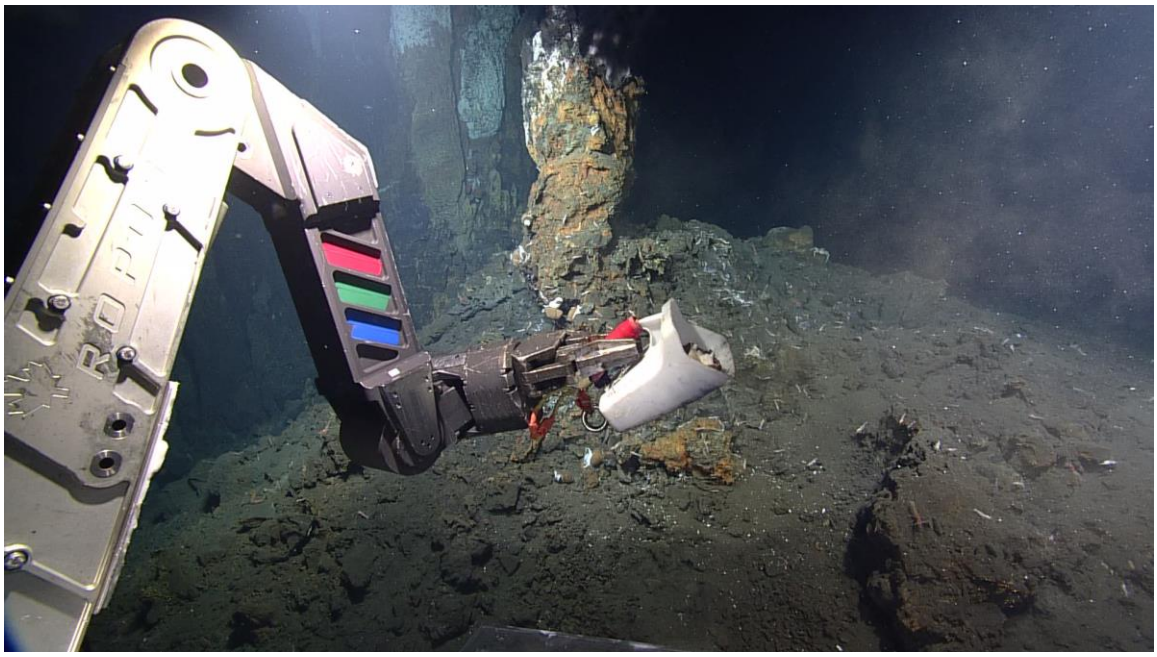

Scoop collection of D1918-R2 pieces.

Hand Sample Description

The sample consists of several small pieces that are dominated by non-porous to low porosity, coarse-grained chalcopyrite. The low porosity pieces are defined by a thin grey-black rim surrounding a brassy yellow chalcopyrite-rich interior. The largest non-porous piece exhibits a smooth, dark blue exterior surface composed of covellite, and some iridescence in the chalcopyrite. All the non-porous pieces are particularly dense and heavy for their size. In general, the exterior surfaces contain some minor oxidation and small white patches of bacterial growth.

a. **b.**

Hand samples of D1918-R2. a) Shows the largest piece. b) Shows two smaller pieces.

Thin section slab for D1918-R2. The dark edges on the left and right-hand sides are part of the sample exterior.

Mineral Abundances and Occurrences

Chalcopyrite – 99%

Pyrite – ≤ 1%

Marcasite – < 1%

Covellite – <<1%

Sphalerite – <<1%

Massive chalcopyrite constitutes virtually all the mineralization present in this sample. It forms a dense groundmass very similar to the interior vent lining in the previous section. Pyrite appears as euhedral cubes within pore spaces of chalcopyrite close to the sample exterior. Pyrite and particularly marcasite along the exterior areas are more subhedral and are overgrown by chalcopyrite. Trace covellite forms a thin replacement rim around some edges of chalcopyrite along the sample exterior. Massive sphalerite rims on chalcopyrite are extremely rare, and a few tiny inclusions of sphalerite are present within euhedral pyrite.

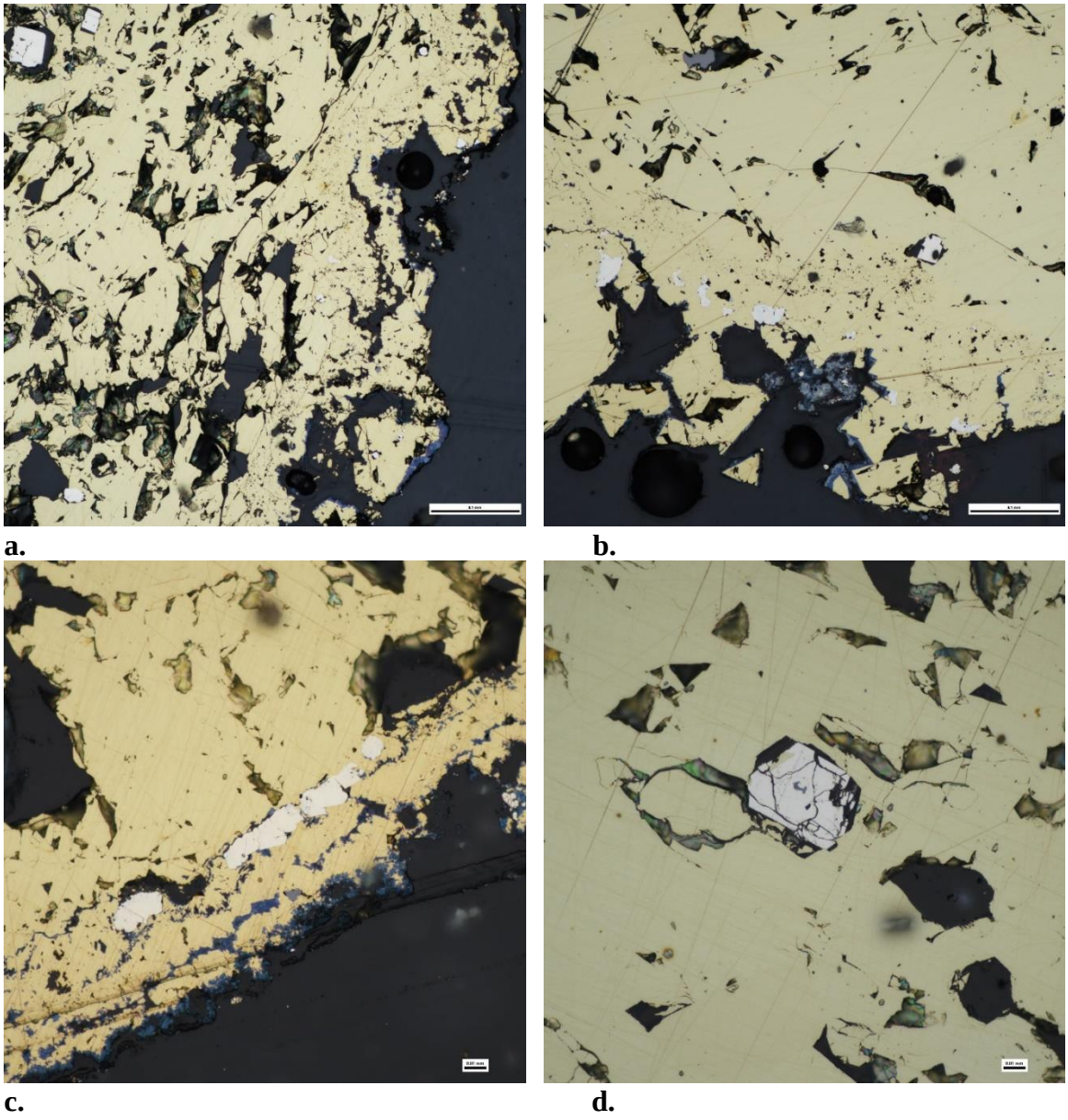

a. **b.**

c. **d.**

Photomicrographs of sample D1918-R2. All photos are taken under reflected light. a) Euhedral pyrite within massive chalcopyrite. Covellite forms a thin lamination on the

edge of chalcopyrite in the bottom right corner. b) Euhedral pyrite and subhedral marcasite within massive chalcopyrite. Sphalerite and covellite appear together along the edges of chalcopyrite. c) Subhedral marcasite formed near the exterior edge, with thinly laminated covellite replacing massive chalcopyrite. Covellite also penetrates chalcopyrite grains along fractures. d) Tiny fractured euhedral pyrite within the central vent interior of massive chalcopyrite. These grains are extremely rare.

D1918 – R3:

Site Description

This sample was collected from the same hydrothermal mound as D1918-R2.

Scoop collection of D1918-R3. Sample piece is the large sulphide talus block visible next to the bucket attachment.

Hand Sample Description

This sample can be divided into three distinct layers. The first layer contains coarse-grained chalcopyrite crystals (1 – 5 mm), characteristic of the inner lining of an active chimney associated with high-temperature venting. Most of the crystals are yellow gold in colour and sometimes have a distinct iridescent appearance. The second layer is a mixture of dull-white anhydrite-rich layers with moderately defined, alternating bands of a light grey groundmass composed of chalcopyrite, sphalerite, and pyrite ± marcasite. The final layer is composed of a dark grey groundmass composed of sphalerite and barite intermixed with fine-grained chalcopyrite. This exterior contains patches of heavily oxidized sulphide material, indicated by light orange to deep orange-brown, earthy colours.

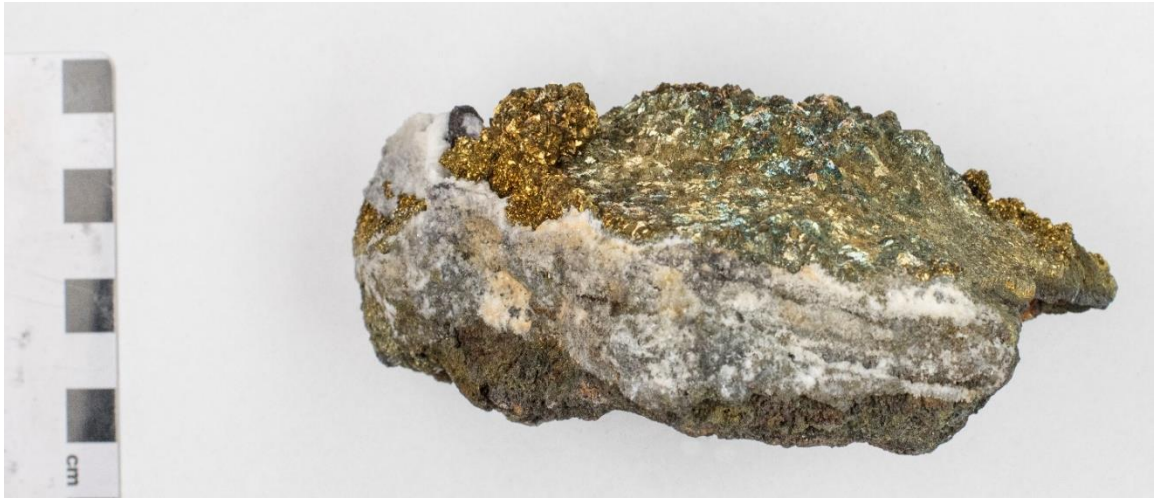

Hand sample of D1918-R3. Shows the zonation of minerals throughout the chimney wall.

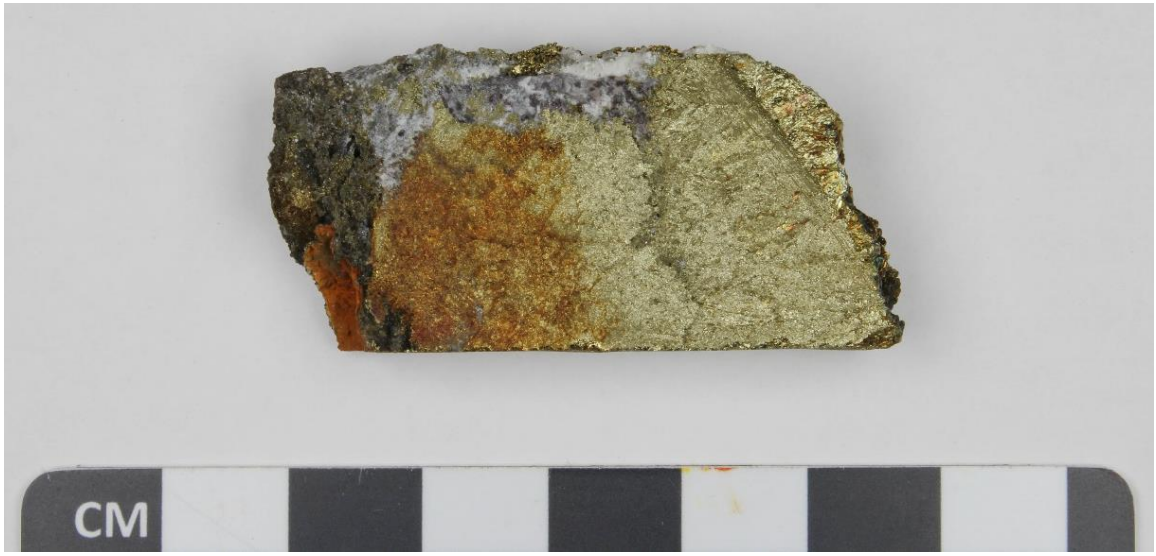

Thin section slab of D1918-R3. Oxidation of chalcopyrite is present towards the sample exterior (left).

Mineral Abundances and Occurrences

Chalcopyrite – 75%

Anhydrite – 25%

Barite – < 1%

Bornite – < 1%

Pyrite – < 1%

Hematite – < 1%

Marcasite – << 1%

Covellite – << 1%

The sample contains two distinct zones: a porous chalcopyrite- and anhydrite-rich interior ± pyrite, and a thick layer of dense, massive chalcopyrite representing the interior vent lining. As with the previous two samples, massive chalcopyrite growth is present throughout most of the sample, and it dominates the interior vent lining. Anhydrite is mostly anhedral with some subhedral tabular to bladed crystal masses with a wide range in sizes. It is abundantly intermixed with chalcopyrite towards the sample exterior but is completely absent in the exterior crust. Rare, bladed barite is intermixed with anhydrite. Towards the anhydrite-rich zone only, bornite commonly replaces massive chalcopyrite. This replacement occurs along the edges of chalcopyrite grains with associated pore space and in many cases penetrates chalcopyrite along thin interior fractures. Bornite also contains disseminated replacement by covellite along these fractures. Pyrite occurs as small, massive blebs, or as tiny euhedral crystals of trace abundance. Pyrite and marcasite also form very small, thin laminations along the boundary of the two distinct zones. Traces of primary clusters of euhedral hematite are found on the edges of chalcopyrite-bornite-covellite, forming within the interstices of chalcopyrite.

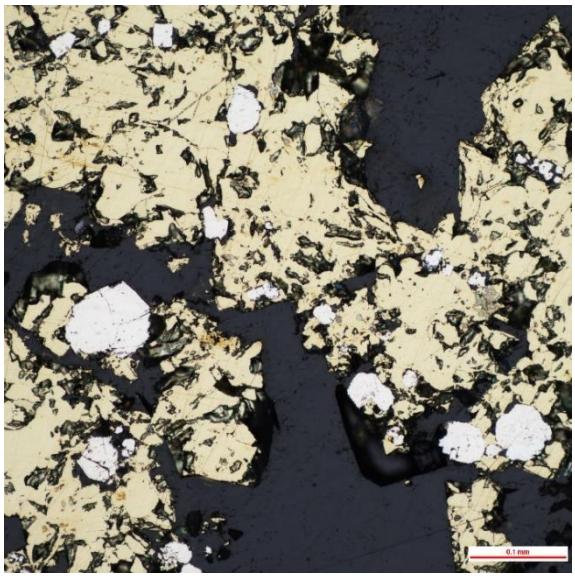

a.

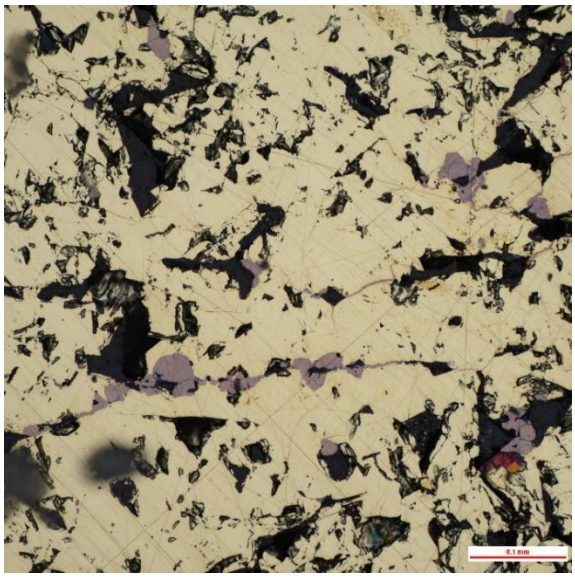

b.

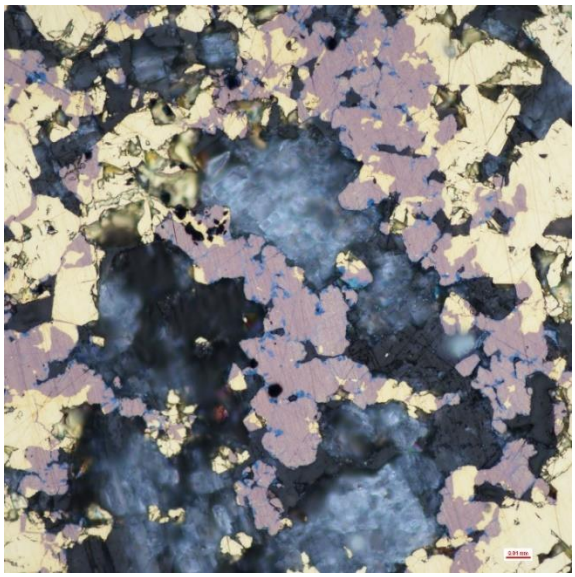

c.

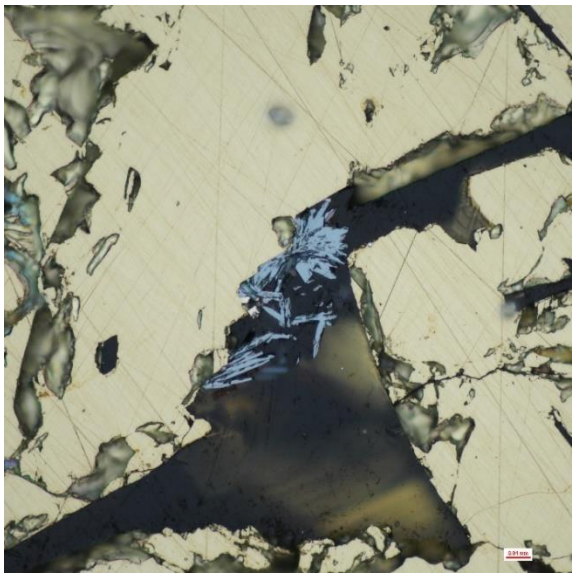

d.

Photomicrographs of sample D1918-R3. All photos were taken under reflected light, except for c, which was taken using both reflected and transmitted light. a) Subhedral to euhedral pyrite is overgrown by massive chalcopyrite. b) Massive chalcopyrite within the thick interior chalcopyrite lining. Bornite is grown along the edges of chalcopyrite, within pore spaces, and along internal fractures. c) Extensive bornite replacement of chalcopyrite accompanied by covellite. Anhydrite growth has infilled pore spaces between chalcopyrite and bornite. d) Tiny needle-like, subhedral hematite is grown within the interstices of massive chalcopyrite.

D1918 – R4:

Site Description

Several pieces of sulphide and sulphate material were sampled from the tip of an active, focused black smoker chimney. The exiting hydrothermal fluid was visibly boiling within a few centimetres of the vent orifice. After initial fluid sampling of the boiling fluids, ROPOS “carefully” removed pieces of the chimney top. Three pieces were obtained, ranging from small to large.

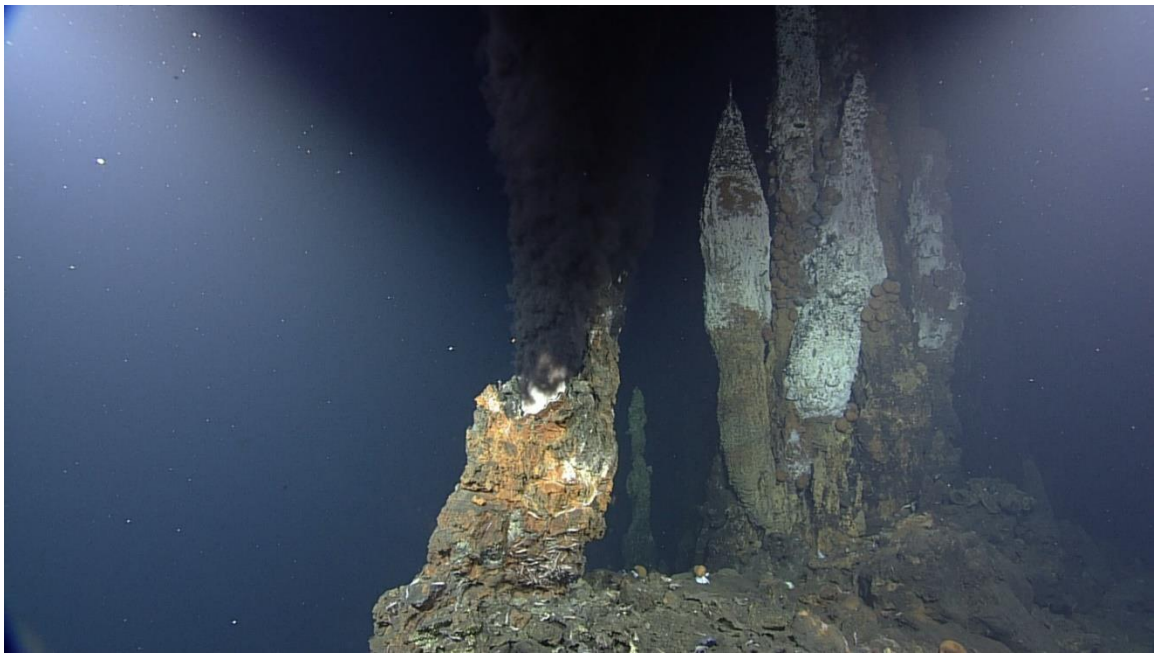

Black smoker hydrothermal chimney exhibiting boiling at the vent orifice. D1918-R4 and D1918-R5 were both grabbed from the tip.

Hand Sample Description

The sample is a small section taken from a much larger sample piece (gifted to the Kingdom of Tonga), but is representative of the whole sample. Half of the sample exterior is lined with coarse-grained chalcopyrite (up to 50 mm), typical of the inner lining of a high-temperature black smoker chimney. The other half is a light-grey to dark-grey mixture of anhydrite, chalcopyrite, pyrite, and minor secondary Cu-sulphide minerals. Throughout the sample there are brassy yellow chalcopyrite-rich, and dull-white anhydrite-rich bands, that lack any well-ordered zonation. The sample exterior is relatively fresh, and therefore contains little oxidation.

a. **b.**

Hand sample pieces of D1918-R4. a) Shows the smaller of the two, this piece was used for petrological analysis. b) Shows the larger piece, which was gifted to the Kingdom of Tonga.

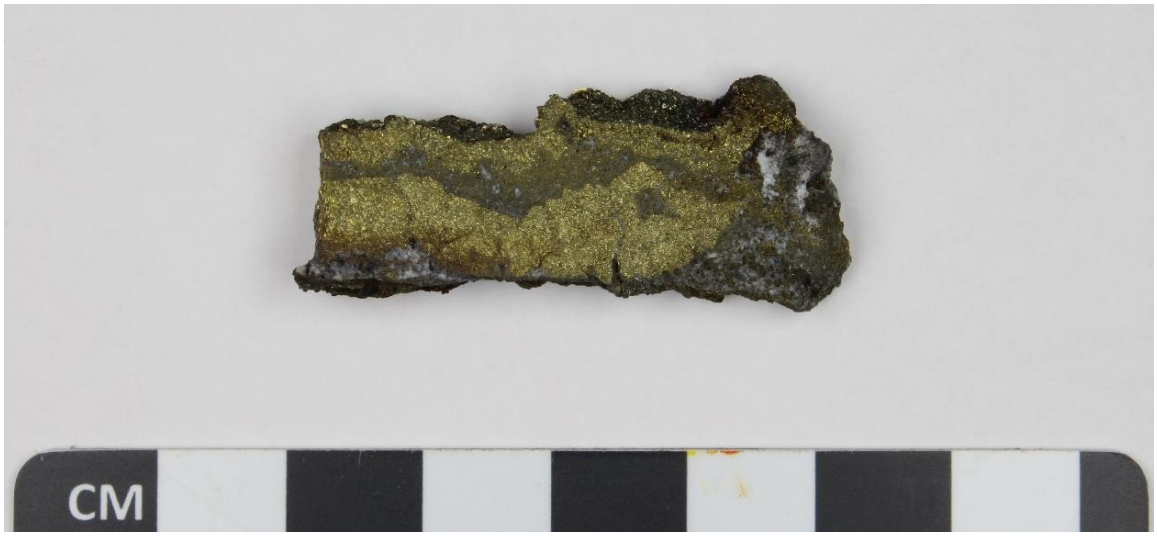

Thin section slab of D1918-R4, cut from the small sulphide piece.

Mineral Abundances and Occurrences

Chalcopyrite – 65-70%

Anhydrite – 29-34%

Barite – ≤ 1%

Pyrite – < 1%

Bornite – < 1%

Digenite – << 1%

Hematite – <<< 1%

Tetrahedrite-Tennantite – <<<< 1%

This sample is very similar in mineralogy to the previous sample. The sample contains two distinct zones: a porous chalcopyrite- and anhydrite-rich interior ± pyrite, and a thick layer of dense, massive chalcopyrite representing the interior vent lining. As with the previous two samples, massive chalcopyrite growth is present throughout most of the sample, and it dominates the interior vent lining. Anhydrite is mostly anhedral with some subhedral tabular to bladed crystal masses with a wide range of sizes. It is abundantly intermixed with chalcopyrite away from the vent lining and forms a small vein in the middle of the section bounded by dense chalcopyrite layers. Rare, bladed barite is intermixed with anhydrite. Near the outer anhydrite-rich zone, bornite replaces massive

chalcopyrite. This replacement occurs along the edges of chalcopyrite grains and in many cases penetrates chalcopyrite along thin interior fractures. The replacement then transitions to digenite within a localized area. Small anhedral to subhedral grains of tetrahedrite-tennantite appear within chalcopyrite, bornite, and digenite in this zone. Exsolution lamellae of bornite and digenite are also an isolated occurrence near the anhydrite-rich interior and do not exhibit the typical basket-weave texture observed in other samples. Pyrite occurs as small, massive blebs, or as tiny euhedral crystals throughout the sample in trace abundance. Pyrite also forms very small, thin laminations along the boundary of the two distinct zones. Traces of primary clusters of euhedral hematite are found in the bornite-digenite zone, forming within the interstices of chalcopyrite.

a.

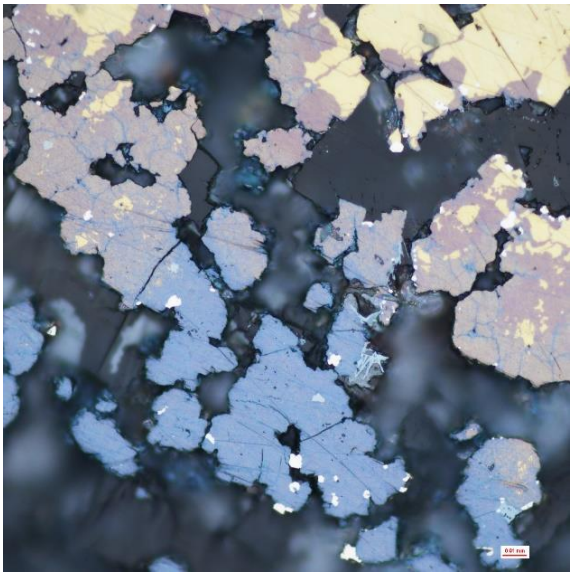

b.

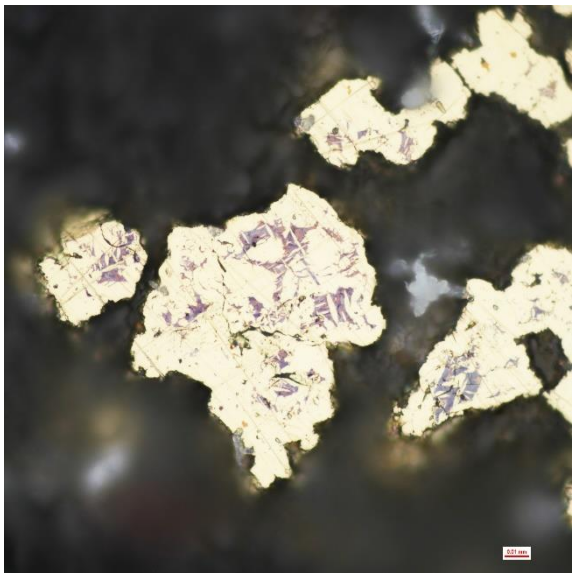

c.

d.

Photomicrographs of sample D1918-R4. All photos are taken under reflected light. a) Boundary between massive chalcopyrite layer and a massive chalcopyrite and anhydrite-rich layer. b) Exterior replacement of chalcopyrite by bornite. Chalcopyrite and bornite have a transitional replacement by digenite closer towards the exterior surface. Covellite has also replaced these sulphides along cracks. c) Exsolution texture in chalcopyrite containing bornite and digenite exsolution lamellae. d) Tiny needle-like growths of hematite within the pore space of near exterior massive chalcopyrite, other crystals groups are also radiating. Minor bornite and digenite replacement is present on the edges, and within cracks in chalcopyrite.

D1918 – R5*:

*** Sample was logged improperly during the ROV dive. Sample identifies with the D1918-R4 collection and is a piece collected from the active boiling chimney.**

Site Description

The sample was obtained during the collection of the previous sample from the tip of the boiling chimney.

Hand Sample Description

This sample contains two sulphide pieces that are similar in composition but have slightly different features. The larger of the two pieces is primarily composed of yellow-gold chalcopyrite crystals (1 – 2 mm), and an intermixed anhydrite and fine-grained dark grey, anhydrite and chalcopyrite-rich groundmass ± pyrite and marcasite. Anhydrite has some well defined, small crystals that occur in clusters. The smaller of the two pieces has the same mineralogy, however the chalcopyrite crystals are overall slightly larger (2 – 3mm), and they also form a thin layer as in D1918-R3 and D1918-R4. The dark grey groundmass is coarse-grained as well (1 – 3 mm), and there is a large cluster of sulphate crystals that exhibit a strange, light green to orange discolouration.

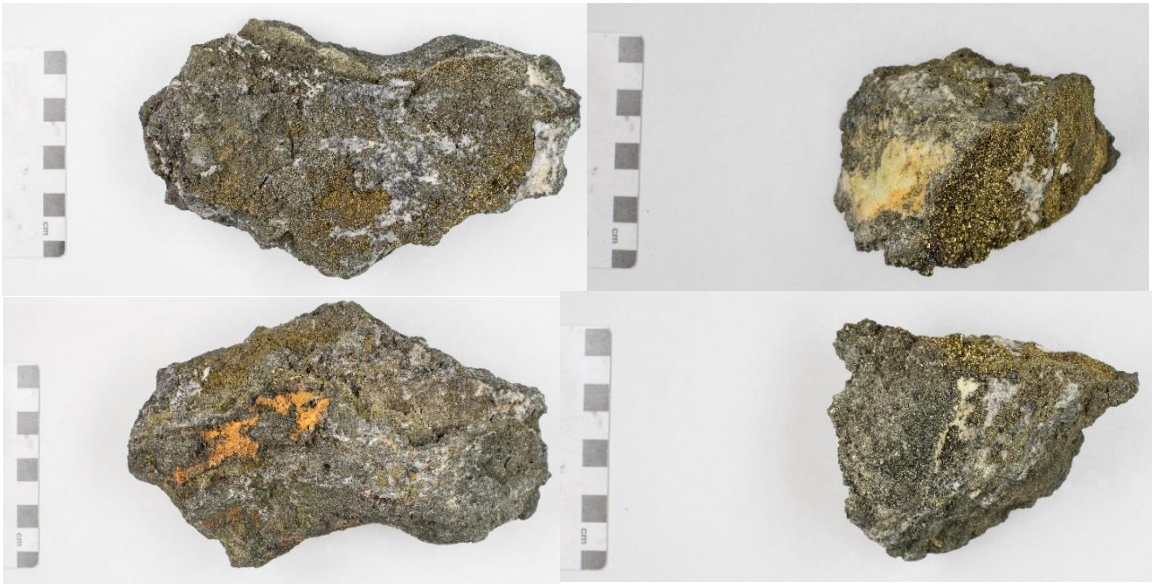

Hand samples for D1918-R5. Top and bottom left photographs show both sides of the larger sulphide piece. Top and bottom right photographs show major features of the smaller sulphide piece.

Thin section slab of D1918-R5.

Mineral Abundances and Occurrences

Anhydrite – 65%

Chalcopyrite – 32%

Pyrite – 3%

Marcasite – <1 %

Barite – < 1%

Sphalerite – << 1%

The sample contains a heterogenous porous mixture of anhydrite and massive chalcopyrite. A thin layer of dense, massive chalcopyrite is also bounded by the mixture. Unlike the previous two samples, anhydrite is the dominant mineral. Anhydrite crystals are largely anhedral with some subhedral, stubby to elongate crystal masses. It is abundantly intermixed with chalcopyrite away from the vent lining and forms a small vein in the middle of the section bounded by dense chalcopyrite layers. Pyrite ± marcasite mostly occur as small disseminated subhedral grains throughout the sample in minor abundance. However, they also occur together as slightly ovoid rings resulting from the overgrowth of vent organisms, preserving their morphological forms. Euhedral pyrite overgrowths of pre-existing pyrite grains highlight distinct growth stages. Small

subhedral bladed and tabular crystals of barite (with a few radiating masses) are only present in minor abundance on the very edge of the dense massive chalcopyrite layer. Trace sphalerite appears with chalcopyrite as very thin alternating bands. These layers often also contain small subhedral pyrite.

a.

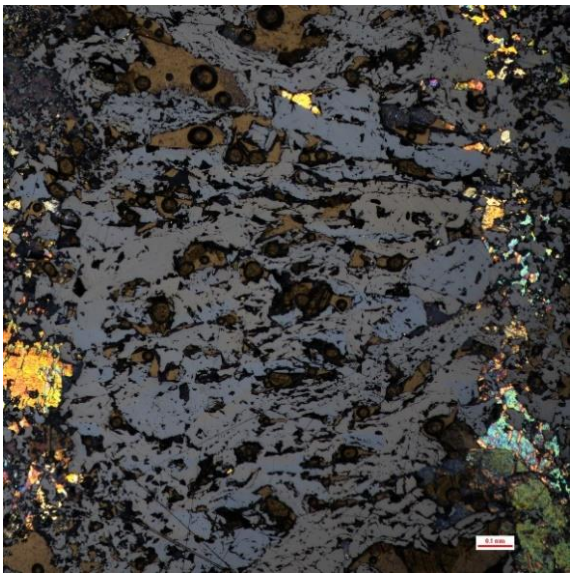

b.

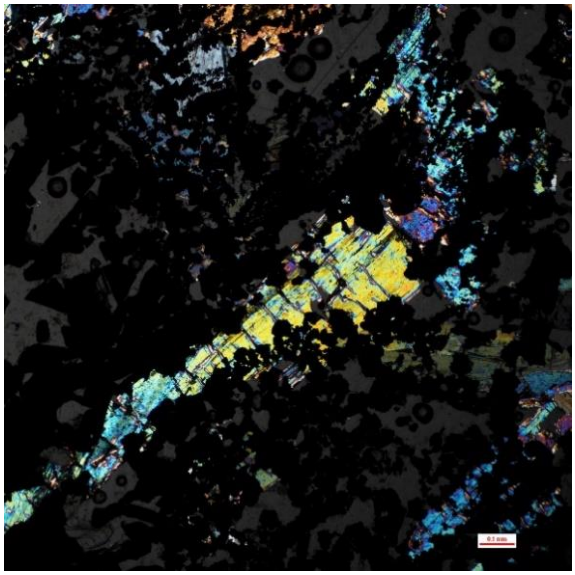

c.

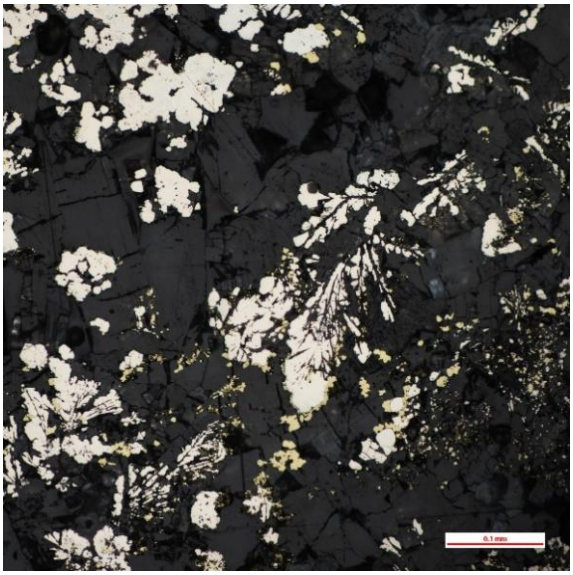

d.

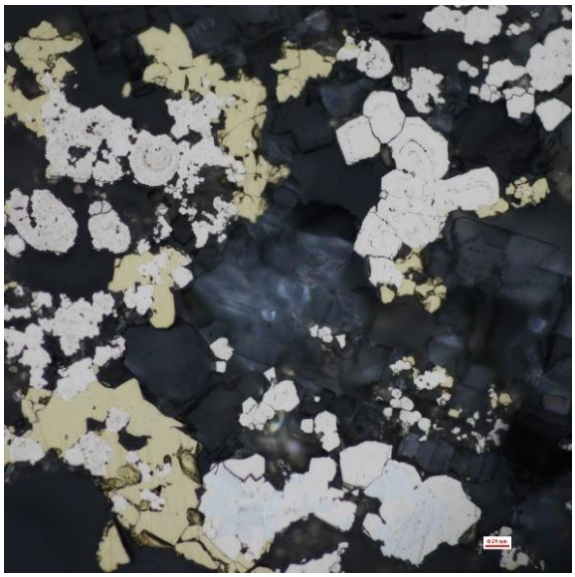

e.

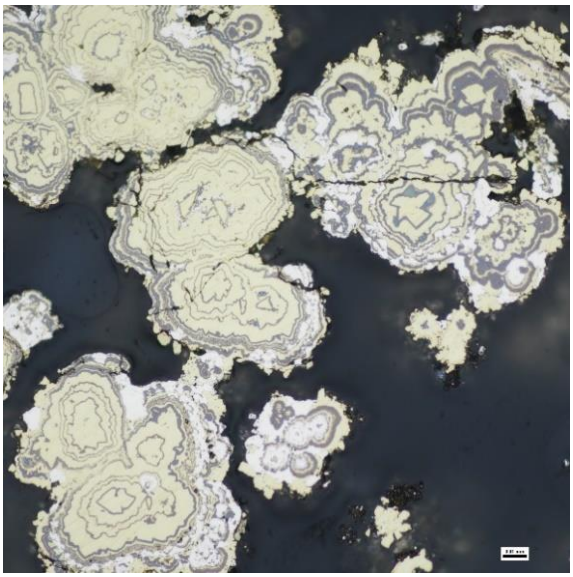

f.

Photomicrographs of sample D1918-R5. All photos are taken under reflected light, except for c, which is under transmitted light, and B, which uses a combination of both. a) Relict chalcopyrite-dominated vent lining surrounded by anhydrite-dominated growths on either side. b) Cross-polarized light (XPL) of the previous photo to highlight the lack of anhydrite growth within the vent lining. c) Subhedral anhydrite crystals with sulphide overgrowth. This is evidence anhydrite formed before the sulphides. d) Subhedral pyrite with coarse-grained anhydrite. Relict plumose texture highlighted by mantled pyrite. Barite crystals have been resorbed. e) Anhedral chalcopyrite with subhedral and colloform pyrite ± marcasite. Growth zones exhibited in some subhedral pyrite. f) Thin alternating bands of sphalerite within chalcopyrite with intergrowths of pyrite. Evidence of a complex history of growth and replacement.

D1918 – R6:

Site Description

This sample is from the base of a steep-sided, tall-standing, large inactive chimney complex with extensive oxidative weathering. It is difficult to see from the dive videos, but there may also be some active spires as well. The obtained sample piece is sulphide talus material, found amongst a mass of other large and small sulphide talus blocks.

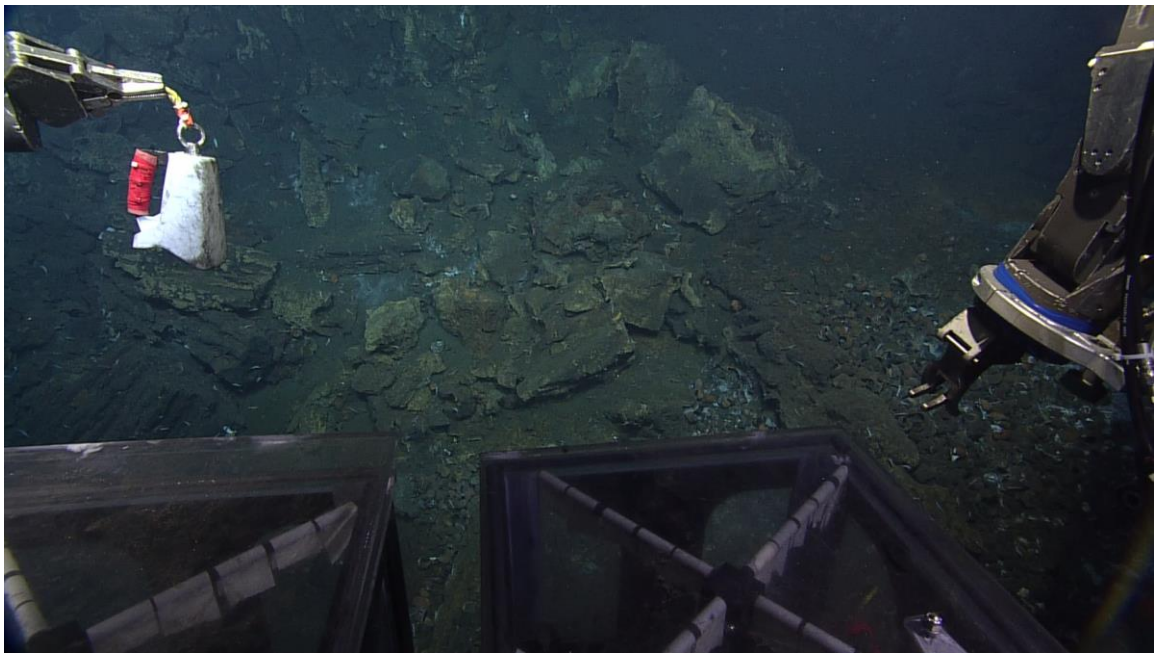

Talus slope from which D1918-R6 is grabbed.

Hand Sample Description

This sample is a large block of sulphide and sulphate material, that resembles an extinct chimney trunk. The interior groundmass is mostly dark grey composed of barite intermixed with sphalerite and minor pyrite. The innermost material exhibits a yellow-gold colour, dominated by chalcopyrite with coarse barite crystals (1 – 3 mm) found in vugs. Throughout the first couple of centimeters of the exterior, an intense red-orange-yellow discolouration indicates a possible presence of realgar or orpiment. Most of the exterior is heavily oxidized, with orange-brown Fe-oxides and oxyhydroxides, formed on a thin barite-dominated crust (~ 2 mm).

a.

b.

Hand sample of D1918-R6. a. Shows the side view of the large main sulphide piece. b) Shows a slice through the center, a cross-sectional view of an extinct vent.

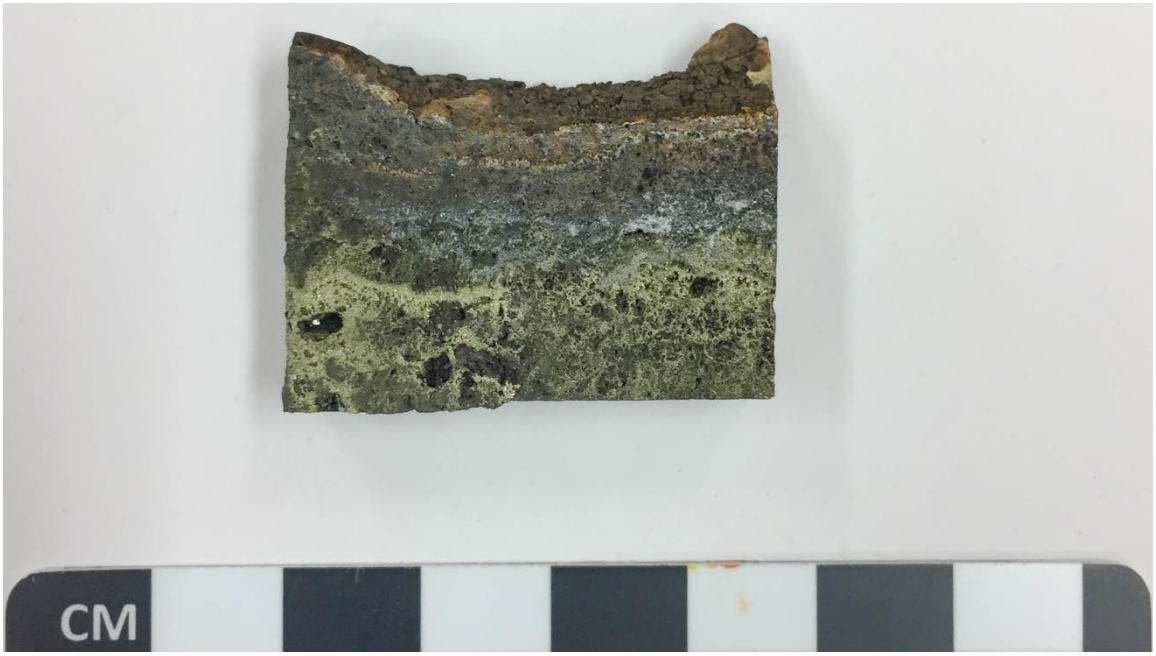

Thin section slab of D1918-R6.

Mineral Abundances and Occurrences

Chalcopyrite – 50-55%

Barite – 35-40%

Sphalerite – 7%

Pyrite – 3%

Marcasite – < 1%

Amorphous Silica – < 1%

Galena – << 1%

Pb-As sulphosalts – << 1%

Tetrahedrite-Tennantite – << 1%

The sample contains two separate zones: a dense massive chalcopyrite-dominated interior, and a barite- and sphalerite-rich exterior. Massive chalcopyrite dominates the interior zone with localized growth of sphalerite ± galena within pore spaces. Massive sphalerite commonly overgrows plumose barite and pyrite. It is largely contained between an outer marcasite ± pyrite crust, and the massive chalcopyrite interior. There are also some occurrences of dendritic sphalerite in this zone, some of which has been replaced by

chalcopyrite. Chalcopyrite disease in sphalerite is prevalent in the transitional area from the barite- and sphalerite-dominated exterior to the chalcopyrite-dominated interior. Barite occurs mostly as euhedral to subhedral bladed and tabular crystals, sometimes as radiating masses. Plumose texture with overgrowths of pyrite blebs and massive sphalerite is common. Barite is fine-grained around the exterior, but a few large crystals are found within the interior in voids. Relict barite crystals appear to be resorbed in some massive chalcopyrite, located at the outer margin of the chalcopyrite-dominated zone. These spaces are now infilled by amorphous silica. Pyrite mostly occurs as massive and circular blebs, that often exhibit colloform texture. Tiny disseminated subhedral to euhedral crystals are also present, but primarily in pore spaces within the massive chalcopyrite zone. Marcasite forms a massive exterior crust that contains fine-grained barite crystals and pyrite blebs. Thin alternating bands of marcasite and sphalerite are sometimes found in colloform pyrite. Localized anhedral to subhedral grains of tetrahedrite-tennantite are found with chalcopyrite. Minor replacement of chalcopyrite occurs along its edges. Localized clusters and small inclusions of galena and Pb-As sulphosalts occur within sphalerite within the same area as tetrahedrite-tennantite.

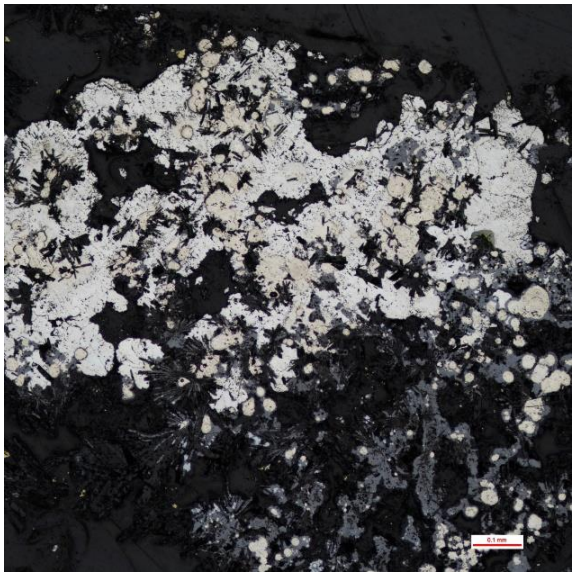

a.

b.

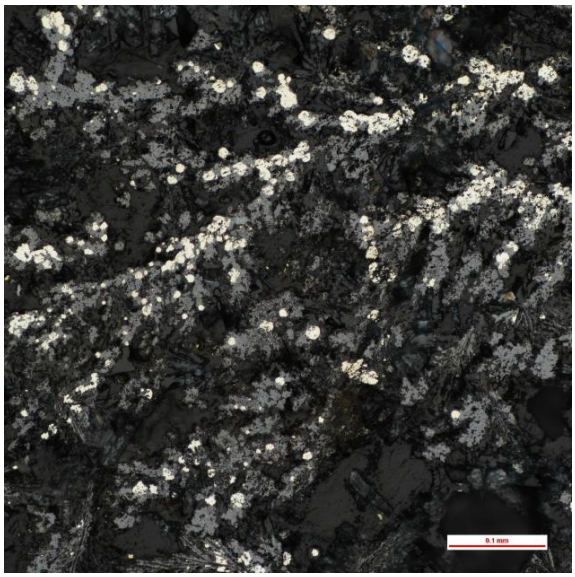

c.

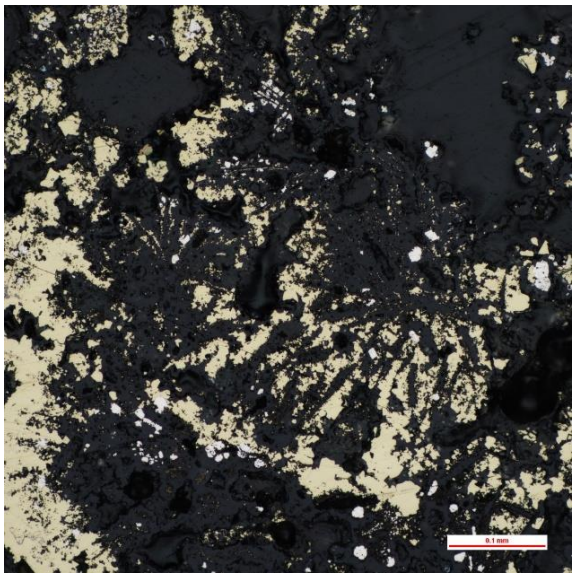

d.

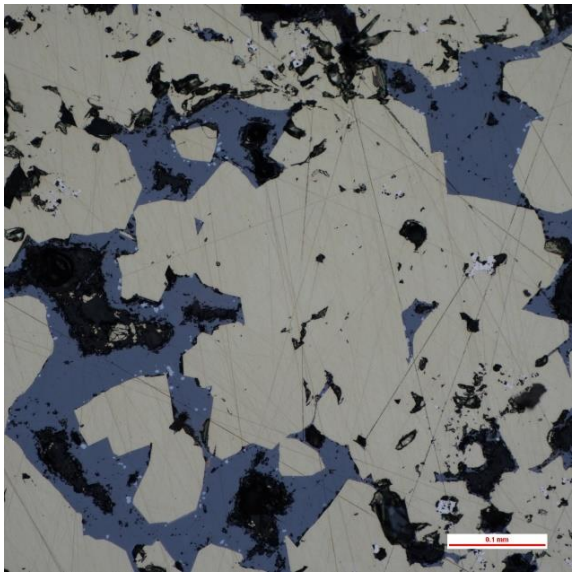

e.

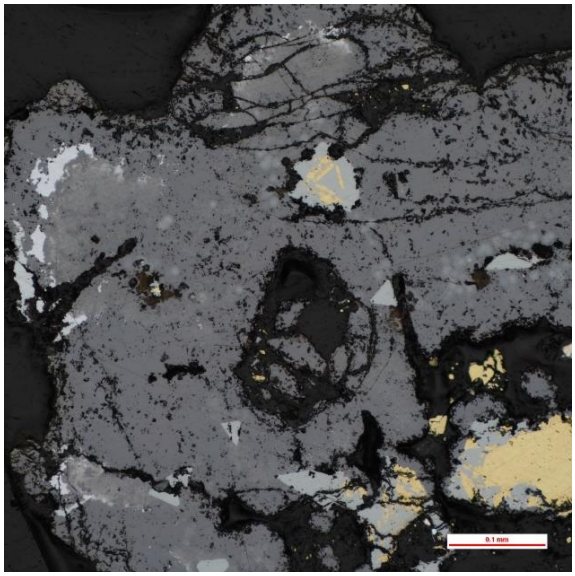

f.

Photomicrographs of sample D1918-R6. All photos are taken under reflected light. a) Massive marcasite has overgrown fine-grained, exterior barite and colloform pyrite. Sphalerite becomes the dominant sulphide mineral for a short distance towards the interior. b) Plumose barite mantled by pyrite blebs and subsequently overgrown by sphalerite. c) Dendritic sphalerite. Commonly formed by massive overgrowth of pyrite blebs in the sphalerite-rich zone. d) Chalcopyrite overgrowth of bladed barite crystals, which have been resorbed and infilled by late amorphous silica. Chalcopyrite overgrowth and replacement of sphalerite increases towards the sample interior. e) Subhedral chalcopyrite is thickly grown within interior vent walls. Late-stage sphalerite and galena are overgrown within inner pore space. f) Local occurrences of tetrahedrite-tennantite form with chalcopyrite. Sphalerite forms afterwards as late-stage mineralization with

galena. Faint haloes of galena can be seen in sphalerite, next to the anhedral grains, showing transitional replacement of galena by sphalerite.

D1918 – R7:

Site Description

This sample originates from the base of an inactive chimney that toppled over during the sampling process. The chimney was part of a larger steep-sided sulphide mound that contains two separate tall chimney complexes. An abundance of old and collapsed chimneys are littered on the flanks of the mound. Although most of the chimneys along the sides of the mound are inactive, towards the tops of the two chimney complexes, diffuse venting is present in beehive structures that emit white and black smoke.

The yellow-topped chimney in the middle was knocked over by the grab arm during sampling, D1918-R7 is from the base of the in situ remains.

Hand Sample Description

The sample is primarily characterized by a porous groundmass of white barite-rich zones intermixed with dark-grey barite- and sphalerite-rich zones. Where the groundmass has a yellowish colouration are localized enrichments of fine-grained chalcopyrite intermixed with sphalerite, pyrite ± marcasite. There is abundant barite towards the exterior of the samples, with the outer carapace also exhibiting an orange-brown oxidation surface with white patches of bacterial growth.

Hand sample for D1918-R7.

Thin section slab for D1918-R7.

Thin Section Descriptions

Mineralogy:

Barite – 50%

Sphalerite – 20%

Chalcopyrite – 20%

Pyrite – 8%

Marcasite – 2%

Galena – < 1%

Covellite – < 1%

Tetrahedrite-Tennantite – << 1%

The sample is dominated by a barite-sphalerite-rich zone with large patches of chalcopyrite-rich mineralization. Barite occurs as euhedral to subhedral bladed and tabular crystals. Many smaller crystals are more subhedral to anhedral. Grain size varies considerably throughout the sample with coarse-grained crystals occurring within open pore space, and along edges of the sample. Fine-grained crystals occur within the interior and along some exterior edges. These crystals are heavily overgrown by pyrite blebs and massive sphalerite. Coarse-grained barite is generally found within the chalcopyrite-rich zones, clearly grown on the edges of massive chalcopyrite within pore spaces. Secondary replacement of chalcopyrite by covellite is rare. Sphalerite is mostly massive, but also exhibits dendritic texture. Inclusions of galena are common in sphalerite. Minor chalcopyrite disease is observed in some massive sphalerite. Chalcopyrite is massive throughout. Pyrite is mostly found as massive or blebby grains, while also forming mineralized rings that preserve the form of vent organisms. Many of these forms are partially infilled by pyrite ± sphalerite and chalcopyrite. Pyrite also occurs as more subhedral to euhedral grains overgrowing chalcopyrite and sphalerite. A minor abundance of massive marcasite forms an exterior crust around fine-grained barite. Marcasite also appears to be intergrown with pyrite in some cases. Localized anhedral to subhedral grains of tetrahedrite-tennantite are found along the edges of massive chalcopyrite.

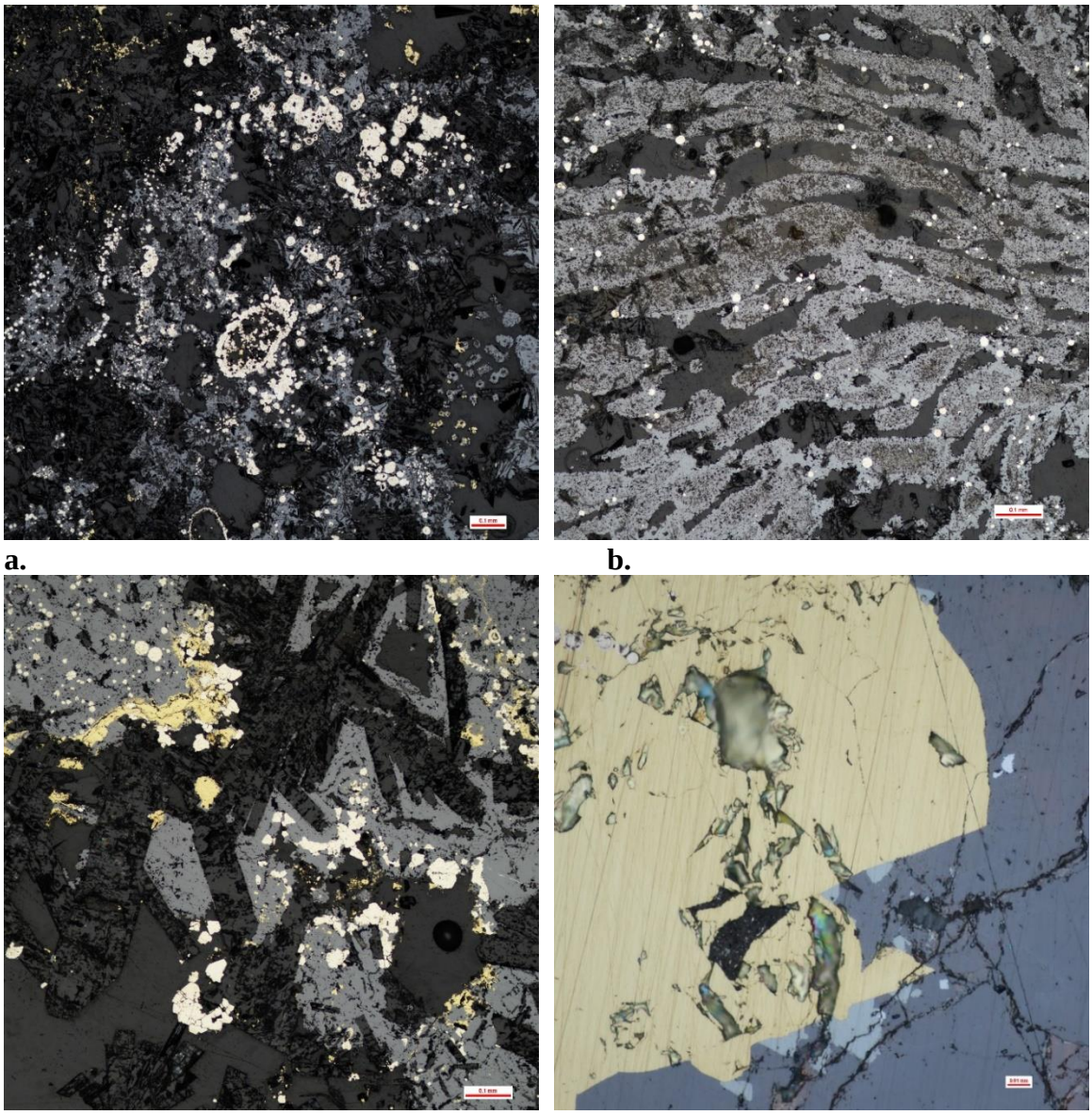

a. **b.**

c. **d.**

Photomicrographs of sample D1918-R7. All photos are taken under reflected light. a) Extensive fine-grained barite growth towards the sample exterior. Blebs and rings of pyrite are then overgrown by later sphalerite. Pyrite rings represent the mantling of the forms of vent organisms. b) Dendritic sphalerite is indicative of rapid quenching of hydrothermal fluids. Many of the stripes contain small inclusions of pyrite. c) Multiple stages of sulphide overgrowth on coarse-grained, euhedral bladed barite. Minor overgrowth of chalcopyrite is present, taking place before later barite. Late overgrowths of massive sphalerite and subsequent marcasite. d) Tiny grains of tetrahedrite-tennantite are sometimes found along the edges of chalcopyrite. Late sphalerite overgrowths contain minor, small inclusions of galena.

D1918 – R8:

Site Description

This sample is a piece of chimney wall, taken from the top of an active vent that slowly emitted a black smoke. This chimney is part of a tall chimney complex; one of the two chimney complexes described in the previous sample.

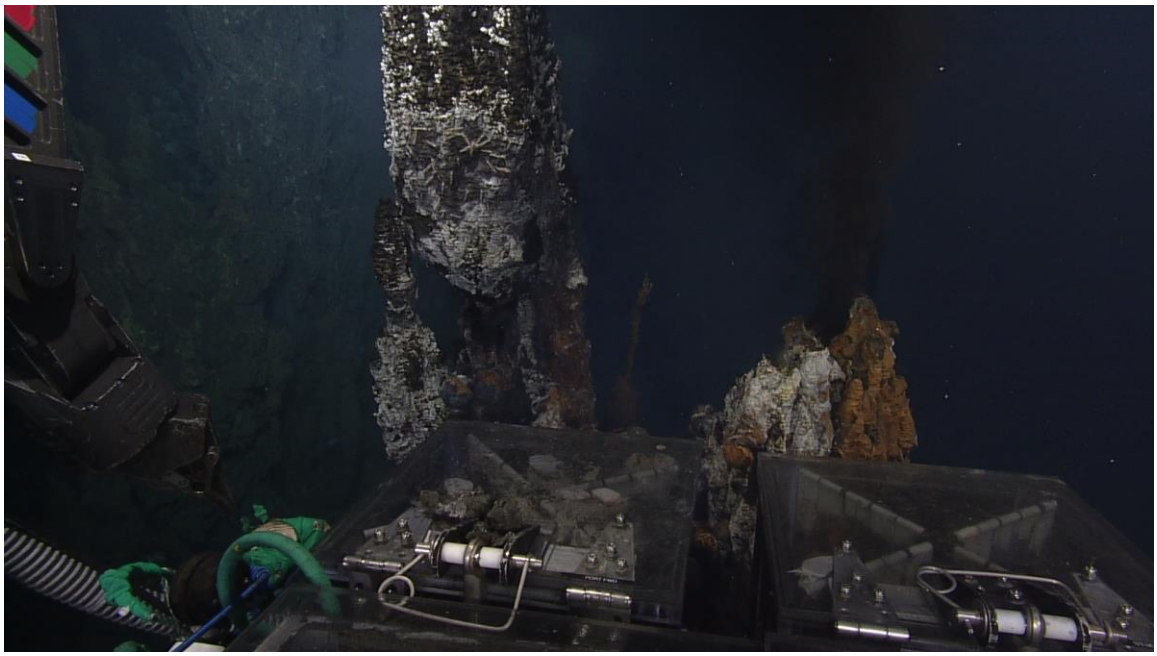

The tip of the black smoker chimney on the right-hand side was grabbed, D1918-R8.

Hand Sample Description

This sample contains a few small (≤ 2 cm wide) intact vents branching off from the exterior, one of which was actively venting before its extraction. Systematic mineral zoning of high-temperature to low-temperature mineral assemblages can be seen from interior to exterior. The innermost material is highly porous and dominated by fine-grained chalcopyrite. Coarser grained sulphides (≤ 1 mm) which coats the innermost fluid conduit. Towards the exterior the groundmass becomes dominated by barite and sphalerite with some pyrite ± marcasite and localized chalcopyrite. This is reflected by its light grey colour. The exterior surface is weathered orange-brown with some patches of white bacterial growth.

Hand sample for D1918-R8. Top left and right photographs show the vent exterior and interior, respectively. Bottom photograph shows a top-down view, highlighting the mineral zoning from interior to exterior.

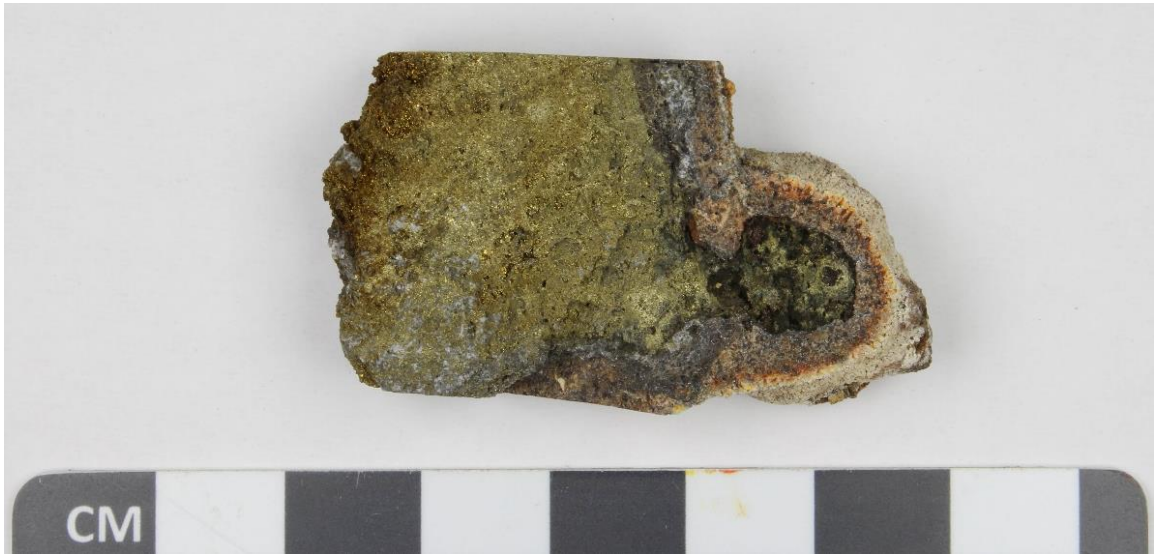

Thin section slab of D1918-R8. Thin section slab was cut from this face. The central vent interior makes up most of the sample (on the left). The vent exterior can be seen bordering much of the yellow-gold chalcopyrite-rich mineralization. The peripheral vent consists of the porous chalcopyrite-rich infill (on the right).

Mineral Abundances and Occurrences

Chalcopyrite – 53%

Barite – 20%

Sphalerite – 10%

Pyrite – 10%

Anhydrite – 5%

Marcasite – 2%

Tetrahedrite-Tennantite – < 1%

Galena – < 1%

The sample contains two separate parts: a dense chalcopyrite-dominated interior vent lining, and a barite-sphalerite-dominated chimney exterior. Massive chalcopyrite makes up most vent lining, but also contains anhydrite, small blebs of pyrite ± marcasite, and trace tetrahedrite-tennantite. Anhydrite is coarse-grained with bladed and tabular crystals and is only present in the chalcopyrite lining. Chalcopyrite growth within the small, infilled vent is associated with increased porosity and a greater variety of sulphide minerals. The abundance of sphalerite and pyrite is increased within the small, infilled vent. Sphalerite is massive and is found overgrowing pyrite and plumose barite. Plumose barite enclosed by these overgrowths appear to have been resorbed. Trace galena occurs as inclusions within sphalerite or as thin rims on overgrown pyrite, but also mantles some chalcopyrite in the small, infilled vent. Barite is only abundant in the chimney exterior, forming plumose texture with subsequent pyrite, sphalerite, and chalcopyrite overgrowths. Barite crystals are mostly euhedral to subhedral bladed crystals, with trace euhedral to subhedral tabular forms in the vent lining. Radiating acicular crystals are common towards the vent exterior and are overgrown by a massive marcasite crust ± pyrite. Massive sphalerite in the vent exterior appears the same as the overgrowth phase seen in the infilled vent. Towards the sample interior, sphalerite is increasingly replaced by chalcopyrite. In this transition zone, chalcopyrite disease in common in sphalerite, as well as alternating growth bands of chalcopyrite and sphalerite. Pyrite is mostly present as colloform masses and blebs, or as euhedral to subhedral grains found only in the vent lining. Localized anhedral to subhedral grains of tetrahedrite-tennantite are found with chalcopyrite. Minor replacement of chalcopyrite occurs along its edges.

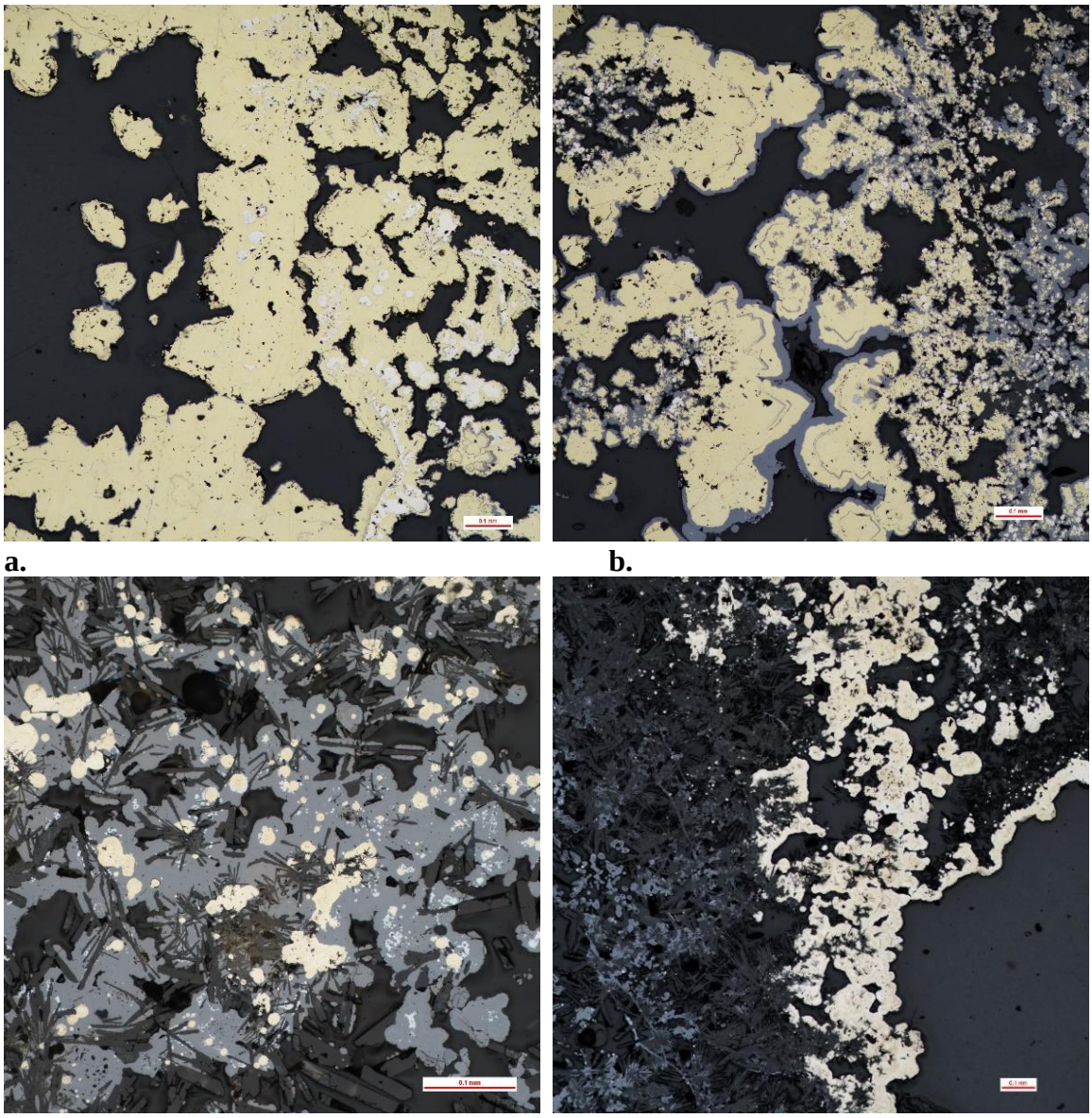

Photomicrographs of sample D1918-R8. All photos are taken under reflected light. a) Massive chalcopyrite with small, disseminated pyrite. This assemblage is characteristic of much of the central vent. b) Chalcopyrite replacing sphalerite along the boundary between the central vent interior and exterior. The abundance of sphalerite increases towards the exterior (right-hand side). Late-phase sphalerite mantles chalcopyrite, suggesting hydrothermal activity in the system may be waning. c) Bladed barite mantled by pyrite masses and blebs, which are subsequently overgrown by sphalerite. Galena is grown on the boundaries of the colloform masses and blebs, and as inclusions within sphalerite. Characteristic growth within the central and peripheral vent exterior. e) Massive colloform marcasite and pyrite crust locally forms along the barite-dominated exterior.

D1918 – R9:

Site Description

This sample is a piece of old, dead collapsed chimney material that appears at the base of a low-relief talus mound, perhaps on the edges of a larger sulphide chimney complex. There are no signs of chimney growth on the mound material within the immediate vicinity and may be restricted to the nearby chimney complex.

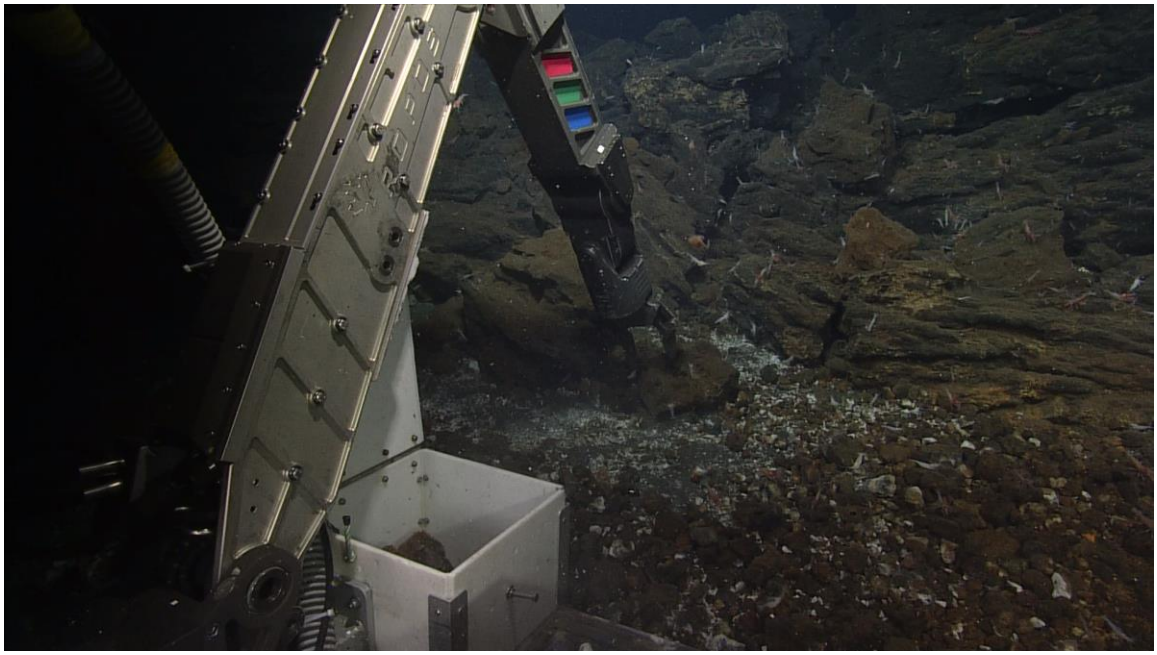

ROV ROPOS grabbing rock sample D1918-R9 from the base of a low-relief mound littered with dead sulphide chimneys.

Hand Sample Description

The interior of the sample is a brassy-yellow to light-grey groundmass composed of chalcopyrite, pyrite, and minor barite. It is generally very fine-grained and highly porous, with some possible localized vugs or small fluid conduits lined with coarser-grained (≤ 1 mm) chalcopyrite. The exterior surface has a heavily oxidized orange-brown appearance with multiple white patches, indicating chemosynthetic bacterial growth.

a. **b.**

Hand sample for D1918-R9. a) Shows the only visible fresh surface. b) Shows the weathered exterior.

Thin section slab for D1918-R9.

Mineral Abundances and Occurrences

Chalcopyrite – 65-70%

Pyrite – 25-30%

Barite – 5%

The sample is largely dominated by massive chalcopyrite, with varying porosity throughout the sample interior. Textures found in pyrite Small disseminated grains of pyrite form within chalcopyrite within the innermost part of the sample. Pyrite becomes more massive towards the sample exterior, but only where chalcopyrite still dominates. Most pyrite found in the interior is overgrown by chalcopyrite. Ovoid rings of pyrite are

common but lack sulphide mineral infill. Dendritic pyrite also forms within a small area towards the sample exterior, while the outermost region contains a thin oxidized pyrite crust. Here, pyrite is notably euhedral. Euhedral to subhedral bladed and tabular crystals of barite are the dominant mineral phase within the thin exterior layer. Crystal size varies slightly but is generally fine-grained. Some barite crystal masses are radiating. Only a trace of disseminated grains of chalcopyrite are found in the outer crust.

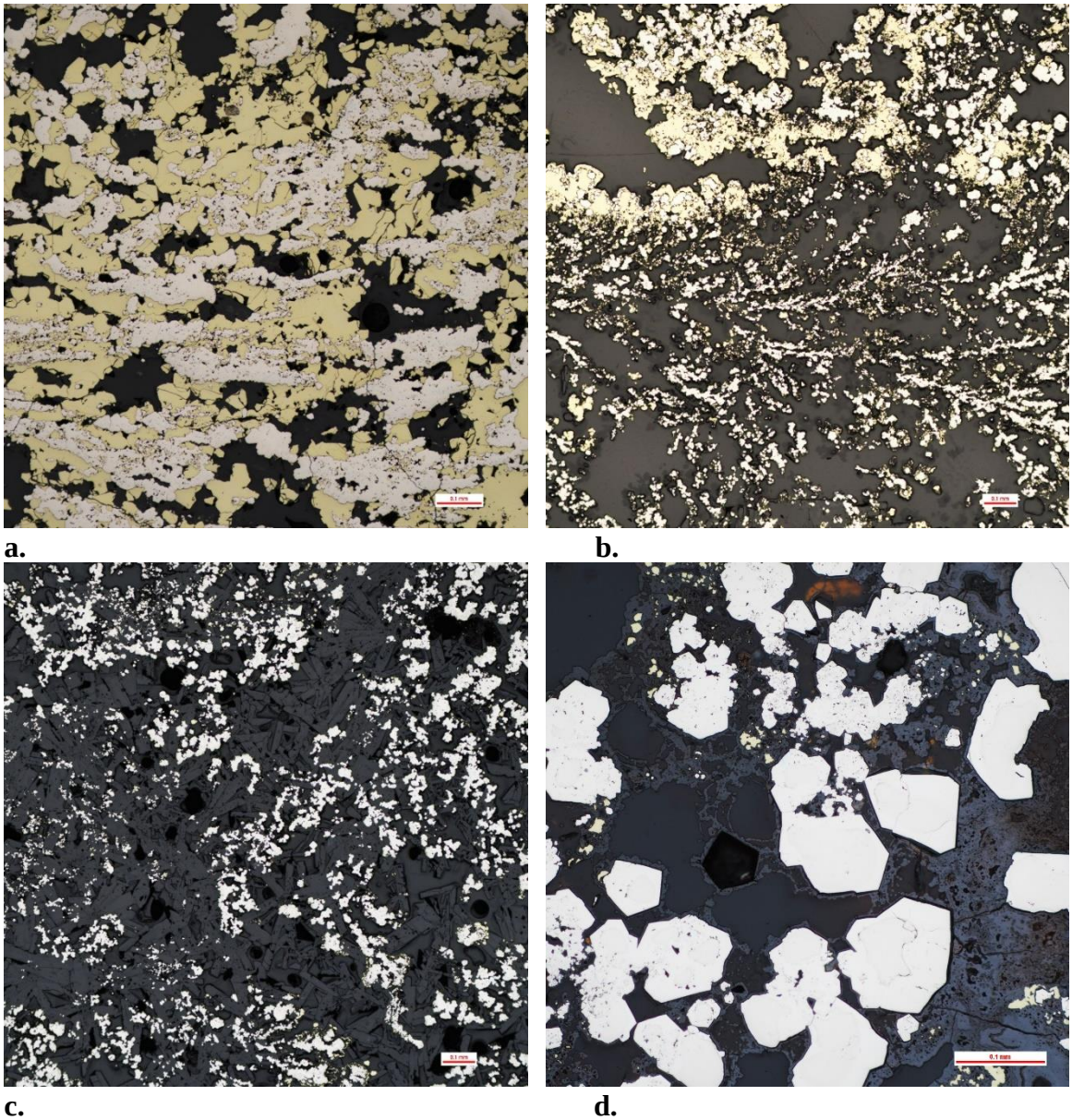

a. **b.**

c. **d.**

Photomicrographs of sample D1918-R9. All photos are taken under reflected light. a) Massive (almost dendritic) pyrite overgrown by massive chalcopyrite. b) Dendritic pyrite overgrown by chalcopyrite; texture is common near the sample exterior. c) Euhedral bladed barite with pyrite overgrowths. Barite is radially grown in some spots. d) Euhedral

pyrite crystals are locally abundant in the near exterior. Fe-oxides coat these crystals and form thin bands along the exterior edge of the sample.

D1918 – R10:

Site Description

This sample originates from an area of clear, diffuse venting and “shimmering water”. This is present a few metres away from a focused, black smoker chimney exhibiting boiling hydrothermal fluids. However, these vent pathways may originate from the same source, as both sites are proximal to one another and may exist on the same mound structure. The sample itself is a piece of inactive sulphide, which constitutes the remains of a collapsed chimney. From the dive video, it is unclear exactly where the site lies relative to the nearby talus slope and chimney complex.

Top: Oblique view above the surrounding area where D1918-10 was collected. The bed of white snails beside the thin, white tube worms on the right side is where the sample is collected. Bottom: ROV ROPOS grabbing the sample.

Hand Sample Description

The sample is a small piece of sulphide material that mostly exhibits a low-temperature mineral assemblage. The grey groundmass is quite porous, composed largely of

marcasite, pyrite, sphalerite, barite, and some chalcopyrite. The exterior has an orange-brown colour and contains white patches of bacterial growth.

Hand sample for D1918-R10. Top photograph shows the weathered exterior surface. Bottom photograph shows a partial fresh surface.

Thin section slab of D1918-R10. Thin section was cut from this face.

Mineral Abundances and Occurrences

Marcasite – 25%

Pyrite – 20%

Sphalerite – 20%

Barite – 20%

Chalcopyrite – 13%

Galena – 2%

The sample is characterized by a near equal distribution of marcasite, pyrite, barite, and sphalerite ± galena. Barite occurs mostly as euhedral to subhedral bladed crystals with some euhedral tabular crystals subsequently overgrown by pyrite, marcasite, and massive sphalerite. Fine-grained acicular barite tends to occur closer to the exterior weathered surface, while larger crystals occur within open pore spaces with no subsequent overgrowth of sulphides. Complex and varied growth of pyrite suggests that there may be at least three generations of growth. The first appears as small circular blebs and colloform masses overgrown by massive sphalerite, the second as euhedral to subhedral grains within chalcopyrite, and thirdly as massive pyrite intergrown with marcasite. Mineralized ovoid rings of pyrite are also common throughout and sphalerite often coats many of these forms with a later mantling of coarse-grained barite. Chalcopyrite envelops euhedral to subhedral grains of pyrite but is also being mantled by massive pyrite and marcasite. Massive sphalerite is sometimes intergrown with chalcopyrite but is most commonly found as overgrowths of all other sulphide minerals. Where sphalerite growth is most abundant, minor galena also occurs as inclusions or intergrowths with sphalerite.

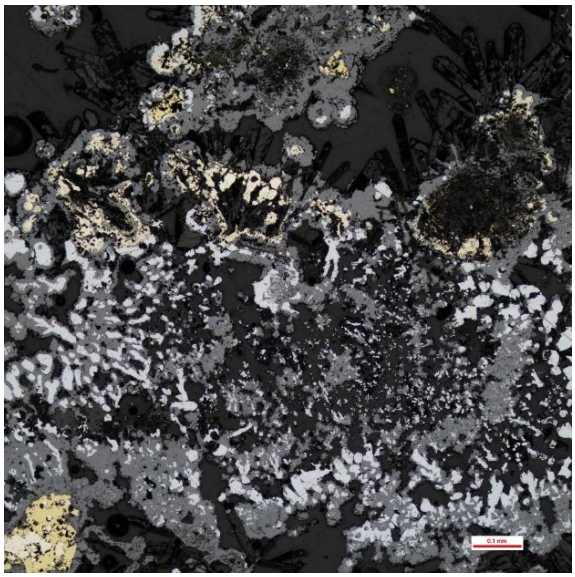

a.

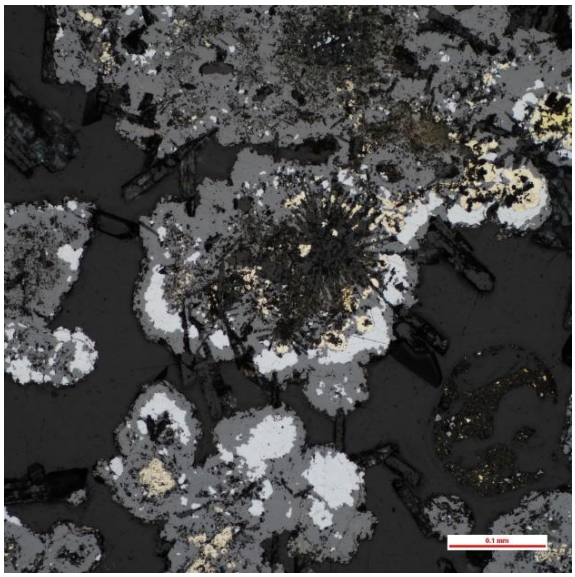

b.

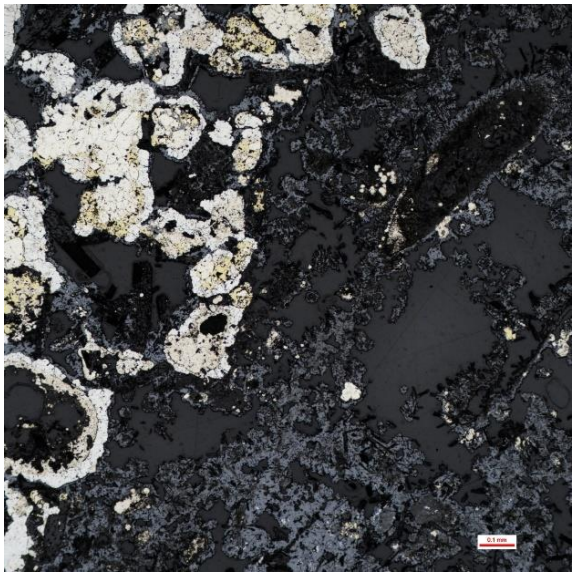

c.

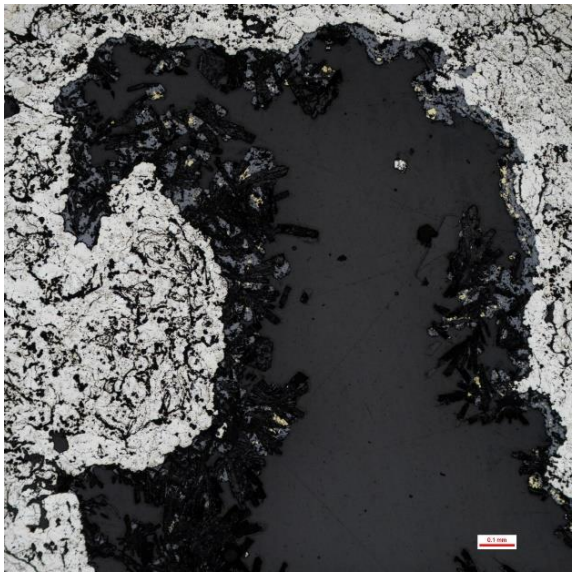

d.

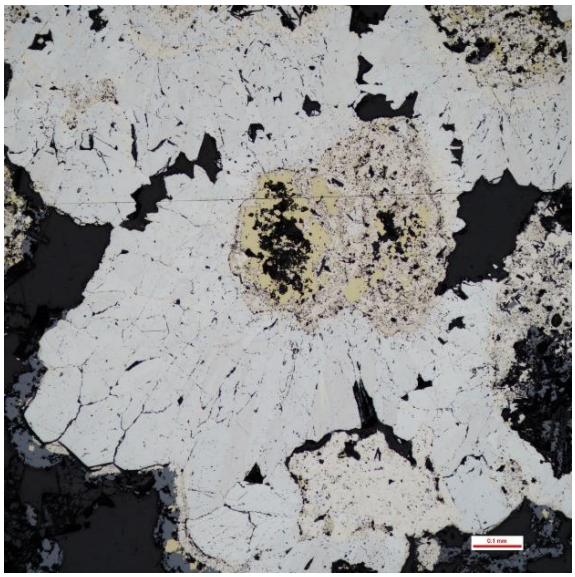
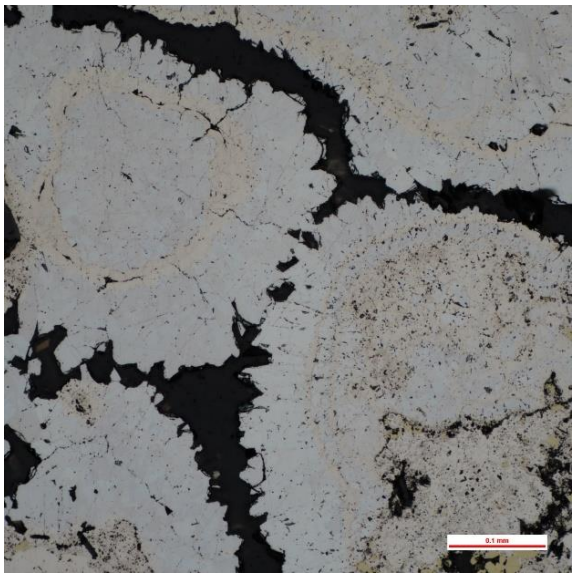

e. **f.**

Photomicrographs of sample D1918-R10. All photos are taken under reflected light. a) Typical mineral associations of the sphalerite-rich zone. Massive sphalerite is seen overgrowing pyrite, chalcopyrite, and early-stage barite. Local galena occurs as inclusions or intergrowths with sphalerite. Late, coarse-grained barite is found growing on the boundaries of massive sphalerite in porous void spaces. b) Early barite mantled by pyrite blebs with subsequent overgrowth of sphalerite and galena. Late barite is present within pore spaces. c) Defined boundary between the sphalerite-rich zone and massive pyrite-marcasite zone. A slightly ovoid sphalerite ring has formed (top-right), similarly to those mineralized by pyrite. d) Open pore spaces within the massive pyrite-marcasite zone are often lined with coarse bladed barite crystals, with subsequent overgrowth of sphalerite and chalcopyrite. e) Early-stage pyrite and chalcopyrite are massively overgrown by marcasite. Distinct crystals can often be observed in the marcasite. Late-stage sphalerite, chalcopyrite, and barite can be observed, similar as the previous image. f) Growth stages between pyrite (yellowish) and marcasite (white) are clearly defined. An alternating growth of both minerals is common in this zone.

D1918 – R11:

Site Description

This sample was collected at the base of a tall, inactive chimney complex wall. It is immediately next to a neighbouring chimney complex exhibiting diffuse, clear hydrothermal fluid flow. From the dive video, the chimney complexes appear to be located on the top of a large sulphide mound.

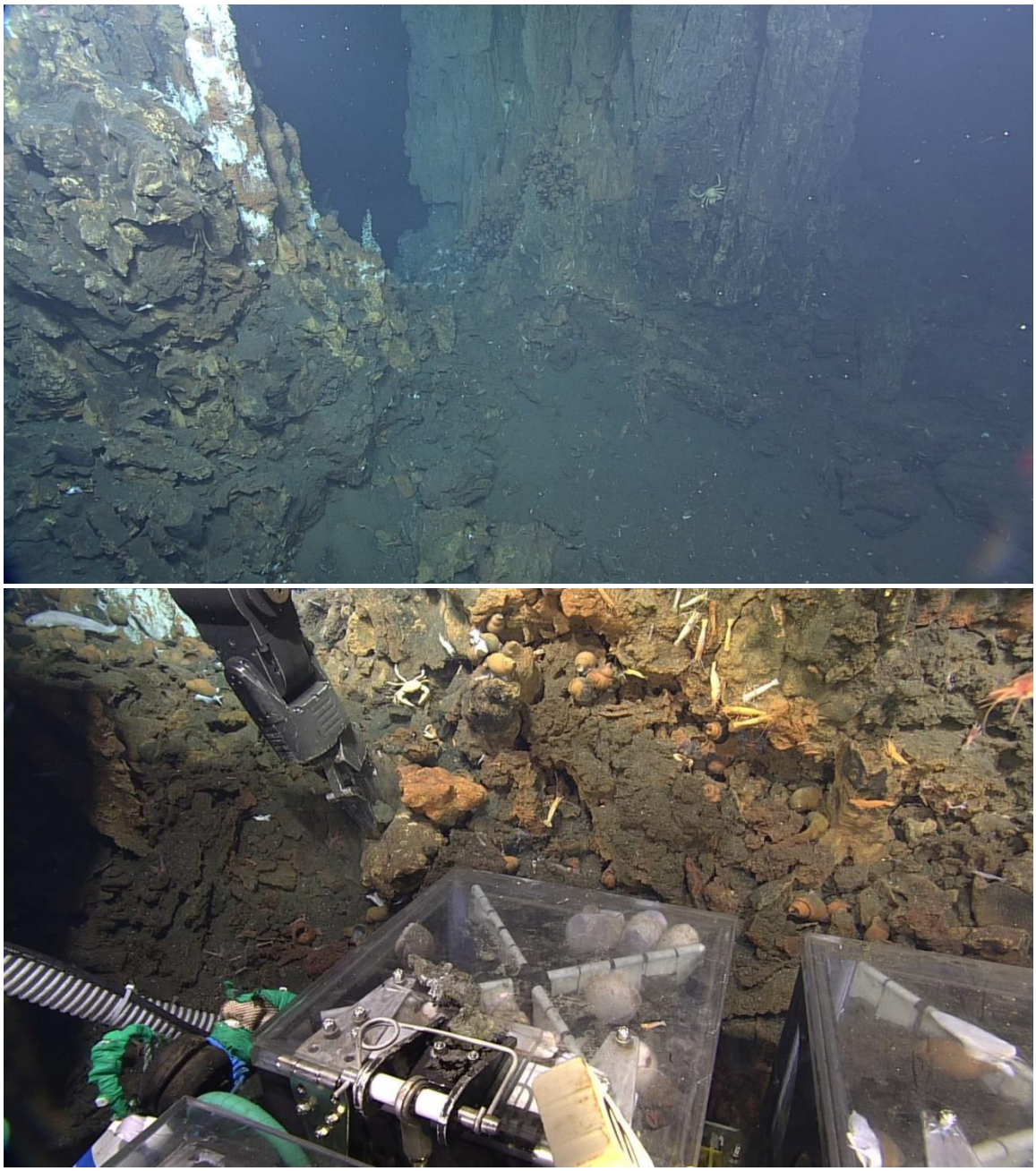

Top: Two large chimney complexes that sit atop a large sulphide mound where D1918-R11 was collected. Bottom: ROV ROPOS grabbing a piece of sulphide talus (D1918-R11).

Hand Sample Description

The sample is a small piece of sulphide material which has preserved some unique mineralization. The groundmass in general is very porous and has a dark-grey to yellow-gold colouration, indicating localized chalcopyrite-rich mineralization intermixed with

sphalerite and barite. Some of the porous chalcopyrite-rich mineralization has an iridescent “peacock” appearance, and contains localized coatings of dull, green atacamite. The exterior of the sample is a weathered and oxidized orange-brown. Porosity ~ 30 – 40%.

a.

b.

Hand sample of D1918-R11. a) Fresh surface. Traces of green atacamite can be seen on this surface. b) Weathered exterior.

Thin section slab for D1918-R11. Thin section was cut from this face. “Peacock” iridescence is clearly visible in the chalcopyrite-rich zone.

Mineral Abundances and Occurrences

Chalcopyrite – 58%

Barite – 30%

Pyrite – 10%

Sphalerite – 2%

Tetrahedrite-Tennantite – < 1%

Massive chalcopyrite dominates the interior of the sample with abundant barite. Fine-grained euhedral to subhedral crystals of barite are observed mostly in plumose texture near the exterior. Euhedral to subhedral bladed and tabular crystals of barite are also found in clustered veins within the chalcopyrite-dominated interior and appear to represent a later stage of growth. Small pyrite blebs and massive colloform pyrite commonly mantles plumose barite. Late subhedral pyrite also forms in localized porous spaces. Minor pyrite forms ovoid rings. Chalcopyrite is most commonly observed as massive overgrowths of earlier plumose barite and pyrite within the interior. These overgrowths transition to become more sphalerite dominated towards the exterior. In this transitional zone, chalcopyrite and dendritic sphalerite are commonly intergrown. Thin bands of late sphalerite are also seen rimming massive chalcopyrite and coarse-grained barite within the interior. Traces of tetrahedrite-tennantite are observed as intergrowths with chalcopyrite towards the exterior region of the sample. Euhedral grains are also present on the edges of massive chalcopyrite, coarse-grained barite, and as inclusions in sphalerite.

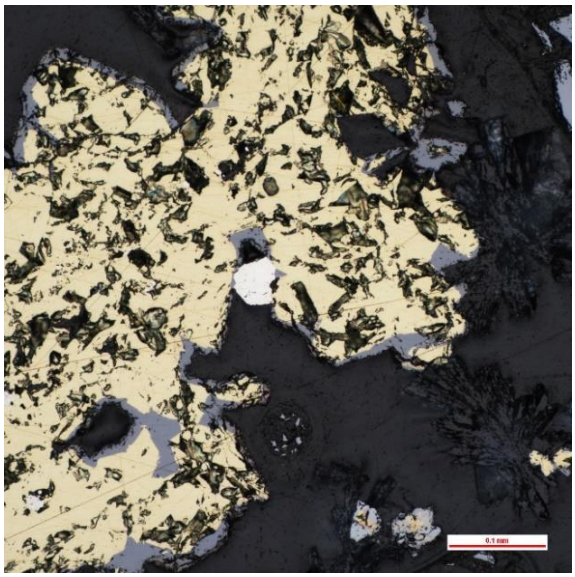

a.

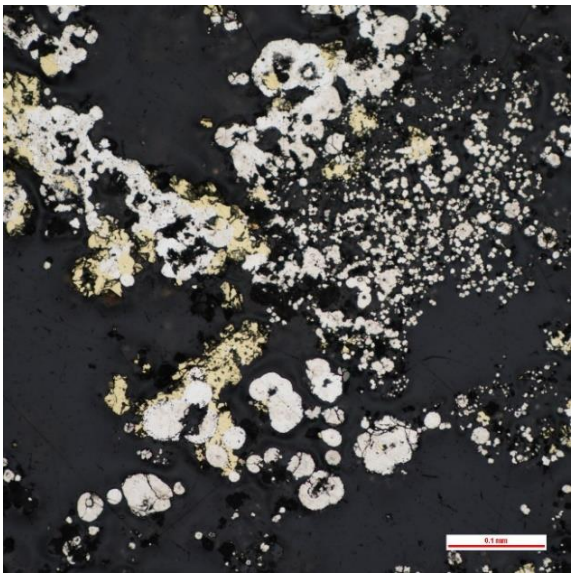

b.

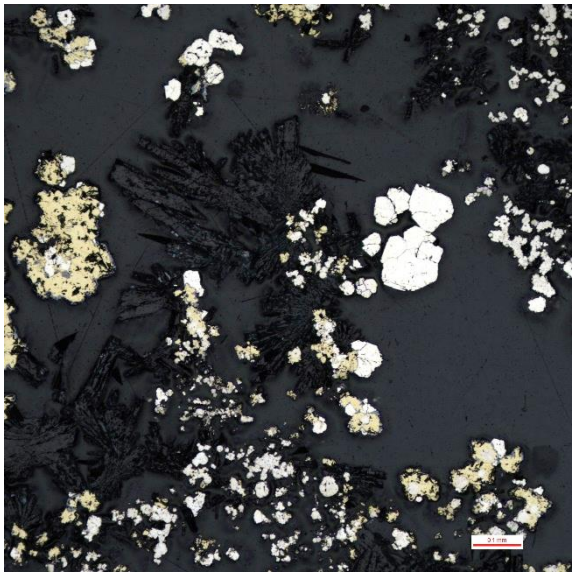

c.

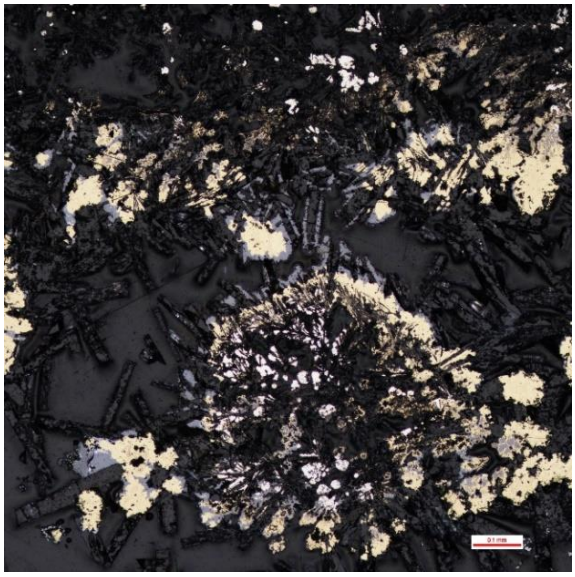

d.

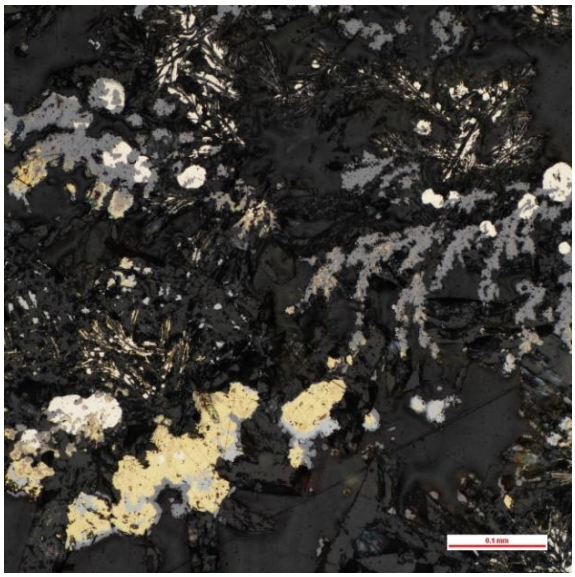

e.

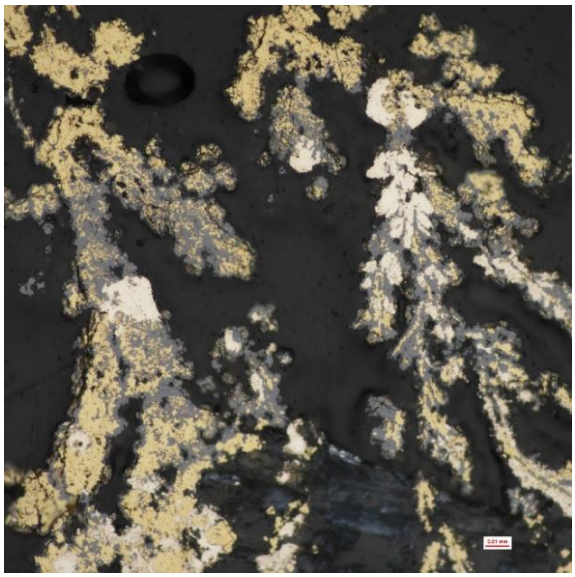

f.

Photomicrographs of sample D1918-R11. All photos are taken under reflected light. a) Massive chalcopyrite with late-stage overgrowth of sphalerite, barite, and subhedral pyrite. Tetrahedrite-tennantite (bottom-right) appears to occur after chalcopyrite also serving as a replacement mineral. b) Minor chalcopyrite overgrowth of massive and colloform pyrite. c) Late sphalerite, subhedral pyrite, and barite form on the edges of massive chalcopyrite grains and early pyrite. d) Localized growth of sulphides exhibits sequential mineral zoning. Pyrite blebs mantle fine-grained barite, with later chalcopyrite overgrowths. An assumed intermediary growth event of sphalerite is largely overprinted by replacement and growth of chalcopyrite. Coarse-grained barite and subsequent overgrowth of sphalerite and minor galena in the central pore space represents late-stage mineralization. e) Mixed sulphide groundmass dominated by fine-grained barite, dendritic sphalerite, and some blebby pyrite. Chalcopyrite is intergrown with tetrahedrite-tennantite and mantled by late sphalerite. f) Dendritic sphalerite that has been largely replaced by chalcopyrite. It may instead represent a relict plumose texture. The primary growths of bladed barite appear to have been psuedomorphed by sphalerite and the initial mantles of pyrite are still intact.

D1918 – R12:

Site Description

This sample was accidentally scooped-up while collecting white snails on the steep-slope on the inactive chimney complex described in D1918-R7. This sample was obtained shortly before D1918-R7 but was not initially identified and logged as a rock sample.

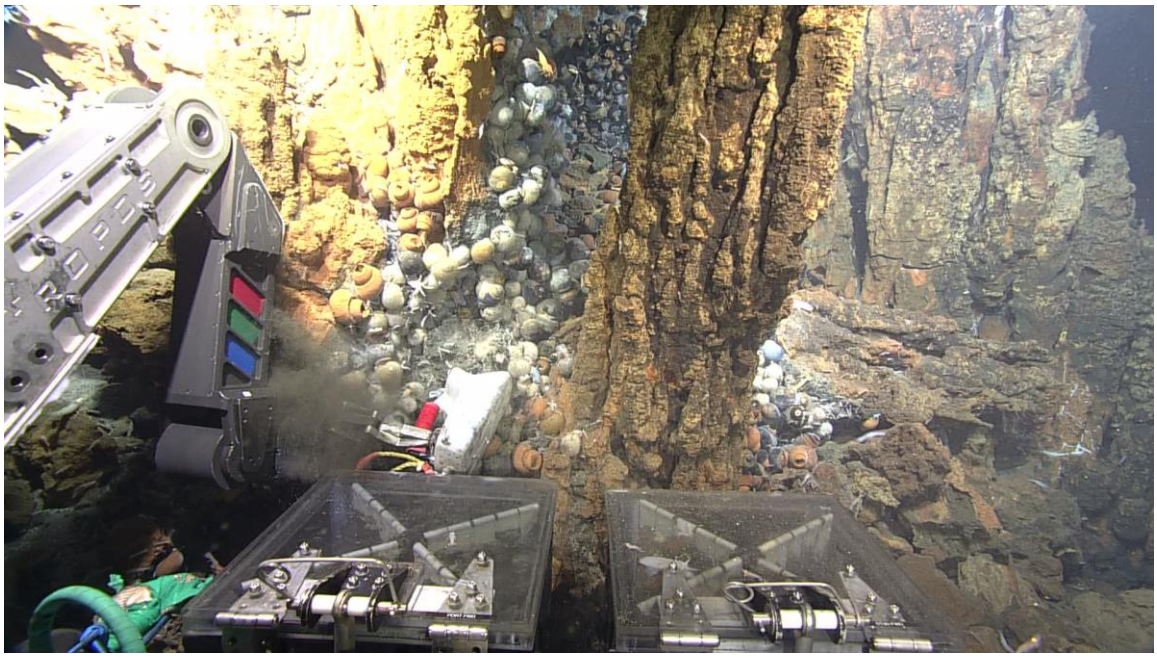

Sample D1918-R12 was inadvertently collected during a scoop sampling of white snails on the walls of an active chimney complex.

Hand Sample Description

The sample is composed of a variably porous groundmass consisting of several zones of mineralization. The highly porous grey-black portion of the sample is dominated by sphalerite and pyrite. Lighter grey sections likely reflect the same mineralization, but with an increased abundance of barite, but are more porous. The porous yellow-white regions of the groundmass are dominated by chalcopyrite with barite, and some sphalerite and pyrite. Uniquely, the sample does not contain any weathered or oxidized surfaces. Porosity ~ 40 – 50%.

Hand sample for D1918-R12.

Thin section slab for D1918-R12. Thin section slab was cut from this face.

Mineral Abundances and Occurrences

Barite – 40%

Sphalerite – 30%

Chalcopyrite – 15%

Pyrite – 10%

Marcasite – 5%

Galena – < 1%

Covellite – << 1%

Barite is mostly found as fine-grained, euhedral bladed crystals that are often radiating. Acicular barite is present as well. Slightly larger crystals are grown within more porous space and represent a separate stage of growth. These crystals possess little sulphide overgrowth. Pyrite occurs as masses and blebs (rarely exhibit colloform texture) that sometimes grow on the edges of fine-grained barite. Massive overgrowths of earlier pyrite blebs also occur with marcasite. Slightly subhedral grains of massive marcasite are also intimately associated with massive pyrite. The association of pyrite and marcasite together appears to be random, however it is possible that marcasite is also being recrystallized into pyrite. Ovoid pyrite rings are present and contain little internal mineral growth (aside from minor barite and chalcopyrite), but abundant sphalerite overgrowth. Massive sphalerite overgrowths of barite, pyrite, and marcasite are common throughout the sample. Dendritic texture is observed in some interior massive sphalerite, where little sulphides or barite are enveloped. Most of the cores of this sphalerite appears to be relatively unaltered by oxidation. Thin layers of galena surround cores that appear to be more deteriorated. Minor galena is contained within some massive sphalerite and appears along the edges of the same grains. Chalcopyrite is restricted to one region, where it is the dominant mineral and may have replaced sphalerite. It occurs as localized, massive overgrowths of barite, pyrite, and some residual sphalerite. Select massive chalcopyrite grains have sphalerite and galena occurring along their grain edges, as well as penetrating into the crystals. Some pyrite and marcasite are also found to overgrow and mantle chalcopyrite. Traces of covellite appear as a replacement of chalcopyrite. Unique elongated euhedral crystals are contained within a small pyrite ring.

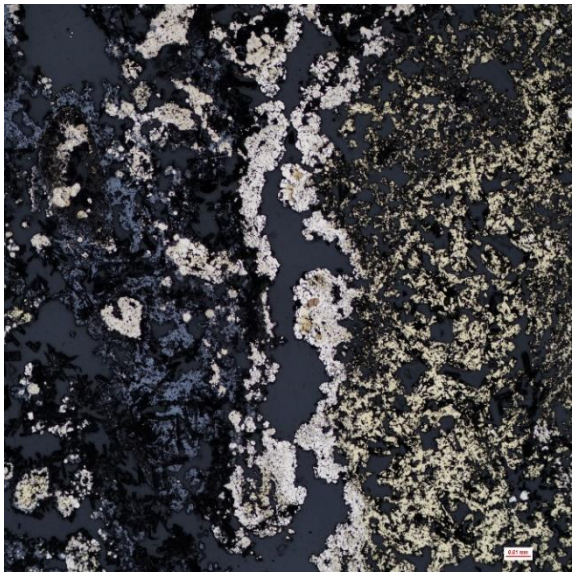

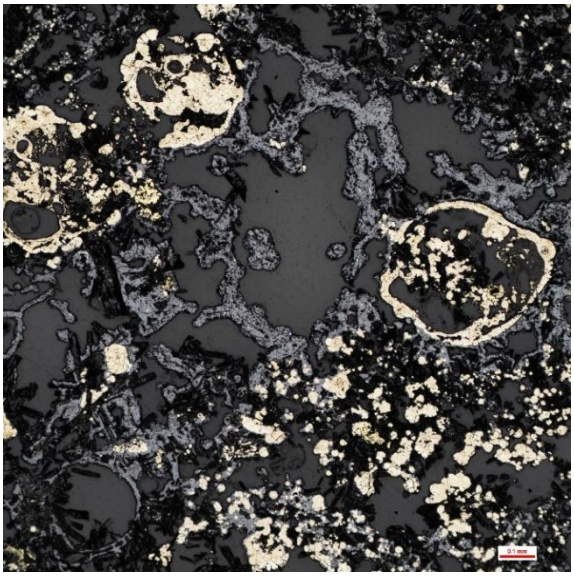

a. **b.**

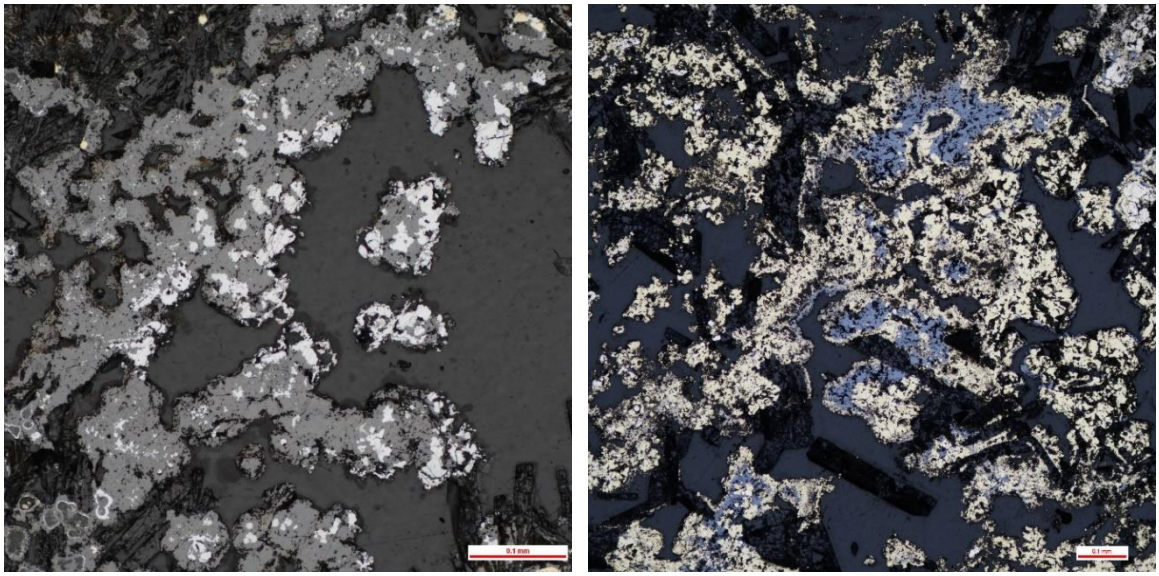

c. **d.**

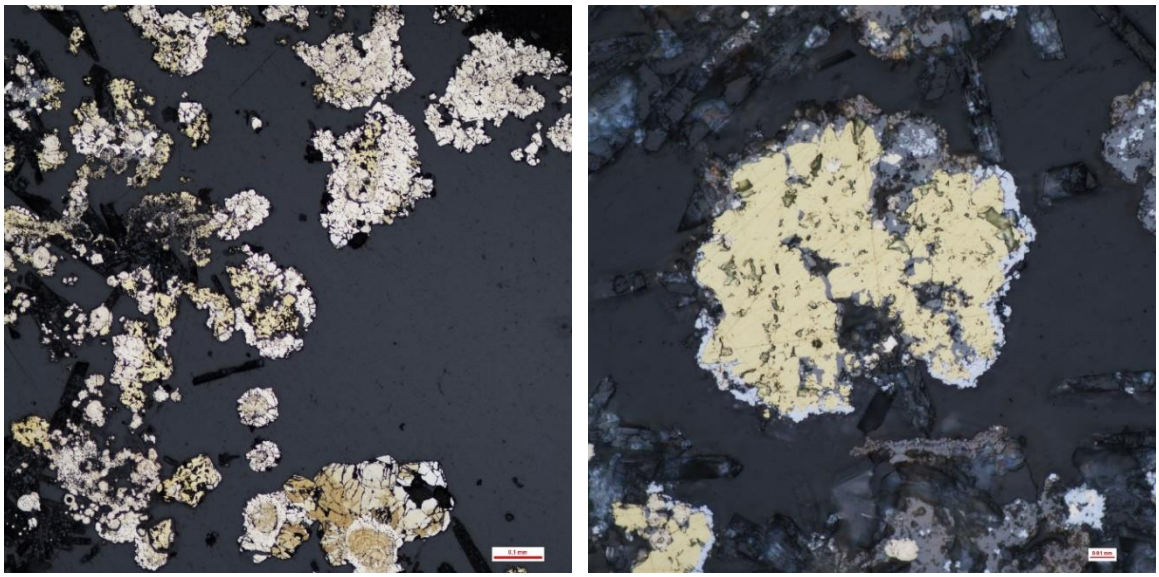

e. **f.**

Photomicrographs of sample D1918-R12. All photos are taken under reflected light. a) Distinct mineral zoning of sphalerite- and barite-rich (left) and chalcopyrite-rich (right) mineralization. Pyrite and marcasite are present in both zones and locally separate the zones as a large vug within pore space. b) Pyrite masses and mineralized rings are common within the sphalerite- and barite-rich zone. c) Intergrowths of sphalerite and galena. d) Replacement of sphalerite in the chalcopyrite-rich zone. Very little remnant sphalerite exists within this zone. e) Multiple generations of pyrite and marcasite growth. Both minerals are seen overgrowing chalcopyrite as well. f) Late mantling of sphalerite and galena on grains of chalcopyrite.

D1918 – R13:

Site Description

This sample was accidentally scooped-up while collecting orange snails on a chimney wall of the inactive chimney complex described in D1918-R7. Like the previous sample, it was later identified and logged as a rock sample. The three samples: D1918-R7, D1918-R12, and D1918-R13 are all virtually from the same location.

Like the previous sample, D1918-R13 was also unintentionally collected during a scoop sampling of orange snails. The sulphide sample originates from the heavily oxidized chimney wall.

Hand Sample Description

The sample is a thin piece of an inactive, heavily oxidized chimney wall. The interior of the sample shows a fresh, highly porous dark grey-black groundmass, with few visible grains. It is primarily composed of barite, sphalerite, and pyrite, with some yellow chalcopyrite-rich areas. Light grey regions indicate an increased presence of barite. The exterior is intensely oxidized and exhibits a distinct deep-orange colouration. Porosity ~ 40 – 50%.

Hand samples for D1918-R13. Photograph showing fresh surface for one hand sample and the weathered surface for another. The respective surfaces are near identical for both pieces.

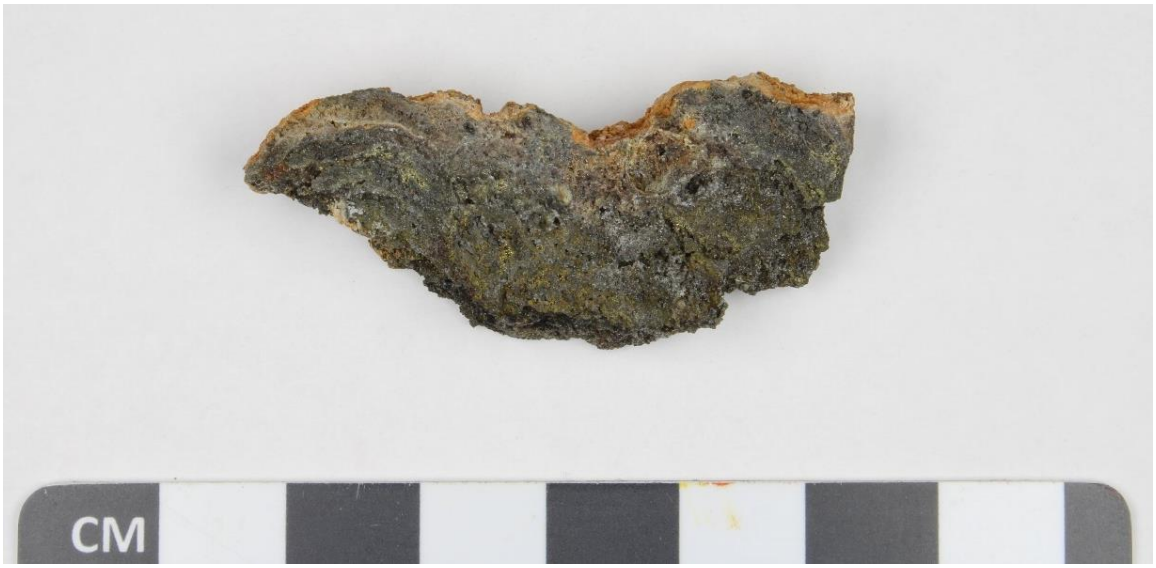

Thin section slab for D1918-R13. Thin section was cut from this face.

Mineral Abundances and Occurrences

Barite – 55%

Sphalerite – 20%

Chalcopyrite – 15%

Pyrite – 8%

Marcasite – 2%

Tetrahedrite - Tennantite – < 1%

Galena – < 1%

Covellite – << 1%

This sample is a great example of a very steep thermal gradient across an exterior chimney wall. There are clearly defined boundaries between chalcopyrite dominant regions within the interior, to intergrown chalcopyrite and sphalerite in the central zone, to a barite and sphalerite-dominated exterior (where there is no chalcopyrite present). Euhedral to subhedral bladed and tabular crystals of barite are mostly found within the central region of the sample, many of which are overgrown by various sulphide minerals. Plumose texture is the predominant occurrence of these crystal forms, whereas euhedral to subhedral radiating acicular crystals are found exclusively in the sample exterior. Coarse-grained late-stage barite growth can sometimes be found within open pore spaces in the sample interior, grown on the edges of massive chalcopyrite. Like barite and chalcopyrite, the localized abundance of sphalerite differs considerably throughout the sample. It is absent in the outermost barite-dominated zone, it dominates the central zone of the sample, and is extensively replaced in the innermost chalcopyrite-rich zone. Where it is most abundant, massive sphalerite forms around barite and pyrite ± marcasite in plumose texture and also forms dendritic texture. Traces amounts of galena are found as small irregular inclusions within massive sphalerite, and in some instances is also seen mantling sphalerite. Within the sample interior, massive chalcopyrite has overgrown and potentially replaced much of the previous sphalerite. Although some sphalerite is seen mantling chalcopyrite along interior vent linings. Pyrite is highly varied in this sample: (1) massive in colloform and semi-mineralized rings with marcasite, (2) as disseminated euhedral to subhedral crystals, and (3) as disseminated, rounded to sub-rounded blebs that exhibit colloform and framboidal texture. Pyrite blebs are commonly found growing on the edges of plumose barite or enclosed within dendritic sphalerite. More euhedral forms are present as intergrowths with chalcopyrite or contained within. Occasionally small euhedral to subhedral pyrite is grown on the edges of massive chalcopyrite. Marcasite typically forms within the colloform bleb interiors and is intergrown with pyrite in the sample interior. Disseminated anhedral to subhedral grains of tetrahedrite-tennantite occur intimately with chalcopyrite in trace abundances. Covellite only appears as trace replacement of chalcopyrite towards the sample exterior. It has a unique occurrence as relatively large crystals within a small pyrite ring. It is commonly found with sphalerite as well.

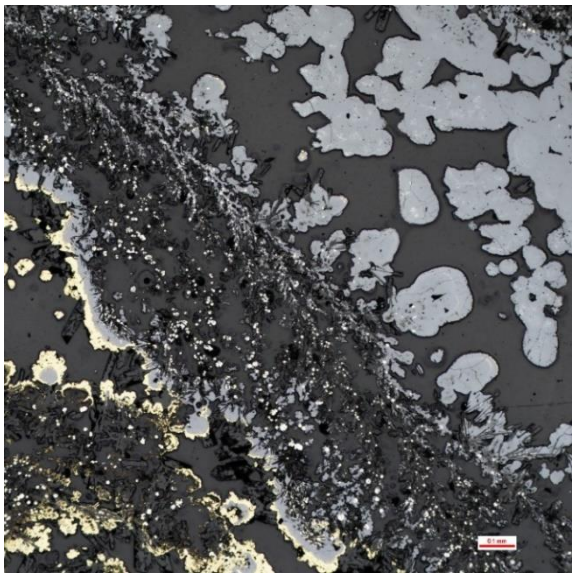

a.

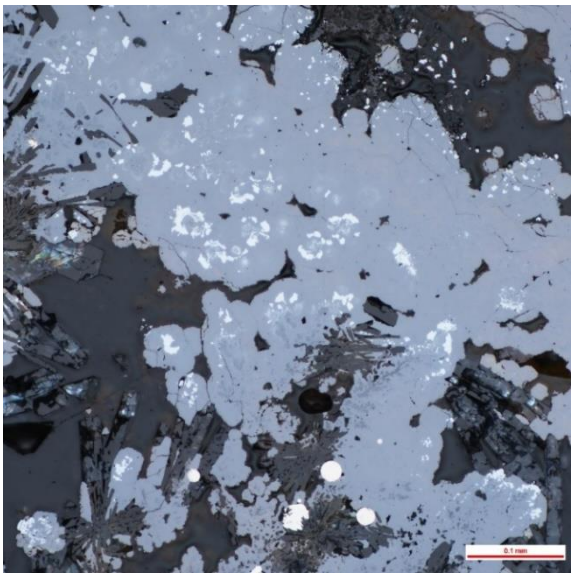

b.

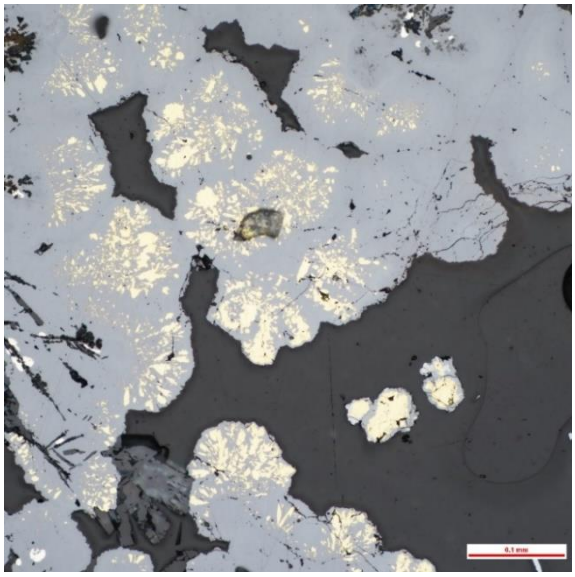

c.

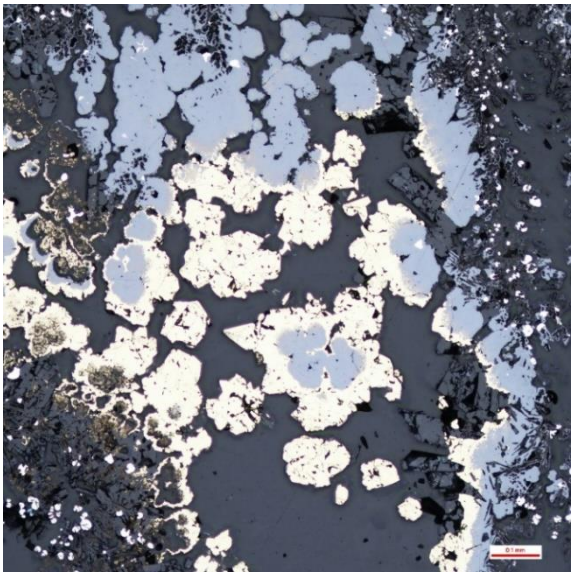

d.

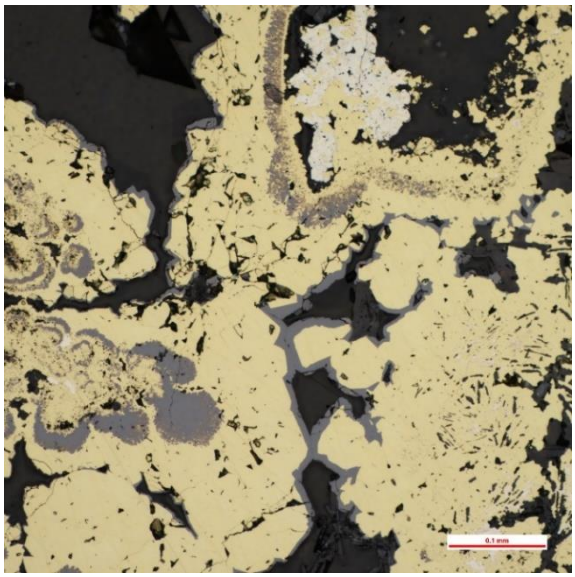

e.

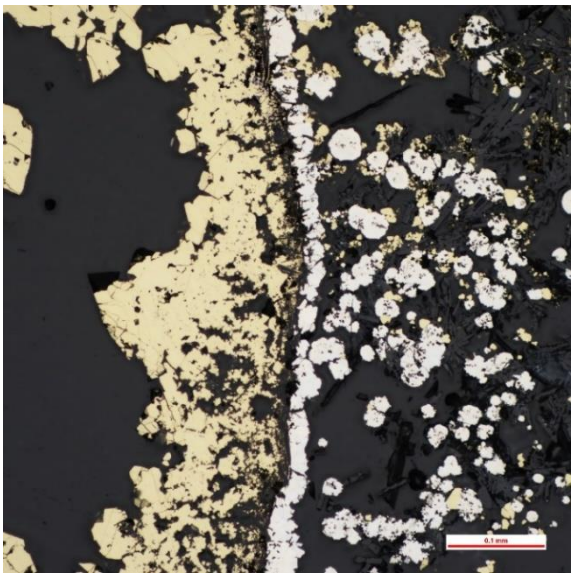

f.

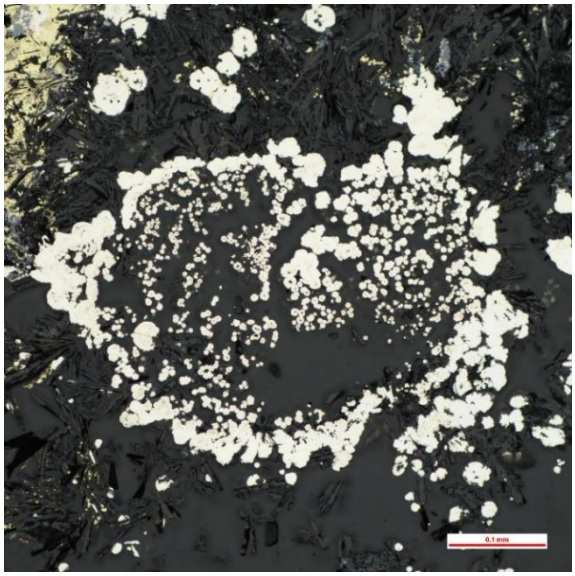

g.

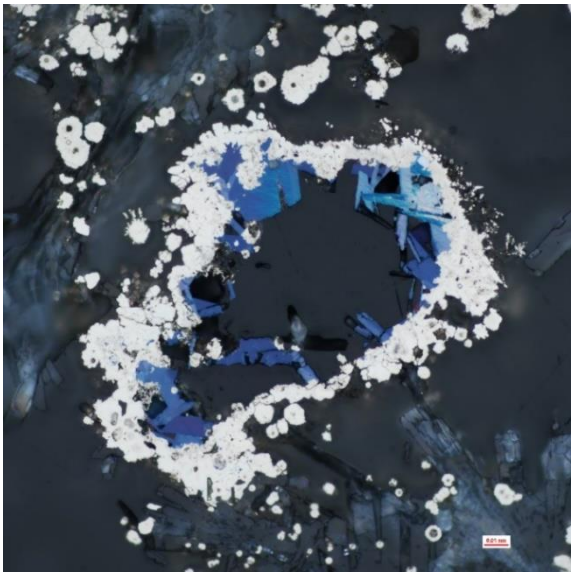

h.

Photomicrographs of sample D1918-R13. All photos are taken under reflected light. a) Distinct transition from large, massive sphalerite to plumose barite overgrown by massive sphalerite. Two common forms of sphalerite are seen within the interior. Chalcopyrite replaces sphalerite in minor abundance towards the chimney interior. b) Near-exterior massive sphalerite contains irregular inclusions of galena. c) Patchy chalcopyrite disease in sphalerite. d) Higher degree of sphalerite replacement by chalcopyrite, occurs closer to the interior, particularly in pore spaces. Late-stage coarse barite sometimes forms along the walls of void space. e) The majority of sphalerite has been replaced in the innermost sulphide groundmass. Late-stage sphalerite mantles the edges of some chalcopyrite. f) Thick layer of chalcopyrite lines a thin wall of pyrite ± marcasite. g) Slightly ovoid pyrite

± marcasite ring enclosing tiny semi-framboidal pyrite. h) Slightly ovoid pyrite ± marcasite ring containing euhedral covellite along the inner walls.

D1919 – R1:

Site Description

This sample was located at the base of a small sulphide chimney complex and is the remains of the base of a small inactive spire. The chimney complex has three main spires with diffuse-flowing white smoke at its top, and diffuse low-temperature hydrothermal flow out of small beehive structures along the trunk walls. It is also immediately adjacent to a similar featured, but much taller chimney complex, which is positioned next to a steep talus slope.

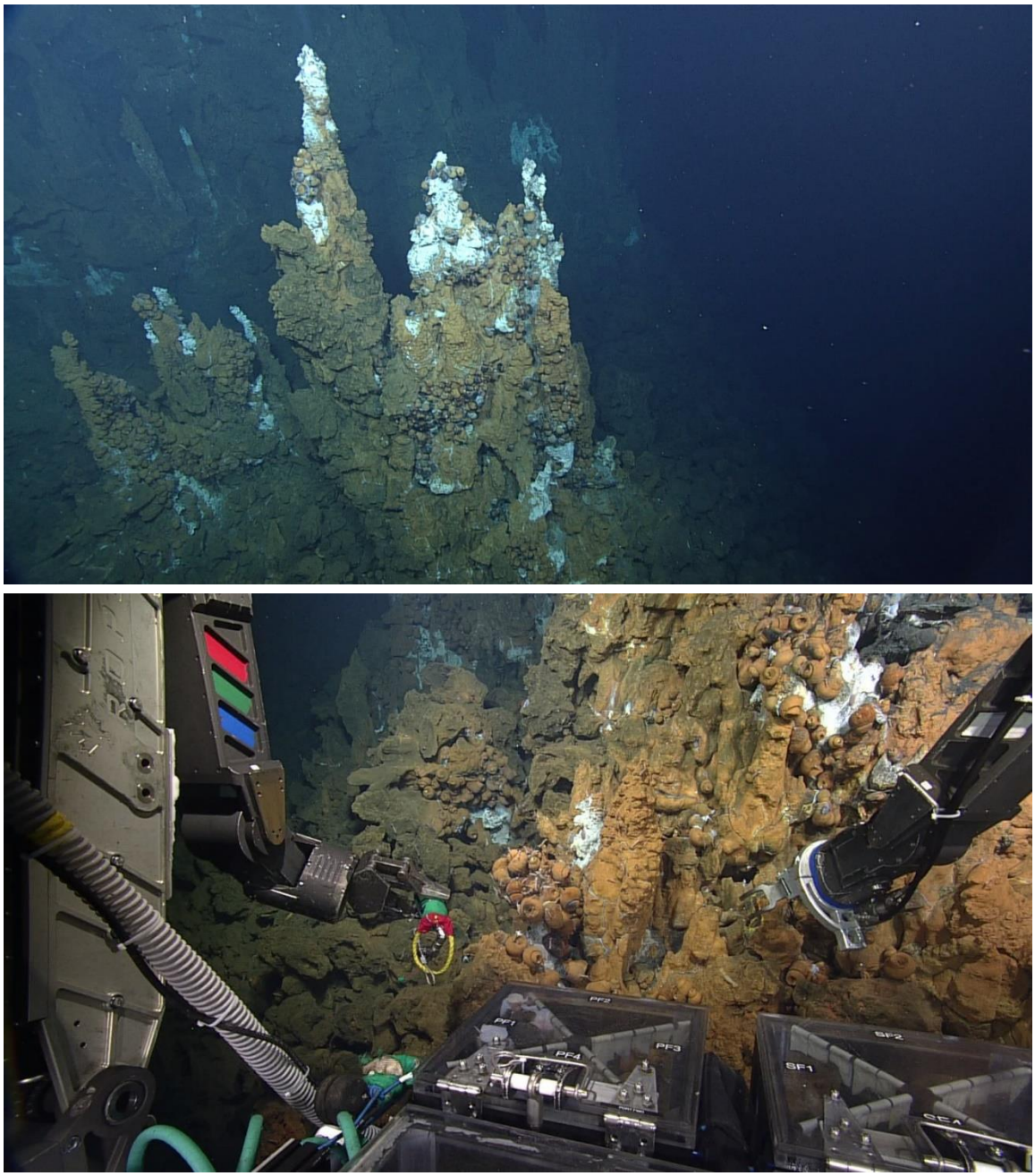

Top photograph shows the small active white smoker chimney complex where D1919-R1 was collected. Bottom photograph shows the exact location where the small inactive chimney piece was grabbed.

Hand Sample Description

The fine-grained interior groundmass is primarily dark-grey, moderately porous, and composed of barite and sphalerite with minor pyrite. This sample also has some thin interior coatings of what looks like orpiment or realgar. This appears to have formed

towards the exterior and is identified by a range of colouration from yellow to an intense orange and deep red. The sample exterior contains a thick, red-orange iron-oxide coating. Porosity = 50% (1st growth zone); 60% (2nd growth zone).

a. **b.**

Hand sample for D1919-R1. Left photograph shows a partial fresh surface and weathered surface which covers the remainder of the rock sample. Right photograph is a slice through the sample interior, showing distinct growth zones. The thin section slab was cut from this slice.

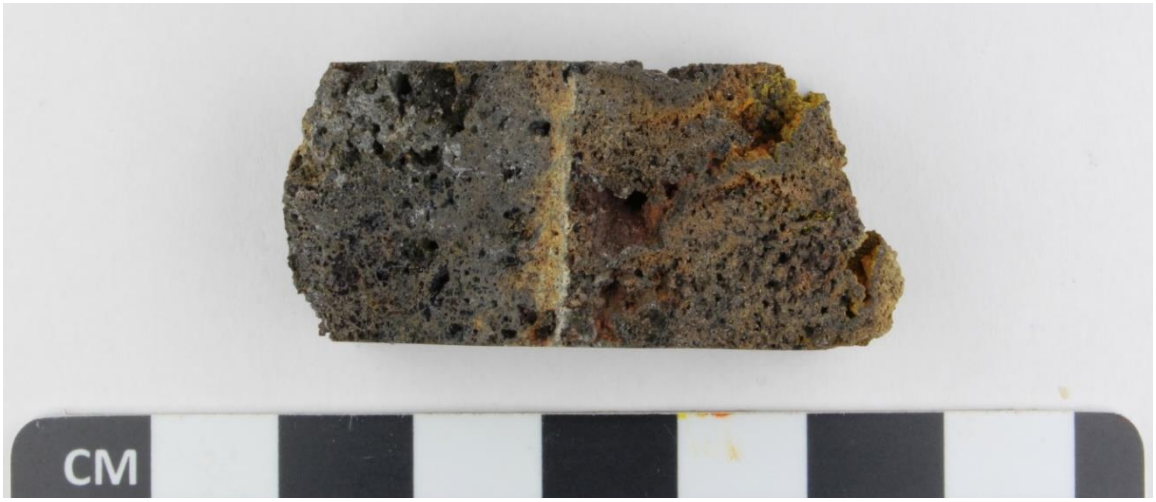

Thin section slab for D1919-R1. Thin section was cut from this face. Two growth zones are visible and will be referred to as the first growth zone (left) and the second growth zone (right).

Mineral Abundances and Occurrences

Barite – 50% (1st growth zone), 54% (2nd growth zone)

Sphalerite – 39% (1st growth zone), 39% (2nd growth zone)

Pyrite – 10% (1st growth zone), 5% (2nd growth zone)

Pb-As & Pb-As-Sb sulphosalts – 1% (1st growth zone), 2% (2nd growth zone)

Marcasite – < 1% (1st growth zone), < 1% (2nd growth zone)

Chalcopyrite – < 1% (1st growth zone), << 1% (2nd growth zone)

Galena – << 1% (2nd growth zone only)

There are two main growth zones separated by a thin wall of fine-grained barite and massive pyrite and marcasite. The two zones share a similar relative abundance of minerals but have slightly different porosities. The characteristics of each mineral phase are also consistent throughout the whole sample, unless otherwise indicated. Barite occurs mostly as euhedral to subhedral bladed and tabular crystals with some minor anhedral grains. Finer-grained bladed crystals tend to occur in plumose texture or as radiating acicular crystals that are exclusive to the edge of the first growth zone (adjacent to a thin layer of pyrite and marcasite which separates the two growth zones). Coarse-grained barite is instead found along the edges of interior pore spaces. Overall grain size decreases from the interior of the first growth zone towards the thick pyrite and marcasite layer. Within the first growth zone, plumose barite is abundantly mantled by pyrite. Pyrite also is commonly found as small, rounded to sub-rounded blebs that sometimes form in colloform masses with traces of marcasite and in some cases as slightly ovoid rings. Pyrite in all instances may be overgrown by sphalerite, and some chalcopyrite. Chalcopyrite is locally intergrown with sphalerite or overgrowing it. Sphalerite in places appears to rim some of this chalcopyrite as well, and occasionally contains sulphosalt inclusions. Exclusive to more porous areas, subhedral sulphosalt grains mantle pre-existing minerals (mostly sphalerite, chalcopyrite, and barite).

Within the second growth zone, plumose barite is less frequent and instead tends to form more radiating bladed masses. Overall, barite crystals are also slightly larger within this growth zone. Colloform and blebby pyrite still occurs along the edges of barite but tend to be more prevalent in more porous spaces. Sphalerite pervasively overgrows barite and pyrite, with trace inclusions of galena. There are a few localized areas dominated by barite, where sphalerite or pyrite overgrowth is greatly reduced. Marcasite appears with pyrite within the thin wall between growth zones and in some disseminated grains of pyrite. Traces of galena appear as tiny inclusions within massive sphalerite. Minor chalcopyrite is replacing sphalerite along its edges. Pb-As sulphosalts are present as massive overgrowths of pre-existing barite and sulphides in porous space (same as in the first growth zone).

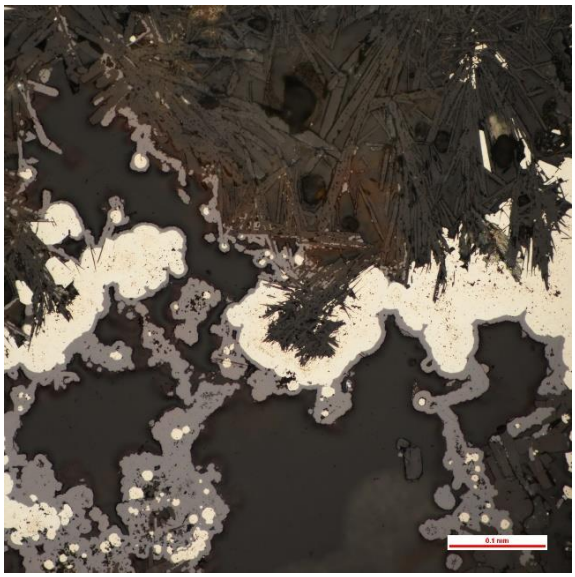

a.

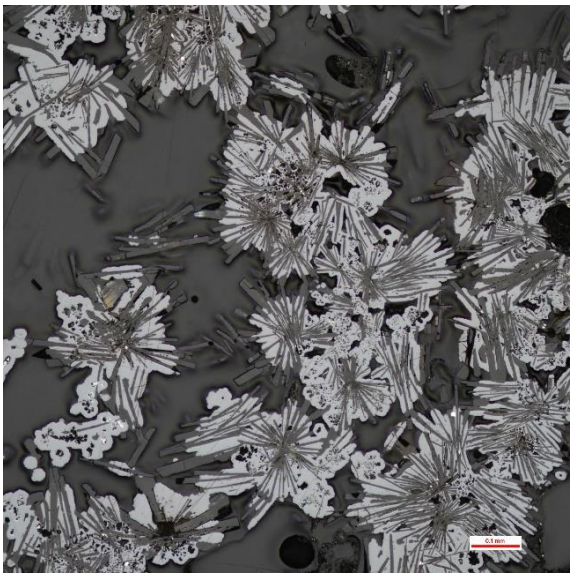

b.

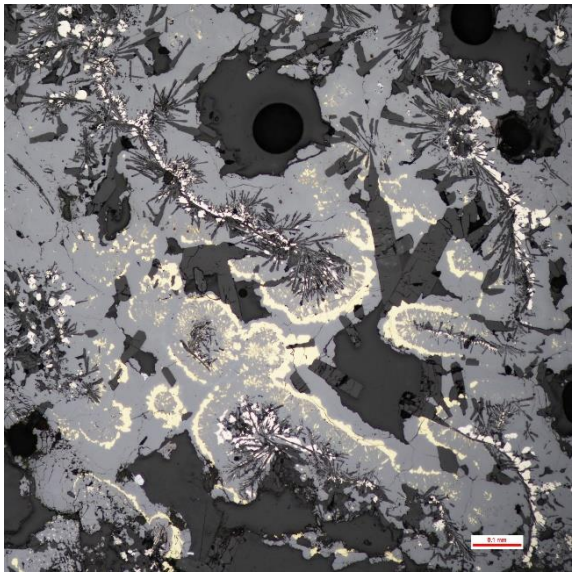

c.

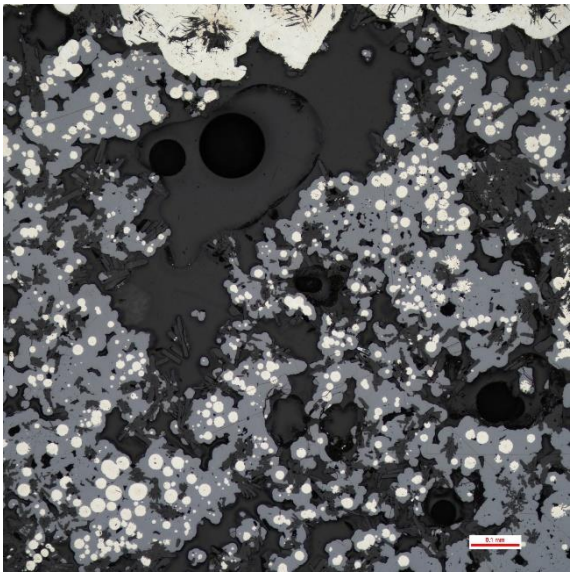

d.

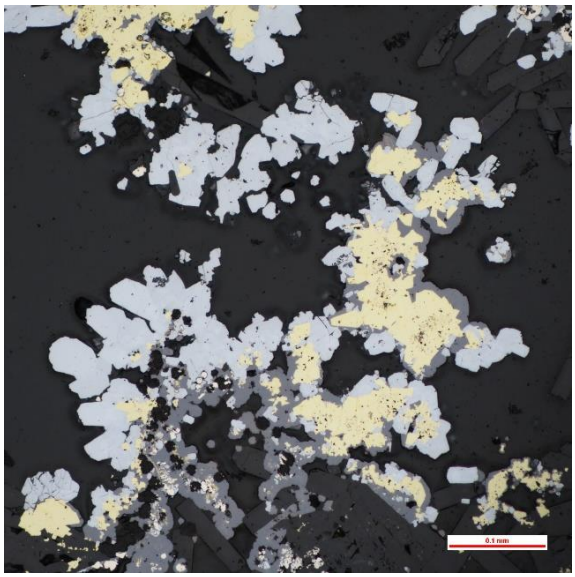

e.

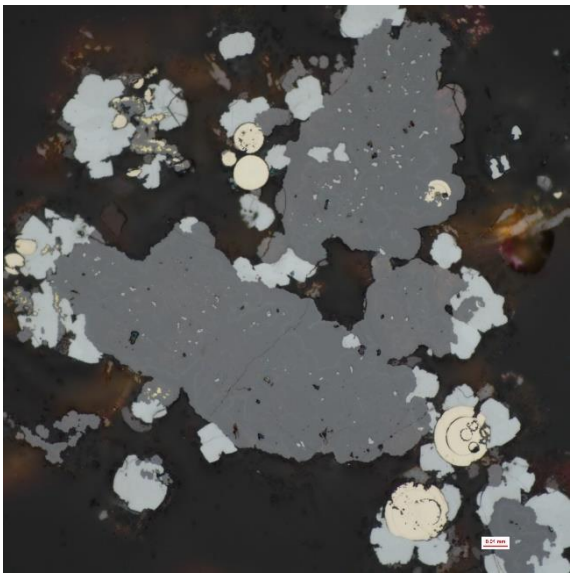

f.

Photomicrographs of sample D1919-R1. All photos are taken under reflected light. a) Central massive pyrite and marcasite wall separating two growth zones. The wall has overgrown bladed and acicular barite that forms a thick layer at the edge of the first growth zone (top). The second growth zone (bottom) has massive sphalerite overgrowing blebs and massive pyrite, as well as barite (see d). Overall, this growth zone is similar to the interior of the first growth zone. b) Massive sphalerite mantling fine-grained bladed barite rosettes. Characteristic of both growth zones, but pyrite is more abundant in the first growth zone. c) Plumose barite is mantled by pyrite and overgrown by massive sphalerite. Chalcopyrite intergrowths with massive sphalerite tend to be locally associated with more porous areas (interior of first growth zone). d) Sphalerite overgrowing barite and rounded blebs of pyrite (common in the second growth zone). e) Sphalerite mantles chalcopyrite, while subhedral sulphosalts form on the edges of both sulphide phases. f) Massive sphalerite and colloform pyrite overgrown by sulphosalts. Tiny inclusions of galena are present within sphalerite.

D1919 – R2:

Site Description

This sample is a piece of an extinct sulphide chimney located on the steep talus slope of a tall semi-active chimney complex. The tallest chimneys here are thin and topped with what appears to be extinct beehive structures. Active venting can be found along the walls of a large chimney trunk. Here, there are small beehive structures diffusely emitting clear to white hydrothermal fluids. The abundance of large, extinct sulphide blocks suggests that this chimney complex was once much larger, and prolonged inactivity has caused many extinct chimneys to collapse.

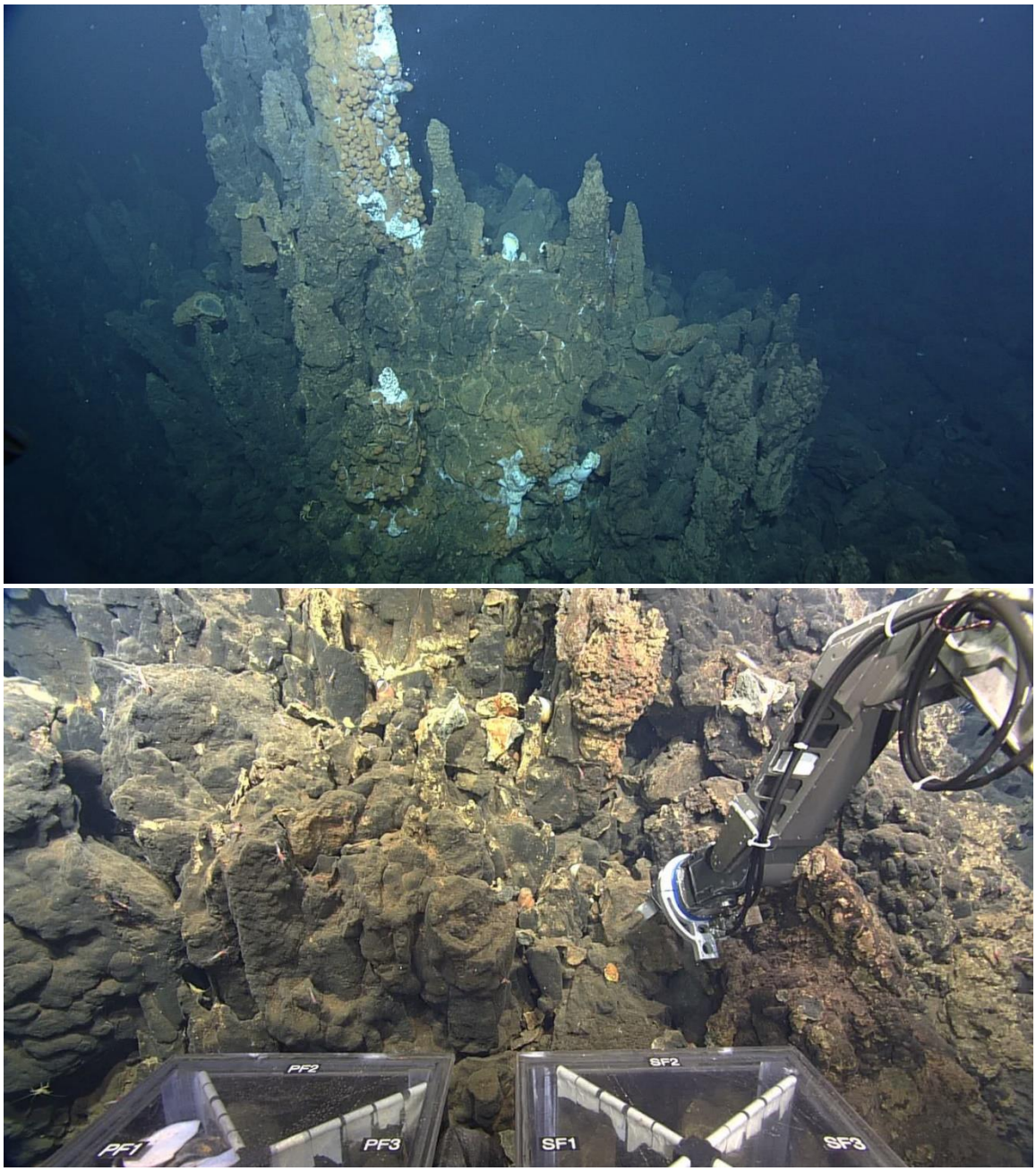

Top photograph shows the chimney complex where sample D1919-R2 was grabbed from. The exact location is beyond the lower extent of the photograph, along the sulphide talus slope. Bottom photograph shows the ROV ROPOS grabbing the sulphide sample.

Hand Sample Description

The heavily oxidized appearance of the sample exterior hides distinct features or styles of mineralization of the sample interior. Upon cutting through the hand sample, at least three zones of chimney growth are easily identifiable. The zones of sulphide expansion are

separated by thin white layers of barite (~ 1 – 4 mm). Each zone is highly porous, and generally a light grey to dark-grey and yellow-brown colouration based on variations in abundance of Zn-Cu and Ba. The outermost zone (Zone A) appears to be mostly devoid of chalcopyrite and is characterized by the highest degree of oxidation. The middle zone (Zone B) seems to be the most abundant in chalcopyrite, with rather pervasive oxidation throughout. The innermost zone (Zone C) is the most barite-rich, with little to no oxidation.

Hand sample for D1919-R2. Top left and right photographs show the general weathered exterior, with sparsely exposed fresh surfaces. Bottom photograph is a slice through the interior of the sample, highlighting the various growth zones.

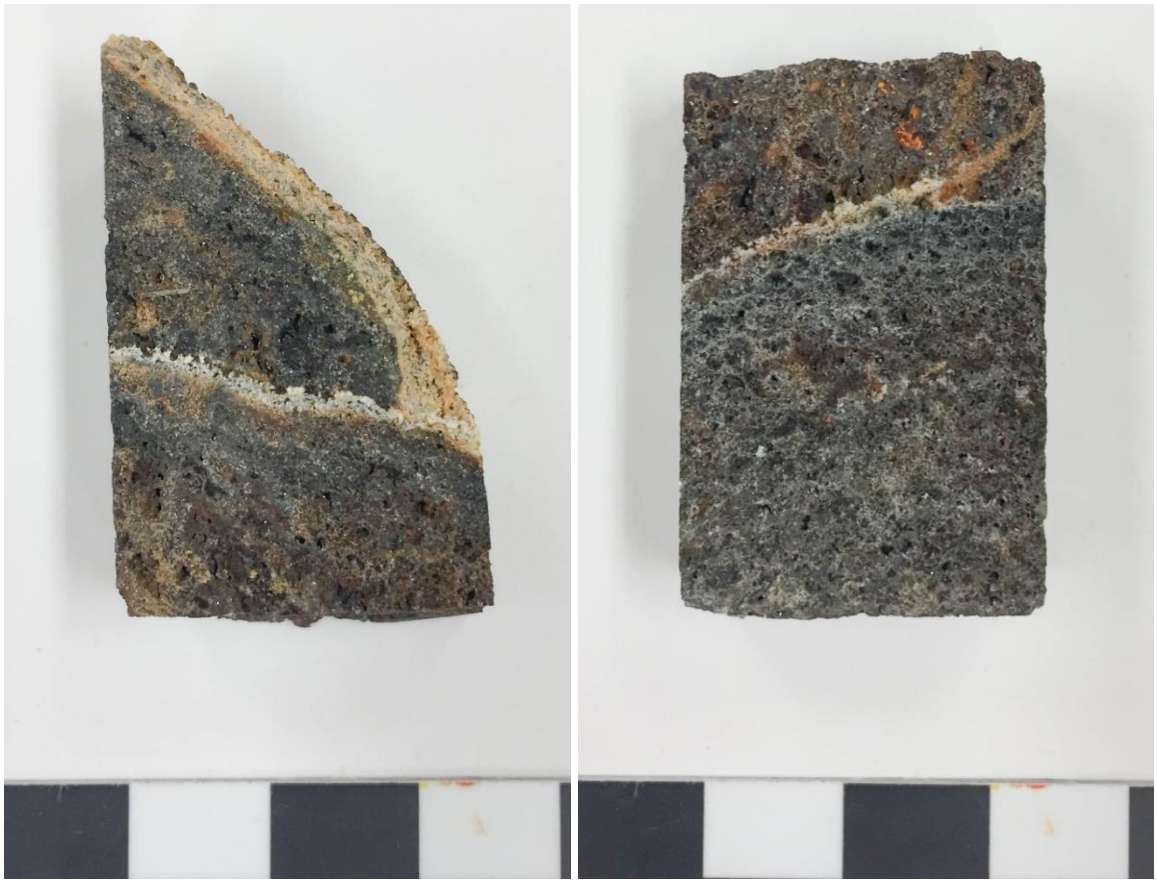

Thin section slabs for D1919-R2. Left photograph shows D1919-R2-1 containing growth zones A and B. Right photograph shows D1919-R2-2 containing growth zones B and C. (These letter codes match geochemical powders). Thin sections were cut from these faces.

Mineral Abundances and Occurrences

R2-1 & R2-2

Barite – 65-70% (Zone A), 45-50% (Zone B), 55-60% (Zone C)

Sphalerite – 25-30% (Zone A), 45-50% (Zone B), 35-40% (Zone C)

Galena – 2-3% (Zone A), 4% (Zone B), 2-3% (Zone C)

Pyrite – 2-3% (Zone A), ≤ 1% (Zone B), 2-3% (Zone C)

There are three distinct zones of sulphide growth that contain similar mineral textures but vary in the abundance of certain minerals. Barite occurs mostly as euhedral to subhedral bladed and tabular crystals. Some radiating clusters and plumose textures are observed in

barite-dominated exterior. Barite crystals tend to be fine-grained throughout the interior and exterior of each zone and relatively coarse-grained within large pore spaces, except for Zone C. Growth of massive sphalerite occurs abundantly in all zones but is basically absent in the barite-dominated exterior of Zone A. Dendritic sphalerite is a somewhat localized occurrence. The centers of these areas are pitted, deteriorated, and rich in Fe-oxide. Galena mostly occurs as minor massive overgrowths of other sulphide minerals or as small inclusions contained within massive sphalerite. Here, galena may grow directly on the edges of colloform pyrite. Rare subhedral grains are present on the edges of coarse-grained barite crystals and porous massive sphalerite. Pyrite occurs as rounded masses and individual circular blebs that may directly grow on the edges of small barite crystals. Pyrite blebs and masses sometimes exhibit colloform texture with rare occurrences of alternating layers of sphalerite.

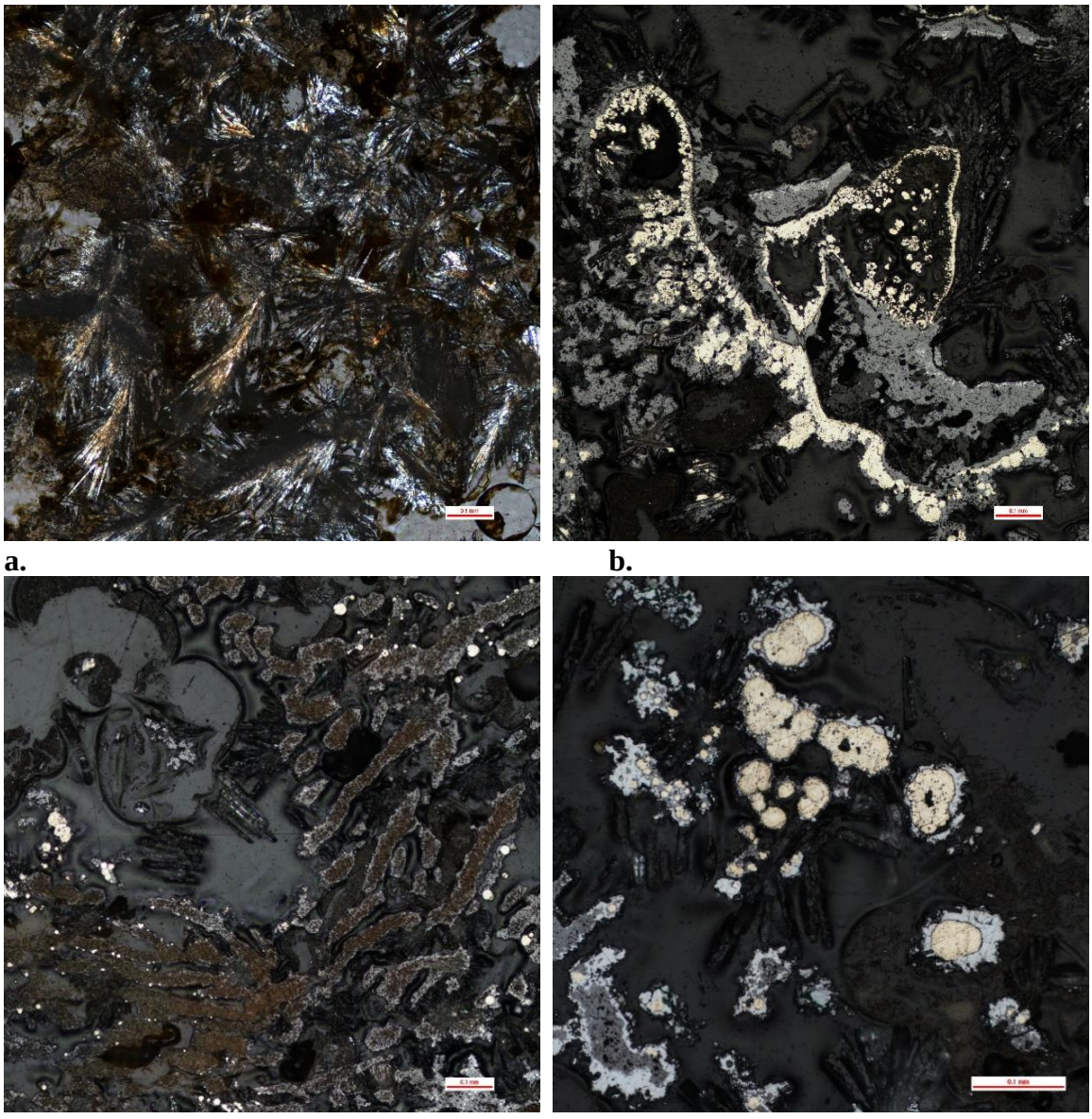

a. **b.**

c. **d.**

e. **f.**

Photomicrographs of sample D1919-R2. All photos are taken from D1919-R2-1 under reflected light, except for a, which is captured under transmitted light. a) Barite-dominated exterior rind, with some dark-brown Fe-oxides. Plumose texture is commonly observed here and is rarely overgrown by sulphides; XPL. b) Unique pyrite growth within the interior of Zone A, that may represent a mineralized vent organisms or a complex, localized overgrowth of fine-grained barite. Tiny, bladed barite crystals in some cases appear to have been psuedomorphed by sphalerite (as evidenced in the pyrite layer). Disseminated galena appears in massive sphalerite. c) Dendritic texture in sphalerite can be found within the interiors of Zone A and Zone B. The centers of massive sphalerite grains appear deteriorated and contain Fe-oxide. The grain edges are visibly more intact, and chemically reflect unaltered sphalerite. d) Colloform masses and blebs of pyrite are overgrown by sphalerite and/or galena. e) Masses and blebs of pyrite sometimes show partial replacement by sphalerite. Early, fine-grained barite is commonly mantled by pyrite blebs and subsequently overgrown by sphalerite (similar to plumose texture). Coarse-grained barite is generally grown on the edges of these pre-existing sulphides in more porous void space. f) Rare colloform pyrite contains alternating layers of sphalerite.

D1919 – R3:

Site Description

This sample was collected from a small diffusely venting chimney spire within a larger chimney complex. The associated sulphide mound has a much lower relief than other observed mounds. The central chimneys are not quite as tall as previous sample sites but contain some unique features. The tallest of the chimneys was topped with a large beehive structure diffusely venting black smoke, however, in the interest of science, it was deliberately knocked over by the ROPOS arm. The trunk of the toppled chimney also

contained smaller beehives with the same characteristic venting. Diffuse venting was also occurring from surrounding small spires and emitted a clearer hydrothermal fluid.

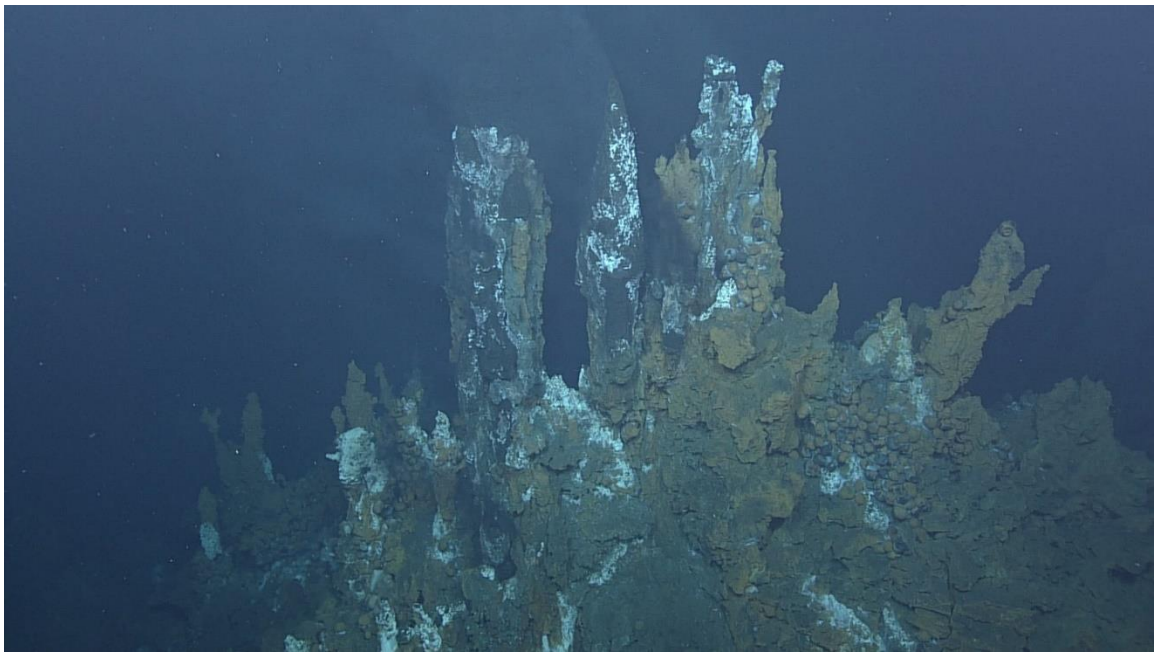

a.

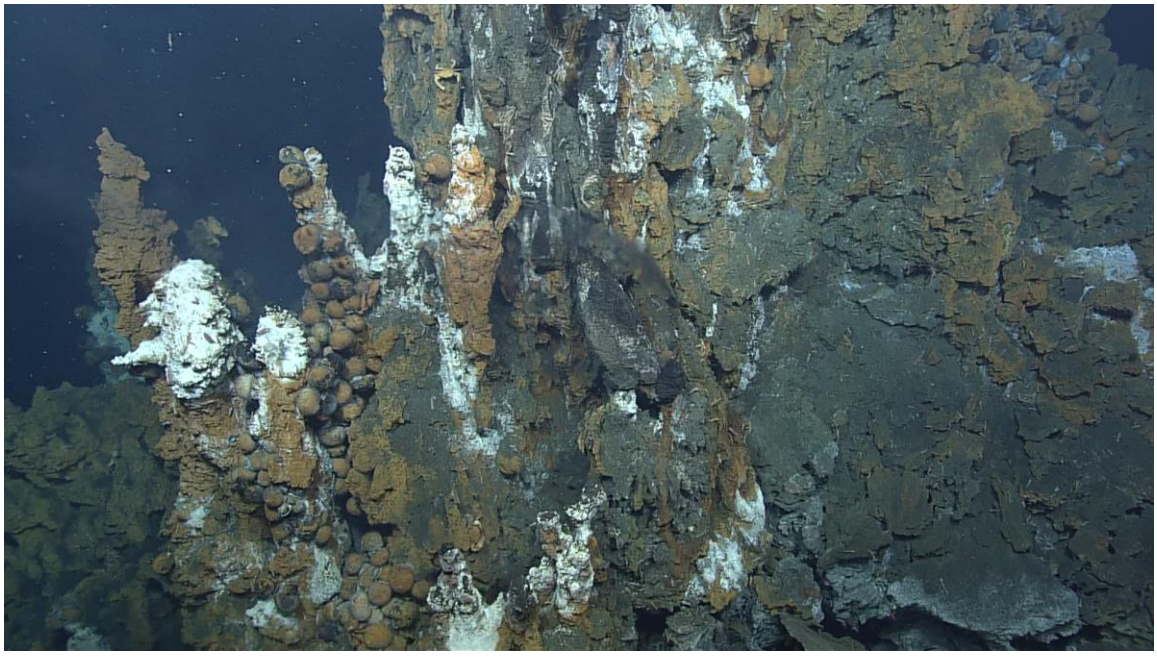

b.

Large active chimney complex where D1919-R3 was grabbed. a) Black smoker vents mostly topped with beehive structures. b) Side of complex wall where the sample was collected.

Hand Sample Description

This sulphide sample is comprised of several sections of one diffusely venting chimney. The chimney trunk interior has several zones of mineralization and a complex network of fluid pathways. The fine-grained, porous groundmass has a highly varied style of mineralization. The innermost areas are generally yellow-brown, chalcopyrite-rich areas that reflect high-temperature formation conditions. Sphalerite dominates towards the dark to light grey outer sections and has an intimate association with barite. The outer crust is primarily composed of barite and an intense red-orange-yellow colouration suggests the presence of realgar or orpiment. The most unique feature within the trunk interior is that it contains a central fluid conduit lined with coarse-grained sphalerite (up to 1 mm). This suggests there is significant late-stage mineralization of lower temperature sulphide minerals. The chimney is topped with a sulphide cap, which appears to have similar mineral zoning, but a lack of apparent fluid conduits. The entire sample is heavily oxidized with white patches of bacterial growth. The chimney trunk exterior also features small rounded "nobs" (~ 1 – 2 cm), which may represent relict fluid vents.

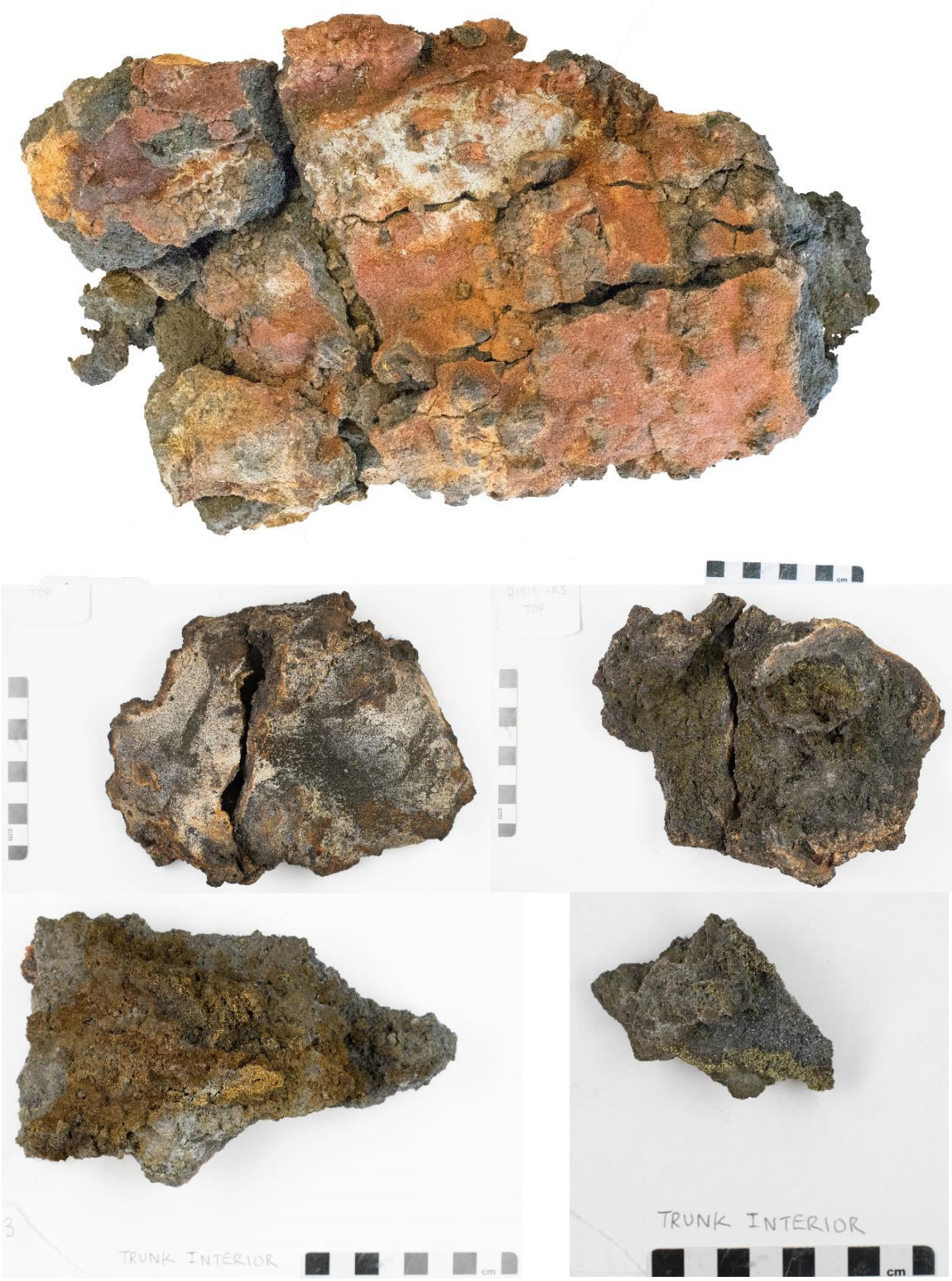

Hand samples for D1919-R3. Top photograph is the entire sample as one piece, except for the chimney cap (TOP). Sample was extremely fragile, and quickly broke apart when

trying to photograph sections of it. Middle left and right photographs show the chimney cap which broke into several pieces, left photograph shows the chimney cap exterior, while the right photograph shows the fresh interior, D1919-R3-TOP. Bottom left and right photographs were two pieces obtained from the trunk interior (top left section in top left photograph), D1919-R3-TRUNK-1 and D1919-R3-TRUNK-2, respectively.

Thin section slabs for D1919-R3. Top left: D1919-R3-TOP-A. Top right: D1919-R3-TOP-C. Bottom left: D1919-R3-TRUNK-1. Bottom right: D1919-R3-TRUNK-2. Thin sections were cut from these faces, except for D1919-R3-TRUNK-1.

Mineral Abundances and Occurrences

TOP-A

Barite – 65%

Sphalerite – 25%

Pyrite – 5%

Chalcopyrite – 3%

Galena – 2%

Tetrahedrite-Tennantite – < 1%

Barite mostly occurs as euhedral to subhedral bladed and tabular crystals or as acicular crystals that are exclusive to the outermost exterior crusts. Grain sizes vary between coarse-grained barite occurring within open pore spaces, and fine-grained barite occurring within the interior groundmass. The overall grain size is reduced towards the exterior of the sample. Late-stage, coarse-grained barite grows along the edges of chalcopyrite linings and is subsequently mantled by sphalerite and galena, as well as tetrahedrite-tennantite. Colloform pyrite or circular blebs of pyrite are often seen overgrowing or thinly mantling clusters or individual blades of barite, although plumose texture is not apparent. In most cases pyrite is subsequently mantled by minor subhedral galena and overgrown by massive sphalerite. Dendritic sphalerite is present within the interior adjacent to some chalcopyrite-lined fluid pathways. Circular blebs of pyrite are contained within dendritic sphalerite. Massive chalcopyrite linings are localized within the interior, while intergrowths and replacement occur with some massive sphalerite. Some late-stage sphalerite mantles massive chalcopyrite and coarse-grained barite within more open pore space. Chalcopyrite has limited growth in isolated pore spaces along the edges of pre-existing minerals. This occurs mostly with sphalerite and some very minor tetrahedrite-tennantite. Tetrahedrite-tennantite is present as irregular, sometimes subhedral or triangular-shaped grains grown along the edges of chalcopyrite or as small inclusions. Galena appears to be intergrown with sphalerite in most cases, as it is generally contained within sphalerite or grown irregularly at its edges.

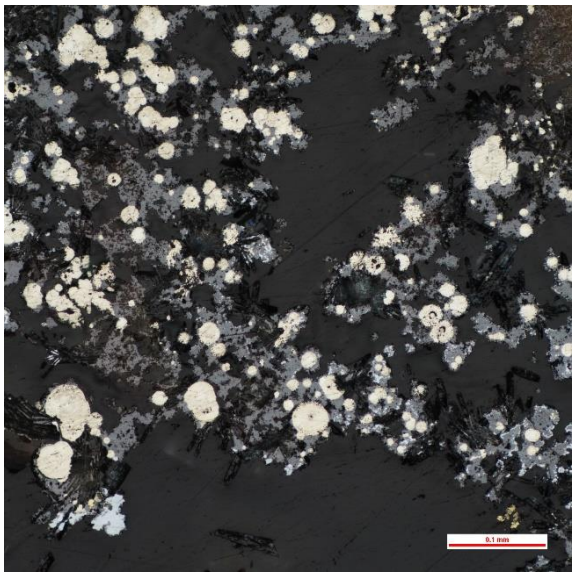

a.

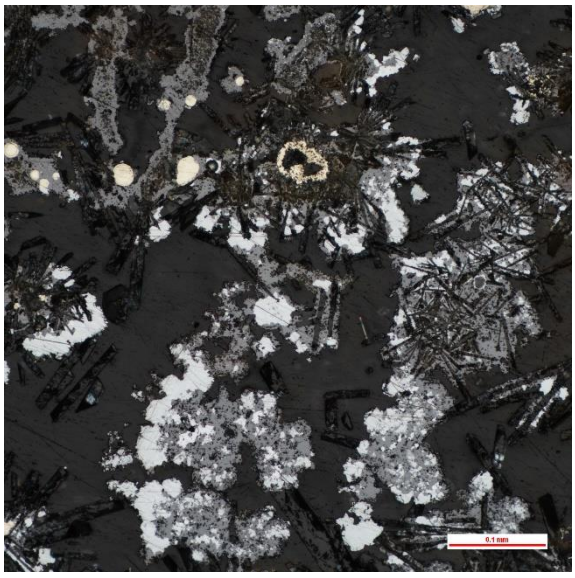

b.

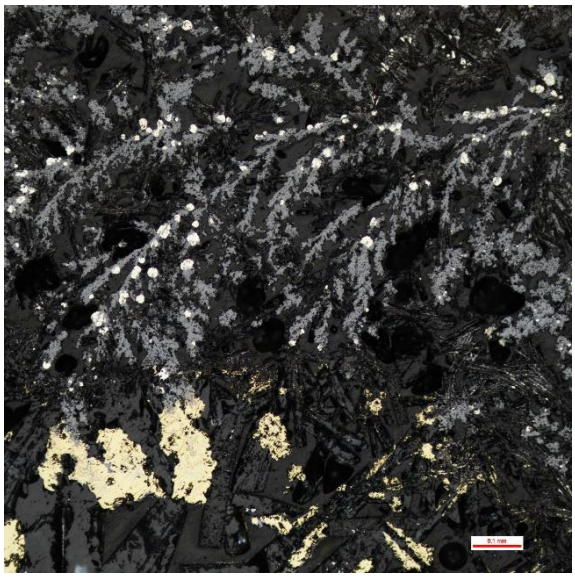

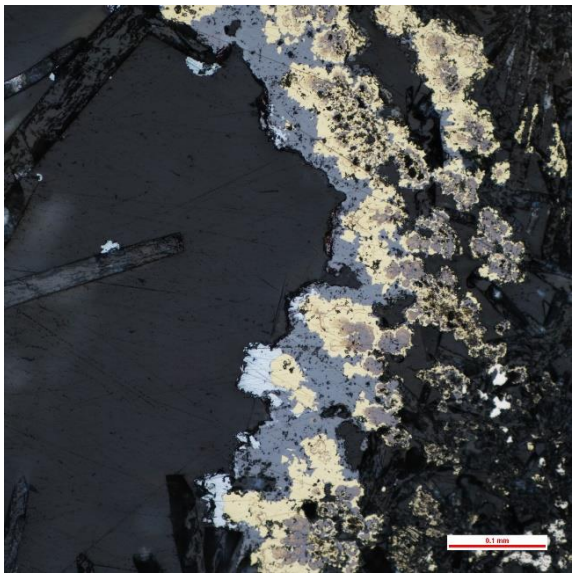

c. **d.**

Photomicrographs of sample D1919-R3 TOP A. All photos are taken under reflected light, except for f, which is captured under transmitted light. a) Massive or colloform pyrite is commonly overgrown by sphalerite. b) Fine-grained barite with galena and sphalerite overgrowths. Dendritic texture can be seen in some massive sphalerite (top). Coarse-grained barite in general is characterized by little sulphide overgrowth. c) Dendritic sphalerite. Pyrite mantling is sometimes incorporated within the texture. Barite is often overgrown, by sphalerite in these areas. Late, coarse-grained barite is grown in porous void space (bottom) with chalcopyrite replacing sphalerite. d) Intergrowth of sphalerite and chalcopyrite. Overgrowths and inclusions of galena are occasionally present with on the edges of coarse-grained barite.

TRUNK 2

Barite – 50%

Sphalerite – 25%

Chalcopyrite – 15%

Pyrite – 5%

Marcasite – 5%

Galena – < 1%

Tetrahedrite – Tennantite – < 1%

Barite crystals are mostly euhedral to subhedral and there is a stark contrast in crystal size between small bladed and very large bladed and tabular crystals. Larger crystals tend to occur in more open pore spaces, however, there is also a substantial overlap of both grain sizes. The largest barite crystals form as the inner lining of the main chimney vent. Fine-

grained barite is often mantled by massive or blebby pyrite or marcasite, and subsequently overgrown by massive sphalerite. A massive marcasite and pyrite layer separates two major sulphide-rich zones; (1) A sphalerite- and barite-dominated zone that has major, localized chalcopyrite overgrowth and possible replacement of sphalerite. Chalcopyrite, sphalerite, galena, and tetrahedrite-tennantite mantle large, bladed barite crystals along the main chimney vent lining. (2) A groundmass composed of barite, sphalerite, and pyrite ± marcasite, with a notable increase of chalcopyrite. Massive sphalerite can be found throughout the sample, while dendritic sphalerite is common within the first zone and is intergrown with pyrite and chalcopyrite. Massive chalcopyrite is commonly intergrown with massive sphalerite but may also be replacing it in areas where it is most abundant. Pyrite occurs mostly as subhedral to euhedral grains in abundance with massive marcasite or as very small circular blebs within massive sphalerite or chalcopyrite. Dendritic pyrite is also common and is overgrown by sphalerite or chalcopyrite. Both pyrite and marcasite are intergrown within a thin, massive layer that separates the two major sulphide zones. Galena occurs as small inclusions within massive sphalerite. Tetrahedrite-tennantite is present as anhedral to subhedral, or sometimes triangular-shaped grains, on the edges of interior coarse-grained barite and chalcopyrite. Rare inclusions are also seen in this area within sphalerite and contain small intergrowths of chalcopyrite.

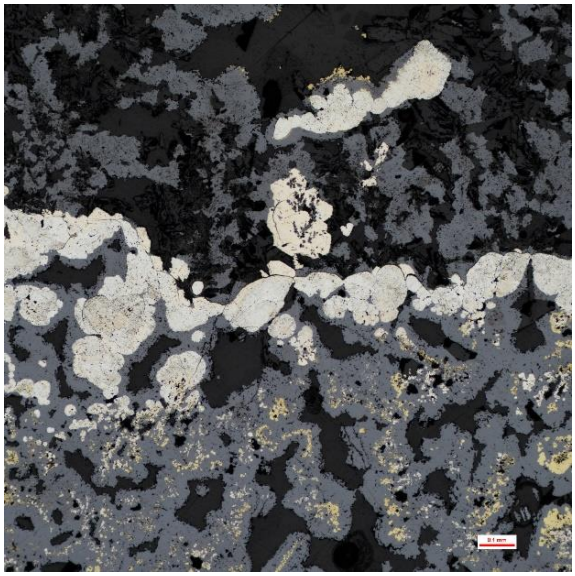

a.

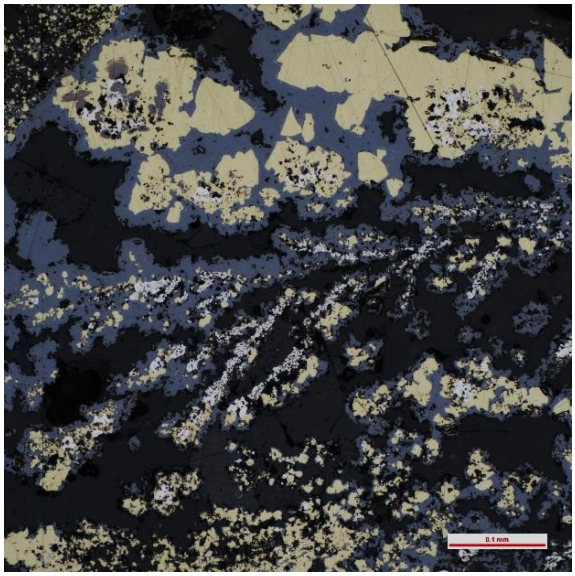

b.

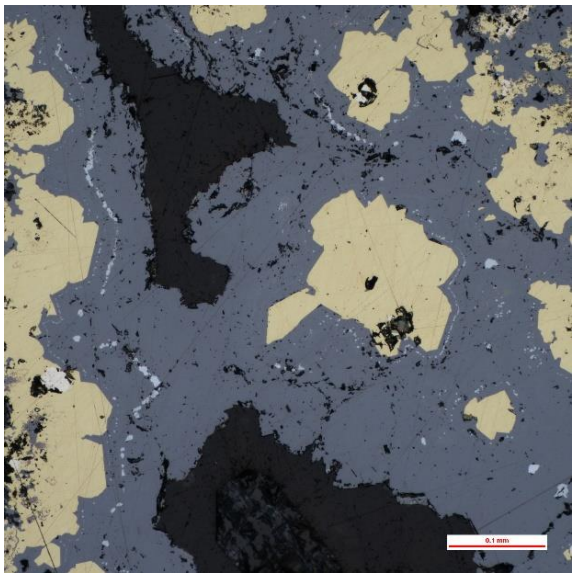

c.

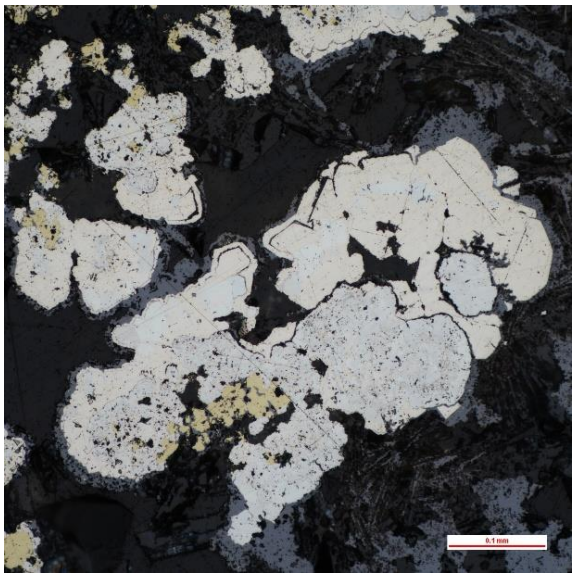

d.

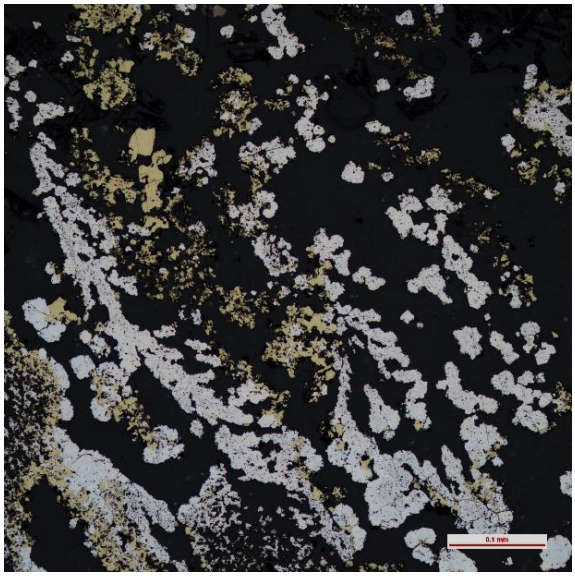

e.

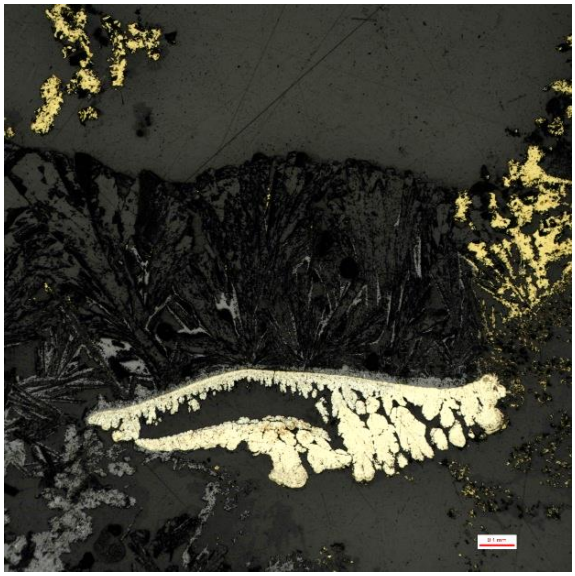

f.

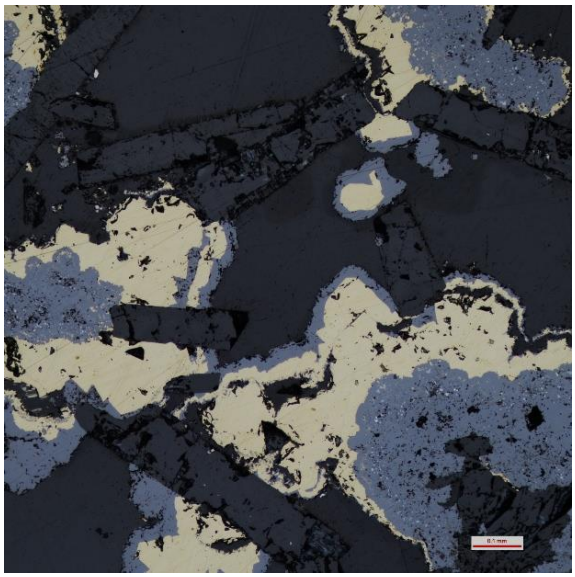

g.

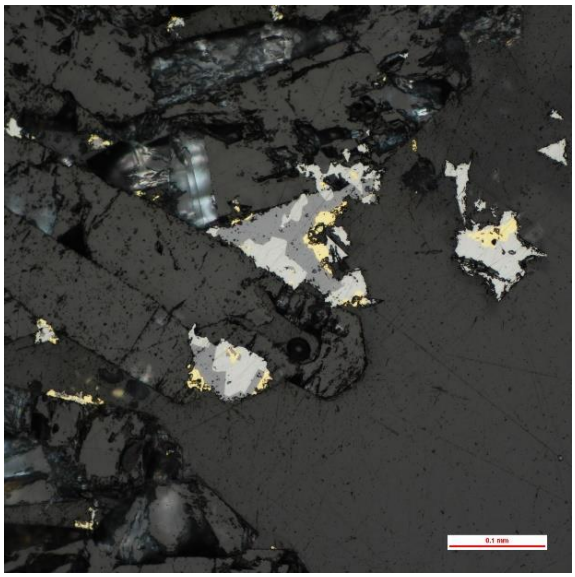

h.

Photomicrographs of sample D1919-R3 TRUNK 2. All photos are taken under reflected light. a) Central pyrite/marcasite wall separates two main growth zones. b) Dendritic sphalerite containing pyrite and chalcopyrite. Massive chalcopyrite at the top is overgrown by subsequent sphalerite. c) Subhedral, massive chalcopyrite occurs within localized clusters. Late-sphalerite has infilled much of this pore space with tiny inclusions of galena. Galena may exhibit a distinct thin layer of intergrowth with massive sphalerite. d) Pyrite and marcasite exhibit zoned growth with minor sphalerite. e) Dendritic pyrite is present with chalcopyrite closer to areas of abundant massive chalcopyrite growth. The absence of sphalerite suggests that chalcopyrite may have locally replaced sphalerite. f) Unusual mineral associations within the main chimney vent lining. Chalcopyrite is present but is generally restricted to one small area, where it is dominant. Late-barite grows along the surface of a small vug of dendritic pyrite. g) Coarse-grained barite along the interior conduit is overgrown by alternating growth of sphalerite and chalcopyrite. h) Coarse-grained barite also exhibits minor growth of tetrahedrite-tennantite with sphalerite and disseminated chalcopyrite.

D1919 – R4:

Site Description

This sample was collected from the base of the sulphide mound that contains the chimney complex described in the previous sample. The base of this mound is littered with collapsed sulphide chimneys and sulphide talus blocks. This site is also located at the base of the chimney complex described in D1919-R2, which may explain the multitude of talus material.

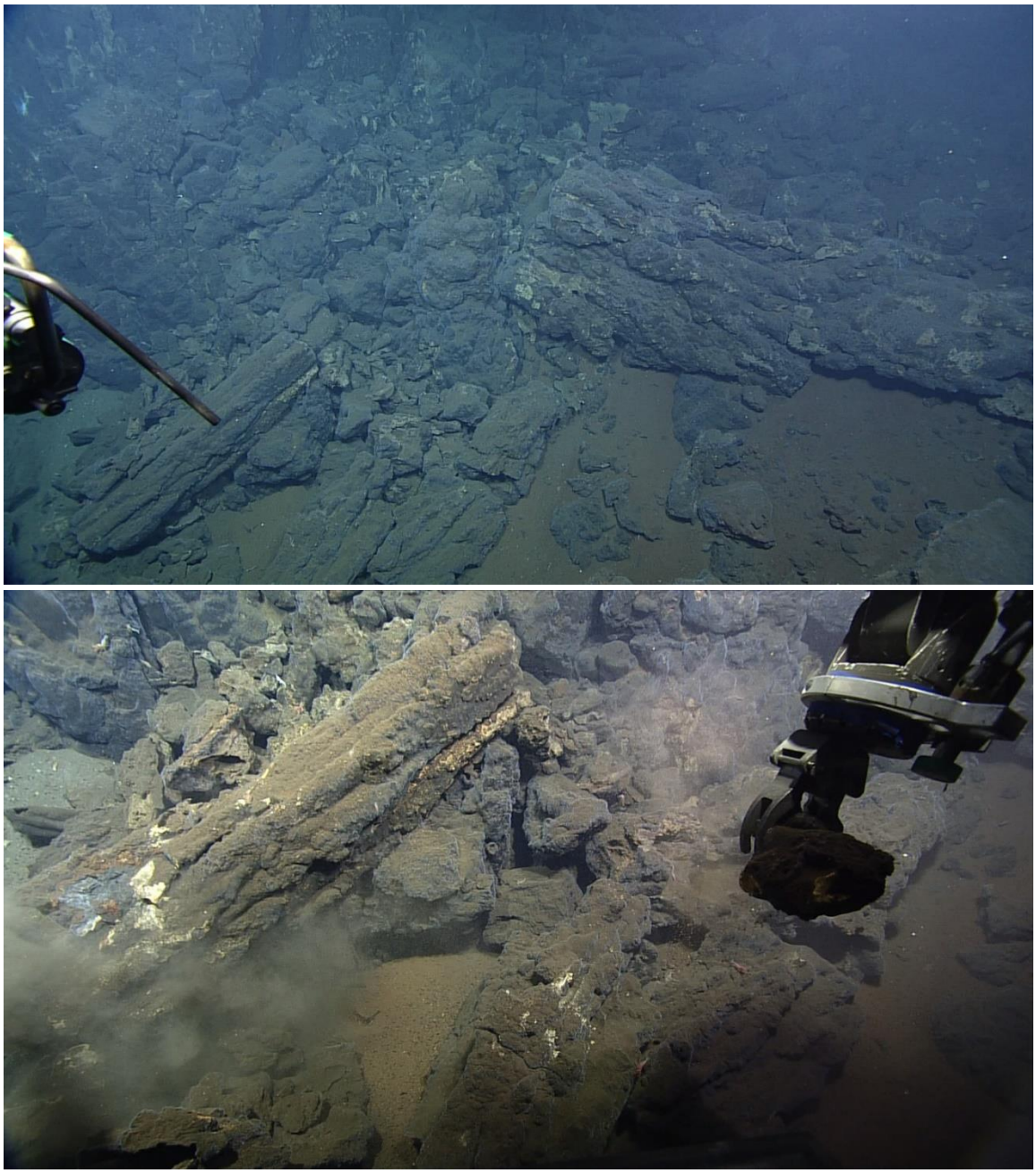

Top photograph shows base of sulphide mound where D1919-R4 was grabbed. Bottom photograph shows the large dead sulphide chimney trunk where the sample was collected (right side where the sulphide sediments are in suspension, and fresh surface of the collapsed chimney is exposed).

Hand Sample Description

The high degree of oxidation on the sample exterior, made initial observation of the interior mineralization virtually impossible. Upon cutting through the sample, two distinct

zones were identified: a dark-grey sphalerite-rich and chalcopyrite-poor interior, and a red-brown to yellow-brown oxidized barite-rich rind. Both zones are fine-grained, and porous, with a well-defined boundary between them. The oxidized crust is generally up to a centimeter in thickness.

Hand sample for D1919-R4. Left photograph shows the small fresh surface, and weathered exterior that characterizes the remaining exterior surface. Right photograph shows a small slice through the sample interior, taken from a thinner section of the large sample. Thin section slab was cut from this slice.

Thin section slab from D1919-R4. Thin section was cut from this face.

Mineral Abundances and Occurrences

Barite – 60-65%

Sphalerite – 30-35%

Pyrite – 3%

Galena – 2%

Pb-As Sulphosalt – < 1%

Chalcopyrite – < 1%

Covellite – << 1%

Barite is extremely pervasive within the sample and occurs as clustered euhedral bladed and tabular crystals with some radiating masses. Crystal size is reduced slightly towards the exterior barite-dominated rind, where few sulphide minerals are present. Relatively coarse-grained barite crystals are found within open pore spaces of massive sphalerite that contain no sulphide mineral overgrowths. Sphalerite appears massive throughout the entire sample interior and forms overgrowths around barite, colloform pyrite, and galena. Dendritic texture in sphalerite is observed in sphalerite close to the exterior barite-dominated exterior rind. Minor pyrite is seen mostly in colloform texture or as disseminated circular blebs. Very minor euhedral pyrite is contained within chalcopyrite. Colloform pyrite appears on some edges of fine-grained barite and is subsequently mantled by galena and sphalerite. Alternating layers of sphalerite are also present within some of the colloform growths. Several of the colloform growths are fractured and contain subsequent infill of sphalerite. Galena occurs on the edges of colloform pyrite, and as small inclusions contained within massive sphalerite. Some growth of galena can also be seen on the edges of massive sphalerite, but none was observed on coarse-grained barite. Pb-As sulphosalts can be seen mantling massive sphalerite in open pore spaces or as small, disseminated inclusions within sphalerite. These sulphosalts are distinguishable from galena by their strong anisotropy. Chalcopyrite is only present as anomalous, small grains within the sample interior that contain euhedral pyrite and massive sphalerite. Disseminated clusters of covellite form with minor sphalerite found in the exterior barite-dominated rind.

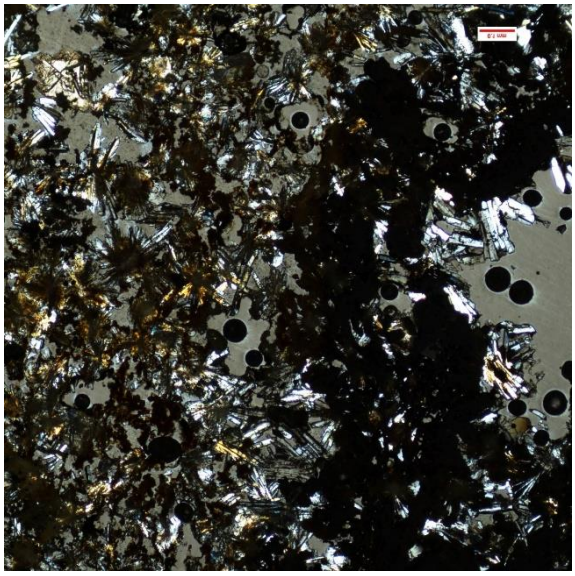

a.

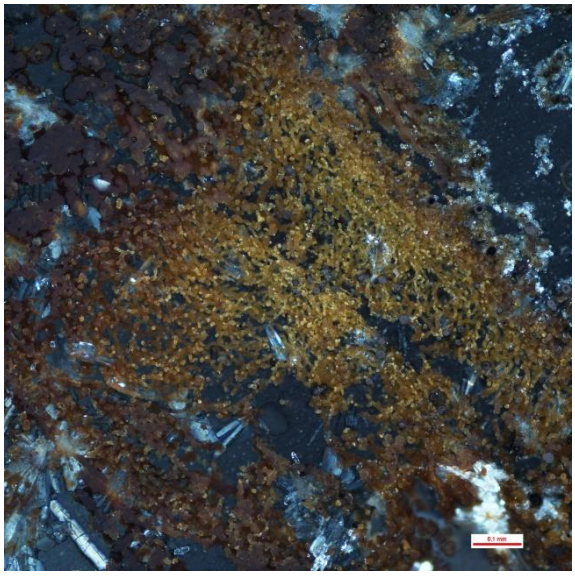

b.

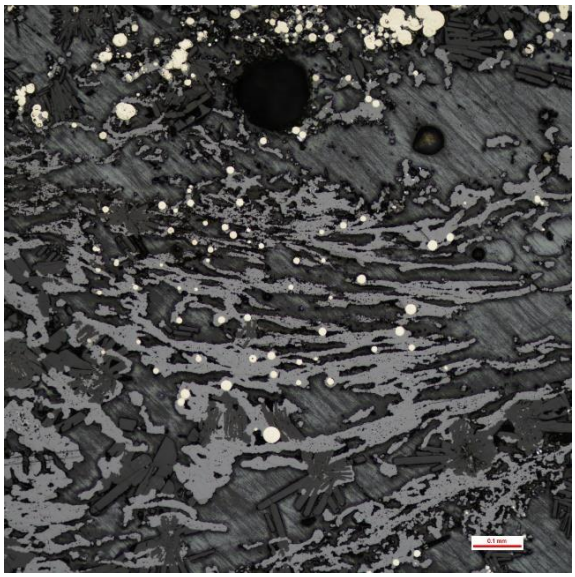

c.

d.

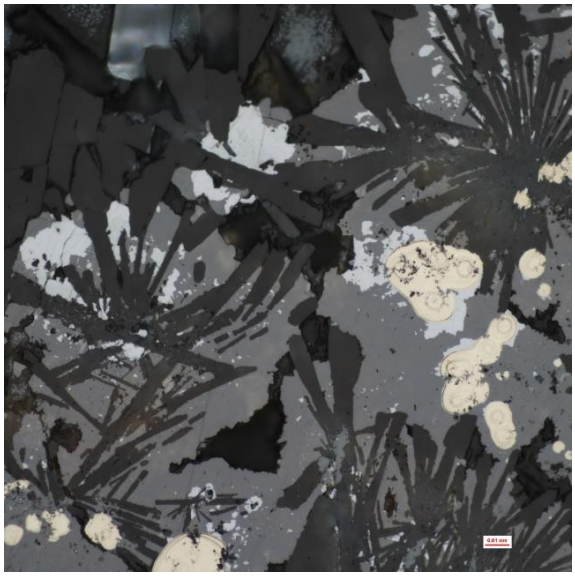

e.

f.

Photomicrographs of sample D1919-R4. All photos are taken under reflected light, except for a, which uses a combination of both reflected and transmitted light. a) Well-defined boundary separating the sphalerite-rich interior (right) and barite-dominated, oxidized exterior layer (left); XPL. b) Barite and sphalerite-rich interior. XPL. c) Colloform and disseminated circular blebs of pyrite, with barite, and dendritic sphalerite. d) Bladed barite, with some radiating clusters mantled by colloform pyrite and overgrown by massive sphalerite. Late-stage galena grows on the boundaries of colloform pyrite and sphalerite, found within open pore spaces, although it is likely intergrown with sphalerite. The scratched appearance within pore spaces (bottom) is due to residual carbon coating from SEM analysis. e) Close-up of barite, galena, sphalerite, and colloform pyrite, to highlight the order of mineral formation. Colloform pyrite mantles early barite, with

overgrown galena and sphalerite. f) Unique replacement texture within some colloform pyrite within the barite-dominated exterior layer. Highly fractured and destroyed colloform growths contain alternating bands of sphalerite replacement and/or infilling.

D1919 – R5:

Site Description

This sample was grabbed from the base of a small, partially active chimney complex at the top of a steep-sided massive sulphide mound. It is a piece of inactive sulphide talus. Surrounding it, were some enormous blocks of similar material. The chimney complex itself is small relative to some of the other sites visited, however there is high-temperature venting present.

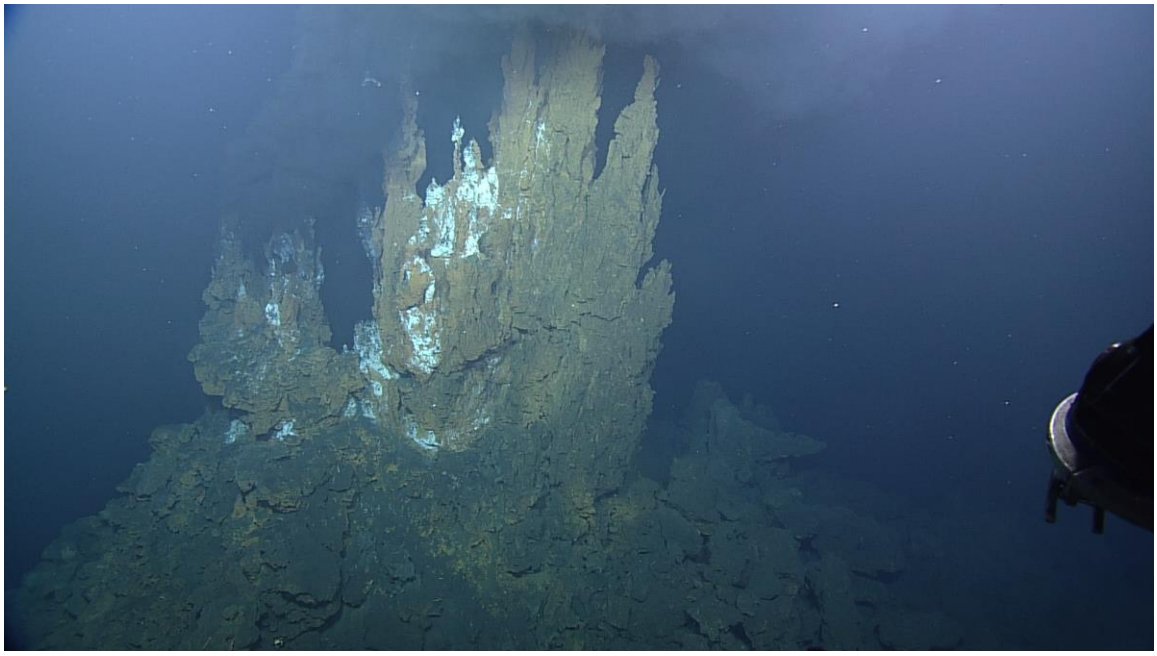

a.

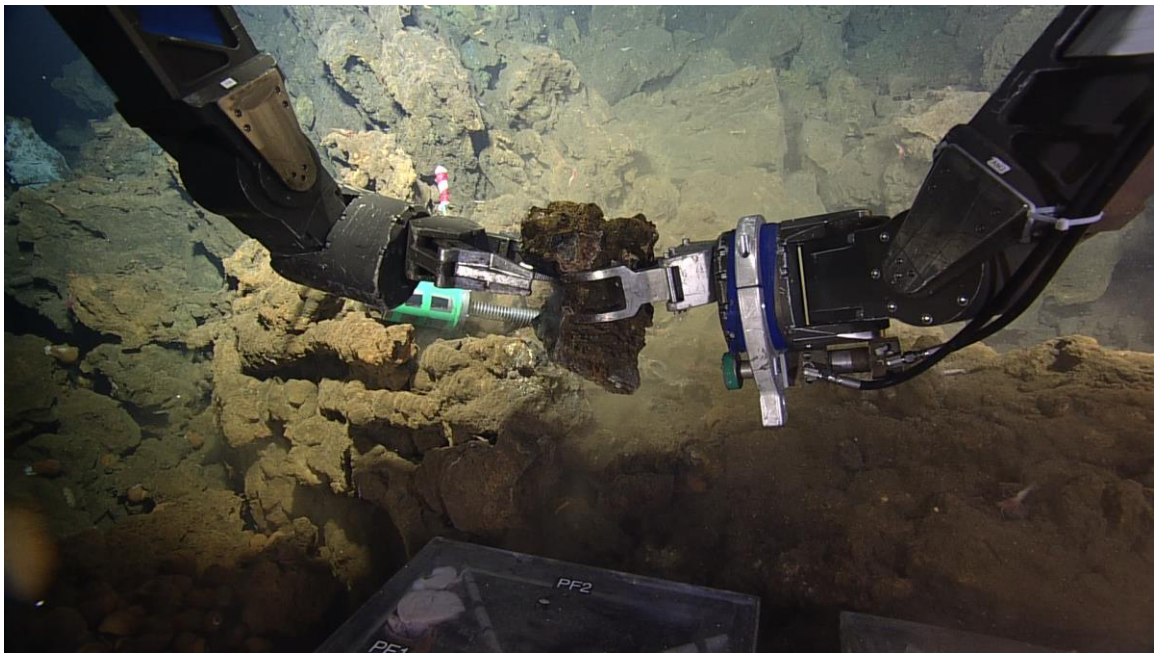

b.

Active chimney complex where D1919-R5 was collected. a) Black smoker chimneys are venting next to an inactive grouping of chimneys. b) Rock sample collected from the talus slope base beneath the active vents.

Hand Sample Description

This sample is comprised of two pieces, which were broken apart during the sampling process. In general, the sample consists of a fine-grained, porous, dark-grey to light-grey groundmass dominated by barite and sphalerite. In the larger of the two pieces, there are three potential examples of past and/or present fluid conduits. One of these exhibits a distinct yellow-gold chalcopyrite lining, while the other two appear to be clogged with late-stage vent infill. A slice through the smaller piece best shows that paleo-venting was stopped at some point, and subsequent mineralization occurred, filling in the fluid conduits. This infill material is dominated by chalcopyrite and coarse-grained bladed barite (~ 1 – 3 mm) and is far more porous than the general groundmass. Both sample pieces are quite oxidized (orange-brown crusts) and contain patches of intense orange-yellow colouration indicating a presence of realgar or orpiment.

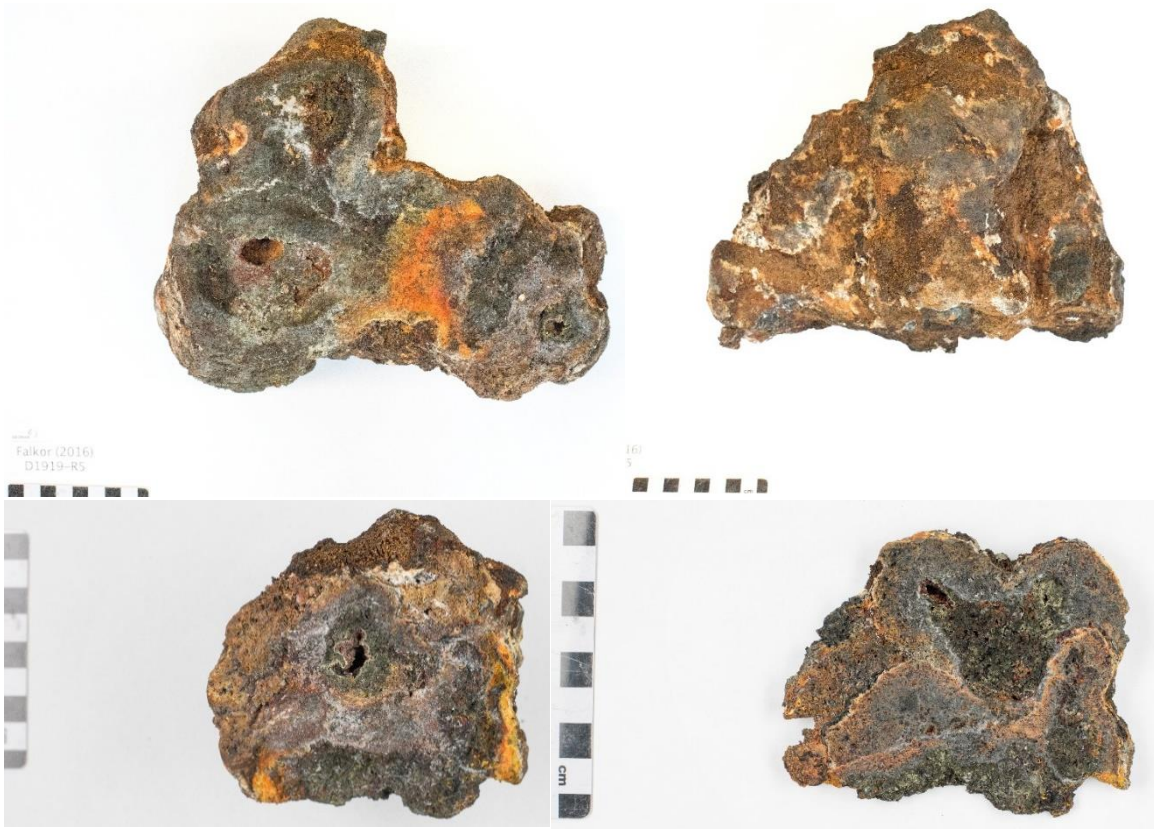

Hand samples for D1919-R5. Top left photograph shows the top-down view of the main chimney trunk. Top right photograph shows the weathered chimney wall exterior surface. Bottom right photograph shows a small piece that broke off the main chimney piece during sampling. Bottom right photograph is a slice through the small piece, was used for thin section analysis.

Thin section slab of D1919-R5. The thin section was cut from this face.

Mineral Abundances and Occurrences

Barite – 47%

Sphalerite – 25%

Chalcopyrite – 20%

Pyrite – 5%

Galena – ≤ 1%

Tetrahedrite – Tennantite – ≤ 1%

Amorphous Silica – ≤ 1%

There are two distinct zones observed in the sample thin section: (1) A sphalerite-rich groundmass with fine-grained barite, and (2) a more porous, chalcopyrite-rich zone with abundant large barite crystals. Barite crystals in the sphalerite-rich zone are mostly subhedral to euhedral, fine-grained bladed and tabular types with coarser crystals found in pore spaces. There is also some fine-grained radiating bladed and acicular crystals and plumose barite. In plumose texture, thin blades of barite are overgrown by pyrite masses and blebs and subsequently overgrown by sphalerite. Several extremely coarse-grained

subhedral to euhedral bladed and tabular crystals are present within the chalcopyrite-rich zone (up to 50 mm). Sphalerite is massive and present as overgrowths of fine-grained barite and early pyrite, as well as late overgrowth of massive chalcopyrite in the chalcopyrite-rich zone. Pyrite occurs as masses or circular blebs with disseminated colloform texture throughout the sample. These occurrences are overgrown by both massive sphalerite and chalcopyrite. Galena is typically massive and found within massive sphalerite as inclusions and as late overgrowth along the boundaries of massive sphalerite, chalcopyrite, and coarse-grained barite. Irregular, sometimes subhedral or triangular-shaped grains of tetrahedrite-tennantite are present in chalcopyrite-rich zones. They generally grow on the edges of massive chalcopyrite but can also be found in some abundance within massive sphalerite. Minor amounts of amorphous silica are found within the interstices of coarse-grained barite, massive chalcopyrite, tetrahedrite-tennantite, and massive sphalerite.

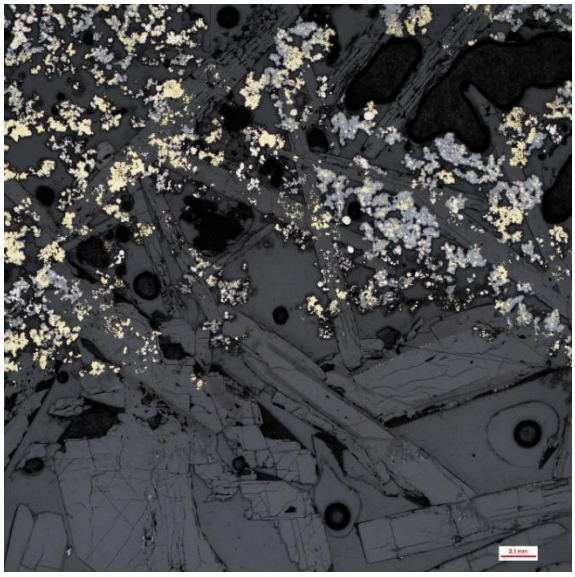

a.

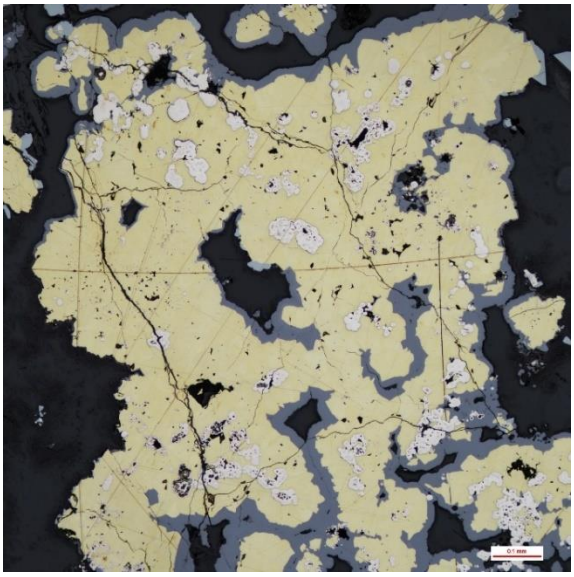

b.

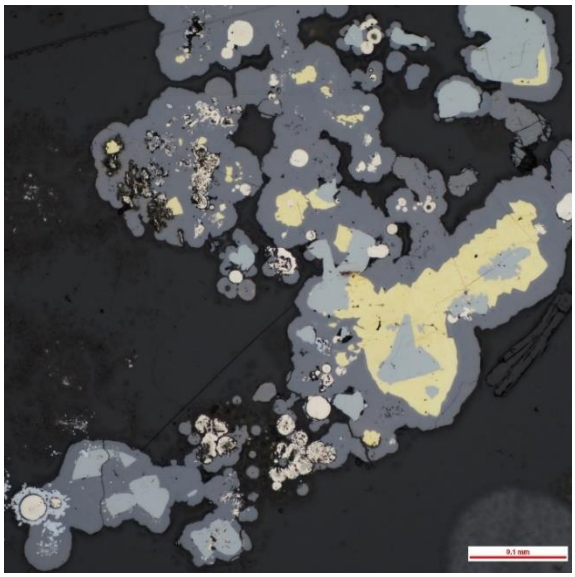

c.

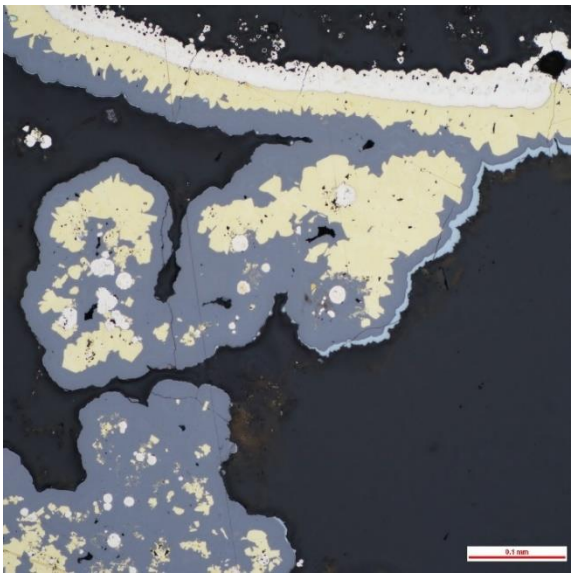

d.

Photomicrographs of sample D1919-R5. All photos are taken using reflected light. a) Extremely coarse-grained bladed and tabular barite grows in porous space. Overgrowth of fine-grained sulphides is common. b) Massive chalcopyrite and enveloped pyrite are thinly mantled by sphalerite. c) Tetrahedrite-tennantite is sometimes intergrown with massive chalcopyrite or overgrown by sphalerite. d) Wall of a mineralized pyrite ring is thinly mantled by chalcopyrite and subsequently overgrown by massive sphalerite. Thin mantling of galena may locally form.

D1919 – R6:

Site Description

This sample originates from the tip of one of two central active black smoker chimneys, present in the complex mentioned in the previous sample description. These vents were originally topped with beehive structures, until the ROV grab arm knocked them over, exposing a wide inner fluid conduit. The walls of these central chimneys also appear to contain smaller beehive structures, venting a similar black smoke. There are a few other adjacent chimneys that are taller. One of them is a very slender chimney, diffusely venting clear hydrothermal fluids, while the others are all inactive.

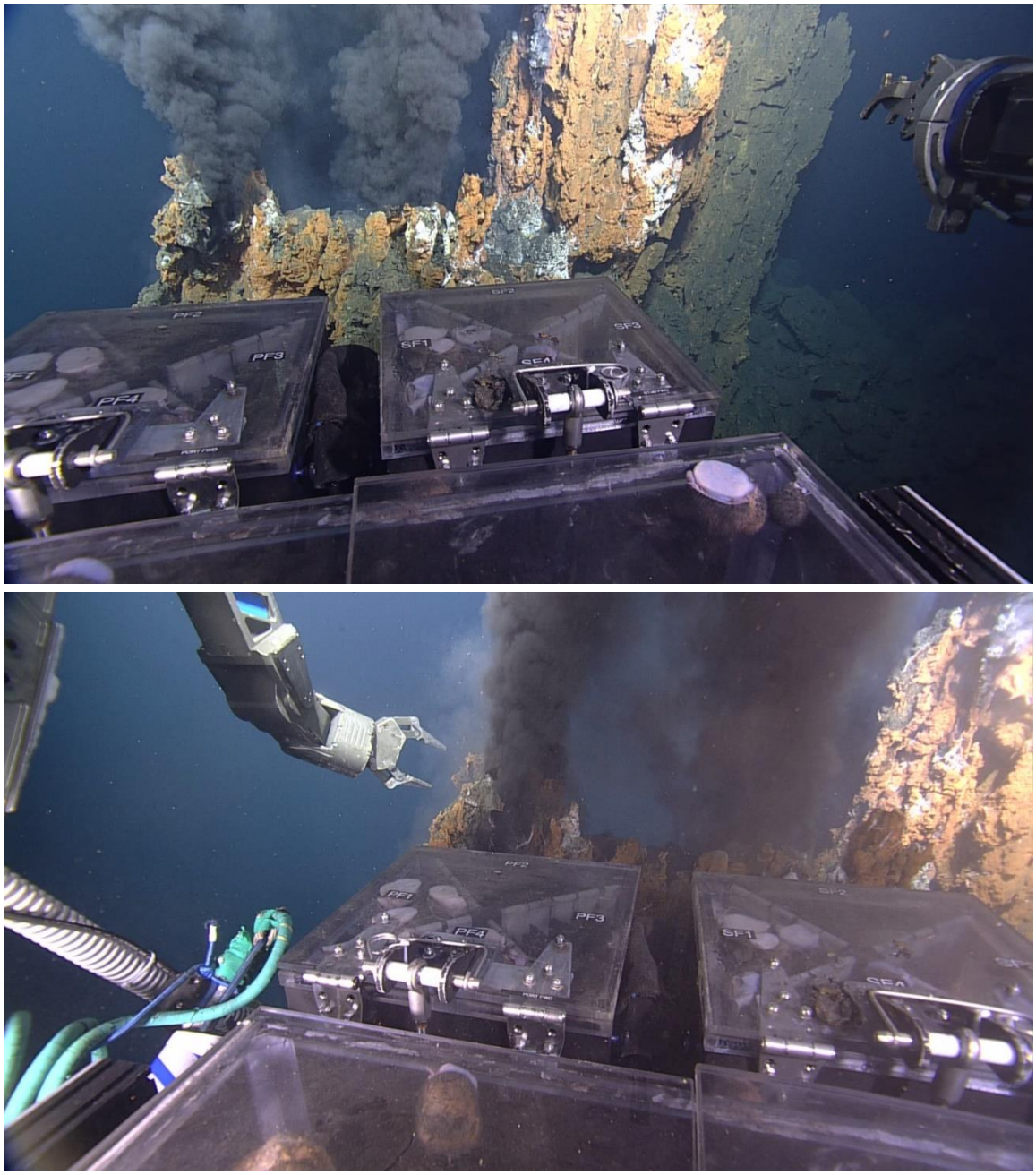

Active chimney complex where D1919-R6 was collected. Two major vents within the complex are venting black smoke.

Hand Sample Description

This sample consists of a grouping of two small pieces (D1919-R6A) and a larger piece (D1919-R6B) that are rather distinct. D1919-R6A has a fine-grained, porous, grey groundmass dominated by barite with abundant sphalerite, some pyrite, and minor galena and chalcopyrite. The two pieces both have one highly weathered, orange-brown surface

with pervasive white bacterial growth. The cut pieces show that oxidation infiltrates deep within the interior. D1919-R6B has a similar mineral assemblage, but is notably coarser-grained and more porous, and completely dominated by anhydrite with minor chalcopyrite. It also lacks any major surficial weathering.

Hand samples for D1919-R6. Top left and right photographs show fresh and weathered surfaces for D1919-R6A, respectively. Bottom left and right photographs show two sides of D1919-R6B, largely consisting of fresh sulphide chimney material.

a.

b.

Thin section slabs for sample D1919-R6. Thin sections were cut from these faces. a) D1919-R6A. b) D1919-R6B.

Mineral Abundances and Occurrences

R6A

Barite – 50%

Sphalerite – 35%

Pyrite – 10%

Pb-As sulphosalts – 3%

Chalcopyrite – 2%

Barite mostly occurs as small euhedral bladed or radiating acicular clusters. Towards the sample interior plumose texture is very common. Barite crystals are exclusively acicular towards the sample exterior and contain less sulphide overgrowth. The size of bladed crystals increases in areas of greater porosity, as well as the frequency of euhedral to subhedral tabular crystals. Late, euhedral bladed barite crystals occur within pore spaces, along the edges of massive chalcopyrite and sphalerite. Pyrite mostly occurs as small, rounded to semi-rounded blebs that often exhibit colloform texture. Pyrite blebs are very common, grown on the edges of plumose barite. Ovoid rings of pyrite form from the mineralization of vent organisms. Sphalerite is massive, particularly where there is greater porosity. Thin sphalerite overgrowth of fine-grained or plumose barite is common throughout the interior and becomes steadily absent towards the exterior. Dendritic sphalerite occurs locally within the interior, and contains fewer other phases compared to plumose texture. Minor massive chalcopyrite forms locally within small porous areas.

Subsequent overgrowths of late sphalerite line chalcopyrite in these areas. Chalcopyrite is also found as overgrowths of barite, where it likely has replaced sphalerite. Chalcopyrite disease of sphalerite occurs in very localized abundance. Moving away from the porous areas, chalcopyrite becomes almost absent. Pb-As sulphosalts occurs as disseminated inclusions within massive sphalerite. In some sphalerite it appears that initial sulphosalts are transitionally replaced, as it is sparsely contained within sphalerite giving it a patchy appearance. In these cases, Pb-As sulphosalts also become more abundant along the edges of sphalerite.

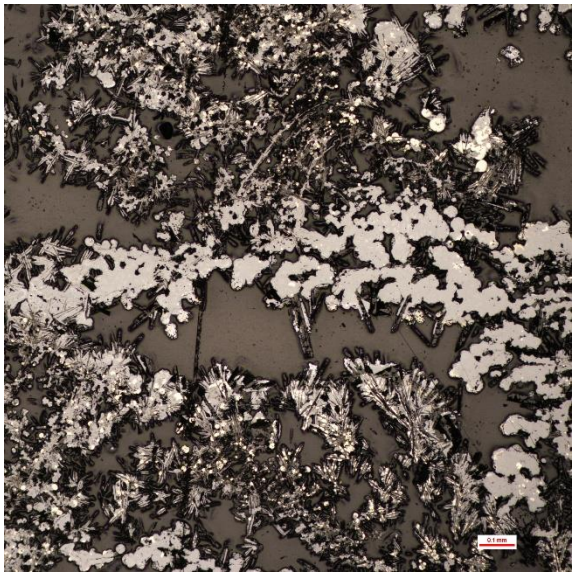

a.

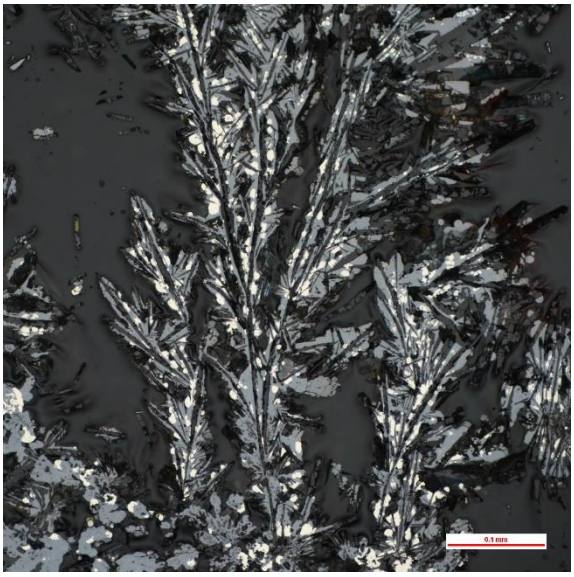

b.

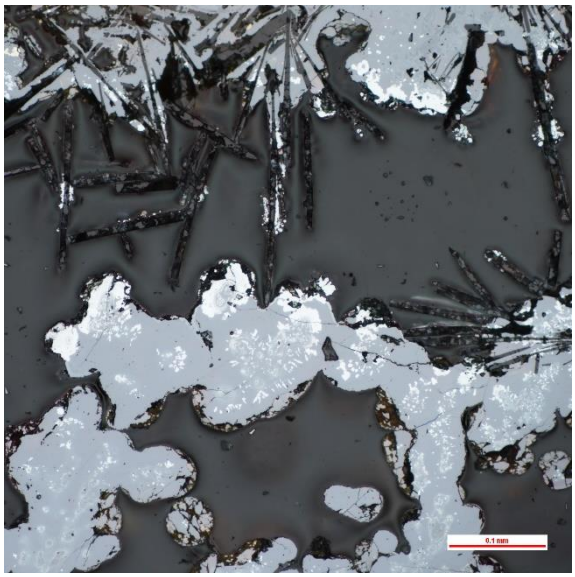

c.

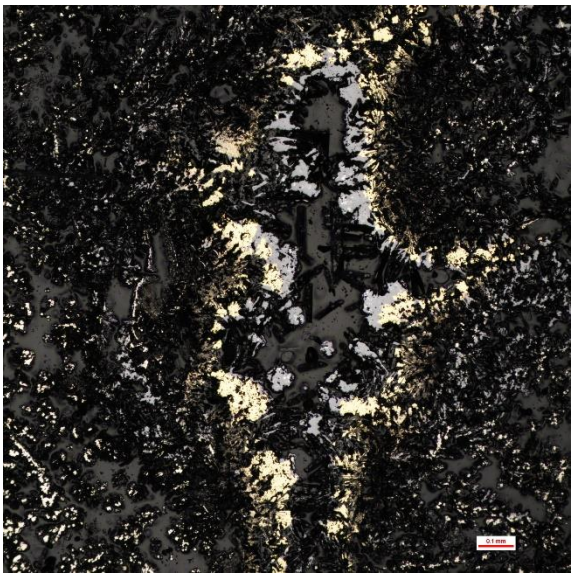

d.

Photomicrographs of sample D1919-R6A. All photos are taken under reflected light. a) Dendritic sphalerite with minor pyrite. Plumose texture in barite, overgrown by sphalerite

is very common. The general groundmass is extremely porous. b) Classic example of plumose texture, seen commonly throughout the sample. Pyrite mantles thin, bladed barite which is then overgrown by sphalerite. c) Pb-As sulphosalts intergrown with massive sphalerite. d) Localized massive chalcopyrite in open void space, overgrown by late-stage sphalerite. Late-stage euhedral bladed barite has also partially filled these voids.

R6B

Mineral Abundances and Occurrences

Anhydrite – 95%

Chalcopyrite – 5%

Pyrite – < 1%

Sphalerite – << 1%

Bornite – << 1%

Digenite – <<< 1%

Anhydrite has some elongate euhedral crystals, but are mostly subhedral to anhedral elongate, stubby, and fibrous masses. Grain size of anhydrite varies considerably, but the spatial distribution of crystals seems to be arbitrary. There are many compact clusters of very fine-grained crystals, while coarse-grained crystals occur generally within larger pore spaces. Chalcopyrite occurs mostly as very fine, disseminated grains on the edges of anhydrite or contained within some anhydrite crystals, suggesting that intergrowth is common. Larger massive chalcopyrite grains are present in areas with greater porosity. Minor pyrite can be found mantling chalcopyrite with minor massive sphalerite. These grains are typically small irregular growths, but a few subhedral or euhedral grains were observed. Sphalerite only occurs as thin overgrowths of pyrite and chalcopyrite. Bornite grains are irregular with massive chalcopyrite. Exsolution lamellae are absent and bornite grains are exclusive to the interior of select chalcopyrite grains. Digenite only appears in one location and is associated with bornite.

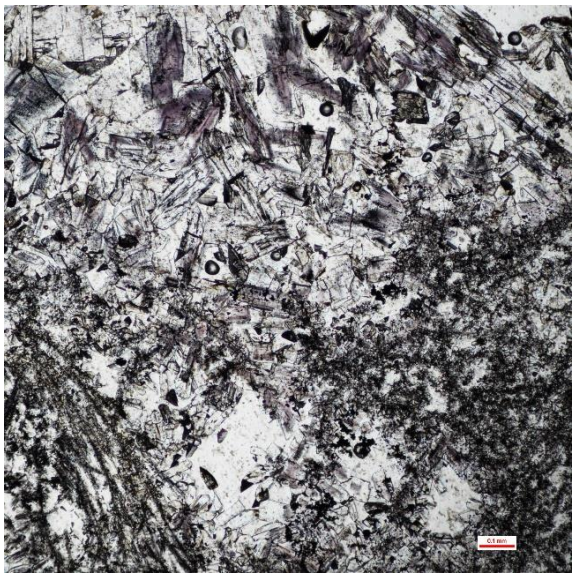

a.

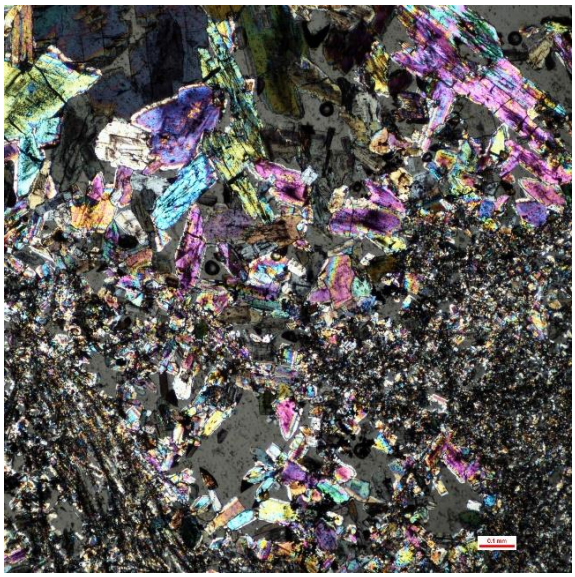

b.

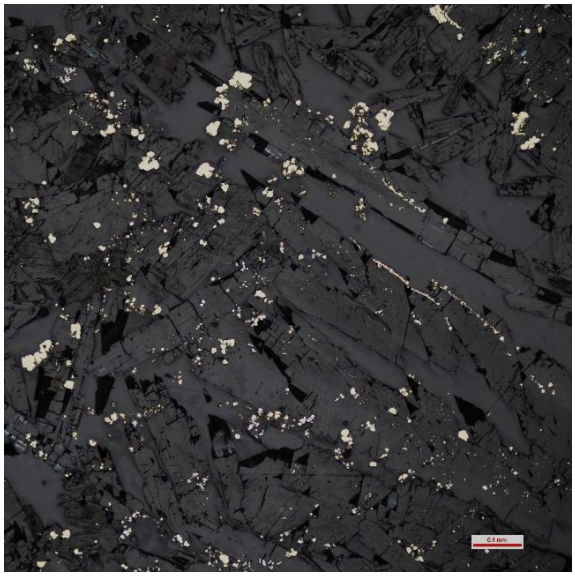

c.

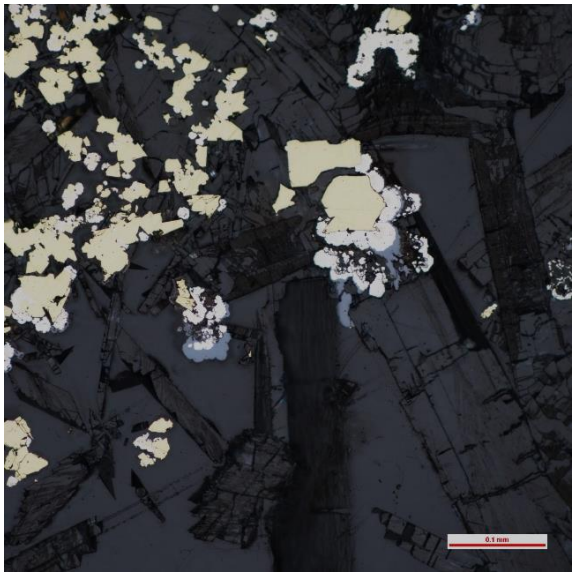

d.

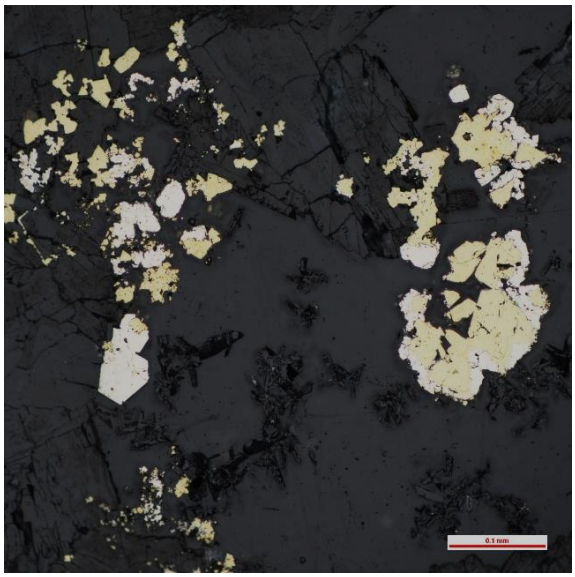

e.

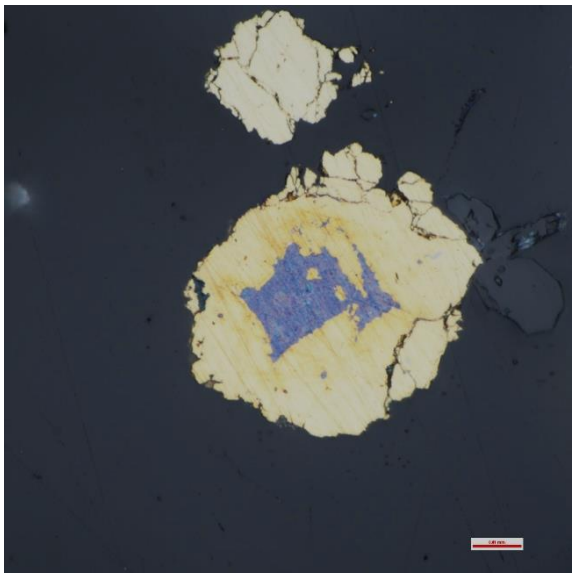

f.

Photomicrographs of sample D1919-R6B. All photos are taken under reflected light, except for a and b, which are taken using transmitted light. a) The sample groundmass is entirely dominated by anhydrite. b) Cross-polarized light (XPL) highlights the different crystal habits of anhydrite: (1) coarse, subhedral to anhedral, elongate and stubby crystals; (2) thin fibrous crystals; and (3) fine-grained compact masses. c) Fine-grained disseminated chalcopyrite mantles course anhydrite crystals. d) Chalcopyrite is mantled by pyrite and trace sphalerite. e) Euhedral to subhedral pyrite overgrowing chalcopyrite. f) Rare occurrence of bornite and digenite within chalcopyrite.

D1920 – R2:

Site Description

Three samples were grabbed from the base of a group of small, inactive sulphide chimneys. The unusually short chimneys appear to be heavily oxidized and suggest that former hydrothermal activity was short-lived. This is also supported by the reduced size and abundance of sulphide talus at the base of these chimneys. Despite this, the site does exhibit minor active venting, in perhaps the earliest stages of chimney growth. There are very short (a few centimetres), cone-shaped vents diffusely venting low-temperature "shimmering water". The young vents are covered in white to yellow-white crusts likely composed of barite or anhydrite, as well as bacterial mats.

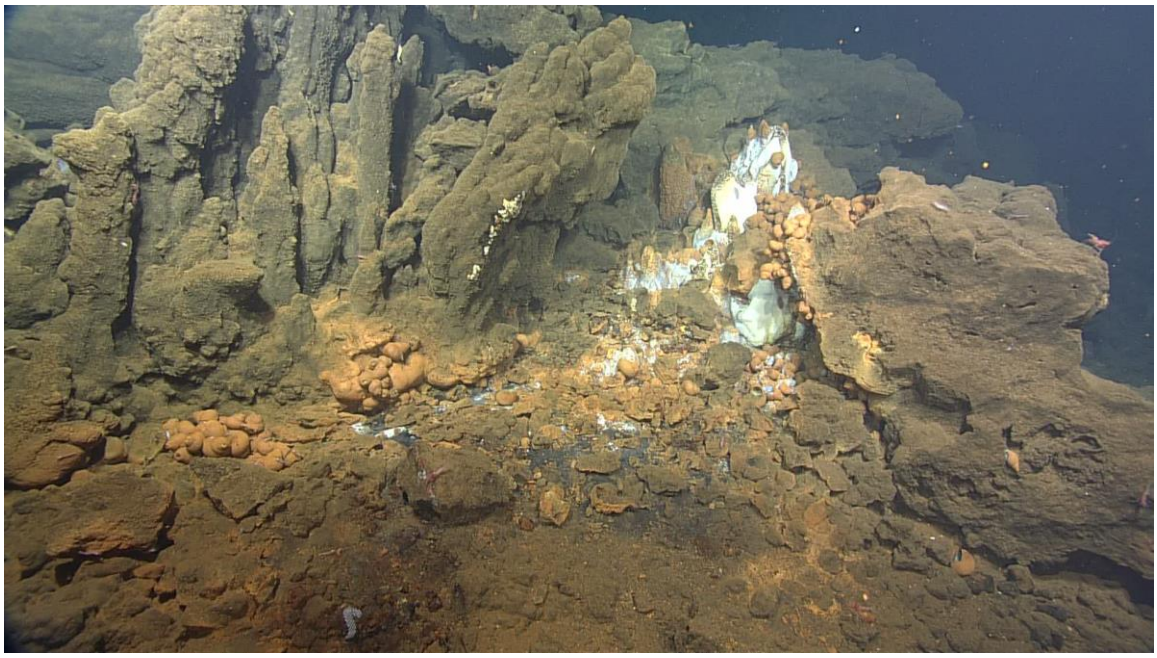

a.

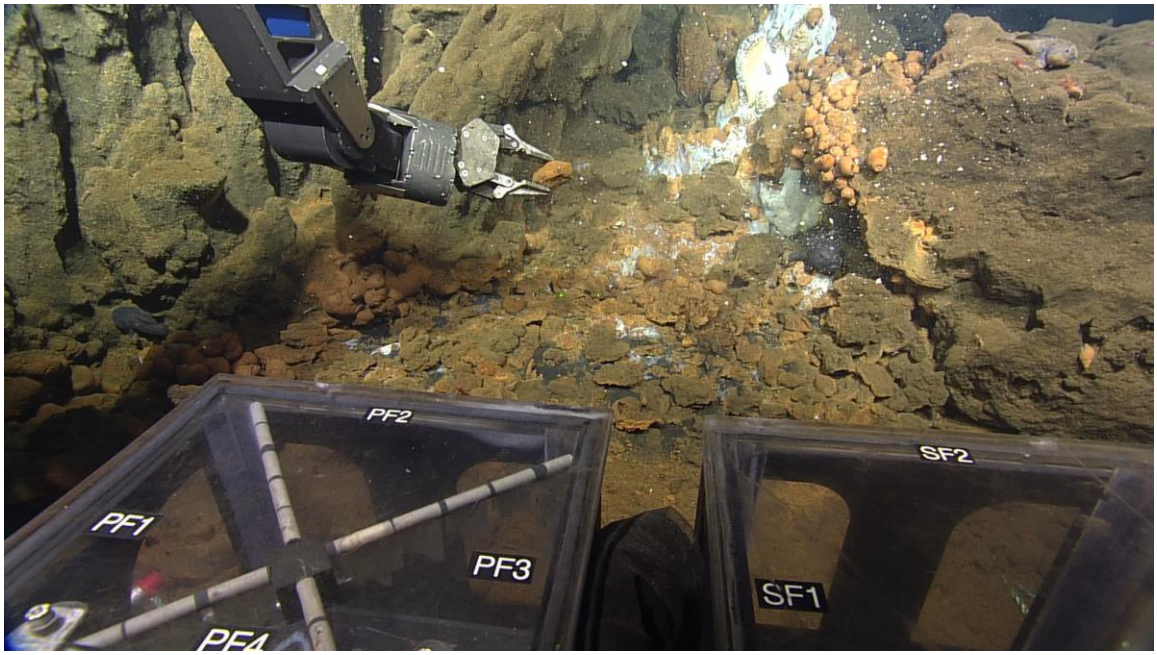

b.

Site where D1920-R2 was collected. a) Group of inactive sulphide chimneys surrounding an isolated spot of low-temperature, clear-fluid venting. b) ROV ROPOS collecting the small sulphide sample.

Hand Sample Description

The sample has a relatively homogeneous interior mineralization compared to many of the other samples. The exterior surface of the hand sample is heavily oxidized and does show any fresh surfaces. A slice of the interior displays a fine-grained, porous, dark-grey groundmass, mostly composed of barite, sphalerite, and galena with minor chalcopyrite. The sample has a light orange coloured rind of barite and oxidized sulphides that range in thickness from about 2 mm to as much as 1 cm. A unique dull black layer of Mn-oxide cuts through the exterior rind.

a. **b.**

Hand sample for D1920-R2. a) Highly weathered exterior. b) Middle of the sample interior. Thin Mn-oxide rind can be seen on the right-hand side.

Thin section slab for D1920-R2. Thin section was cut from this face.

Mineral Abundances and Occurrences

Barite – 67%

Sphalerite – 25%

Galena – 4%

Pyrite – 2%

Chalcopyrite – 1%

Tetrahedrite – Tennantite – ≤ 1%

Amorphous Silica – < 1%

Euhedral to subhedral, bladed barite crystals are very common within the sample interior, and are sometimes radiating, while thin acicular barite crystals are generally only found towards the exterior. Grain size varies with smaller, thinner crystals are found towards the exterior and larger crystals within some interior pore spaces. Plumose barite is also present within the interior groundmass, where it is overgrown by massive sphalerite. Massive sphalerite also largely overgrows pyrite and minor chalcopyrite and is closely associated with galena. Within the interior dendritic sphalerite is observed but is uncommon. Massive or anhedral grains of galena are found within massive sphalerite and as late-stage growth observed on the edges of coarse-grained barite, sphalerite, and tetrahedrite-tennantite, although the former growth type is more common. Pyrite mostly occurs as small, rounded to sub-rounded blebs or in masses. It is also seen forming a thick, discontinuous layer towards the exterior overgrowing fine-grained barite. Pyrite masses and blebs exhibit a weak colloform texture and appear to have alternating thin bands of sphalerite. Pyrite blebs do not commonly mantle barite, unlike what is generally observed in early pyrite from other samples. Chalcopyrite occurs sparsely within the groundmass, and only appears as disseminated anhedral grains within massive sphalerite and along the edges of pyrite blebs. Tetrahedrite-tennantite is typically found as anhedral to subhedral or triangular-shaped grains that are associated either with chalcopyrite or mantled by late galena. Some amorphous silica occurs within the interstices of coarse-grained barite and massive sphalerite. The sample exterior exhibits a Mn-oxide layer about 1 – 3 mm thick, surrounded by barite on both sides.

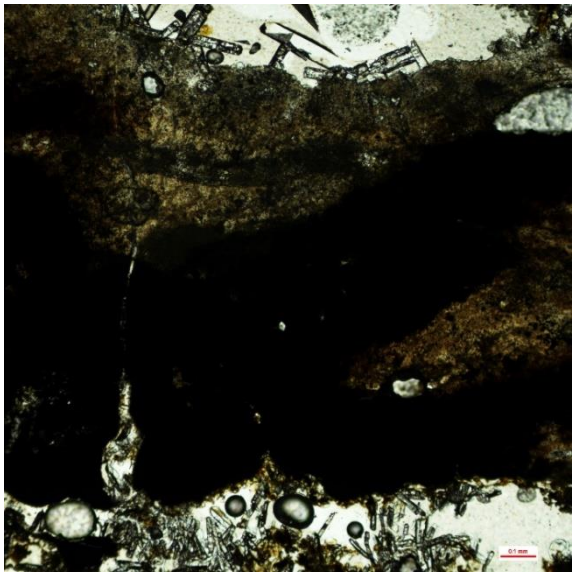

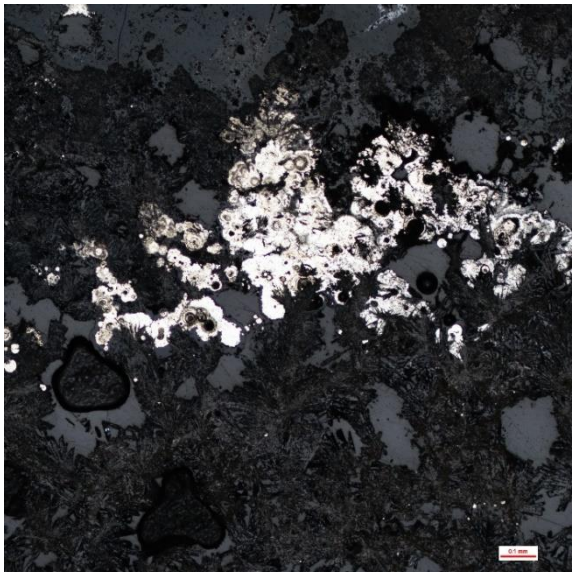

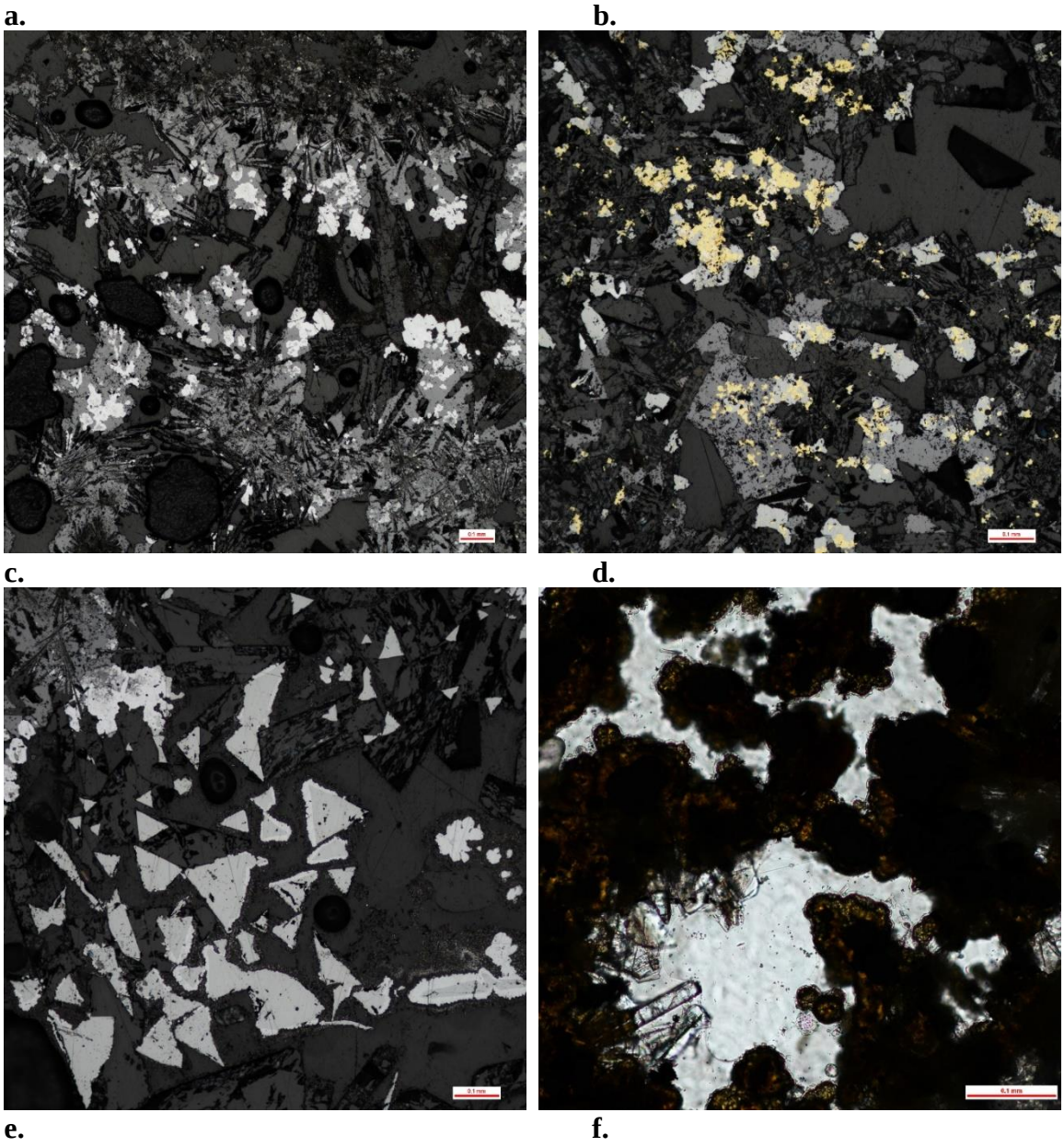

Photomicrographs of sample D1920-R2. All photos are taken using reflected light except for a and f, which are taken using transmitted light. a) Thick exterior layer dominated by barite features a layer of Mn-oxide. Bladed barite grows on both sides of this layer. b) Discontinuous, massive pyrite cluster overgrows fine-grained acicular barite in the sample exterior. c) Coarse-grained barite, massive sphalerite, and late-stage galena are commonly found together within porous space. d) Sparse occurrence of chalcopyrite commonly forms with tetrahedrite-tennantite. e) Galena is commonly seen thinly mantling tetrahedrite-tennantite. f) Thin layers of late-stage amorphous silica can sometimes be seen forming around barite and late-sulphides (in this case sphalerite).

D1920 – R3:

Site Description

Three sample pieces were collected at the base of the talus slope associated with a small chimney complex. The slope is small and steep-sided, with an abundance of sulphide talus material. Atop the slope, the small chimney complex contains several small white-coated, beehive structures that are diffusely venting clear hydrothermal fluids. Most of the chimney tops are inactive, aside from a couple of beehive topped spires.

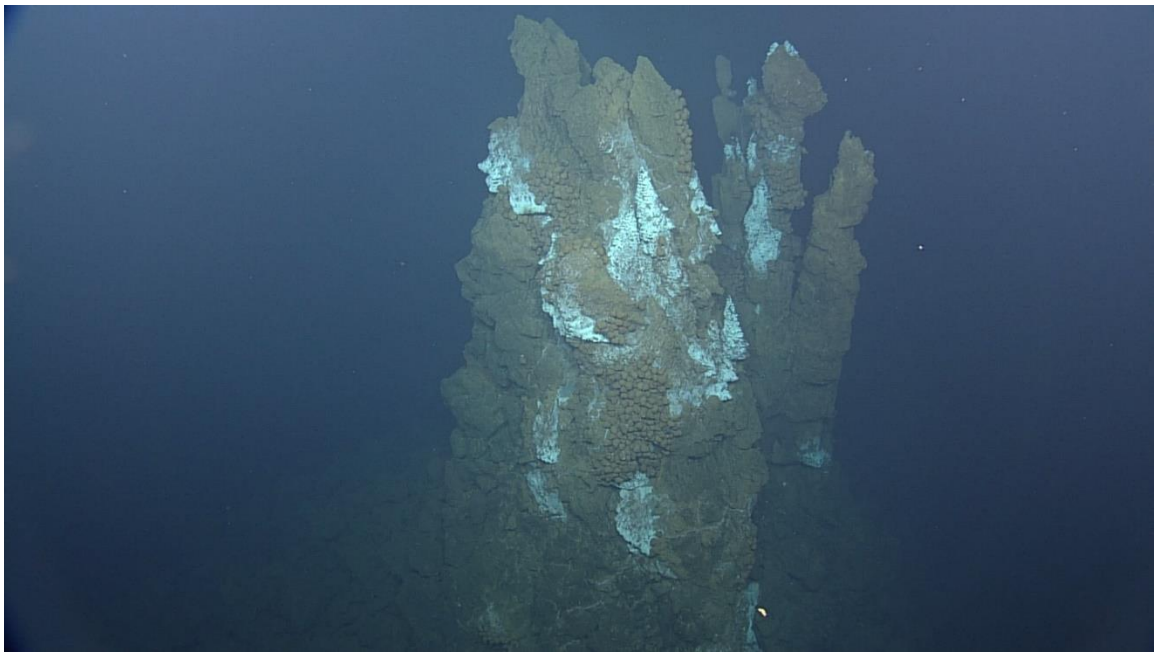

a.

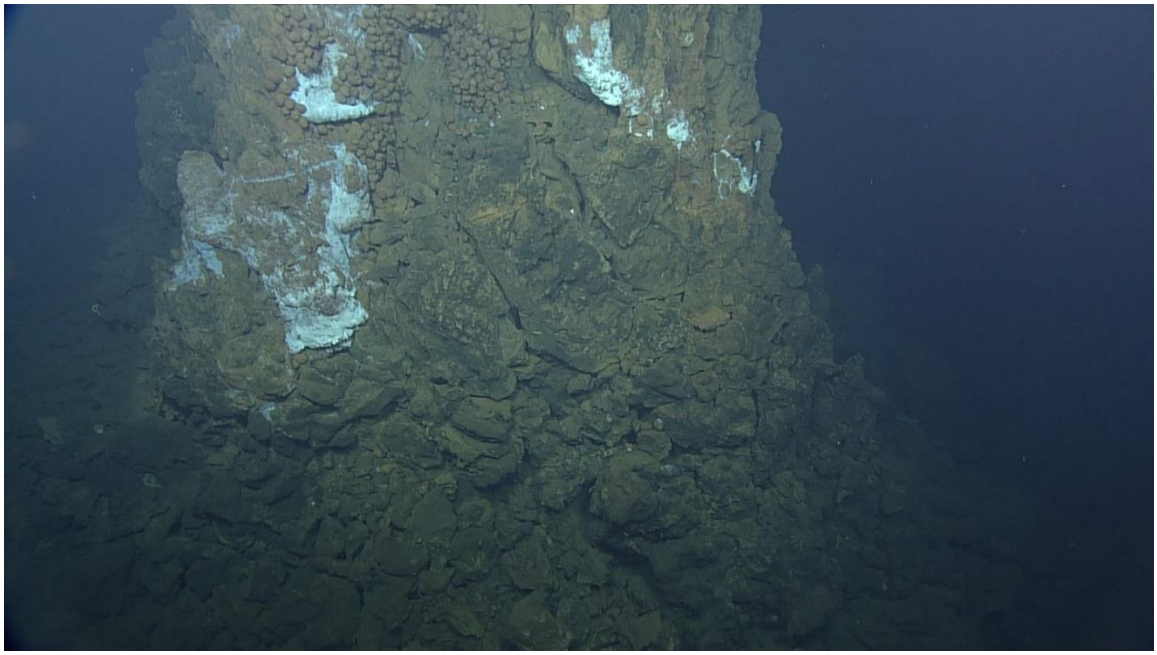

b.

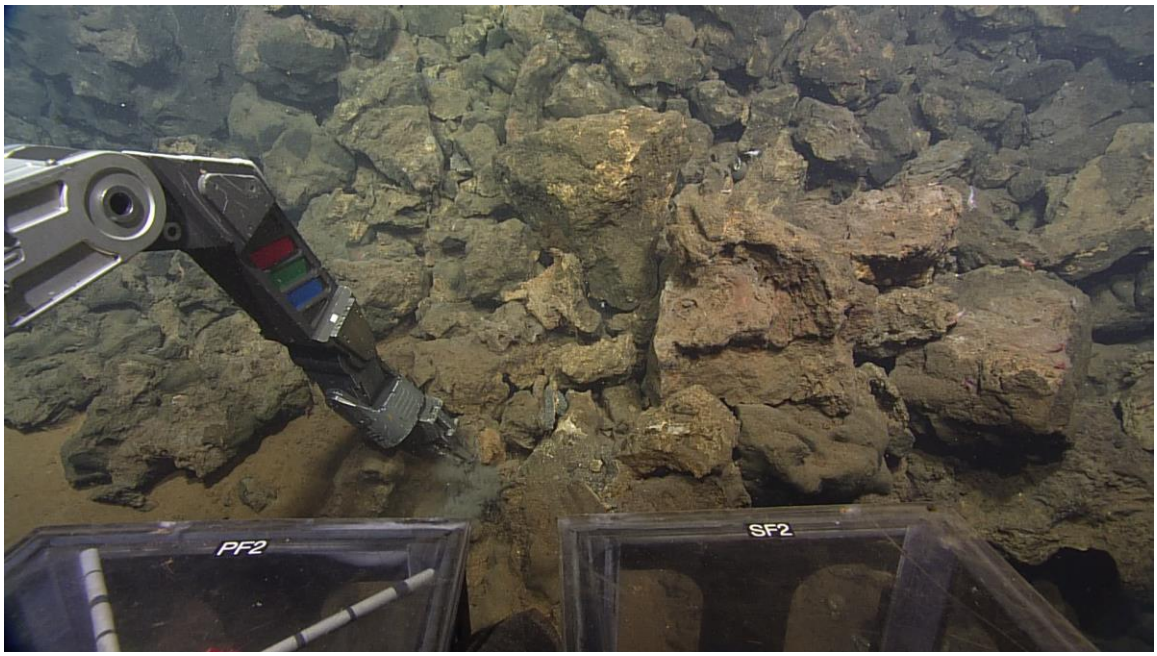

c.

Site where D1920-R3 was collected. a) Largely inactive chimney complex, with white-coated beehives. b) Steep-sided talus slope at the base of the chimney complex. c) ROV ROPOS collecting the rock sample.

Hand Sample Description

This sample has a light-grey to dark-grey fine-grained groundmass, with relatively low porosity. It mainly consists of barite and sphalerite, with minor pyrite and chalcopyrite. Portions of the fine-grained groundmass exhibit a vitreous luster, due to the large presence of barite. Intense, orange-coloured minerals (realgar and/or orpiment) may be present in a thin distinct band within the groundmass. A clear majority of the exterior surface is covered in a red-brown iron-oxide coating.

Hand sample for D1920-R3.

Thin section slabs for D1920-R3. Thin section was cut from this face.

Mineral Abundances and Occurrences

Barite – 50-55%

Sphalerite – 35-40%

Pyrite – 6%

Chalcopyrite – 3%

Pb-As sulphosalts – ≤ 1%

Covellite – < 1%

Thin, bladed, and radiating acicular barite crystals are pervasive throughout the sample. Plumose texture in barite is very common within the interior. These barite crystals are often mantled by pyrite and are almost always overgrown by massive sphalerite. Crystal sizes are quite small within the interior but increase in size within some pore spaces. Pyrite mostly occurs as small, disseminated blebs but may also form in masses, with colloform banding, or as rare framboids. Thin ovoid pyrite rings are common and are infilled by barite, sphalerite, pyrite and minor to trace chalcopyrite and covellite. The rings are typically completely infilled by these other minerals. Massive sphalerite overgrows much of the pyrite and barite present in the sample. Growth is thicker in more porous space and is often accompanied by minor massive chalcopyrite. Transmitted light highlights that the massive sphalerite has a strong compositional zoning, with dark Fe-rich, Zn-poor inner mineralization and lighter Fe-poor, Zn-rich outer mineralization. Chalcopyrite occurs locally as massive growths along the edges of massive sphalerite growths in areas of increased porosity. Some of this chalcopyrite also appears to be intergrown with sphalerite or overgrown by it from subsequent mineralization. Chalcopyrite disease is present in trace abundance with massive sphalerite as well. Late-stage Pb-As sulphosalts are grown on the edges of some chalcopyrite and sphalerite within areas of increased porosity. These grains are mostly anhedral to subhedral clusters of grains with some rare euhedral forms. Small, irregular-shaped grains of covellite are dispersed throughout the sample interior and may account for replacement of chalcopyrite. A thin Fe-Mn-oxide rind bounds the sample interior on both ends. This rind is largely composed of fine-grained bladed to acicular barite with very fine-grained sphalerite and pyrite

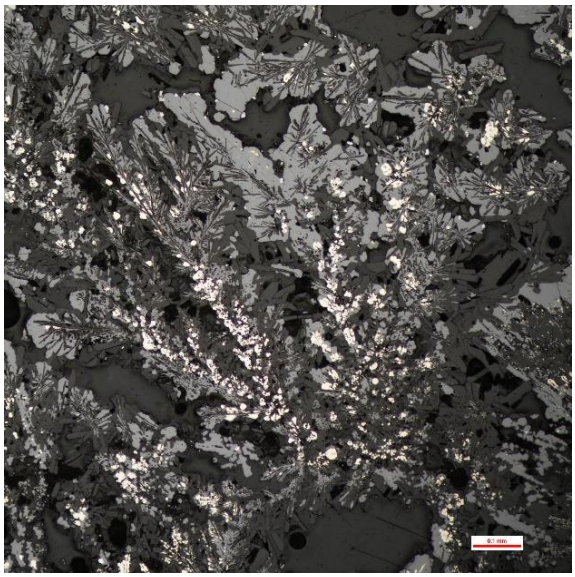

a.

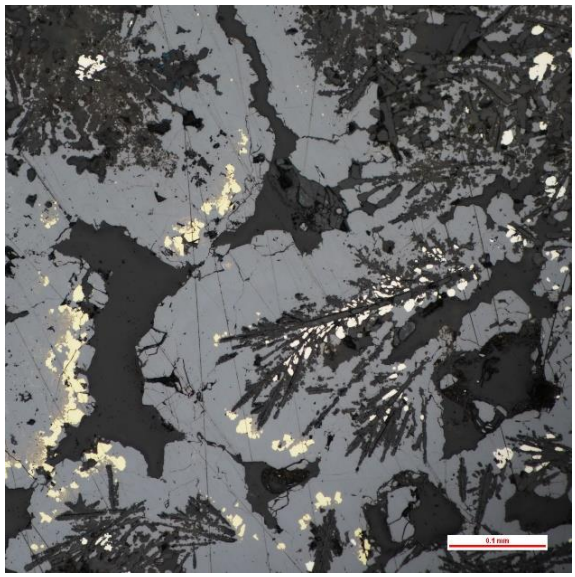

b.

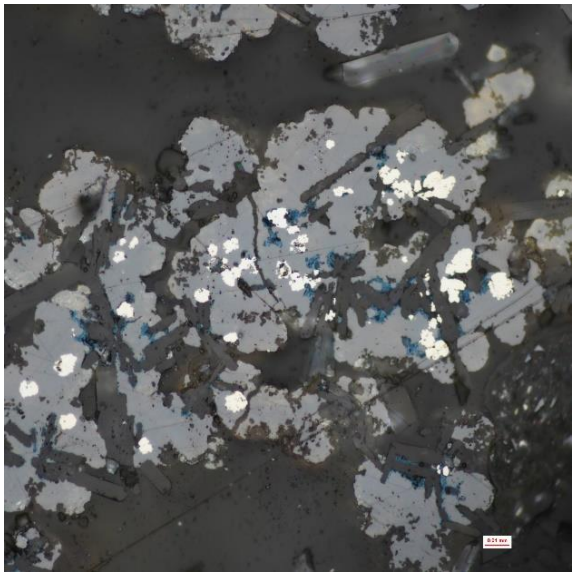

c.

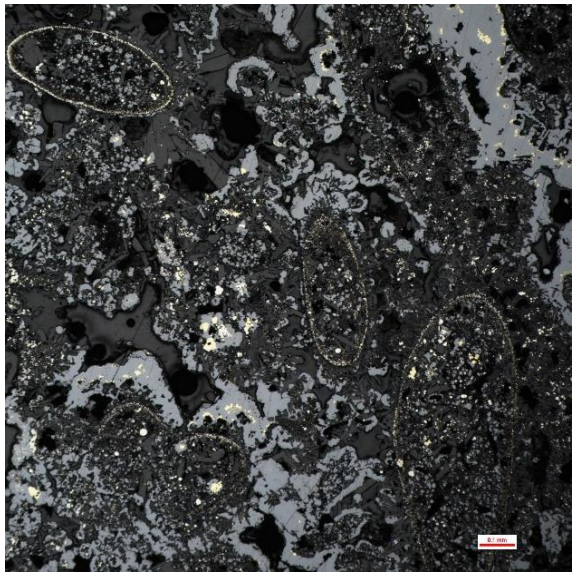

d.

Photomicrographs of sample D1920-R3. All photos are taken under reflected light. a) Plumose texture in barite is seen pervasively within the interior. Barite is commonly mantled by pyrite and overgrown by massive sphalerite. b) Close-up view of minor chalcopyrite intergrown with massive sphalerite overgrowth. Plumose texture in barite with mantled pyrite. c) Small, subhedral blebs of pyrite within massive sphalerite are also associated with trace covellite. d) Barite- and sphalerite-dominated groundmass contains several thin, ovoid pyrite rings.

D1920 – R5:

Site Description

This sample was collected from a gently dipping talus slope, at the base of what appears to be an inactive chimney complex. The piece of sulphide was located amidst a multitude of large sulphide talus blocks and extinct sulphide chimneys. The high degree of oxidation on the walls of the chimneys, as well as the apparent absence of biological communities suggest that the site is inactive. Unfortunately, the dive videos do not provide a very good viewing of this.

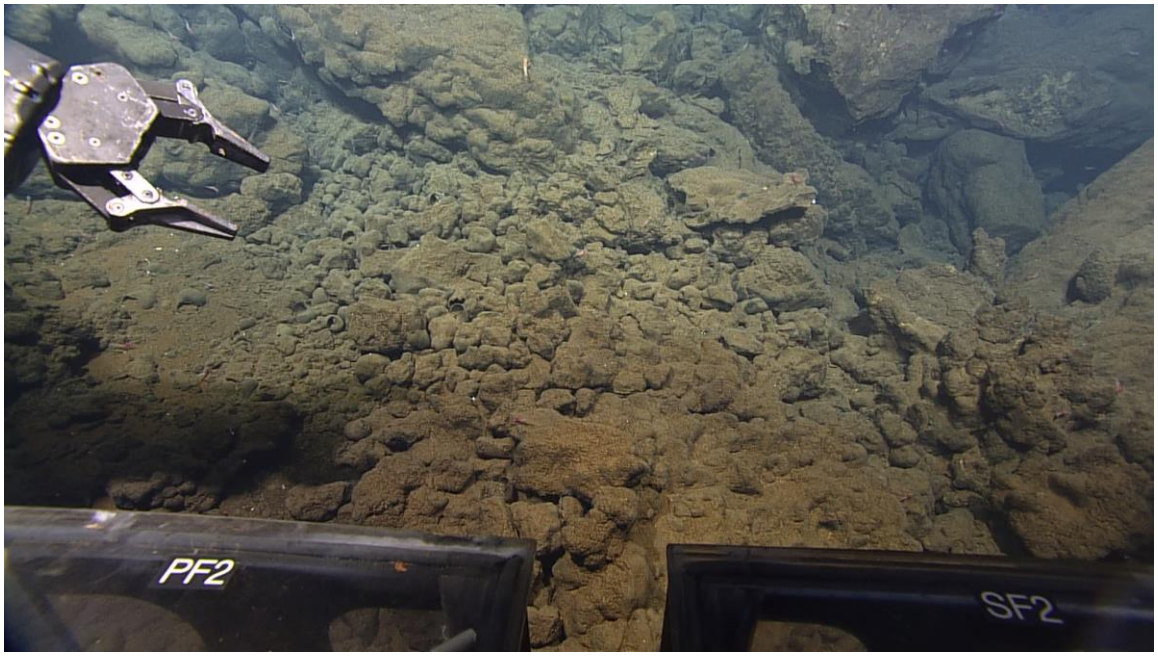

Site where D1920-R5 was collected amongst a pile of sulphide talus.

Hand Sample Description

This sample is a small piece of sulphide material, which has some interesting features. It is composed of a dense, low porosity, dark-grey groundmass rich in barite and chalcopyrite with some pyrite. While much of the groundmass is fine-grained (<< 1 mm), there are several localized vugs of coarse-grained chalcopyrite (~ 0.5 – 1 mm) and large bladed barite crystals (~ 1 – 2 mm). Approximately half of the sample shows the heavily oxidized orange-brown exterior. The exterior also exhibits a very minor occurrence of dull-green atacamite in small, clustered masses (up to 1 cm).

Hand sample for D1920-R5. The photograph shows both the fine-grained interior and the heavily oxidized exterior.

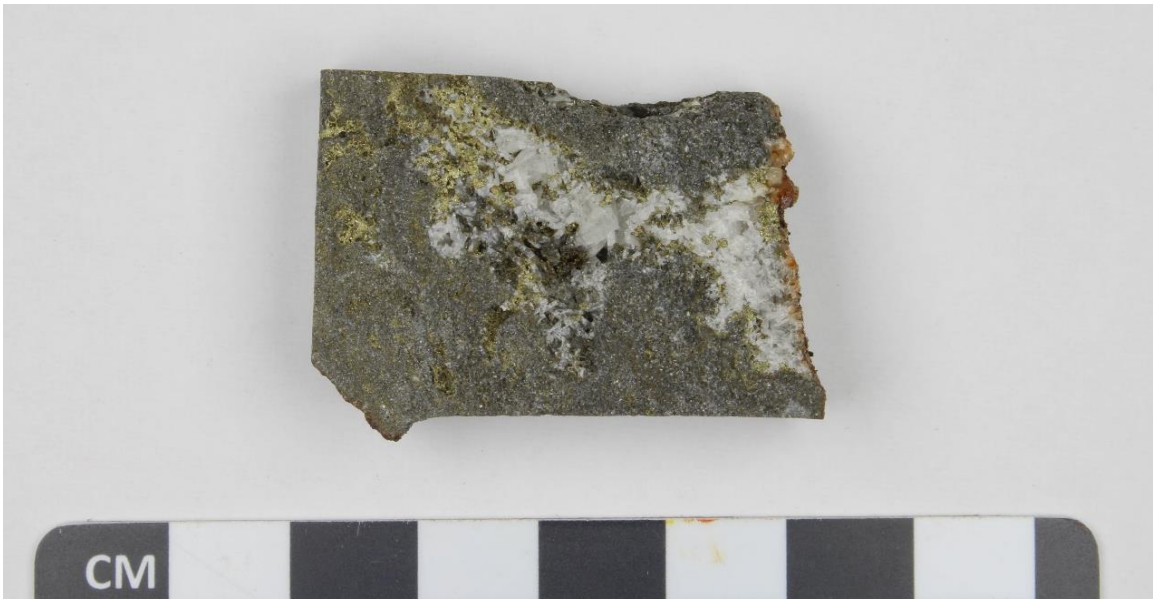

Thin section slab for D1920-R5. Thin section was cut from this face.

Mineral Abundances and Occurrences

Barite – 70%

Chalcopyrite – 20-25%

Pyrite – 5-10%

Barite occurs mostly as subhedral to euhedral, fine-grained bladed and tabular crystals. There are several extremely coarse-grained subhedral to euhedral bladed and tabular crystals (~ 50 mm). These large crystals are present in one main cluster, which can easily be seen even in the hand sample images. Plumose barite is present within the main groundmass but is not nearly as common as bladed barite. As observed in other samples, pyrite commonly is seen mantling plumose and bladed barite crystals. Distinct subhedral and rare euhedral pyrite also occurs within the porous, massive chalcopyrite. Disseminated, massive to tiny circular blebs of pyrite are commonly overgrown by massive chalcopyrite. In most cases chalcopyrite completely envelops these pyrite masses and blebs. There is no visible trace of sphalerite or galena.

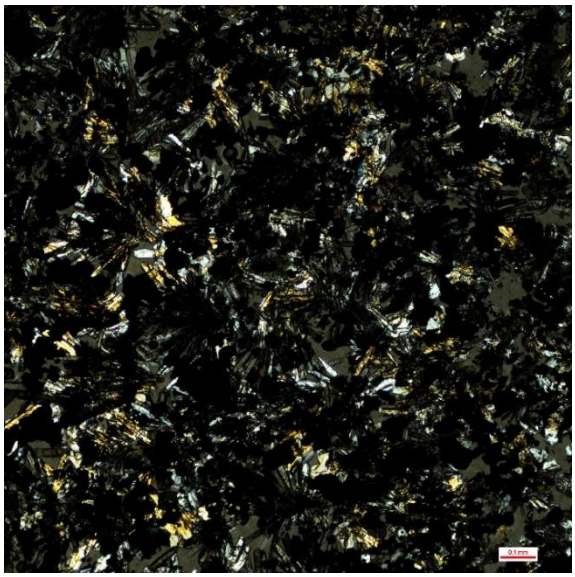

a.

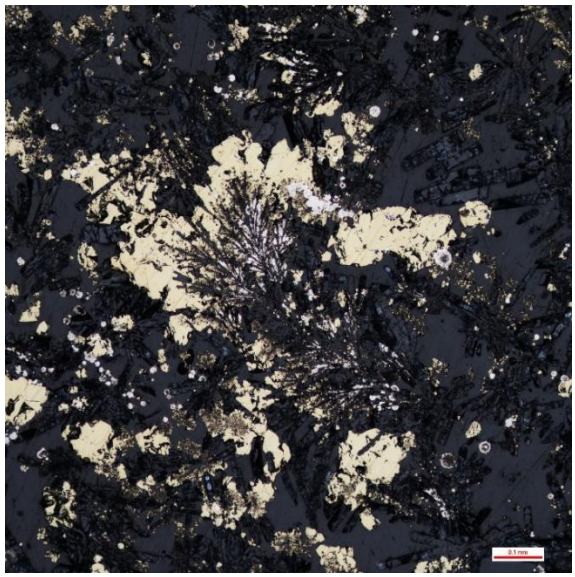

b.

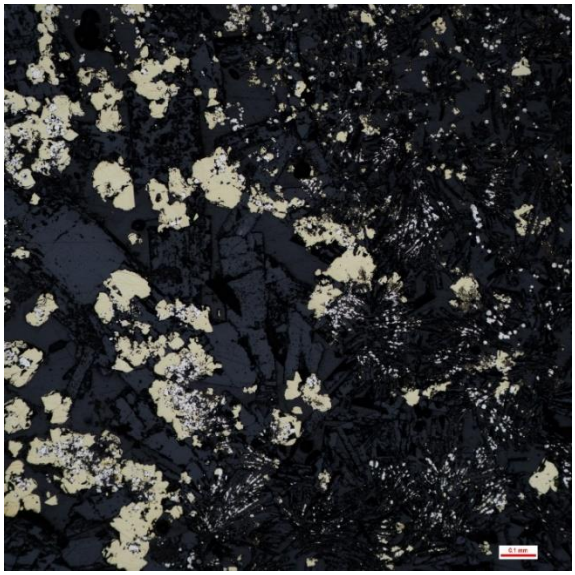

c.

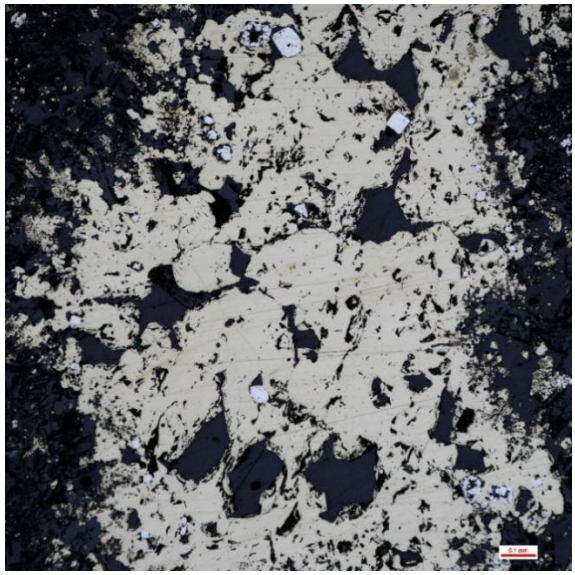

d.

Photomicrographs of sample D1920-R5. All photos are taken under reflected light, except for a, which was taken using transmitted light. a) General interior groundmass consisting of relatively fine-grained bladed barite and sulphide growth (black, isotropic grains). b) Plumose barite texture. Thin bladed barite is mantled by pyrite and subsequently overgrown by massive chalcopyrite. Surrounding bladed barite represents a separate event of formation. c) Porous space often contains coarse-grained euhedral bladed barite and extensive massive chalcopyrite mineralization. d) Pore spaces can also contain thick mineralization of massive chalcopyrite. In these growths there is often euhedral to subhedral pyrite within.

D1920 – R7:

Site Description

This sample was collected from the flanks of a large, steep-sided massive sulphide mound. The mound slope is characterized by scattered blocks of sulphide material, as well as a high abundance of fine, red metalliferous sediment. A top the mound slope is a large central chimney complex with white, bacteria-coated chimneys that are diffusely venting clear hydrothermal fluids. Higher temperature grey to black smoke is also venting from small accessory chimneys along the walls of the complex. Some of the peripheral extinct chimney exteriors are lined with thin, white cracks of bacterial mats; a feature not yet observed in the video records.

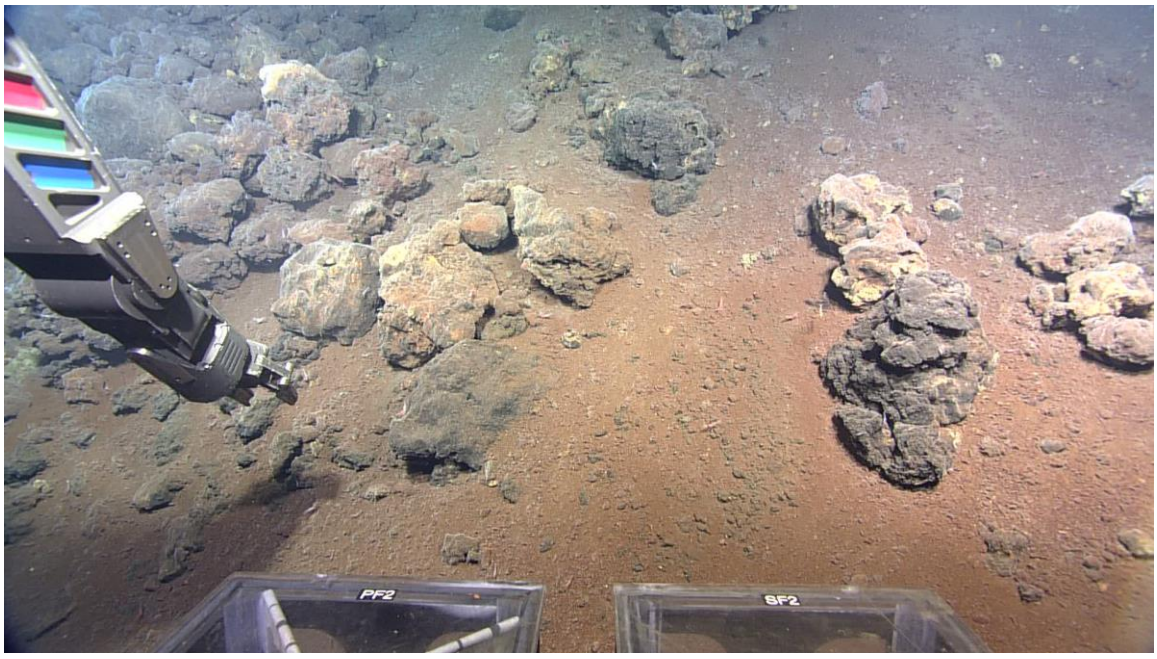

Heavily sedimented talus slope where samples D1920-R7, D1920-R8, and D1920-SED are collected. The position of the ROV arm is where D1920-R7 was collected.

Hand Sample Description

Most of the interior is defined by a fine-grained, slightly porous, dark-grey groundmass. There are some light-grey sections exhibiting slightly larger crystal sizes. Its composition primarily consists of barite and sphalerite, with some chalcopyrite and minor pyrite. There are localized vugs dominated by pyrite, with an abundance of chalcopyrite, and coarse-grained barite. The exterior is covered in a pervasive red-brown iron-oxide coating with some very localized growths of dull-green atacamite. It may be worth noting that the sample is relatively heavy for its size.

Hand sample for D1920-R7. The photograph shows both the fine-grained fresh surface and heavily oxidized exterior.

Thin section slab for D1920-R7. Thin section was cut from this face.

Mineral Abundances and Occurrences

Barite – 50% (interior), 20% (exterior)

Sphalerite – 20 – 25% (interior), 2% (exterior)

Chalcopyrite – 20 – 25% (interior), 18% (exterior)

Pyrite – 4% (interior), 60% (exterior)

Galena - < 1%

Covellite – < 1%

The thin section is divided into two sections; (1) the main interior groundmass abundant in barite, sphalerite, and chalcopyrite, and (2) the exterior rind dominated by pyrite. Barite commonly occurs as euhedral to subhedral bladed and tabular crystals, or fine-grained bladed crystals sometimes forming in compact, radial masses. Plumose texture in barite is uncommon, and contains little sulphide overgrowth, which is rather unique. Lastly, rare acicular crystals are present in the exterior rind. Barite crystals have two main size groups, with smaller crystals present in the interior groundmass and exterior rind, and larger crystals along the walls of porous spaces (seen best between interior and exterior sections). Massive pyrite is the dominant mineral within the exterior rind. Within the interior groundmass it occurs mostly as small, disseminated blebs and framboids grown on the edges of bladed barite crystals. Colloform growths are present as well and some contain chalcopyrite within their center. Massive sphalerite is common in the sample interior where it has overgrown barite and pyrite. It can also be found rimming chalcopyrite grains. Within the exterior rind, sphalerite and galena have large subhedral to euhedral grains that are contained within massive pyrite. This occurrence is quite unusual; however, the sphalerite grains may instead be wurtzite, a ZnS polymorph. Chalcopyrite

can be found as irregular-shaped grains throughout both sections of the sample. It can commonly be found overgrowing pyrite within the interior, and forms intergrowths with massive sphalerite. In the exterior rind it occurs as small inclusions in massive pyrite. Rare, fractured grains of pyrite contain chalcopyrite as infill material. Small anhedral grains of covellite occurs within the open space between the interior and exterior layers, where it has likely replaced chalcopyrite. Here it is found rimming barite, sphalerite and is contained within chalcopyrite grains.

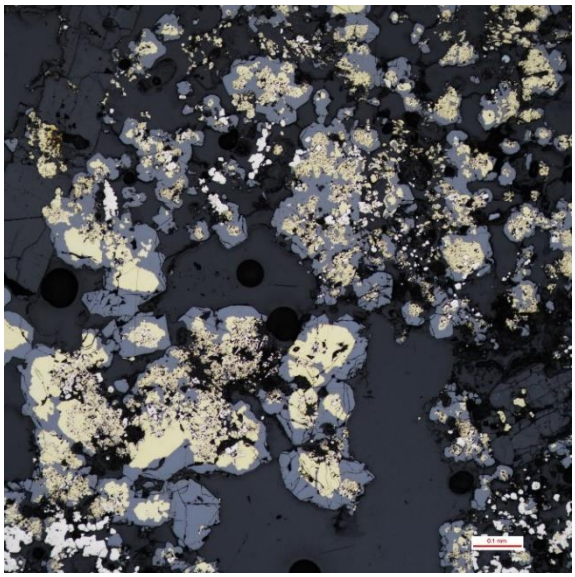

a.

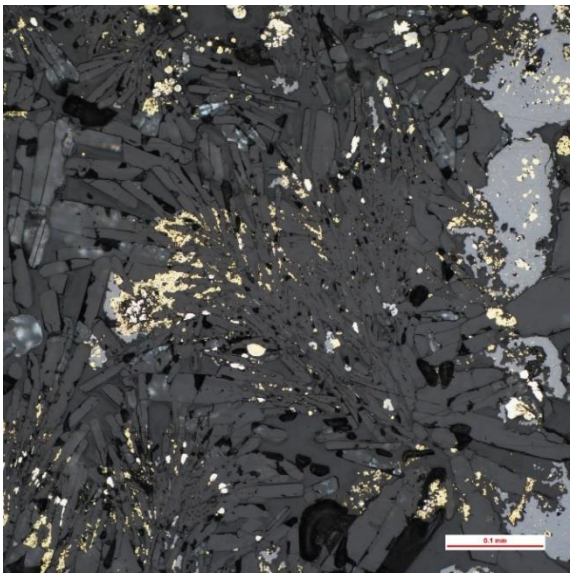

b.

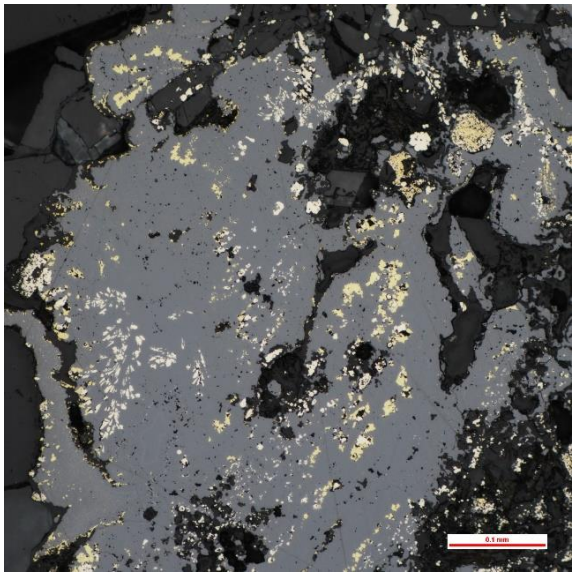

c.

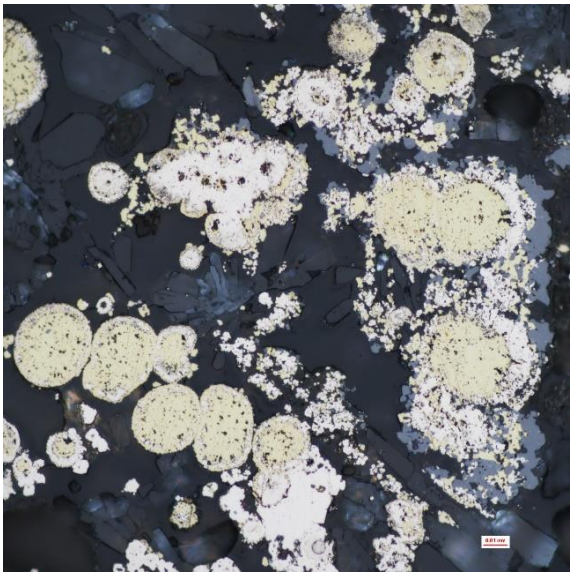

d.

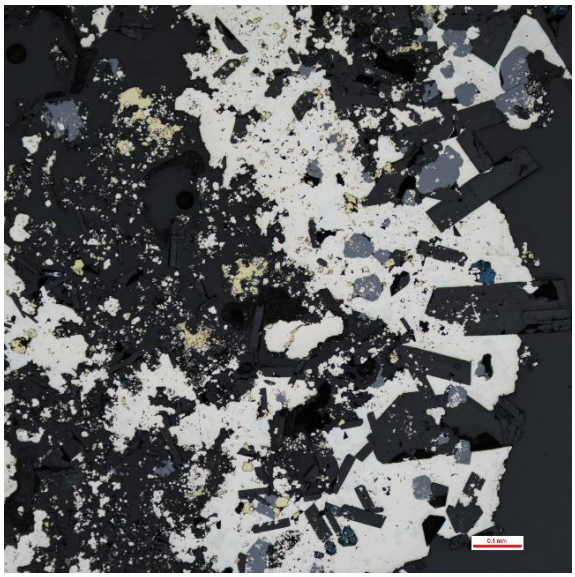

e.

f.

Photomicrographs of sample D1920-R7. All photos are taken under reflected light, except c, which is taken using both reflected and transmitted light. a) Fine-grained pyrite within chalcopyrite, with sphalerite overgrowths. Common observation within the interior groundmass. b) Plumose texture in barite, with minor chalcopyrite mantling. The degree of overgrowth of barite varies considerably within the interior. c) Massive sphalerite with some chalcopyrite intergrowths. Pyrite shows remains of plumose texture, but the barite appears to be resorbed and infilled with sphalerite. d) Unique texture, where chalcopyrite has replaced pyrite in colloform masses. e) Boundary of the exterior rind, the interior is located to right side (out of view) adjacent to a large open space. Coarse-grained barite is overgrown by massive pyrite. Sphalerite appears as disseminated subhedral to euhedral grains. Chalcopyrite and covellite also appear in the exterior. f) Euhedral sphalerite in massive pyrite with minor covellite. Tiny inclusions of pyrite are present within sphalerite, which may suggest that these phases are intergrown.

D1920 – R8:

Site Description

This sample was collected from the same steep-sided mound slope described in the previous sample. The two samples were located within meters of each other.

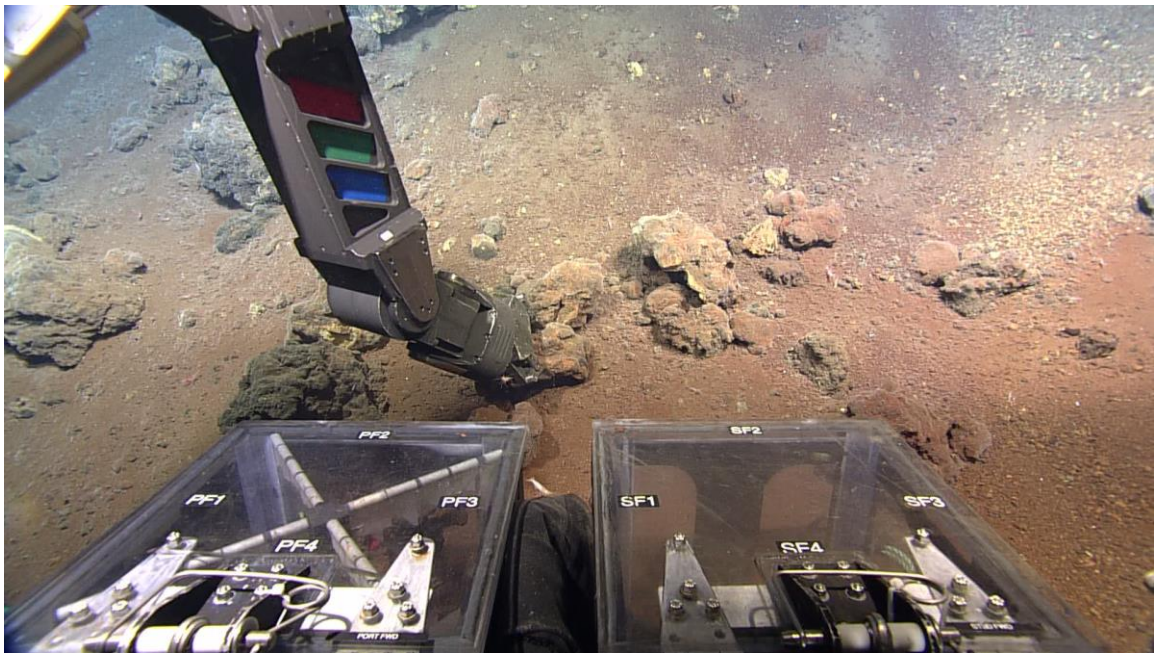

Heavily sedimented talus slope where samples D1920-R7, D1920-R8, and D1920-SED are collected. The position of the ROV arm is where D1920-R8 was collected.

Hand Sample Description

This sample is very similar in appearance to D1920-R7, which is likely uncoincidental, as they were both essentially collected from same location. The interior is a fine-grained, porous, dark-grey groundmass largely composed of sphalerite, barite, chalcopyrite, and pyrite (I assume for now). The cut thin section slab shows an interesting relationship between barite and sphalerite, in which there is preferential banding of one or the other phases, with noticeable boundaries between them. However, the significance of this may not reflect the entire sample. The exterior is a heavily oxidized orange-brown colour and contains a few dispersed patches of white bacterial growth.

Hand sample for D1920-R8. Photograph shows the lack of fresh exposed interior surface, much of the sample exterior is heavily oxidized.

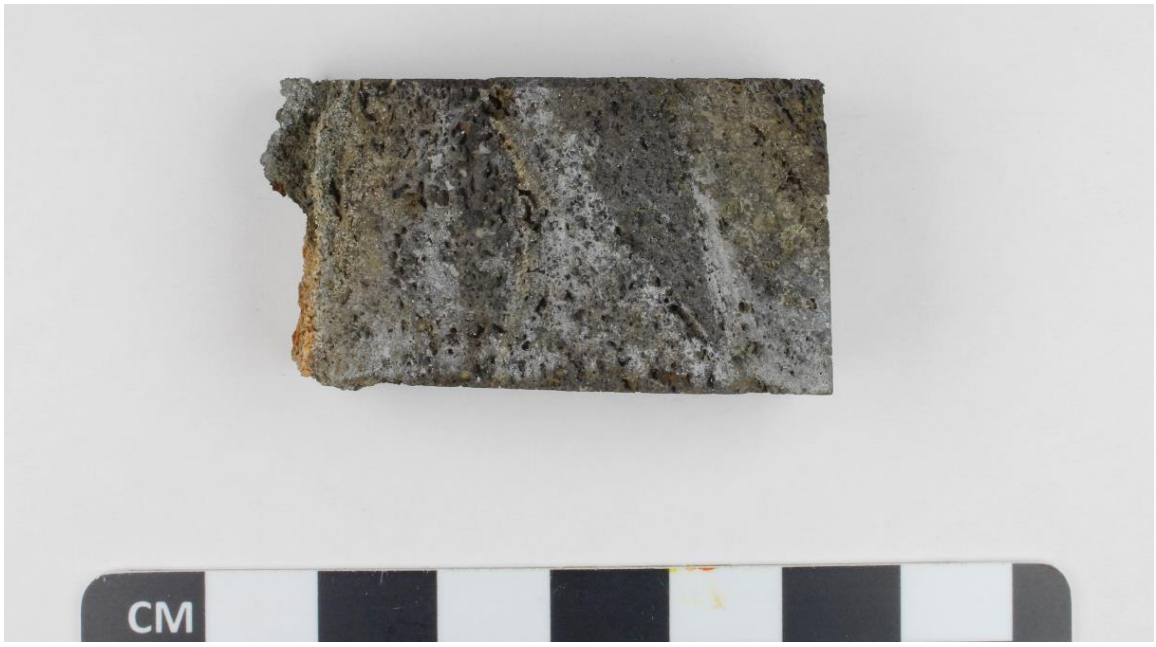

Thin section slab for D1920-R8. Thin section was cut from this face.

Mineral Abundances and Occurrences

Sphalerite – 50%

Barite – 40%

Pyrite – 9%

Chalcopyrite – 1%

Galena – < 1%

Covellite – << 1%

Sphalerite and barite are the dominant phases present in the sample groundmass. Sphalerite is massive and has abundant overgrowth of barite and many sulphide phases. Massive mineralization appears to be thicker in areas of increased chalcopyrite mineralization. Dendritic sphalerite occurs within the sample interior in the porous groundmass, containing little to no barite or pyrite. Interior barite largely consists of coarse-grained euhedral to subhedral bladed and tabular crystals grown within pore spaces, while the exterior is characterized by an increase in fine-grained radiating bladed and acicular crystals. Plumose barite is also found within the sample interior, but more commonly appears near the exterior. Fine-grained interior barite is commonly overgrown by pyrite masses and blebs and subsequently overgrown by massive sphalerite, whereas coarse-grained barite grows along the edges of massive sphalerite. Pyrite is mostly massive or occurs as disseminated euhedral to anhedral small blebs and framboids grown on the edge of barite crystals and often overgrown by sphalerite. There are also some blebs and masses that exhibit colloform texture. Colloform pyrite occurs within some interior blebs but is most often observed within masses and blebs in the exterior layer. A massive exterior layer of pyrite has overgrown fine-grained radiating acicular barite. Chalcopyrite is present as small, disseminated grains or as anhedral intergrowths in areas of thick massive sphalerite growth. It is also seen along the edges of massive sphalerite in some large pore spaces. Galena occurs as tiny, disseminated inclusions within massive sphalerite, or coarser massive grains that are seen growing on the edges of coarse-grained barite. Small anhedral grains of secondary covellite are found rimming barite and contained within sphalerite grains in more porous areas. It is likely a replacement product of chalcopyrite.

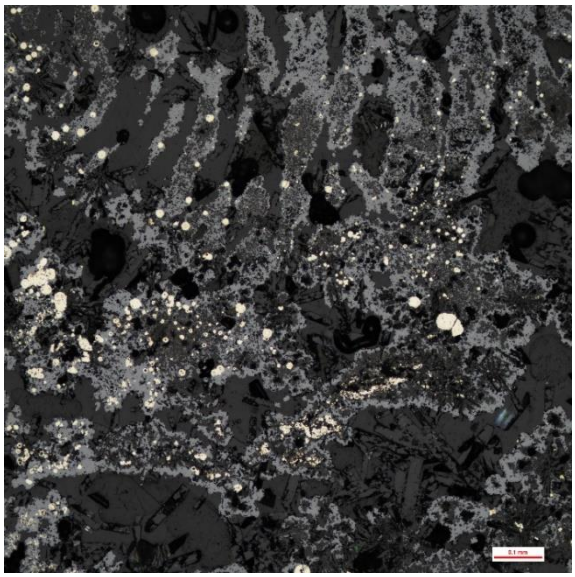

a.

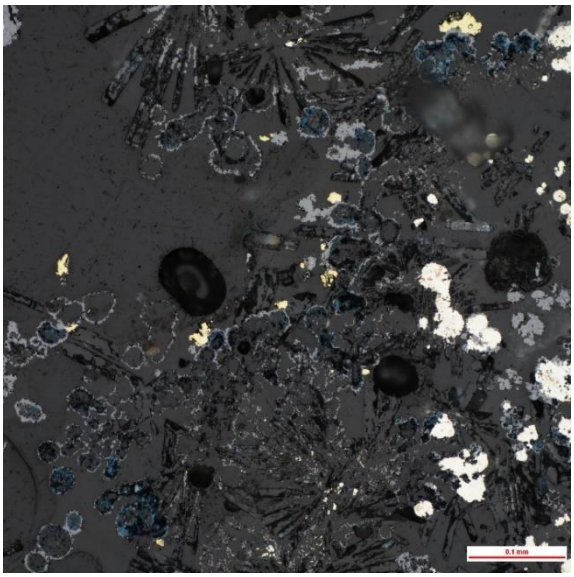

b.

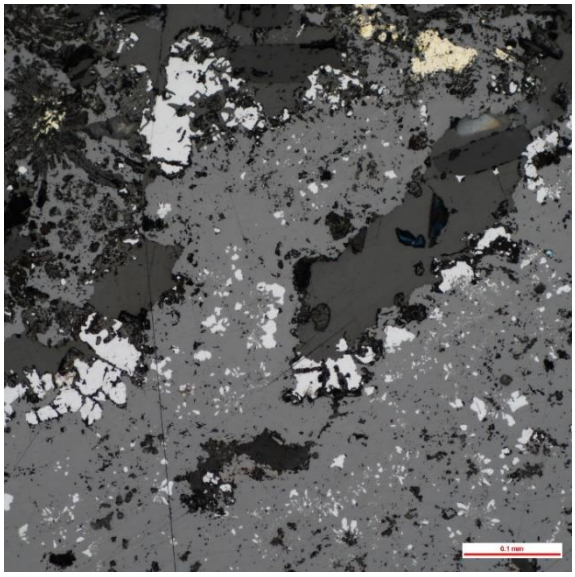

c.

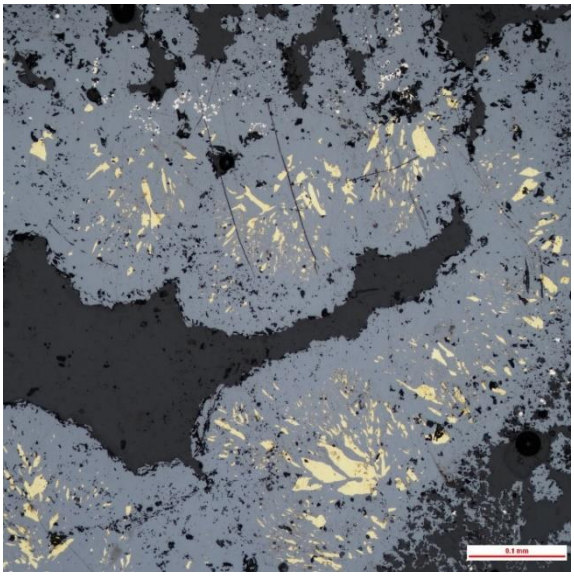

d.

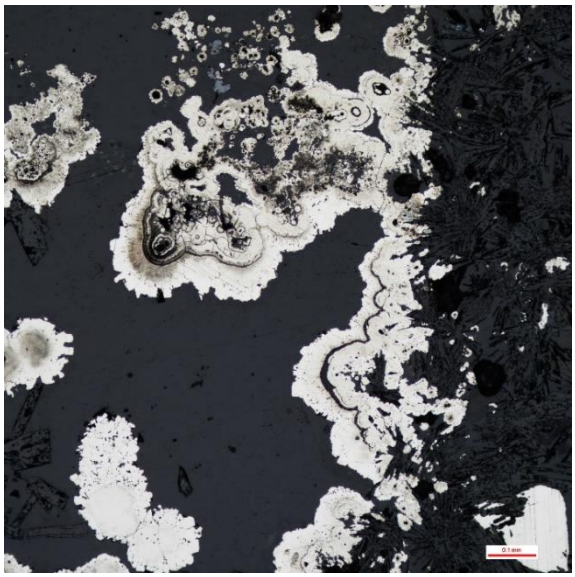

e.

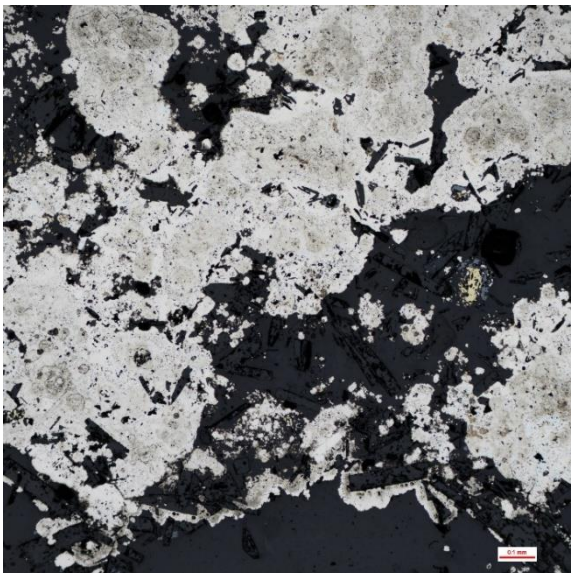

f.

Photomicrographs of sample D1920-R8. All photos are taken using reflected light. a) Dendritic texture in sphalerite towards the top of the photo, with minor pyrite blebs contained within. Coarse-grained barite often is found within pore spaces adjacent to massive sphalerite. b) Some massive sphalerite, which appears pitted out in the interior, contains tiny grains of covellite. c) Massive sphalerite often contains tiny inclusions of galena. Galena may also occur along the edges of the same sphalerite grains. The abundance of grain in localized areas suggests that these are intergrowths. d) Minor intergrowths of chalcopyrite are found with massive sphalerite that locally grows as thick layers. Chalcopyrite is rarely seen overgrowing sphalerite. e) Layered exterior pyrite growths with some colloform texture are found overgrowing fine-grained acicular barite. f) With the previous growth phase, thick mineralization of massive pyrite also occurs, overgrowing coarse-grained barite.

D1920 – SED:

Site Description

This sample was collected from the same site as D1920-R7 and D1920-R8.

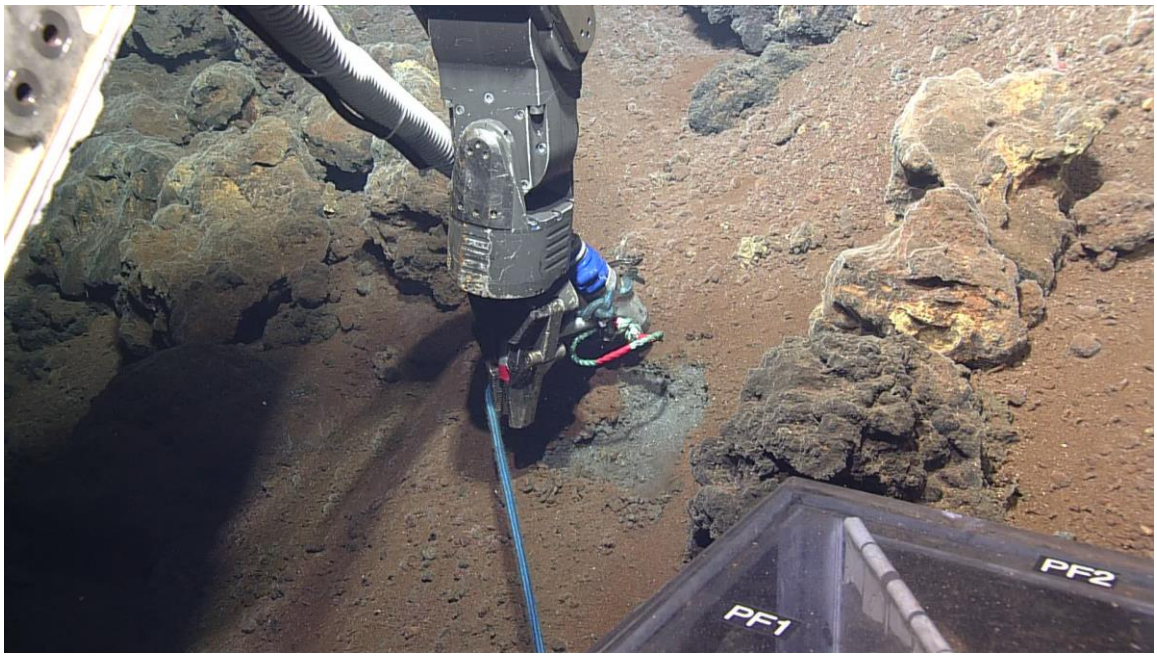

ROPOS uses a suction hose to collect fine metalliferous sediments that cover the talus slope (D1920-SED). The grey patch just below the hose head shows the underlying layer of metalliferous sediments to be largely unoxidized.

Hand Sample Description

The sample consists of fine-grained chalcopyrite and barite-rich metalliferous sediments. Analysis of the low porosity sediments using a stereo microscope shows the largest crystals in the dark-grey groundmass to be tabular and bladed barite crystals (< 1 mm). They give off an obvious vitreous luster when illuminated and have a recognizable crystal habit. An iridescent colouration is visible in the groundmass as well, perhaps from chalcopyrite or bornite. There is also likely a notable presence of pyrite and possibly sphalerite (as the whole-rock geochemical data suggests). Most of the sediment sizes are much smaller than 1 mm up to 1 mm, but a few grains are as large as 1 cm. All the grains are covered by some degree in exterior oxide material. There is no thin section for this sample.

D1920 – R9:

Site Description

This sample was broken off from the trunk segment of a large extinct chimney. The once tall chimney now lies in pieces on the seafloor in between two massive sulphide mounds. The chimneys location makes it difficult to determine which mound it originates from. One of the adjacent mounds has an abundance of tall-standing chimney complexes towards its peak, with a mixture of low temperature diffuse venting white smokers and beehive structures, and inactive chimney spires.

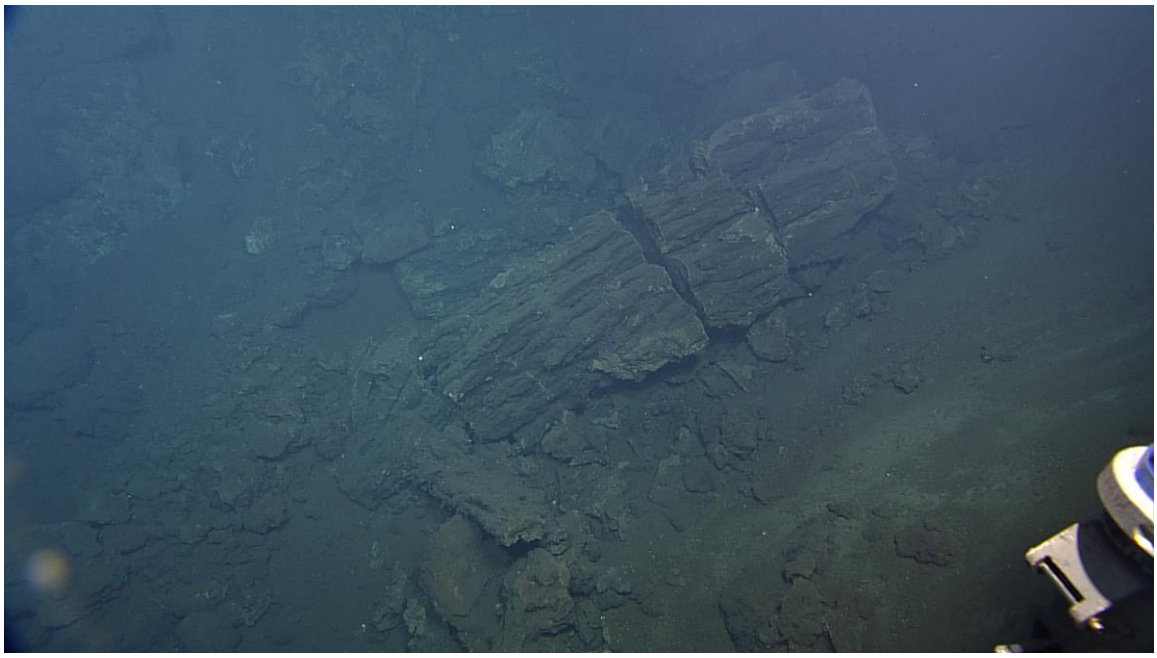

a.

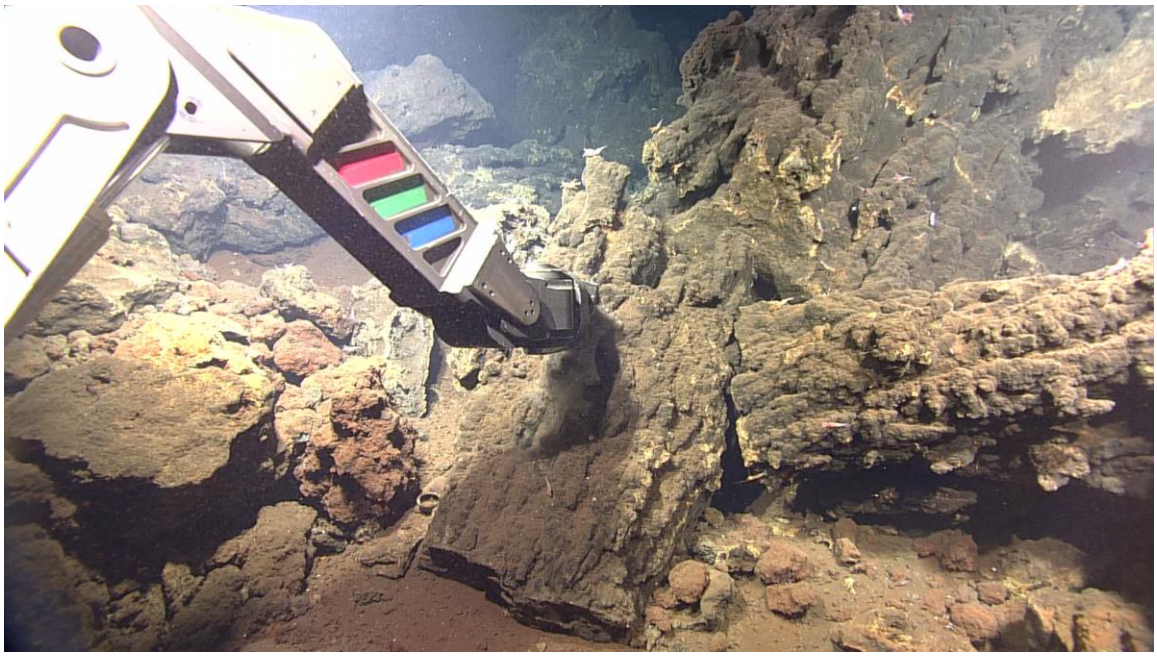

b.

Site where D1920-R9 was collected. Top photograph shows the surrounding area of the large dead sulphide chimney. The bottom photograph shows the position of where the ROV arm broke-off a piece of the chimney.

Hand Sample Description

At first glance, this sample appears to be the top of a slender sulphide chimney, however it is just an offshoot vent from the trunk of a much larger extinct sulphide chimney. The sample interior is very distinct, as even just a thin section displays the entire cross-sectional features of sulphide growth within the chimney. The interior of the chimney displays thin yellow-gold chalcopyrite rims (~ 0.5 mm) around inactive fluid conduits, which have been coated with red-brown oxides. Towards the chimney exterior, chalcopyrite is still present in the fine-grained, porous, grey groundmass, but barite and sphalerite dominate the mineral assemblage. The exterior surface is a heavily oxidized orange-brown, which covers a thin carapace of barite.

Hand sample for D1920-R9. Photograph shows the small, exposed portion of the chalcopyrite-rich chimney interior, sulphate-rich carapace, and heavily oxidized exterior.

Thin section slab for D1920-R9.

Mineral Abundances and Occurrences

Barite – 40%

Chalcopyrite – 25-30%

Sphalerite – 20-25%

Pyrite – 6%

Pb-As & Pb-As-Sb sulphosalts – 2%

Tetrahedrite-Tennantite – 2%

The thin section contains 3 main zones: (1) the barite-rich exterior, (2) the chalcopyrite-rich interior vent linings, and (3) the interior transition zone between the previous two zones. Barite occurs as euhedral to subhedral bladed and tabular crystals, with small, radiating bladed and acicular crystals found exclusively towards the exterior. There is a great difference in barite grain size, with finer grains found within the exterior and interior groundmass, and coarser grains in porous spaces including the interior vent linings. Plumose barite is abundant in the transition zone groundmass. Chalcopyrite is mostly massive in interior vent linings or sometimes present as disseminated grains in massive sphalerite. As with most other samples, there is little to no chalcopyrite present in the exterior zone. Thin layers of pyrite are occasionally contained within massive chalcopyrite linings, which suggests that both phases are intergrown. Sphalerite largely occurs as massive overgrowths of barite, chalcopyrite, pyrite, Pb-As sulphosalts, and tetrahedrite-tennantite within the sample interior groundmass, however it may also form a thin mantling of chalcopyrite along the inner vent lining. Massive sphalerite has distinct yellow to red-orange internal reflections visible in both PPL and XPL, highlighting that it is quite Fe-poor. Dendritic sphalerite and pyrite are common textures in the transition zone. Pyrite is mostly present as euhedral to subhedral grains, however several rounded blebs and colloform masses are also present. Massive pyrite exists in a thin crust formed on a small portion of the exterior. Pb-bearing sulphosalts are observed as tiny anhedral grains. Some larger grains appear more massive in form. Tetrahedrite-tennantite grains are similarly anhedral, with some isolated triangular-shaped grains. All sulphosalt phases are generally found mantling chalcopyrite within massive sphalerite along interior vent linings.

a.

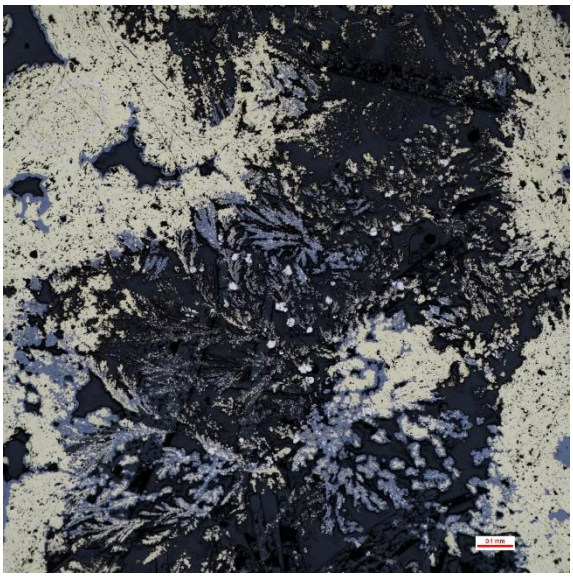

b.

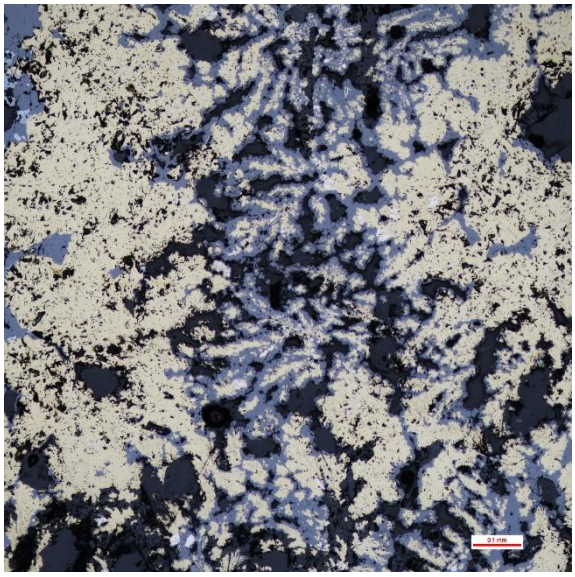

c.

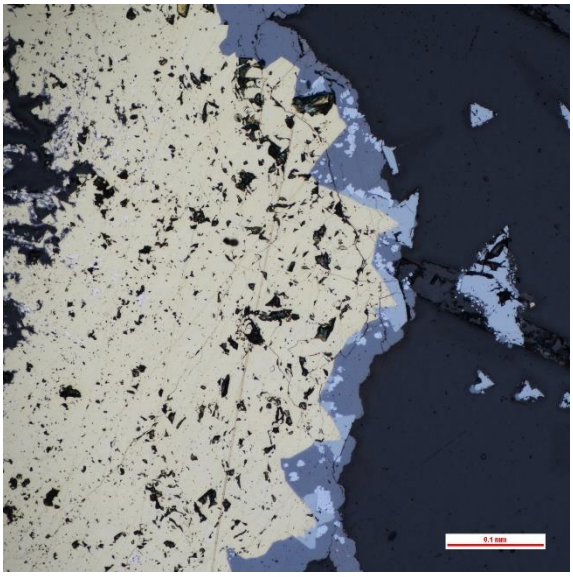

d.

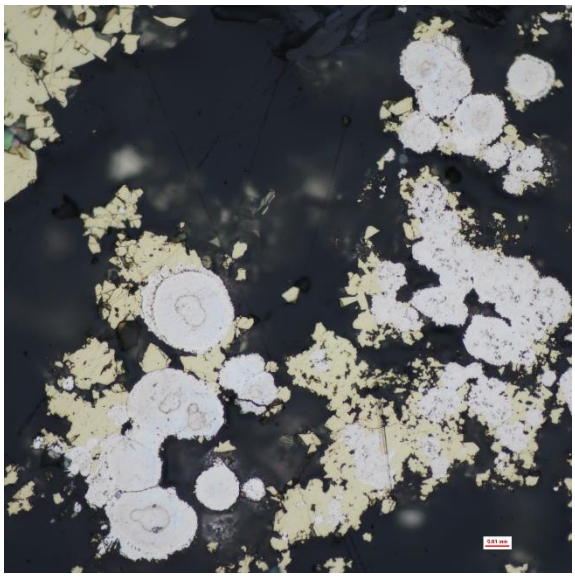

e.

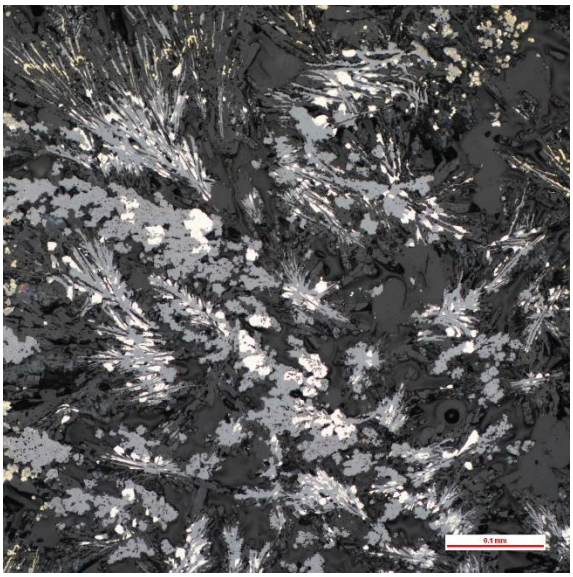

f.

Photomicrographs of sample D1920-R9. All photos are taken under reflected light. a) Transition from the chalcopyrite-rich interior vent lining to the interior groundmass. The boundary at which barite becomes dominant is well defined. b) Inter-vent mineralization is generally classified by plumose barite, overgrown by sphalerite and chalcopyrite. c) Region within the inter-vent that has seen considerably increased chalcopyrite mineralization. d) Chalcopyrite-lined interior vent. Chalcopyrite is sometimes overgrown by sphalerite, tetrahedrite-tennantite, and Pb-As sulphosalts. e) Colloform pyrite masses mantled by chalcopyrite. f) Plumose texture in barite, mantled by pyrite and overgrown by sphalerite. Common observation towards the exterior.

D1920 – R10:

Site Description

This sample was collected from the seafloor, just a few meters away from the fallen, extinct chimney described in the previous sample. It is currently unclear if this sulphide piece is petrographically related to D1920-R9, or if its origin is distinct.

Site where D1920-R10 was collected. ROV arm is positioned where the sample was grabbed, right in front of the dead chimney of the previous sample.

Hand Sample Description

This sample is a rather small piece of sulphide material with an extremely high porosity. The groundmass is fine-grained and has a distinct light grey to yellow-grey metallic luster, reflected by the high abundance of pyrite, marcasite, and minor chalcopyrite. The sample exterior contains some orange-brown oxidation, as well as some relatively coarse masses of atacamite (~0.5 cm). Despite its porosity, the oxidation does not infiltrate deep into the interior.

Hand sample for D1920-R10. Photograph shows a contrast of fresh and weathered surfaces.

Thin section slab for D1920-R10. Thin section was cut from this face.

Mineral Abundances and Occurrences

Pyrite – 40%

Barite – 30%

Marcasite – 25%

Chalcopyrite – 5%

Sphalerite – << 1%

There are two distinct occurrences of pyrite present: (1) small, subhedral to anhedral grains contained within chalcopyrite, grown free from marcasite, and (2) massive, complex intergrowths with marcasite that retain some euhedral to subhedral forms. Barite mostly occurs as euhedral to subhedral bladed and tabular crystals, and occasionally the bladed crystals occur in radiating masses. There is a wide range of grain sizes in bladed crystals, and their spatial distribution appears to be arbitrary and complex. Marcasite occurs in abundance as massive intergrowths with pyrite, or in massive growths absent of pyrite. Rare twinning was observed in select crystals. Minor chalcopyrite is present as massive grains and, in many cases, contains irregular grains of pyrite. Some massive chalcopyrite appears to be overgrown by massively intergrown pyrite and marcasite. Trace amounts of sphalerite occur as massive, disseminated grains.

a.

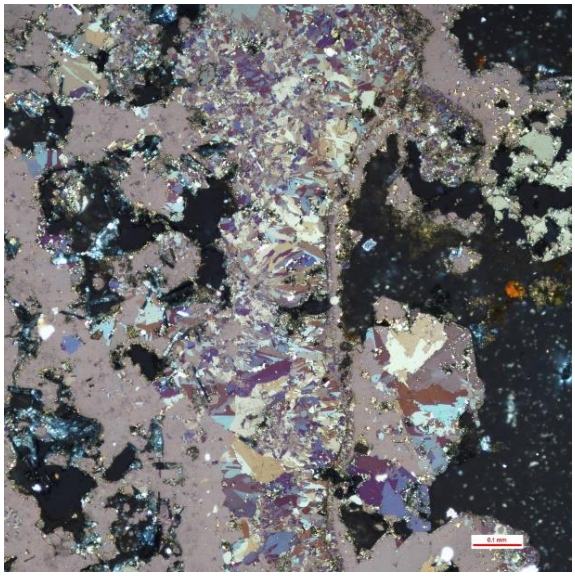

b.

c.

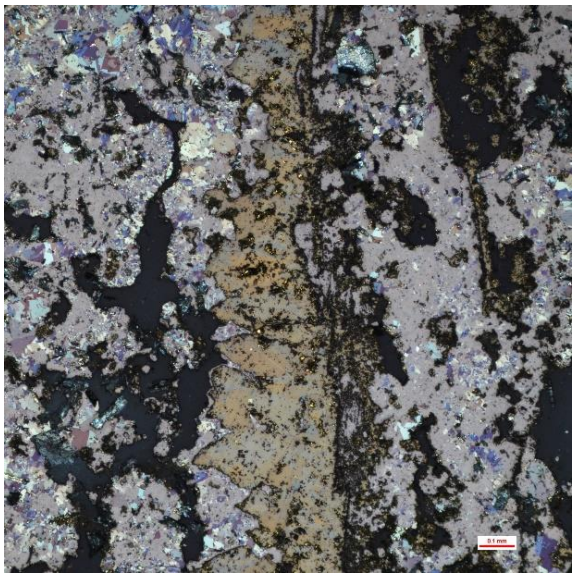

d.

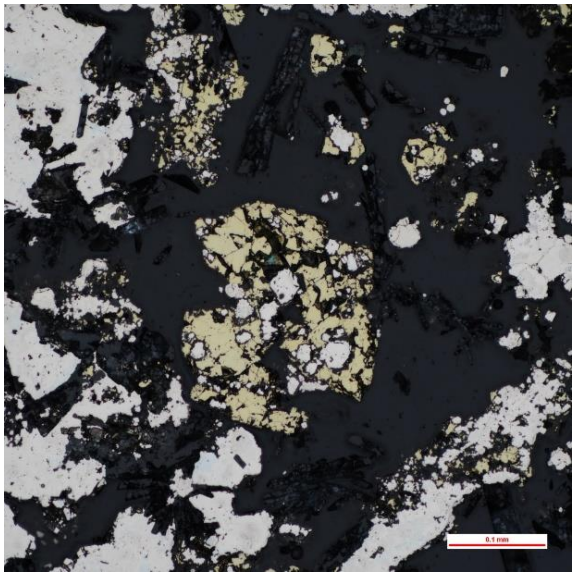

e.

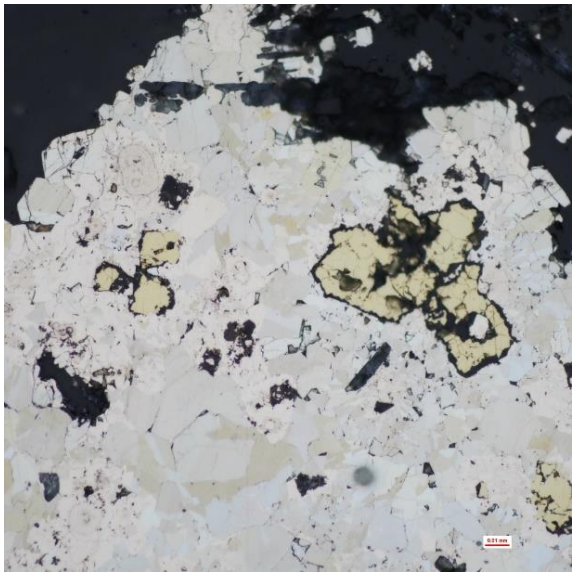

f.

Photomicrographs of sample D1920-R10. All photos are taken under reflected light. a) Multiple stages of growth of pyrite and marcasite. Much of the pyrite and marcasite appear to be intergrown. Marcasite exhibits a distinct bireflectant off-white to yellow colour (PPL). b) Cross-polarized light (XPL) highlights the very strong anisotropy of marcasite, showing multiple bands of growth. c) Band of chalcopyrite overgrowing pyrite and marcasite (on the right-hand side), is then overgrown by a later stage of pyrite and marcasite. d) Previous photograph in XPL. e) Subhedral pyrite within massive chalcopyrite. f) Euhedral pyrite contained within chalcopyrite. Pyrite and marcasite completely overgrow many of these chalcopyrite grains.

D1920 – R11:

Site Description

This sample was collected along the talus slope of a low relief massive sulphide mound. The site is about 20 m downslope of a short black smoker chimney complex. The chimney complex has two central vents emitting black smoke. The central vent appears to be a diffusely venting white smoker chimney, with black coated beehive structures found primarily on the outer walls. A small, isolated inactive chimney complex is located approximately 12 m downslope towards the NE.

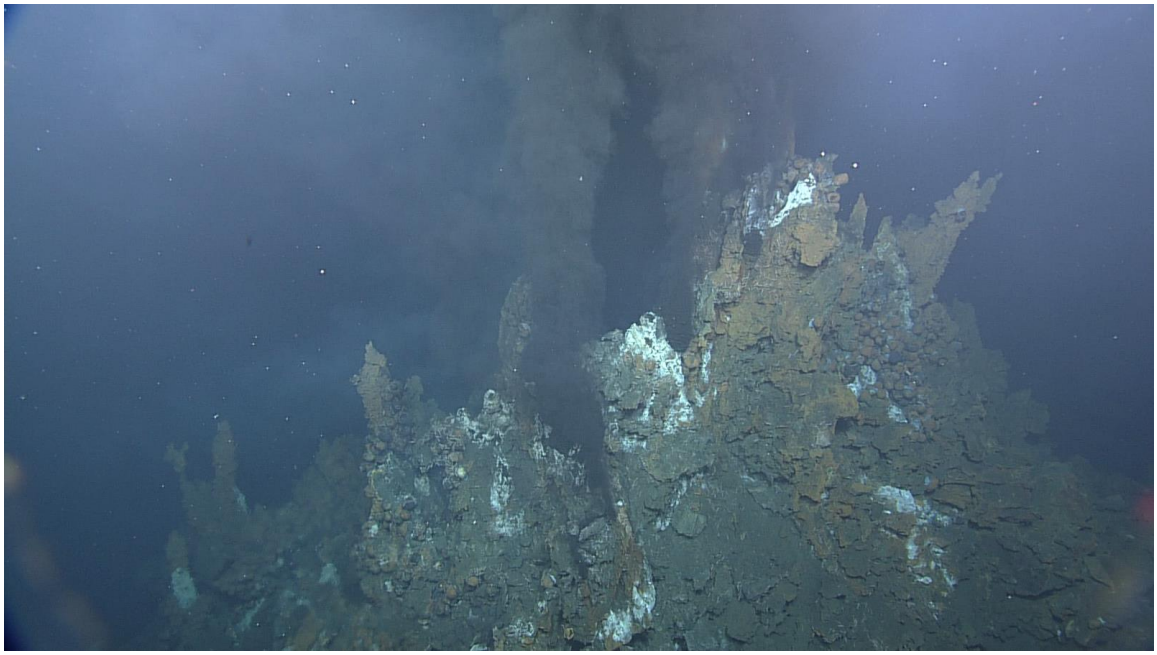

a.

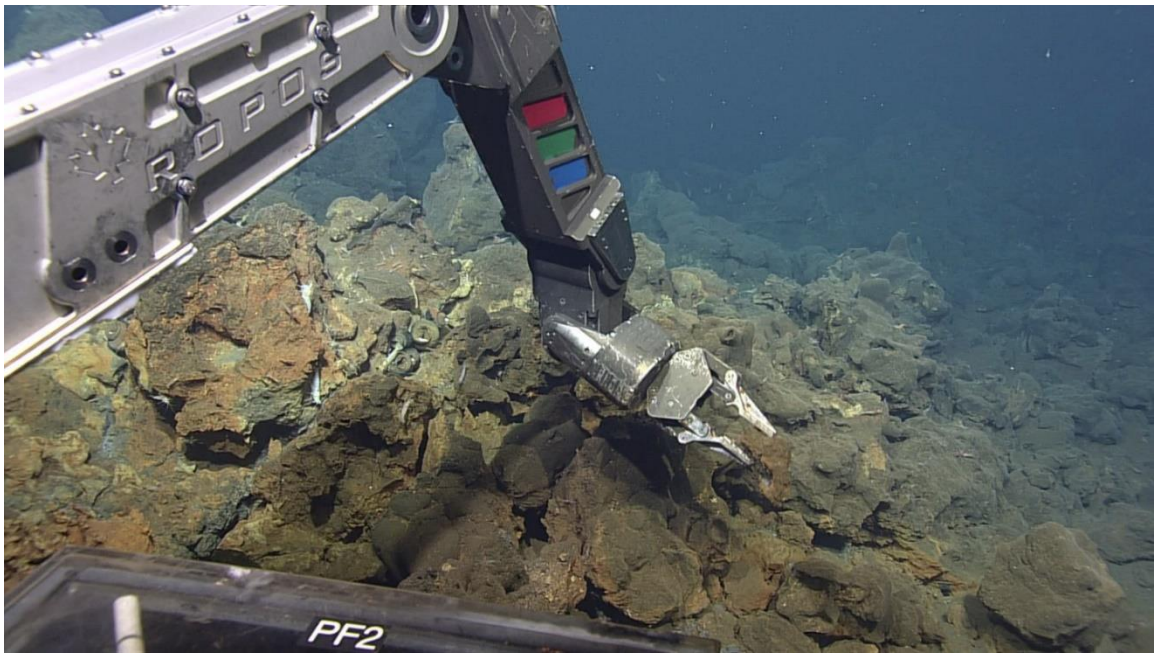

b.

Top photograph shows the black smoker chimney complex atop massive sulphide mound near D1919-R3 and D1920-R11. Bottom photograph shows the collection of D1920-R11, roughly 20 from black smoker chimney complex, along the NW talus slope.

Hand Sample Description

The interior of this sample has a very fine-grained (<< 1 mm), low porosity, light to dark-grey to black groundmass, with abundant patches of white colouration. It is mostly composed of sphalerite and barite, with minor pyrite and chalcopyrite. Barite crystals are distinctly coarser-grained than the rest of the groundmass (up to 1 mm), and many give off a vitreous luster. The sample appears to have a uniform outer carapace of barite, largely concealed by a heavy coating of orange-brown to light brown oxidation.

Hand sample for D1920-R11. Photograph shows a contrast of fresh and weathered surfaces.

Thin section slab for D1920-R11. Thin section was cut from this face.

Mineral Abundances and Occurrences

Sphalerite – 45-50%

Barite – 40-45%

Pyrite – 10%

Chalcopyrite – < 1%

Galena – << 1%

Covellite – << 1%

The sphalerite- and barite-dominated groundmass is relatively homogenous throughout. Sphalerite is mostly massive and is found overgrowing much of the barite and pyrite that has formed before it. Dendritic sphalerite is also present throughout the groundmass. As is typical with dendritic sphalerite in other samples, barite and pyrite do not appear to be large constituents of this texture. Barite occurs as euhedral to subhedral bladed and tabular crystals. Grain size is consistent throughout, however slightly coarser crystals tend to be located within more porous spaces. While much of the barite within the groundmass is overgrown by sphalerite, coarse-grained barite has minimal sulphide overgrowth (e.g., subhedral pyrite and trace sphalerite only). Pyrite occurs as massive clusters with some colloform-like appearances, as small circular blebs, and uncommonly as subhedral grains. Similarly, to barite, much of the pyrite is overgrown by massive sphalerite. Tiny grains of sphalerite were observed as being contained in pyrite, which suggests that pyrite and sphalerite may be intergrown. Ovoid and slightly elongated pyrite rings are present and many of these forms are infilled by other sulphides and barite. Only trace amounts of chalcopyrite can be found within the groundmass. It occurs as small, anhedral intergrowths with massive sphalerite and is typically located along the edges of more porous spaces, where the growth of sphalerite is thickest. Galena occurs as tiny, disseminated anhedral inclusions within massive sphalerite. Tiny irregular patches of covellite occur in trace abundance and are associated with chalcopyrite.

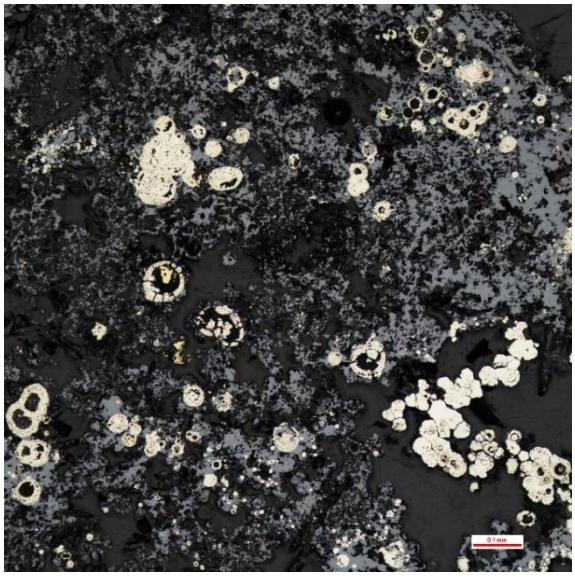

a.

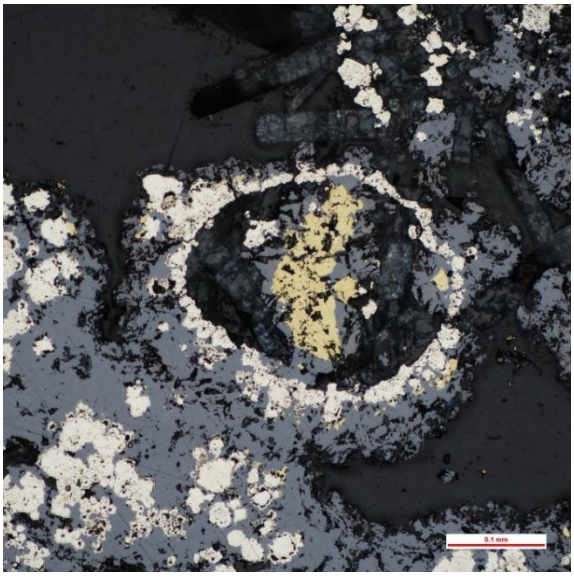

b.

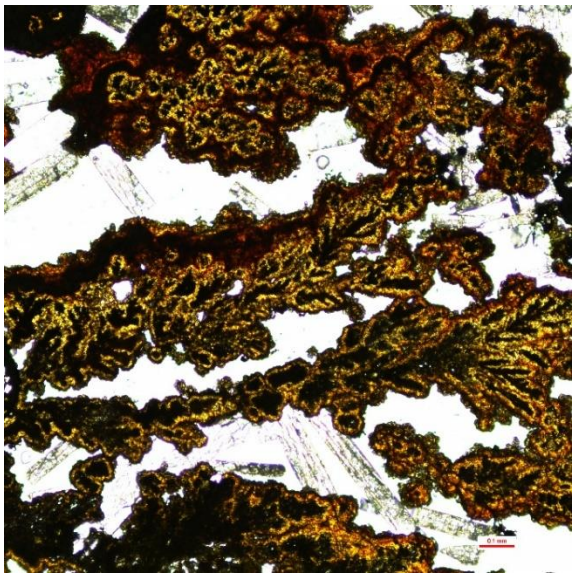

c.

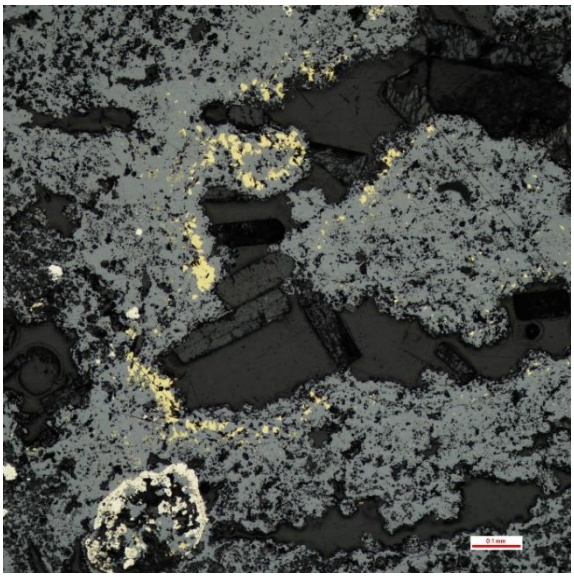

d.

Photomicrographs of sample D1920-R11. All photos were taken under reflected light, except for c, which was taken under transmitted light. a) Blebby and colloform pyrite overgrown by massive sphalerite. Some colloform texture is deteriorated and the interior material appears to be removed. b) Small, mineralized pyrite ring. The interior has been infilled by barite, sphalerite, and chalcopyrite. Coarse-grained barite is observed at the top. c) Sphalerite captured under transmitted light highlights the zoning typically seen in dendritic texture. The grain interiors are Fe-rich, while the exteriors are composed of yellow-orange Zn-rich sphalerite. Some minor colloform banding of sphalerite can be seen at the top. d) Chalcopyrite mineralization occurs near the edges of massive sphalerite, where they appear to be intergrown. Coarse-grained barite is seen growing along the edges of sphalerite into pore spaces.

D1920 – R12:

Site Description

This sample was collected from a complex of inactive chimneys. Here, there is an expansive “forest” of chimneys that are mostly inactive. Within close proximity to the area of collection, white-coated chimneys are diffusely venting clear to white hydrothermal fluids. A few white-coated beehive structures are present atop chimney spires.

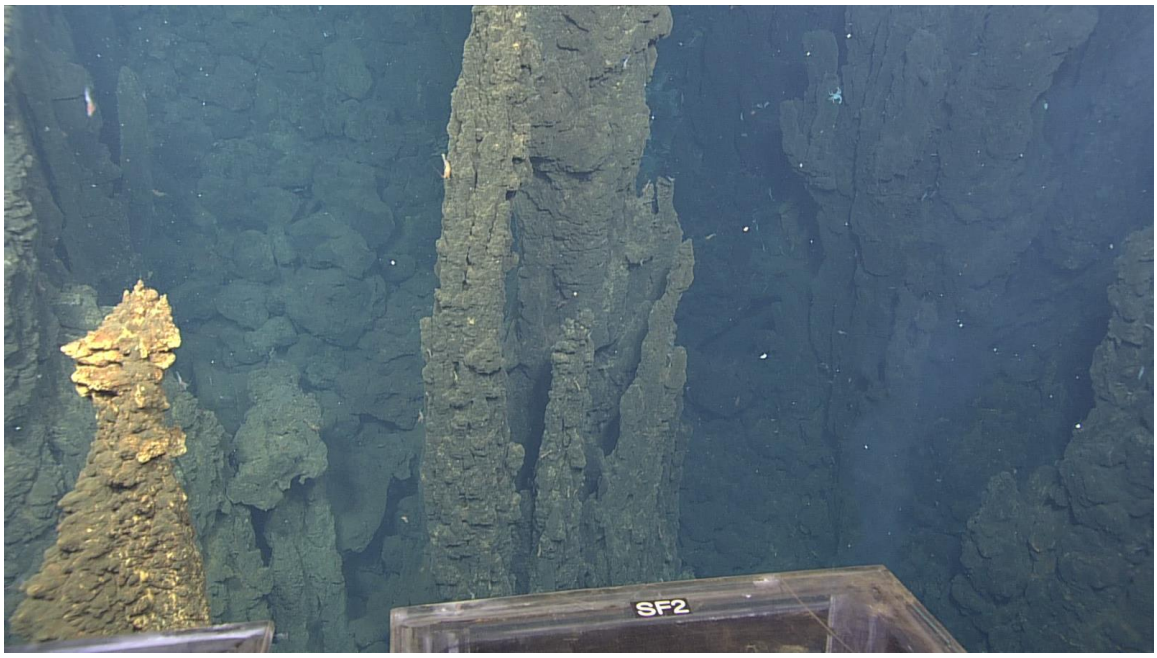

A complex of inactive chimneys, within a large “forest” of primarily inactive chimney spires. Sample D1920-R12 is the relatively short chimney spire directly in the middle of the ROV frame grab.

Hand Sample Description

This sample consists of multiple pieces which when combined, make up a roughly 1 m tall top of an inactive chimney. The mineralogy of chimney is highly variable from top to bottom and in cross-section, however the style of mineralization can be described in a general sense. The chimney center, defined by both open fluid conduit space and clogged pathways, is mostly composed of fine-grained (< 1 mm), porous, black to metallic yellow-green chalcopyrite-rich sulphide material. The porosity of this section varies greatly, as dense, low-porosity chalcopyrite rims are formed around where fluid flow was at its most focused state. The intermediate material, towards the exterior, is composed of a fine-grained, dark-grey sphalerite-rich groundmass, which has lower porosity. This groundmass is also very enriched in barite, with some crystals and clusters up to 2 mm in size. In many cases, barite is present in thin (1 mm) layers, which signify several growth stages within the large chimney. The effects of oxidation have penetrated this section, as much of the groundmass has an altered orange-brown appearance. The outermost material is defined by an outer rim of white-brown barite, which has been intimately associated with oxides. The barite rim is heavily coated with grey-black to orange-brown oxidation with abundant patches of white bacterial growth.

Hand samples for D1920-R12. From the top to the bottom photograph shows the continuation from the top of an inactive chimney to the trunk base, of what was recovered. The top of each section begins on the left side of each photograph.

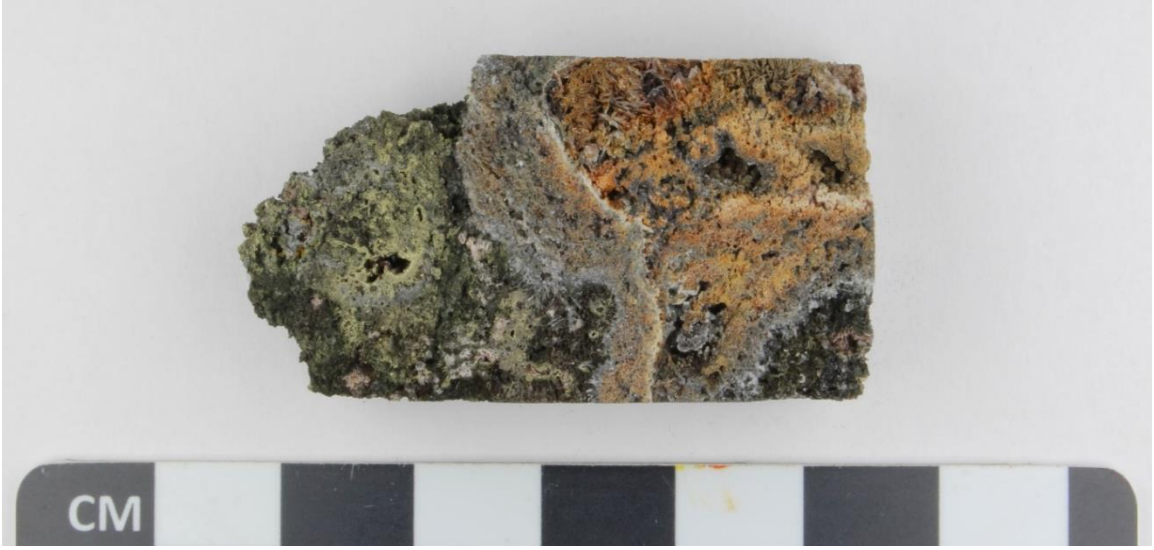

Thin section slab for D1920-R12. Thin section was cut from this face.

Mineral Abundances and Occurrences

Barite – 40-45%

Sphalerite – 25-30%

Chalcopyrite – 20%

Pyrite – 8%

Tetrahedrite – Tennantite – 1%

Pb-As sulphosalts – 1%

Galena – < 1%

Amorphous Silica – < 1%

The thin section for this sample is likely not representative of the entire sample but was selected to highlight multiple different zones. Thin acicular crystals are generally only found towards the oxide-rich exterior, while euhedral to subhedral bladed crystals are pervasive within the barite- and sphalerite-dominated interior. Plumose barite is also commonly observed in the interior and appears to be pseudomorphed by sphalerite in areas of thick, massive sphalerite and chalcopyrite overgrowth. Barite crystal size varies considerably, with smaller thin crystals found towards the exterior. The size of interior crystals is generally consistent but increase slightly within porous spaces. Extremely coarse-grained euhedral barite dominates the chalcopyrite-rich interior zone of the

sample. These barite crystals are notably absent of major sulphide overgrowth or mantling. Sphalerite is mostly present as massive overgrowths of barite and pyrite within the barite- and sphalerite-dominated interior but does also mantle chalcopyrite and tetrahedrite-tennantite within the chalcopyrite-rich interior zone. Rare massive galena occurs with massive sphalerite and is also present as inclusions in sphalerite, an occurrence that is typically seen of galena. Massive galena shows possible replacement or increases of intergrowth within certain areas of massive sphalerite. Dendritic sphalerite was also observed within the barite- and sphalerite-dominated interior, although this is relatively uncommon. Massive chalcopyrite and tetrahedrite-tennantite are common phases within the chalcopyrite-rich interior zone. Chalcopyrite may form intergrowths with sphalerite or overgrowths of barite, pyrite, and sphalerite. Subhedral or triangular-shaped grains of tetrahedrite-tennantite are commonly intergrown with chalcopyrite but are also associated with sphalerite and Pb-As sulphosalts, where chalcopyrite is most abundant. Late sphalerite, Pb-As sulphosalts, and galena are all seen mantling massive chalcopyrite and tetrahedrite-tennantite within porous space in the chalcopyrite-rich zone. Pyrite is mostly massive, but also forms masses or circular blebs that sometimes exhibit colloform banding, dendritic texture, or rare subhedral crystals. Pyrite often mantles plumose barite and is subsequently overgrown by massive sphalerite. Colloform texture is most common within interior pyrite blebs, however it has rare appearances in masses and blebs in the exterior zone. Like dendritic sphalerite, dendritic pyrite sometimes forms within the barite- and sphalerite-dominated interior. Lastly, amorphous silica is present within the interstices of pre-existing sulphides and barite within the interior zones.

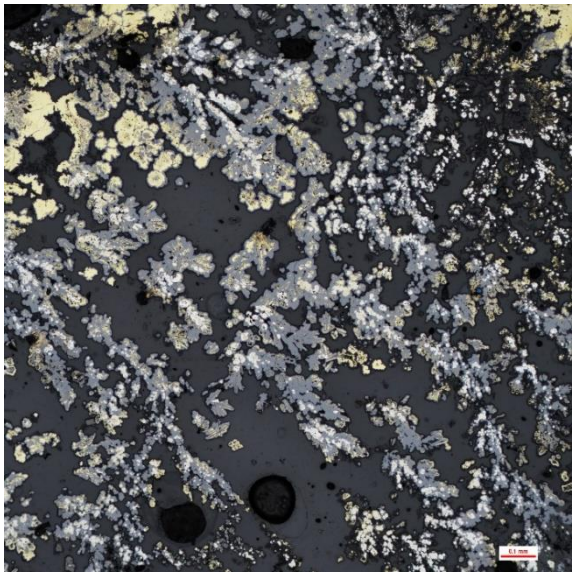

a.

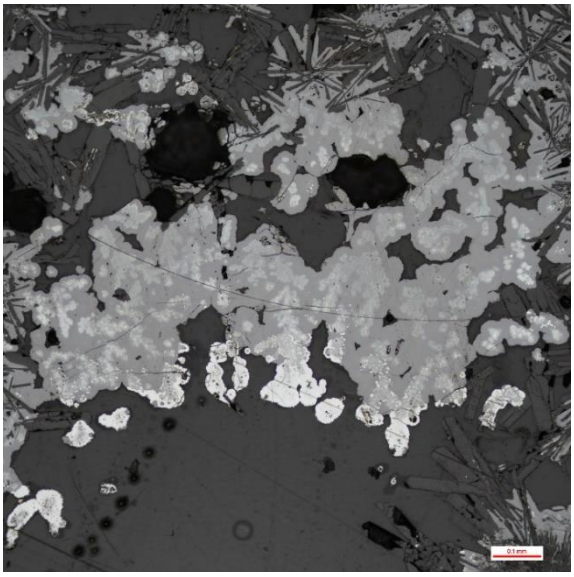

b.

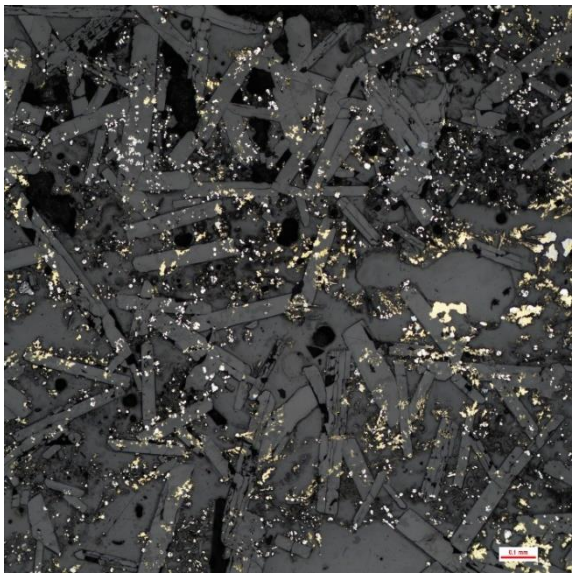

c.

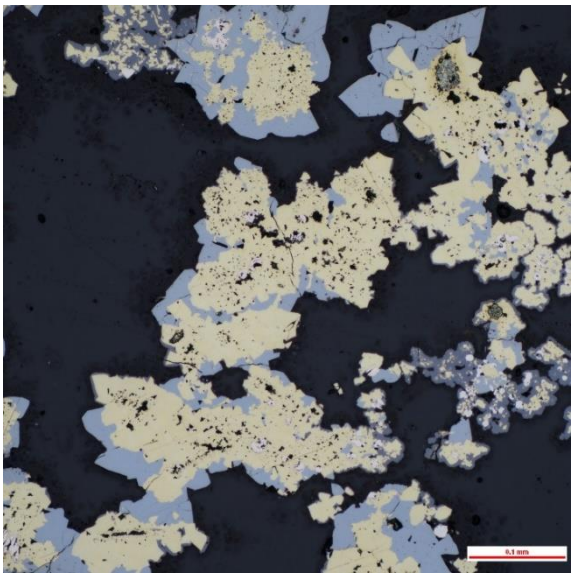

d.

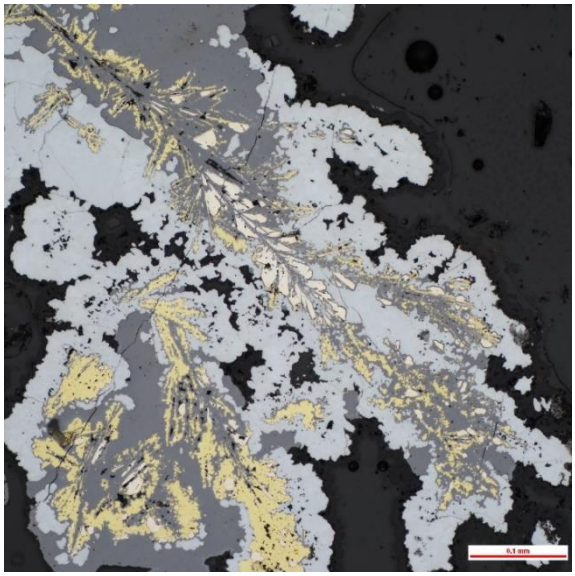

e.

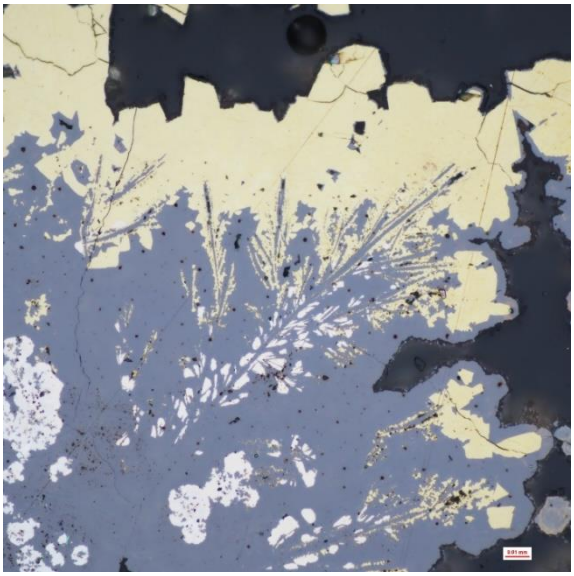

f.

Photomicrographs for sample D1920-R12. All photos are taken using reflected light. a) Dendritic pyrite and sphalerite. b) Massive sphalerite with abundant intergrowths and inclusions of galena, which often appear faint within the interior of sphalerite. This suggests possible replacement by sphalerite. Late-stage galena on the edges of sphalerite is also present. c) Coarse-grained barite is accompanied by minor sulphide growth. d) Tetrahedrite-tennantite in several cases is intergrown with chalcopyrite. Amorphous silica (dark patches) thinly mantles sulphide phases. e) Plumose texture is preserved in thick sulphide overgrowth in the chalcopyrite-rich interior zone. Order of mineralization is consistent with increasing temperatures, where chalcopyrite forms at peak temperatures. Low temperature mineralization of sphalerite, Pb-As sulphosalts and amorphous silica follows. f) Relict plumose texture. It appears that sphalerite has psuedomorphed barite.

D1920 – R13:

Site Description

This sample was collected on the western talus slope of a large, massive sulphide mound. The highly sedimented nature of the slope suggests that the extinct blocks of talus are likely quite old. This could be linked to a felsic eruptive event that predates much of the sulphide material within the Niua South crater. Atop the slope, lies several chimney complexes, both active and inactive. Within some of the inactive complexes are short, bulbous chimneys that contain thin white cracks on their carapace. Most of the active chimneys are heavily covered in white anhydrite. One of the main chimneys is topped with a black-white beehive, diffusely venting white to grey smoke. A nearby chimney is venting low temperature white smoke.

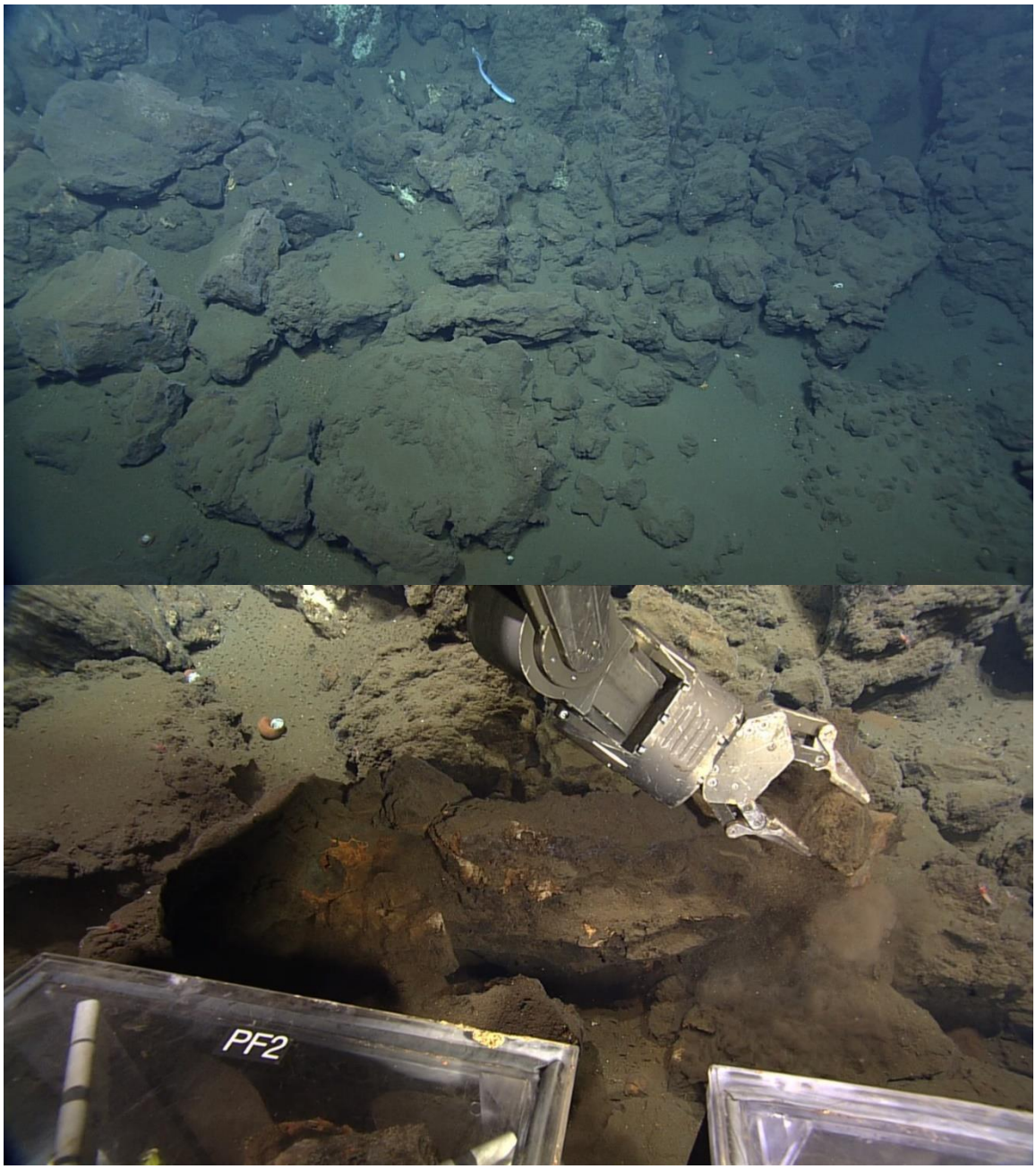

A highly sedimented talus slope which contained sample D1920-R13. The surrounding material may also be pumice. The bottom photograph shows the sample piece in the ROV grab arm.

Hand Sample Description

This sample is distinct, as it is not composed of sulphide material, and instead it is a small piece of pumice. In general, the groundmass is composed of microscopic amorphous glass fragments, and is highly vesicular. The interior groundmass differs in colour based upon

the degree of oxidation present. The innermost material, in which oxidation has not penetrated in any significant amount, is beige. Towards the sample exterior, the groundmass gradationally turns to a dark-grey, and is then abruptly defined by a dull-orange colour. The exterior surface is covered in a heavy layer of brown oxide material. As would be expected of this rock type, it is a very lightweight sample.

Hand sample for D1920-R13. The exterior is mostly weathered, but small fresh interior can be seen in the middle, where the ROV arm left claw marks upon collection.

D1920 – R14:

Site Description

This sample was from what appears to be a low relief talus slope. The overall composition of the surrounding material is unknown, but there is evidence for volcanic material. There is an abundance of material on the slope that is roughly uniform in size, aside from a few large blocks, one of which has apparent columnar jointing. The rock sample was collected from just underneath this block and exhibits flat surfaces that suggest it may have once been part of the larger block.

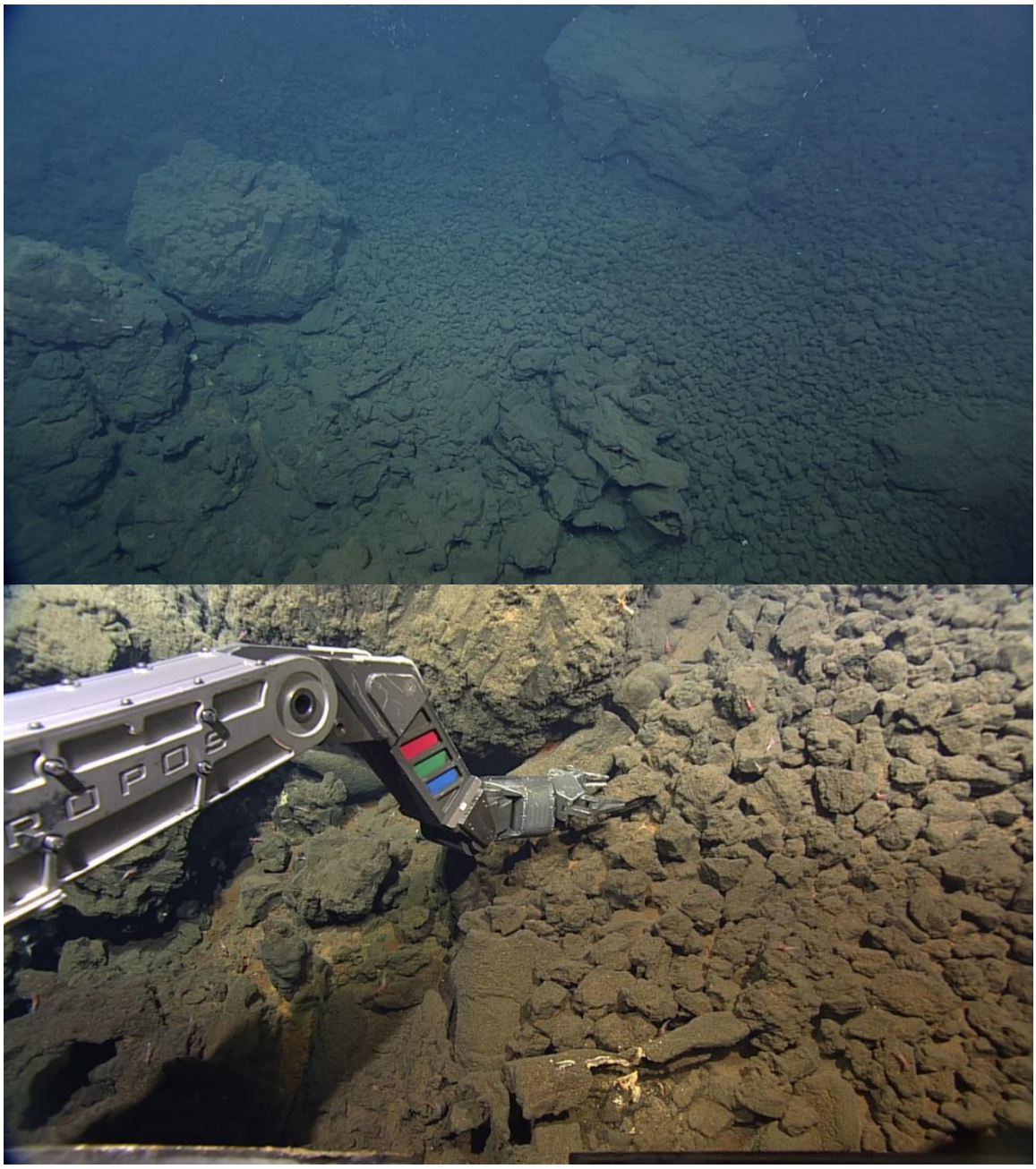

In the top photograph rock sample D1920-R14 was grabbed from the seafloor in front of the block of columnar jointed rhyolite on the left-hand side. The site appears to be the base of a gently sloping talus slope towards the right side of the photograph. In the bottom photograph the ROV picks up a piece of a rhyolitic columnar joint, which originates from the large block behind. This is indicated by the flat faces found on the rock sample that meet along a well-defined edge.

Hand Sample Description

Like the previous sample, this sample is also a piece of lightweight pumice. The highly vesicular groundmass is composed of amorphous glass fragments of primarily microscopic size, however there are a few visible crystals as large as 3 mm. The groundmass has a consistent beige to brown appearance, and its vesicles are lined with a dark-brown oxide coating. The exterior surface of the sample is heavily coated in orange-brown to black oxidation with a minor coverage of white bacterial growth.

Hand sample for D1920-R14. The exterior is mostly weathered, but small fresh interior can be seen in the middle, where the ROV arm left claw marks upon collection.

D1920 – R15:

Site Description

This sample was collected at the base of an active chimney complex, at the point where the chimney base meets the sulphide talus slope. The chimney complex itself appears to be largely venting diffuse, low temperature clear to white hydrothermal fluids. Some of the peripheral chimneys are smaller in size and appear inactive.

Site where D1920-R15 was collected. Top photograph shows the active chimney complex. Bottom photos highlight the chimney wall that the sample was taken from, the spot with the increased abundance of suspended sediments.

Hand Sample Description

This sample is small piece of sulphide material and has a very fine-grained (<< 1 mm), porous, grey-black to yellow-grey groundmass. However, upon cutting into the sample interior a distinct iridescent blue-purple colour can also be seen. It is primarily composed

of barite, chalcopyrite, and bornite, with minor amounts of anhydrite, pyrite, and various Cu-sulphides. The exterior surface has both minor amounts of orange oxidation and white bacterial growth.

Hand sample for D1920-R15. Photographs show opposite sides of the small sample.

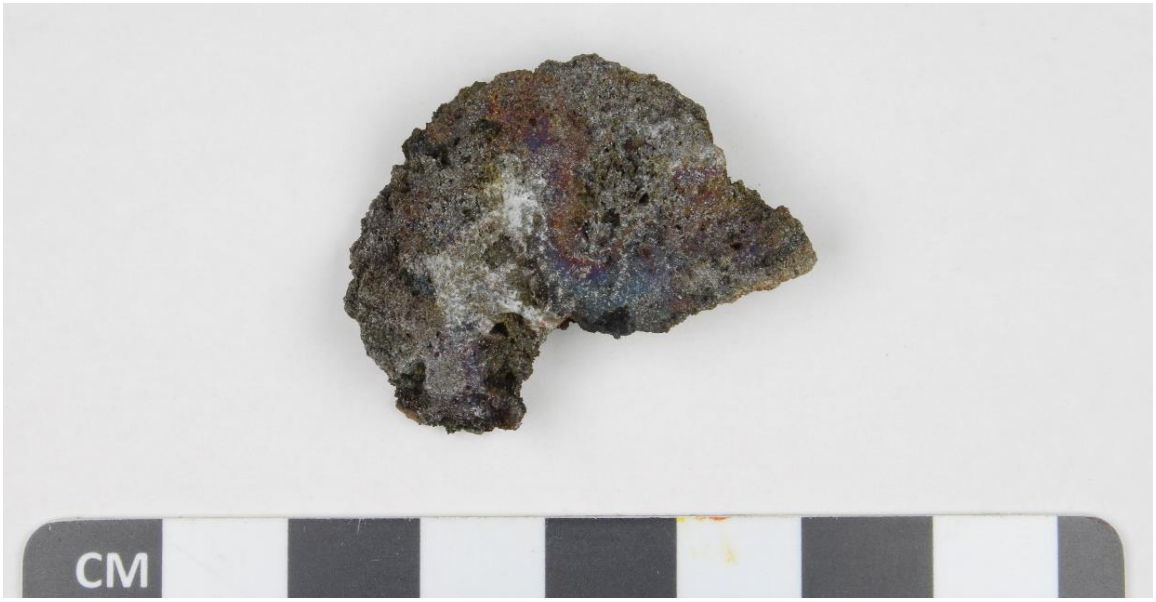

Thin section slab for D1920-R15. Thin section was cut from this face.

Mineral Abundances and Occurrences

Barite – 45%

Chalcopyrite – 25%

Bornite – 15%

Anhydrite – 7%

Tennantite & Tetrahedrite – Tennantite – 3%

Digenite – 3%

Pyrite – ≤ 1%

Sphalerite – ≤ 1%

Covellite – < 1%

Galena – << 1%

Barite occurs as euhedral to subhedral bladed and tabular crystals with some radiating bladed crystals. Grain size within the groundmass is generally relatively small (especially compared to anhydrite). Some coarse-grained crystals are present in porous spaces. Anomalous plumose texture is exhibited in localized areas of the sample exterior. Much of the barite present is overgrown by various sulphide phases. Chalcopyrite, bornite, tetrahedrite-tennantite, digenite, and covellite are intimately associated with one another through complex intergrowth or replacement. Chalcopyrite is the most abundant sulphide phase present and is commonly seen as exsolution lamellae in anhedral bornite grains, mantling bornite, or as intergrowths with tetrahedrite-tennantite. Much of the bornite

present exhibits a distinct exsolution texture with chalcopyrite and digenite forming as the lamellae. Aside from its occurrence in exsolution with chalcopyrite and bornite, digenite appears massive in a localized zone that transitions from chalcopyrite-dominated to bornite-dominated to digenite-dominated. Fine-grained, disseminated grains of covellite occur within chalcopyrite, bornite, and digenite. Covellite forms compact masses that occur along the boundaries of chalcopyrite and bornite, as well as within grains of bornite. It also commonly occurs with digenite in exsolution lamellae. Tetrahedrite-tennantite occurs as massive overgrowths in several places along the edges of chalcopyrite or as anhedral intergrowths with chalcopyrite. Anhydrite occurs as coarse-grained euhedral to subhedral bladed crystals and irregular masses and is curiously intermixed with barite. Trace amounts of pyrite occur as fine-grained semi-framboidal or rounded blebs and subhedral grains. Pyrite blebs are commonly found mantling barite and are typically overgrown by chalcopyrite, while subhedral pyrite are surrounded by bornite and chalcopyrite. In some cases, individual pyrite grains may exhibit interior fractures, some of which have been infilled by chalcopyrite. There are some minor occurrences of colloform pyrite as well. Sphalerite is present in trace abundance along the edges of chalcopyrite, in localized mantling of tetrahedrite-tennantite, and banded intergrowth within chalcopyrite. Tiny euhedral grains of galena are disseminated and grown along the edges of fine-grained barite and present in sphalerite mantling.

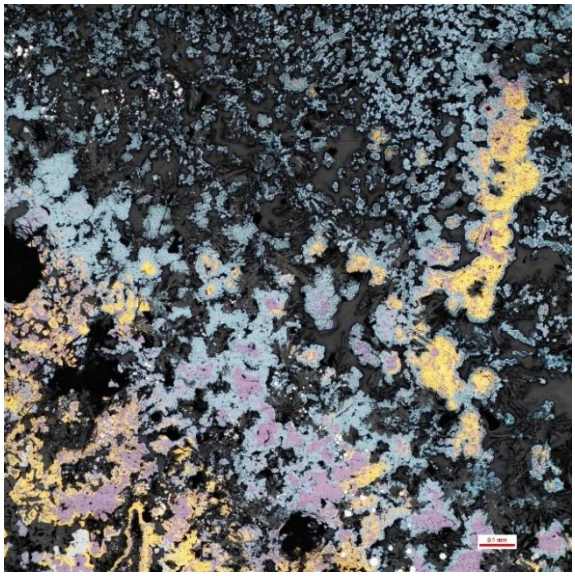

a.

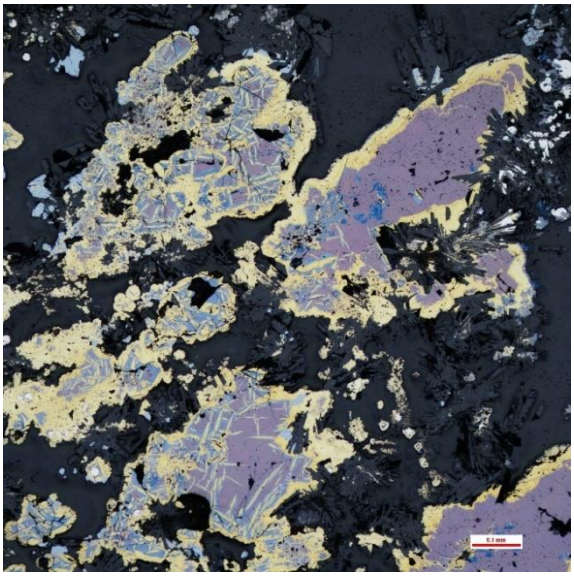

b.

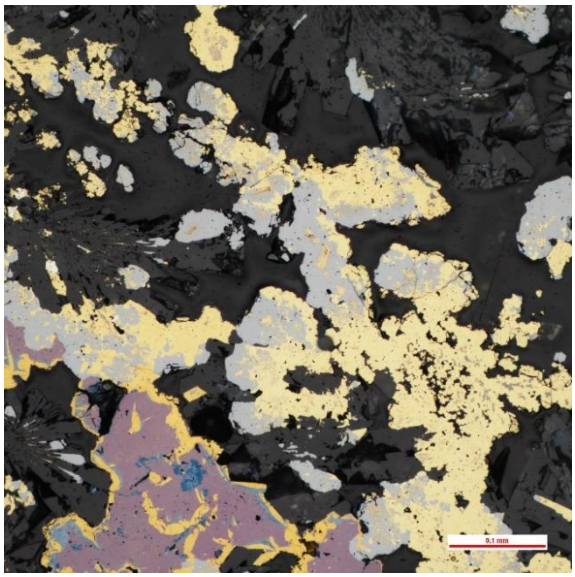

c.

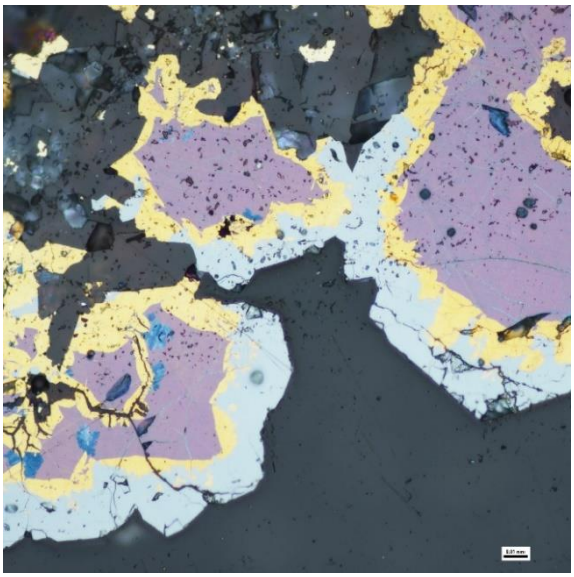

d.

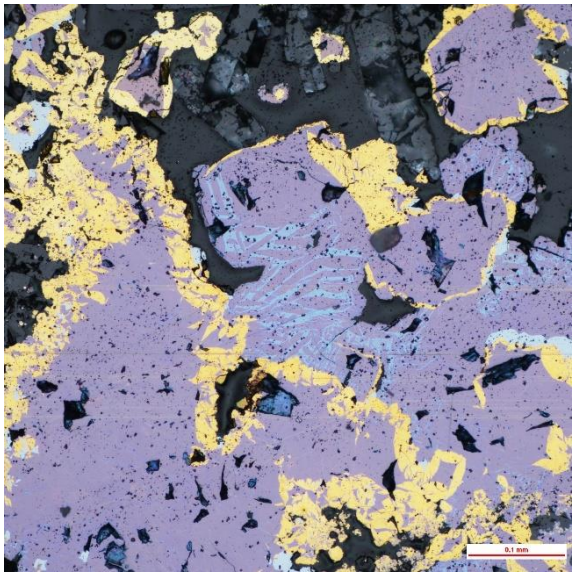

e.

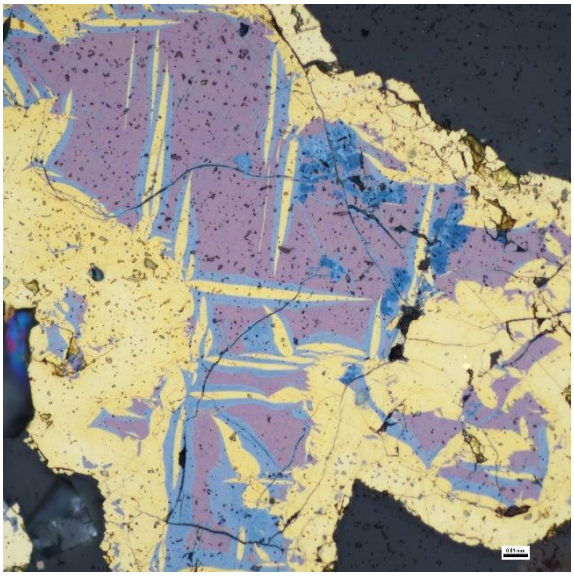

f.

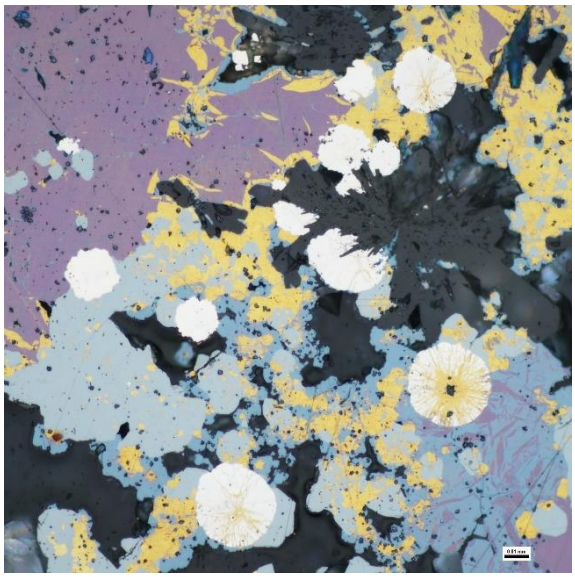

g.

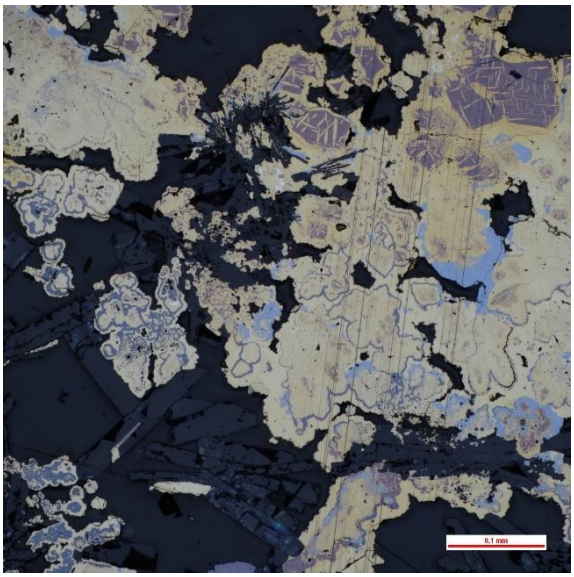

h.

Photomicrographs of sample D1920-R15. All photos are taken under reflected light. a) Transitional growth profile highlighting chalcopyrite and bornite adjacent to a digenite-dominated zone. b) Exsolution texture in bornite. Chalcopyrite is abundant in rimming bornite, as well as in exsolution lamellae with digenite and covellite. c) Tetrahedrite-tennantite intergrowths with chalcopyrite. Growth may occur on nearby sulphides or barite. d) Massive tetrahedrite-tennantite mantling chalcopyrite. e) Thin bands of digenite exsolution in bornite. Chalcopyrite rims bornite. f) High-magnification view of exsolution texture in bornite. Chalcopyrite and digenite are key constituents of the exsolution lamellae, with minor covellite masses replacing bornite. g) Pyrite blebs are infilled by chalcopyrite along thin internal fractures. Overgrowth of pyrite is very common, but pyrite can be seen mantling early barite. h) Banded growth of sphalerite in massive chalcopyrite. Tetrahedrite-tennantite exhibits both intergrown with chalcopyrite and overgrowth of chalcopyrite.

APPENDIX B – Whole-rock geochemistry for hydrothermal sulphide samples.

The following includes all elements analyzed for whole-rock geochemistry.

IGSN	Analyte Symbol	Ag	As	Au	Ba	Br
	Unit Symbol	ppm	ppm	ppb	%	ppm
	Detection Limit	2	1	2	0.002	0.5
	Analysis Method	INAA	INAA	INAA	INAA	INAA
IEMMR0001	D1918-R1	25	904	3530	1.87	bdl
IEMMR0002	D1918-R2	10	66	1720	0.001	1.5
IEMMR0003	D1918-R3	bdl	122	672	0.392	1.7
IEMMR0004	D1918-R4	32	643	5590	1.56	7.4
IEMMR0005	D1918-R5	21	711	4380	0.409	3.3
IEMMR0006	D1918-R6	210	4200	22900	16.2	bdl
IEMMR0007	D1918-R7	97	1720	14500	7.17	19.4
IEMMR0008	D1918-R8	115	2640	15200	7.14	bdl
IEMMR0009	D1918-R9	37	1410	9880	0.464	6.2
IEMMR000A	D1918-R10	264	3280	6080	9.86	2
IEMMR000B	D1918-R11	138	1260	16500	8.31	bdl
IEMMR000C	D1918-R12	175	2160	9020	14.7	bdl
IEMMR000D	D1918-R13	376	2150	24500	14.9	bdl
IEMMR000E	D1919-R1	647	5890	11800	22.1	bdl
IEMMR000F-1	D1919-R2 A	316	2350	14800	27	bdl
IEMMR000F-2	D1919-R2 B	177	6850	444	15.6	bdl
IEMMR000F-3	D1919-R2 C	556	4000	12200	19.9	bdl
IEMMR000G-1	D1919-R3 TOP A	471	4900	8190	26.4	bdl
IEMMR000G-2	D1919-R3 TOP C	299	5290	12400	24.2	bdl
IEMMR000G-3	D1919-R3 TRUNK 1	242	3010	11800	22.8	bdl
IEMMR000G-4	D1919-R3 TRUNK 2	328	2220	25700	20.7	bdl
IEMMR000H	D1919-R4	322	4120	6550	19.4	12.1
IEMMR000I	D1919-R5	389	6640	26900	26.2	bdl
IEMMR000J-1	D1919-R6A	307	5570	11400	18.1	11.3
IEMMR000J-2	D1919-R6B	4	120	3640	0.458	2.8
IEMMR000L	D1920-R2	266	3900	13700	38.3	bdl
IEMMR000M	D1920-R3	415	2310	25900	19.9	bdl
IEMMR000O	D1920-R5	22	276	15100	26.8	7.5
IEMMR000Q	D1920-R7	229	750	25000	8.06	bdl
IEMMR000R	D1920-R8	296	1340	16700	3.88	14.4
IEMMR000S	D1920-SED	117	2300	9090	11.5	bdl
IEMMR000T	D1920-R9	316	7290	16000	9.16	bdl
IEMMR000U	D1920-R10	33	4580	6020	8.52	12.1
IEMMR000V	D1920-R11	125	664	16100	13.3	bdl
IEMMR000W	D1920-R12	201	4430	9890	11.7	bdl
-	D1920-R13	bdl	134	345	0.203	28.4
-	D1920-R14	bdl	434	798	1.81	63.9
IEMMR000Z	D1920-R15	124	6180	50600	15.5	2.6
-	D1920-R16	bdl	3030	234	0.282	37.8

IGSN	Analyte Symbol	Co	Cr	Cs	Fe	Hf
	Unit Symbol	ppm	ppm	ppm	%	ppm
	Detection Limit	0.1	0.5	0.2	0.01	0.2
	Analysis Method	INAA	INAA	INAA	INAA	INAA
IEMMR0001	D1918-R1	208	bdl	bdl	29.4	bdl
IEMMR0002	D1918-R2	159	bdl	bdl	27.9	bdl
IEMMR0003	D1918-R3	18.5	2.5	bdl	27.8	bdl
IEMMR0004	D1918-R4	111	bdl	bdl	20.2	bdl
IEMMR0005	D1918-R5	173	bdl	bdl	14.3	bdl
IEMMR0006	D1918-R6	161	bdl	bdl	7.59	bdl
IEMMR0007	D1918-R7	219	bdl	bdl	21.8	bdl
IEMMR0008	D1918-R8	137	bdl	bdl	16.5	bdl
IEMMR0009	D1918-R9	249	bdl	bdl	34.1	bdl
IEMMR000A	D1918-R10	111	bdl	bdl	9.4	bdl
IEMMR000B	D1918-R11	143	bdl	bdl	20.8	bdl
IEMMR000C	D1918-R12	145	bdl	bdl	9	bdl
IEMMR000D	D1918-R13	129	bdl	bdl	8.4	bdl
IEMMR000E	D1919-R1	78.9	bdl	bdl	3.11	bdl
IEMMR000F-1	D1919-R2 A	63.9	bdl	bdl	2.28	bdl
IEMMR000F-2	D1919-R2 B	14.4	bdl	bdl	1.26	bdl
IEMMR000F-3	D1919-R2 C	89.9	bdl	bdl	3.36	bdl
IEMMR000G-1	D1919-R3 TOP A	201	bdl	bdl	5.28	bdl
IEMMR000G-2	D1919-R3 TOP C	127	bdl	bdl	6.29	bdl
IEMMR000G-3	D1919-R3 TRUNK 1	152	bdl	bdl	7.39	bdl
IEMMR000G-4	D1919-R3 TRUNK 2	172	bdl	bdl	12.4	bdl
IEMMR000H	D1919-R4	98	bdl	bdl	1.22	bdl
IEMMR000I	D1919-R5	229	bdl	bdl	6.92	bdl
IEMMR000J-1	D1919-R6A	189	bdl	bdl	5.32	bdl
IEMMR000J-2	D1919-R6B	44.5	bdl	bdl	3.27	bdl
IEMMR000L	D1920-R2	54.8	bdl	bdl	1.95	bdl
IEMMR000M	D1920-R3	48	bdl	bdl	4.27	bdl
IEMMR000O	D1920-R5	120	bdl	bdl	11.5	bdl
IEMMR000Q	D1920-R7	280	bdl	bdl	5.76	bdl
IEMMR000R	D1920-R8	38.2	bdl	bdl	7.32	bdl
IEMMR000S	D1920-SED	200	8.2	bdl	27.8	bdl
IEMMR000T	D1920-R9	106	bdl	bdl	8.73	bdl
IEMMR000U	D1920-R10	121	bdl	bdl	38.5	bdl
IEMMR000V	D1920-R11	28.7	bdl	bdl	4.98	bdl
IEMMR000W	D1920-R12	133	bdl	bdl	3.59	bdl
-	D1920-R13	365	38	0.8	3.35	bdl
-	D1920-R14	185	35.1	bdl	7.05	bdl
IEMMR000Z	D1920-R15	9.7	bdl	bdl	8.5	bdl
-	D1920-R16	120	5.6	bdl	12.3	bdl

IGSN	Analyte Symbol	Ir	Na	Ni	Sb	Sc
	Unit Symbol	ppb	%	ppm	ppm	ppm
	Detection Limit	2	0.001	50	0.1	0.01
	Analysis Method	INAA	INAA	INAA	INAA	INAA
IEMMR0001	D1918-R1	bdl	0.02	bdl	81	bdl
IEMMR0002	D1918-R2	bdl	0.03	bdl	9	0.05
IEMMR0003	D1918-R3	bdl	0.02	bdl	15	0.41
IEMMR0004	D1918-R4	bdl	0.09	bdl	111	1.95
IEMMR0005	D1918-R5	bdl	0.04	bdl	60	6.63
IEMMR0006	D1918-R6	bdl	0.1	bdl	890	bdl
IEMMR0007	D1918-R7	bdl	0.4	bdl	235	bdl
IEMMR0008	D1918-R8	bdl	0.05	220	560	1.21
IEMMR0009	D1918-R9	bdl	0.07	bdl	61	0.12
IEMMR000A	D1918-R10	bdl	0.05	bdl	1800	bdl
IEMMR000B	D1918-R11	bdl	0.07	bdl	346	bdl
IEMMR000C	D1918-R12	bdl	0.08	bdl	872	bdl
IEMMR000D	D1918-R13	bdl	0.34	bdl	934	bdl
IEMMR000E	D1919-R1	bdl	0.05	bdl	1890	bdl
IEMMR000F-1	D1919-R2 A	bdl	0.04	bdl	1060	bdl
IEMMR000F-2	D1919-R2 B	bdl	0.12	bdl	1950	bdl
IEMMR000F-3	D1919-R2 C	bdl	0.06	bdl	2220	bdl
IEMMR000G-1	D1919-R3 TOP A	bdl	0.17	bdl	1430	bdl
IEMMR000G-2	D1919-R3 TOP C	bdl	0.16	bdl	1490	bdl
IEMMR000G-3	D1919-R3 TRUNK 1	bdl	0.1	bdl	948	0.74
IEMMR000G-4	D1919-R3 TRUNK 2	bdl	0.02	bdl	886	bdl
IEMMR000H	D1919-R4	bdl	0.1	bdl	1840	bdl
IEMMR000I	D1919-R5	bdl	0.16	bdl	1660	bdl
IEMMR000J-1	D1919-R6A	bdl	0.17	bdl	1380	bdl
IEMMR000J-2	D1919-R6B	bdl	0.05	bdl	25	4.3
IEMMR000L	D1920-R2	bdl	0.08	bdl	1060	bdl
IEMMR000M	D1920-R3	bdl	0.07	bdl	1190	bdl
IEMMR000O	D1920-R5	bdl	0.07	bdl	50	bdl
IEMMR000Q	D1920-R7	bdl	0.16	bdl	604	bdl
IEMMR000R	D1920-R8	bdl	0.17	bdl	1620	bdl
IEMMR000S	D1920-SED	bdl	0.14	bdl	193	bdl
IEMMR000T	D1920-R9	bdl	0.13	bdl	2290	bdl
IEMMR000U	D1920-R10	bdl	0.22	140	54	bdl
IEMMR000V	D1920-R11	bdl	0.18	bdl	1060	bdl
IEMMR000W	D1920-R12	bdl	0.08	bdl	1260	bdl
-	D1920-R13	bdl	2.74	bdl	8	11.1
-	D1920-R14	bdl	2.72	bdl	21	11.1
IEMMR000Z	D1920-R15	bdl	0.03	bdl	741	bdl
-	D1920-R16	bdl	2.37	bdl	29	10.8

IGSN	Analyte Symbol	Se	Ta	Th	U	Zn
	Unit Symbol	ppm	ppm	ppm	ppm	%
	Detection Limit	0.5	0.3	0.1	0.1	0.001
	Analysis Method	INAA	INAA	INAA	INAA	INAA
IEMMR0001	D1918-R1	1400	bdl	bdl	bdl	0.603
IEMMR0002	D1918-R2	2680	bdl	bdl	bdl	0.036
IEMMR0003	D1918-R3	2630	bdl	bdl	bdl	0.077
IEMMR0004	D1918-R4	474	bdl	bdl	bdl	0.941
IEMMR0005	D1918-R5	120	bdl	bdl	bdl	0.173
IEMMR0006	D1918-R6	bdl	bdl	bdl	bdl	6.39
IEMMR0007	D1918-R7	bdl	bdl	bdl	bdl	1.44
IEMMR0008	D1918-R8	70	bdl	bdl	bdl	4.31
IEMMR0009	D1918-R9	220	bdl	bdl	bdl	0.046
IEMMR000A	D1918-R10	bdl	bdl	bdl	bdl	25.9
IEMMR000B	D1918-R11	29	bdl	bdl	bdl	1.75
IEMMR000C	D1918-R12	bdl	bdl	bdl	bdl	11.6
IEMMR000D	D1918-R13	bdl	bdl	bdl	bdl	10.2
IEMMR000E	D1919-R1	bdl	bdl	bdl	bdl	29.5
IEMMR000F-1	D1919-R2 A	bdl	bdl	bdl	bdl	18.8
IEMMR000F-2	D1919-R2 B	bdl	bdl	bdl	bdl	37.3
IEMMR000F-3	D1919-R2 C	bdl	bdl	bdl	bdl	32.1
IEMMR000G-1	D1919-R3 TOP A	bdl	bdl	bdl	bdl	15.6
IEMMR000G-2	D1919-R3 TOP C	bdl	bdl	bdl	bdl	21.4
IEMMR000G-3	D1919-R3 TRUNK 1	bdl	bdl	bdl	bdl	14.7
IEMMR000G-4	D1919-R3 TRUNK 2	bdl	bdl	bdl	bdl	15.8
IEMMR000H	D1919-R4	bdl	bdl	bdl	bdl	19.9
IEMMR000I	D1919-R5	bdl	bdl	bdl	bdl	9.9
IEMMR000J-1	D1919-R6A	bdl	bdl	bdl	bdl	16.9
IEMMR000J-2	D1919-R6B	32	bdl	bdl	bdl	0.095
IEMMR000L	D1920-R2	bdl	bdl	bdl	bdl	7.86
IEMMR000M	D1920-R3	bdl	bdl	bdl	bdl	32.1
IEMMR000O	D1920-R5	bdl	bdl	bdl	bdl	0.045
IEMMR000Q	D1920-R7	bdl	bdl	bdl	bdl	9.23
IEMMR000R	D1920-R8	bdl	bdl	bdl	bdl	17
IEMMR000S	D1920-SED	63	bdl	bdl	bdl	3.69
IEMMR000T	D1920-R9	bdl	bdl	bdl	bdl	6.48
IEMMR000U	D1920-R10	bdl	bdl	bdl	bdl	0.176
IEMMR000V	D1920-R11	bdl	bdl	bdl	bdl	28.7
IEMMR000W	D1920-R12	bdl	bdl	bdl	bdl	6.32
-	D1920-R13	bdl	bdl	bdl	9.2	0.058
-	D1920-R14	bdl	bdl	bdl	bdl	0.082
IEMMR000Z	D1920-R15	bdl	bdl	bdl	bdl	0.426
-	D1920-R16	bdl	bdl	bdl	4.1	0.106

IGSN	Analyte Symbol	La	Ce	Nd	Sm	Eu
	Unit Symbol	ppm	ppm	ppm	ppm	ppm
	Detection Limit	0.05	1	1	0.01	0.05
	Analysis Method	INAA	INAA	INAA	INAA	INAA
IEMMR0001	D1918-R1	1.64	bdl	19	bdl	bdl
IEMMR0002	D1918-R2	bdl	bdl	bdl	bdl	bdl
IEMMR0003	D1918-R3	0.59	bdl	bdl	0.02	bdl
IEMMR0004	D1918-R4	3.06	bdl	bdl	0.18	0.25
IEMMR0005	D1918-R5	2.4	bdl	8	0.29	bdl
IEMMR0006	D1918-R6	16.8	9	bdl	bdl	bdl
IEMMR0007	D1918-R7	9.48	bdl	bdl	bdl	bdl
IEMMR0008	D1918-R8	7.53	bdl	bdl	bdl	bdl
IEMMR0009	D1918-R9	0.58	bdl	bdl	bdl	bdl
IEMMR000A	D1918-R10	6.89	bdl	bdl	bdl	bdl
IEMMR000B	D1918-R11	14.2	17	bdl	bdl	bdl
IEMMR000C	D1918-R12	17.9	12	bdl	bdl	bdl
IEMMR000D	D1918-R13	25.6	18	bdl	bdl	bdl
IEMMR000E	D1919-R1	17.8	9	bdl	bdl	bdl
IEMMR000F-1	D1919-R2 A	13.8	bdl	124	bdl	bdl
IEMMR000F-2	D1919-R2 B	7.11	bdl	bdl	bdl	bdl
IEMMR000F-3	D1919-R2 C	13.8	bdl	146	bdl	bdl
IEMMR000G-1	D1919-R3 TOP A	22.8	17	bdl	bdl	bdl
IEMMR000G-2	D1919-R3 TOP C	16.4	10	103	0.13	bdl
IEMMR000G-3	D1919-R3 TRUNK 1	17.7	4	104	bdl	bdl
IEMMR000G-4	D1919-R3 TRUNK 2	15.5	bdl	93	0.07	bdl
IEMMR000H	D1919-R4	9.02	bdl	bdl	bdl	bdl
IEMMR000I	D1919-R5	18.6	20	bdl	bdl	bdl
IEMMR000J-1	D1919-R6A	20.1	17	bdl	bdl	bdl
IEMMR000J-2	D1919-R6B	2.4	4	bdl	0.49	0.12
IEMMR000L	D1920-R2	7.62	bdl	165	bdl	bdl
IEMMR000M	D1920-R3	11.6	bdl	103	0.04	bdl
IEMMR000O	D1920-R5	9.74	bdl	bdl	bdl	bdl
IEMMR000Q	D1920-R7	11	bdl	bdl	bdl	bdl
IEMMR000R	D1920-R8	5.2	bdl	76	bdl	bdl
IEMMR000S	D1920-SED	7.33	2	bdl	0.21	bdl
IEMMR000T	D1920-R9	18.5	8	125	bdl	bdl
IEMMR000U	D1920-R10	4.75	bdl	bdl	0.12	bdl
IEMMR000V	D1920-R11	1.76	bdl	bdl	bdl	bdl
IEMMR000W	D1920-R12	17.3	6	197	0.09	bdl
-	D1920-R13	14.1	26	22	2.06	bdl
-	D1920-R14	16.5	27	30	2.09	bdl
IEMMR000Z	D1920-R15	4.94	bdl	bdl	0.18	bdl
-	D1920-R16	12.2	17	15	2.04	0.41

IGSN	Analyte Symbol	Tb	Yb	Lu	Al	B
	Unit Symbol	ppm	ppm	ppm	%	ppm
	Detection Limit	0.1	0.05	0.01	0.01	10
	Analysis Method	INAA	INAA	INAA	FUS-MS	FUS-MS
IEMMR0001	D1918-R1	bdl	bdl	bdl	0.02	bdl
IEMMR0002	D1918-R2	bdl	bdl	bdl	0.01	bdl
IEMMR0003	D1918-R3	bdl	bdl	bdl	bdl	10
IEMMR0004	D1918-R4	bdl	bdl	bdl	0.01	bdl
IEMMR0005	D1918-R5	bdl	bdl	bdl	bdl	bdl
IEMMR0006	D1918-R6	bdl	bdl	bdl	0.01	bdl
IEMMR0007	D1918-R7	bdl	bdl	bdl	0.1	10
IEMMR0008	D1918-R8	bdl	bdl	bdl	0.02	bdl
IEMMR0009	D1918-R9	bdl	bdl	bdl	0.13	bdl
IEMMR000A	D1918-R10	bdl	bdl	bdl	0.03	bdl
IEMMR000B	D1918-R11	bdl	bdl	bdl	0.09	bdl
IEMMR000C	D1918-R12	bdl	bdl	bdl	bdl	bdl
IEMMR000D	D1918-R13	bdl	bdl	bdl	bdl	bdl
IEMMR000E	D1919-R1	bdl	bdl	bdl	0.03	bdl
IEMMR000F-1	D1919-R2 A	bdl	bdl	0.05	0.01	bdl
IEMMR000F-2	D1919-R2 B	bdl	bdl	0.11	0.03	bdl
IEMMR000F-3	D1919-R2 C	bdl	bdl	bdl	bdl	bdl
IEMMR000G-1	D1919-R3 TOP A	bdl	bdl	bdl	bdl	bdl
IEMMR000G-2	D1919-R3 TOP C	bdl	bdl	bdl	0.02	bdl
IEMMR000G-3	D1919-R3 TRUNK 1	bdl	bdl	bdl	bdl	bdl
IEMMR000G-4	D1919-R3 TRUNK 2	bdl	bdl	bdl	0.04	bdl
IEMMR000H	D1919-R4	bdl	bdl	bdl	bdl	bdl
IEMMR000I	D1919-R5	bdl	bdl	bdl	bdl	bdl
IEMMR000J-1	D1919-R6A	bdl	bdl	bdl	bdl	bdl
IEMMR000J-2	D1919-R6B	bdl	bdl	bdl	bdl	bdl
IEMMR000L	D1920-R2	bdl	bdl	0.09	bdl	bdl
IEMMR000M	D1920-R3	bdl	bdl	bdl	0.03	bdl
IEMMR000O	D1920-R5	bdl	bdl	bdl	0.03	bdl
IEMMR000Q	D1920-R7	bdl	bdl	bdl	0.05	bdl
IEMMR000R	D1920-R8	bdl	bdl	bdl	0.02	bdl
IEMMR000S	D1920-SED	bdl	bdl	bdl	0.03	bdl
IEMMR000T	D1920-R9	bdl	bdl	bdl	bdl	bdl
IEMMR000U	D1920-R10	bdl	bdl	bdl	0.07	bdl
IEMMR000V	D1920-R11	bdl	bdl	bdl	bdl	bdl
IEMMR000W	D1920-R12	bdl	bdl	bdl	bdl	bdl
-	D1920-R13	bdl	1.56	0.16	6.39	50
-	D1920-R14	bdl	1.47	0.25	4.7	100
IEMMR000Z	D1920-R15	bdl	bdl	bdl	bdl	bdl
-	D1920-R16	bdl	1.26	0.11	4.49	90

IGSN	Analyte Symbol	Be	Bi	Ca	Cd	Cu
	Unit Symbol	ppm	ppm	%	ppm	%
	Detection Limit	3	2	0.01	2	0.0002
	Analysis Method	FUS-MS	FUS-MS	FUS-MS	FUS-MS	FUS-MS
IEMMR0001	D1918-R1	bdl	48	0.05	15	26.4
IEMMR0002	D1918-R2	bdl	23	0.05	bdl	33.1
IEMMR0003	D1918-R3	bdl	8	0.88	3	33.4
IEMMR0004	D1918-R4	bdl	75	7.55	28	20.7
IEMMR0005	D1918-R5	bdl	73	15.6	6	10.6
IEMMR0006	D1918-R6	bdl	bdl	0.11	344	3.63
IEMMR0007	D1918-R7	bdl	45	0.06	69	16.4
IEMMR0008	D1918-R8	bdl	62	3.21	141	14
IEMMR0009	D1918-R9	bdl	93	0.04	bdl	28.4
IEMMR000A	D1918-R10	bdl	5	0.05	936	1.07
IEMMR000B	D1918-R11	bdl	9	0.13	72	18.1
IEMMR000C	D1918-R12	bdl	3	0.1	384	2.74
IEMMR000D	D1918-R13	bdl	bdl	0.18	560	3.17
IEMMR000E	D1919-R1	bdl	bdl	0.12	723	0.0541
IEMMR000F-1	D1919-R2 A	bdl	bdl	0.12	489	0.646
IEMMR000F-2	D1919-R2 B	bdl	bdl	0.05	620	0.032
IEMMR000F-3	D1919-R2 C	bdl	bdl	0.1	758	0.228
IEMMR000G-1	D1919-R3 TOP A	bdl	bdl	0.15	573	0.91
IEMMR000G-2	D1919-R3 TOP C	bdl	bdl	0.41	511	1.82
IEMMR000G-3	D1919-R3 TRUNK 1	bdl	bdl	2.82	386	2.44
IEMMR000G-4	D1919-R3 TRUNK 2	bdl	bdl	0.09	367	5.7
IEMMR000H	D1919-R4	bdl	bdl	0.1	694	0.153
IEMMR000I	D1919-R5	bdl	bdl	0.12	357	2.37
IEMMR000J-1	D1919-R6A	bdl	bdl	0.17	570	1.19
IEMMR000J-2	D1919-R6B	bdl	41	25.5	2	3.32
IEMMR000L	D1920-R2	bdl	bdl	0.12	343	0.702
IEMMR000M	D1920-R3	bdl	bdl	0.09	1190	0.648
IEMMR000O	D1920-R5	bdl	bdl	0.08	bdl	10.3
IEMMR000Q	D1920-R7	bdl	bdl	0.08	845	1.68
IEMMR000R	D1920-R8	bdl	9	0.09	1400	1.57
IEMMR000S	D1920-SED	bdl	22	0.12	137	6.98
IEMMR000T	D1920-R9	bdl	bdl	0.18	330	3.14
IEMMR000U	D1920-R10	bdl	6	0.09	5	1.52
IEMMR000V	D1920-R11	bdl	2	0.08	956	0.815
IEMMR000W	D1920-R12	bdl	bdl	0.19	415	1.32
-	D1920-R13	bdl	bdl	2.36	bdl	0.263
-	D1920-R14	bdl	5	2.38	bdl	1.02
IEMMR000Z	D1920-R15	bdl	bdl	1.77	16	21.9
-	D1920-R16	bdl	bdl	2.25	bdl	0.291

IGSN	Analyte Symbol	Dy	Er	Ga	Gd	Ge
	Unit Symbol	ppm	ppm	ppm	ppm	ppm
	Detection Limit	0.3	0.1	0.2	0.1	0.7
	Analysis Method	FUS-MS	FUS-MS	FUS-MS	FUS-MS	FUS-MS
IEMMR0001	D1918-R1	bdl	bdl	5.7	0.1	9.4
IEMMR0002	D1918-R2	bdl	bdl	1.7	bdl	6.3
IEMMR0003	D1918-R3	bdl	bdl	1.3	bdl	6.8
IEMMR0004	D1918-R4	bdl	bdl	7.4	0.2	4.7
IEMMR0005	D1918-R5	bdl	bdl	5.8	0.3	4.5
IEMMR0006	D1918-R6	bdl	bdl	56.9	1.4	30.7
IEMMR0007	D1918-R7	bdl	bdl	16.4	0.5	0.35
IEMMR0008	D1918-R8	bdl	bdl	28.9	1	21.5
IEMMR0009	D1918-R9	bdl	bdl	8	bdl	6.8
IEMMR000A	D1918-R10	bdl	bdl	177	0.7	16
IEMMR000B	D1918-R11	bdl	bdl	24.9	1	10.9
IEMMR000C	D1918-R12	bdl	bdl	52.6	1.1	19.6
IEMMR000D	D1918-R13	bdl	bdl	110	1.1	16.2
IEMMR000E	D1919-R1	bdl	bdl	98.6	0.3	41.7
IEMMR000F-1	D1919-R2 A	bdl	bdl	58.9	1	28.3
IEMMR000F-2	D1919-R2 B	bdl	bdl	8.8	1.3	52.4
IEMMR000F-3	D1919-R2 C	bdl	bdl	115	bdl	37
IEMMR000G-1	D1919-R3 TOP A	bdl	bdl	100	bdl	26.3
IEMMR000G-2	D1919-R3 TOP C	bdl	bdl	89.2	1.1	30.8
IEMMR000G-3	D1919-R3 TRUNK 1	bdl	bdl	68.4	bdl	19.8
IEMMR000G-4	D1919-R3 TRUNK 2	bdl	bdl	66.5	0.1	21.3
IEMMR000H	D1919-R4	bdl	bdl	82.7	0.3	16.3
IEMMR000I	D1919-R5	bdl	bdl	75.2	1.4	43.1
IEMMR000J-1	D1919-R6A	bdl	bdl	93.8	0.2	20.8
IEMMR000J-2	D1919-R6B	0.3	0.1	1.6	0.5	1.4
IEMMR000L	D1920-R2	bdl	bdl	39.4	1.4	17
IEMMR000M	D1920-R3	bdl	bdl	189	bdl	18.8
IEMMR000O	D1920-R5	bdl	bdl	14.3	0.2	6.6
IEMMR000Q	D1920-R7	bdl	bdl	105	0.9	11.6
IEMMR000R	D1920-R8	bdl	bdl	176	bdl	25.6
IEMMR000S	D1920-SED	bdl	bdl	25.3	bdl	10.7
IEMMR000T	D1920-R9	bdl	bdl	67.9	1.7	35.1
IEMMR000U	D1920-R10	bdl	bdl	2.7	bdl	5.8
IEMMR000V	D1920-R11	bdl	bdl	113	bdl	25.3
IEMMR000W	D1920-R12	bdl	bdl	69.8	bdl	39.2
-	D1920-R13	1.9	1.4	11.5	1.8	3.1
-	D1920-R14	2.6	2	10.4	2.4	3.8
IEMMR000Z	D1920-R15	bdl	bdl	18.2	0.9	17.2
-	D1920-R16	2	1.5	10.1	1.9	8.3

IGSN	Analyte Symbol	Ho	In	K	Li	Mg
	Unit Symbol	ppm	ppm	%	ppm	%
	Detection Limit	0.2	0.2	0.1	3	0.01
	Analysis Method	FUS-MS	FUS-MS	FUS-MS	FUS-MS	FUS-MS
IEMMR0001	D1918-R1	bdl	2.5	bdl	bdl	bdl
IEMMR0002	D1918-R2	bdl	2	bdl	bdl	bdl
IEMMR0003	D1918-R3	bdl	1.8	bdl	bdl	bdl
IEMMR0004	D1918-R4	bdl	3.1	bdl	bdl	0.04
IEMMR0005	D1918-R5	bdl	2.4	bdl	bdl	0.02
IEMMR0006	D1918-R6	bdl	6.1	bdl	bdl	bdl
IEMMR0007	D1918-R7	bdl	5.2	bdl	10	0.02
IEMMR0008	D1918-R8	bdl	5.9	bdl	bdl	bdl
IEMMR0009	D1918-R9	bdl	6.3	bdl	3	bdl
IEMMR000A	D1918-R10	bdl	0.6	bdl	bdl	bdl
IEMMR000B	D1918-R11	bdl	7.7	bdl	bdl	bdl
IEMMR000C	D1918-R12	bdl	2.8	bdl	bdl	bdl
IEMMR000D	D1918-R13	bdl	7.7	bdl	bdl	0.03
IEMMR000E	D1919-R1	bdl	4	bdl	6	bdl
IEMMR000F-1	D1919-R2 A	bdl	3	bdl	3	bdl
IEMMR000F-2	D1919-R2 B	bdl	0.2	bdl	4	bdl
IEMMR000F-3	D1919-R2 C	bdl	3.9	bdl	5	bdl
IEMMR000G-1	D1919-R3 TOP A	bdl	4.5	bdl	bdl	bdl
IEMMR000G-2	D1919-R3 TOP C	bdl	4.1	bdl	bdl	bdl
IEMMR000G-3	D1919-R3 TRUNK 1	bdl	4.1	bdl	4	0.07
IEMMR000G-4	D1919-R3 TRUNK 2	bdl	6.7	bdl	bdl	bdl
IEMMR000H	D1919-R4	bdl	2.4	bdl	bdl	0.01
IEMMR000I	D1919-R5	bdl	9.8	bdl	bdl	0.01
IEMMR000J-1	D1919-R6A	bdl	6.3	bdl	bdl	0.01
IEMMR000J-2	D1919-R6B	bdl	1.2	bdl	bdl	0.03
IEMMR000L	D1920-R2	bdl	3.6	bdl	bdl	bdl
IEMMR000M	D1920-R3	bdl	5.2	bdl	bdl	bdl
IEMMR000O	D1920-R5	bdl	2.9	bdl	22	bdl
IEMMR000Q	D1920-R7	bdl	3.2	bdl	7	0.01
IEMMR000R	D1920-R8	bdl	0.7	bdl	11	0.01
IEMMR000S	D1920-SED	bdl	2.8	bdl	bdl	bdl
IEMMR000T	D1920-R9	bdl	11	bdl	bdl	0.02
IEMMR000U	D1920-R10	bdl	0.8	bdl	14	0.02
IEMMR000V	D1920-R11	bdl	0.8	bdl	5	0.02
IEMMR000W	D1920-R12	bdl	3.7	bdl	bdl	0.01
-	D1920-R13	0.4	bdl	1.1	33	0.54
-	D1920-R14	0.6	0.5	0.9	16	0.74
IEMMR000Z	D1920-R15	bdl	5.8	bdl	bdl	bdl
-	D1920-R16	0.4	bdl	0.9	18	0.61

IGSN	Analyte Symbol	Mn	Mo	Nb	Pb	Pr
	Unit Symbol	ppm	ppm	ppm	%	ppm
	Detection Limit	3	1	2.4	0.00008	0.1
	Analysis Method	FUS-MS	FUS-MS	FUS-MS	FUS-MS	FUS-MS
IEMMR0001	D1918-R1	14	38	bdl	0.0858	0.1
IEMMR0002	D1918-R2	11	16	bdl	0.00577	bdl
IEMMR0003	D1918-R3	16	5	bdl	0.0164	bdl
IEMMR0004	D1918-R4	10	32	bdl	0.14	0.4
IEMMR0005	D1918-R5	18	40	bdl	0.0681	0.4
IEMMR0006	D1918-R6	82	41	bdl	0.976	0.7
IEMMR0007	D1918-R7	28	104	6.6	0.254	0.5
IEMMR0008	D1918-R8	20	123	bdl	0.602	0.4
IEMMR0009	D1918-R9	23	194	bdl	0.0492	bdl
IEMMR000A	D1918-R10	96	58	bdl	2.58	0.4
IEMMR000B	D1918-R11	330	204	bdl	0.238	1.1
IEMMR000C	D1918-R12	37	49	bdl	1.02	1.2
IEMMR000D	D1918-R13	150	56	bdl	0.649	1.2
IEMMR000E	D1919-R1	57	10	bdl	1.94	0.6
IEMMR000F-1	D1919-R2 A	24	14	bdl	1.53	0.4
IEMMR000F-2	D1919-R2 B	21	7	bdl	3.25	0.2
IEMMR000F-3	D1919-R2 C	43	20	bdl	2.81	0.4
IEMMR000G-1	D1919-R3 TOP A	43	27	bdl	1.55	0.7
IEMMR000G-2	D1919-R3 TOP C	39	33	bdl	1.67	0.5
IEMMR000G-3	D1919-R3 TRUNK 1	34	56	bdl	1.03	0.7
IEMMR000G-4	D1919-R3 TRUNK 2	36	91	bdl	0.502	0.7
IEMMR000H	D1919-R4	284	10	bdl	3.86	0.3
IEMMR000I	D1919-R5	313	52	bdl	1.39	0.8
IEMMR000J-1	D1919-R6A	45	35	bdl	1.79	1
IEMMR000J-2	D1919-R6B	16	22	bdl	0.0133	0.5
IEMMR000L	D1920-R2	793	14	bdl	1.42	0.4
IEMMR000M	D1920-R3	170	30	bdl	0.991	0.3
IEMMR000O	D1920-R5	219	59	bdl	0.0222	0.4
IEMMR000Q	D1920-R7	64	97	bdl	0.416	0.3
IEMMR000R	D1920-R8	79	19	bdl	1.98	0.1
IEMMR000S	D1920-SED	119	118	bdl	0.151	0.2
IEMMR000T	D1920-R9	1170	34	bdl	1.52	0.8
IEMMR000U	D1920-R10	100	82	bdl	0.0848	0.3
IEMMR000V	D1920-R11	513	31	bdl	0.2	bdl
IEMMR000W	D1920-R12	1220	24	bdl	1.37	0.9
-	D1920-R13	5100	17	18.1	0.0954	2.8
-	D1920-R14	30900	63	11.9	0.249	3.1
IEMMR000Z	D1920-R15	bdl	24	bdl	0.0741	0.2
-	D1920-R16	15300	59	9.4	0.181	2.6

IGSN	Analyte Symbol	Rb	S	Si	Sn	Sr
	Unit Symbol	ppm	%	%	ppm	ppm
	Detection Limit	0.4	0.01	0.01	0.5	3
	Analysis Method	FUS-MS	FUS-MS	FUS-MS	FUS-MS	FUS-MS
IEMMR0001	D1918-R1	0.7	35.7	0.05	15.7	394
IEMMR0002	D1918-R2	1.8	34.6	0.04	9.5	21
IEMMR0003	D1918-R3	0.8	33.7	0.23	29.2	220
IEMMR0004	D1918-R4	bdl	32.7	0.09	7.9	1410
IEMMR0005	D1918-R5	0.8	30.7	0.02	3.8	1750
IEMMR0006	D1918-R6	2.6	15.4	1.02	1.5	3250
IEMMR0007	D1918-R7	1.8	29.7	0.22	bdl	1820
IEMMR0008	D1918-R8	1.1	26.2	0.2	4.4	2230
IEMMR0009	D1918-R9	2.5	36	0.22	8.3	97
IEMMR000A	D1918-R10	0.2	28.3	0.13	bdl	3080
IEMMR000B	D1918-R11	0.9	26.6	0.21	3.1	3660
IEMMR000C	D1918-R12	0.4	18.6	0.05	1.2	5040
IEMMR000D	D1918-R13	1.9	17.1	0.06	1.4	4620
IEMMR000E	D1919-R1	2.3	18.4	0.85	1.2	3150
IEMMR000F-1	D1919-R2 A	1.4	11.8	3.97	1.4	3330
IEMMR000F-2	D1919-R2 B	0.8	20.4	2.35	1.2	2240
IEMMR000F-3	D1919-R2 C	0.9	20	bdl	1.6	2790
IEMMR000G-1	D1919-R3 TOP A	1.1	16.1	bdl	1	4160
IEMMR000G-2	D1919-R3 TOP C	1.1	16.9	0.22	1.3	3610
IEMMR000G-3	D1919-R3 TRUNK 1	1.7	17.5	0.17	1.2	3860
IEMMR000G-4	D1919-R3 TRUNK 2	0.6	21.9	0.08	1.8	3490
IEMMR000H	D1919-R4	bdl	15.2	0.56	bdl	3420
IEMMR000I	D1919-R5	1.7	14.3	2.48	0.9	4620
IEMMR000J-1	D1919-R6A	0.5	18.6	bdl	bdl	5410
IEMMR000J-2	D1919-R6B	bdl	27.2	0.03	bdl	2690
IEMMR000L	D1920-R2	1.5	7.76	0.74	1.9	3020
IEMMR000M	D1920-R3	1.8	18.8	1.2	2.8	2460
IEMMR000O	D1920-R5	1.9	13.8	0.04	1.6	2760
IEMMR000Q	D1920-R7	2.6	16.9	4.04	3	1880
IEMMR000R	D1920-R8	1.3	28	0.03	1.9	1360
IEMMR000S	D1920-SED	0.6	35.2	0.1	2.6	1860
IEMMR000T	D1920-R9	0.9	17.6	1.14	0.7	4000
IEMMR000U	D1920-R10	1.6	43.3	0.15	1.2	1730
IEMMR000V	D1920-R11	1.4	24.2	0.01	1.4	1300
IEMMR000W	D1920-R12	1.8	12.2	0.57	0.7	4580
-	D1920-R13	28.3	0.42	32.5	11.4	526
-	D1920-R14	23	0.82	24.5	3.8	1040
IEMMR000Z	D1920-R15	bdl	17.6	bdl	bdl	4630
-	D1920-R16	19.1	0.27	23.1	1.9	523

IGSN	Analyte Symbol	Te	Ti	Tl	Tm	V
	Unit Symbol	ppm	ppm	ppm	ppm	ppm
	Detection Limit	6	100	0.1	0.1	5
	Analysis Method	FUS-MS	FUS-MS	FUS-MS	FUS-MS	FUS-MS
IEMMR0001	D1918-R1	60	bdl	12.2	bdl	bdl
IEMMR0002	D1918-R2	29	bdl	1.5	bdl	bdl
IEMMR0003	D1918-R3	7	bdl	1.7	bdl	bdl
IEMMR0004	D1918-R4	66	bdl	17	bdl	bdl
IEMMR0005	D1918-R5	80	bdl	22.2	bdl	bdl
IEMMR0006	D1918-R6	bdl	bdl	102	bdl	bdl
IEMMR0007	D1918-R7	11	bdl	45.7	bdl	10
IEMMR0008	D1918-R8	40	bdl	77.2	bdl	bdl
IEMMR0009	D1918-R9	22	bdl	19.9	bdl	21
IEMMR000A	D1918-R10	bdl	bdl	84.5	bdl	14
IEMMR000B	D1918-R11	bdl	bdl	43.1	bdl	6
IEMMR000C	D1918-R12	bdl	bdl	72.3	bdl	bdl
IEMMR000D	D1918-R13	bdl	bdl	82.6	bdl	bdl
IEMMR000E	D1919-R1	bdl	bdl	125	bdl	bdl
IEMMR000F-1	D1919-R2 A	bdl	bdl	30	bdl	bdl
IEMMR000F-2	D1919-R2 B	bdl	bdl	109	bdl	bdl
IEMMR000F-3	D1919-R2 C	bdl	bdl	95.3	bdl	bdl
IEMMR000G-1	D1919-R3 TOP A	bdl	bdl	140	bdl	bdl
IEMMR000G-2	D1919-R3 TOP C	bdl	bdl	129	bdl	bdl
IEMMR000G-3	D1919-R3 TRUNK 1	bdl	bdl	110	bdl	bdl
IEMMR000G-4	D1919-R3 TRUNK 2	bdl	bdl	72.6	bdl	10
IEMMR000H	D1919-R4	bdl	bdl	19.3	bdl	16
IEMMR000I	D1919-R5	bdl	bdl	191	bdl	bdl
IEMMR000J-1	D1919-R6A	bdl	bdl	154	bdl	bdl
IEMMR000J-2	D1919-R6B	21	bdl	1.6	bdl	bdl
IEMMR000L	D1920-R2	bdl	bdl	29.2	bdl	12
IEMMR000M	D1920-R3	bdl	bdl	24.2	bdl	14
IEMMR000O	D1920-R5	bdl	bdl	7.3	bdl	bdl
IEMMR000Q	D1920-R7	bdl	bdl	20.3	bdl	17
IEMMR000R	D1920-R8	10	bdl	26.8	bdl	7
IEMMR000S	D1920-SED	15	bdl	73.5	bdl	21
IEMMR000T	D1920-R9	bdl	bdl	197	bdl	10
IEMMR000U	D1920-R10	bdl	bdl	134	bdl	6
IEMMR000V	D1920-R11	bdl	bdl	19.4	bdl	6
IEMMR000W	D1920-R12	bdl	bdl	116	bdl	bdl
-	D1920-R13	bdl	2000	2.8	0.2	86
-	D1920-R14	bdl	1300	13.6	0.3	345
IEMMR000Z	D1920-R15	bdl	bdl	1.5	bdl	7
-	D1920-R16	bdl	1200	4.9	0.2	291

IGSN	Analyte Symbol	Y
	Unit Symbol	ppm
	Detection Limit	0.1
	Analysis Method	FUS-MS
IEMMR0001	D1918-R1	0.4
IEMMR0002	D1918-R2	0.3
IEMMR0003	D1918-R3	0.3
IEMMR0004	D1918-R4	0.5
IEMMR0005	D1918-R5	1.1
IEMMR0006	D1918-R6	1.6
IEMMR0007	D1918-R7	0.2
IEMMR0008	D1918-R8	1.4
IEMMR0009	D1918-R9	0.3
IEMMR000A	D1918-R10	0.4
IEMMR000B	D1918-R11	1.2
IEMMR000C	D1918-R12	1.3
IEMMR000D	D1918-R13	1.4
IEMMR000E	D1919-R1	0.6
IEMMR000F-1	D1919-R2 A	1.2
IEMMR000F-2	D1919-R2 B	1.4
IEMMR000F-3	D1919-R2 C	0.1
IEMMR000G-1	D1919-R3 TOP A	bdl
IEMMR000G-2	D1919-R3 TOP C	1.1
IEMMR000G-3	D1919-R3 TRUNK 1	0.3
IEMMR000G-4	D1919-R3 TRUNK 2	0.4
IEMMR000H	D1919-R4	0.3
IEMMR000I	D1919-R5	1.6
IEMMR000J-1	D1919-R6A	0.1
IEMMR000J-2	D1919-R6B	1.5
IEMMR000L	D1920-R2	1.8
IEMMR000M	D1920-R3	0.8
IEMMR000O	D1920-R5	0.6
IEMMR000Q	D1920-R7	1.1
IEMMR000R	D1920-R8	0.3
IEMMR000S	D1920-SED	0.1
IEMMR000T	D1920-R9	1.8
IEMMR000U	D1920-R10	0.4
IEMMR000V	D1920-R11	0.3
IEMMR000W	D1920-R12	0.3
-	D1920-R13	11.4
-	D1920-R14	19.6
IEMMR000Z	D1920-R15	0.5
-	D1920-R16	13.7

APPENDIX C – Whole-rock geochemistry (Quality Control)

The following includes reference standard data from Activation Laboratories.

Analyte Symbol	Ag	As	Au	Ba	Br	Co
Unit Symbol	ppm	ppm	ppb	ppm	ppm	ppm
Detection Limit	2	1	2	20	0.5	0.1
Analysis Method	INAA	INAA	INAA	INAA	INAA	INAA
GXR-1 Measured	32	447	3450	790	< 0.5	8.6
GXR-1 Certified	31	427	3300	750	0.5	8.2
GXR-1 Measured	32	447	3460	780	< 0.5	8.6
GXR-1 Certified	31	427	3300	750	0.5	8.2
GXR-1 Measured	32	427	3310	710	< 0.5	8.6
GXR-1 Certified	31	427	3300	750	0.5	8.2
GXR-1 Measured	32	413	3450	710	< 0.5	8.1
GXR-1 Certified	31	427	3300	750	0.5	8.2
GXR-1 Measured	33	427	3400	790	< 0.5	8.6
GXR-1 Certified	31	427	3300	750	0.5	8.2
GXR-1 Measured	33	427	3460	790	< 0.5	8.6
GXR-1 Certified	31	427	3300	750	0.5	8.2
GXR-1 Measured	31	427	3460	790	< 0.5	8.6
GXR-1 Certified	31	427	3300	750	0.5	8.2
OREAS 922 Measured						
OREAS 922 Certified						
OREAS 922 Measured						
OREAS 922 Certified						
OREAS 922 Measured						
OREAS 922 Certified						
OREAS 922 Measured						
OREAS 922 Certified						
OREAS 922 Measured						
OREAS 922 Certified						
OREAS 922 Measured						
OREAS 922 Certified						

Analyte Symbol	Cr	Cs	Fe	Hf	Na	Ni
Unit Symbol	ppm	ppm	%	ppm	%	ppm
Detection Limit	0.5	0.2	0.01	0.2	0.001	50
Analysis Method	INAA	INAA	INAA	INAA	INAA	INAA
GXR-1 Measured	12.6	< 0.2	24.7	< 0.2	0.05	< 50
GXR-1 Certified	12	3	23.6	0.96	0.052	41
GXR-1 Measured	12.3	< 0.2	24.7	< 0.2	0.05	< 50
GXR-1 Certified	12	3	23.6	0.96	0.052	41
GXR-1 Measured	12.6	< 0.2	24.4	< 0.2	0.05	< 50
GXR-1 Certified	12	3	23.6	0.96	0.052	41
GXR-1 Measured	12.6	< 0.2	24.7	< 0.2	0.05	< 50
GXR-1 Certified	12	3	23.6	0.96	0.052	41
GXR-1 Measured	12.6	< 0.2	24.3	< 0.2	0.05	< 50
GXR-1 Certified	12	3	23.6	0.96	0.052	41
GXR-1 Measured	12.6	< 0.2	24.8	< 0.2	0.05	< 50
GXR-1 Certified	12	3	23.6	0.96	0.052	41
GXR-1 Measured	12	< 0.2	24.8	< 0.2	0.05	< 50
GXR-1 Certified	12	3	23.6	0.96	0.052	41
OREAS 922 Measured						
OREAS 922 Certified						
OREAS 922 Measured						
OREAS 922 Certified						
OREAS 922 Measured						
OREAS 922 Certified						
OREAS 922 Measured						
OREAS 922 Certified						
OREAS 922 Measured						
OREAS 922 Certified						
OREAS 922 Measured						
OREAS 922 Certified						

Analyte Symbol	Rb	Sb	Sc	Se	Sr	Ta
Unit Symbol	ppm	ppm	ppm	ppm	ppm	ppm
Detection Limit	10	0.1	0.01	0.5	100	0.3
Analysis Method	INAA	INAA	INAA	INAA	INAA	INAA
GXR-1 Measured	< 10	128	1.65	15.8	< 100	< 0.3
GXR-1 Certified	14	122	1.58	16.6	275	0.175
GXR-1 Measured	10	116	1.66	15.8	< 100	< 0.3
GXR-1 Certified	14	122	1.58	16.6	275	0.175
GXR-1 Measured	< 10	120	1.56	< 0.5	< 100	< 0.3
GXR-1 Certified	14	122	1.58	16.6	275	0.175
GXR-1 Measured	< 10	120	1.51	15.8	< 100	< 0.3
GXR-1 Certified	14	122	1.58	16.6	275	0.175
GXR-1 Measured	< 10	122	1.58	< 0.5	< 100	< 0.3
GXR-1 Certified	14	122	1.58	16.6	275	0.175
GXR-1 Measured	< 10	123	1.58	17.4	< 100	< 0.3
GXR-1 Certified	14	122	1.58	16.6	275	0.175
GXR-1 Measured	10	126	1.62	17.4	< 100	< 0.3
GXR-1 Certified	14	122	1.58	16.6	275	0.175
OREAS 922 Measured						
OREAS 922 Certified						
OREAS 922 Measured						
OREAS 922 Certified						
OREAS 922 Measured						
OREAS 922 Certified						
OREAS 922 Measured						
OREAS 922 Certified						
OREAS 922 Measured						
OREAS 922 Certified						
OREAS 922 Measured						
OREAS 922 Certified						

Analyte Symbol	Th	U	Zn	La	Ce	Nd
Unit Symbol	ppm	ppm	ppm	ppm	ppm	ppm
Detection Limit	0.1	0.1	10	0.05	1	1
Analysis Method	INAA	INAA	INAA	INAA	INAA	INAA
GXR-1 Measured	2.6	34.5	790	7.54	18	17
GXR-1 Certified	2.44	34.9	760	7.5	17	18
GXR-1 Measured	2.6	36.6	800	7.14	17	17
GXR-1 Certified	2.44	34.9	760	7.5	17	18
GXR-1 Measured	2.4	36.6	800	7.5	17	17
GXR-1 Certified	2.44	34.9	760	7.5	17	18
GXR-1 Measured	2.5	33.2	800	7.14	18	17
GXR-1 Certified	2.44	34.9	760	7.5	17	18
GXR-1 Measured	2.4	35.4	760	7.5	18	17
GXR-1 Certified	2.44	34.9	760	7.5	17	18
GXR-1 Measured	2.6	36.4	800	7.48	18	17
GXR-1 Certified	2.44	34.9	760	7.5	17	18
GXR-1 Measured	2.4	35.7	800	7.5	18	18
GXR-1 Certified	2.44	34.9	760	7.5	17	18
OREAS 922 Measured						
OREAS 922 Certified						
OREAS 922 Measured						
OREAS 922 Certified						
OREAS 922 Measured						
OREAS 922 Certified						
OREAS 922 Measured						
OREAS 922 Certified						
OREAS 922 Measured						
OREAS 922 Certified						
OREAS 922 Measured						
OREAS 922 Certified						

Analyte Symbol	Sm	Eu	Tb	Yb	Lu	Al
Unit Symbol	ppm	ppm	ppm	ppm	ppm	%
Detection Limit	0.01	0.05	0.1	0.05	0.01	0.01
Analysis Method	INAA	INAA	INAA	INAA	INAA	FUS-MS
GXR-1 Measured	2.83	0.72	< 0.1	1.99	0.29	3.72
GXR-1 Certified	2.7	0.69	0.83	1.9	0.28	3.52
GXR-1 Measured	2.57	0.72	0.9	1.99	0.29	3.54
GXR-1 Certified	2.7	0.69	0.83	1.9	0.28	3.52
GXR-1 Measured	2.57	0.69	0.8	1.9	0.28	
GXR-1 Certified	2.7	0.69	0.83	1.9	0.28	
GXR-1 Measured	2.57	0.72	0.8	1.97	0.29	
GXR-1 Certified	2.7	0.69	0.83	1.9	0.28	
GXR-1 Measured	2.57	0.69	< 0.1	1.9	0.28	
GXR-1 Certified	2.7	0.69	0.83	1.9	0.28	
GXR-1 Measured	2.57	0.71	< 0.1	1.99	0.28	
GXR-1 Certified	2.7	0.69	0.83	1.9	0.28	
GXR-1 Measured	2.57	0.72	0.8	1.99	0.28	
GXR-1 Certified	2.7	0.69	0.83	1.9	0.28	
OREAS 922 Measured						7.45
OREAS 922 Certified						7.59
OREAS 922 Measured						7.42
OREAS 922 Certified						7.59
OREAS 922 Measured						7.49
OREAS 922 Certified						7.59
OREAS 922 Measured						6.73
OREAS 922 Certified						6.63
OREAS 922 Measured						6.5
OREAS 922 Certified						6.63
OREAS 922 Measured						6.4
OREAS 922 Certified						6.63

Analyte Symbol	Be	Bi	Ca	Cd	Cu	Dy
Unit Symbol	ppm	ppm	%	ppm	ppm	ppm
Detection Limit	3	2	0.01	2	2	0.3
Analysis Method	FUS-MS	FUS-MS	FUS-MS	FUS-MS	FUS-MS	FUS-MS
GXR-1 Measured			0.94			
GXR-1 Certified			0.96			
GXR-1 Measured			0.88			
GXR-1 Certified			0.96			
GXR-1 Measured						
GXR-1 Certified						
GXR-1 Measured						
GXR-1 Certified						
GXR-1 Measured						
GXR-1 Certified						
GXR-1 Measured						
GXR-1 Certified						
GXR-1 Measured						
GXR-1 Certified						
OREAS 922 Measured		10	0.51		2420	5
OREAS 922 Certified		11	0.49		2220	5.75
OREAS 922 Measured		11	0.5		2260	5.4
OREAS 922 Certified		11	0.49		2220	5.75
OREAS 922 Measured		9	0.53		2050	5.4
OREAS 922 Certified		10	0.49		2220	5.75
OREAS 922 Measured	< 3	4	2.09	281	3680	
OREAS 922 Certified	2	4	2	295	3680	
OREAS 922 Measured	< 3	4	2.06	275	3580	
OREAS 922 Certified	2	4	2	295	3680	
OREAS 922 Measured			1.95			
OREAS 922 Certified			2			

Analyte Symbol	Er	Ga	Gd	Ho	In	K
Unit Symbol	ppm	ppm	ppm	ppm	ppm	%
Detection Limit	0.1	0.2	0.1	0.2	0.2	0.1
Analysis Method	FUS-MS	FUS-MS	FUS-MS	FUS-MS	FUS-MS	FUS-MS
GXR-1 Measured						< 0.1
GXR-1 Certified						0.05
GXR-1 Measured						< 0.1
GXR-1 Certified						0.05
GXR-1 Measured						
GXR-1 Certified						
GXR-1 Measured						
GXR-1 Certified						
GXR-1 Measured						
GXR-1 Certified						
GXR-1 Measured						
GXR-1 Certified						
GXR-1 Measured						
GXR-1 Certified						
OREAS 922 Measured	2.6	19.7	5.5	1	0.3	2.7
OREAS 922 Certified	3.38	21.2	6.94	1.2	0.3	2.6
OREAS 922 Measured	3.1	20.1	5.4	1.1	0.3	2.6
OREAS 922 Certified	3.38	21.2	6.94	1.2	0.3	2.6
OREAS 922 Measured	3.4	19.8	5.5	1	0.3	2.6
OREAS 922 Certified	3.38	21.2	6.94	1.2	0.3	2.6
OREAS 922 Measured		25.7			1.8	2.3
OREAS 922 Certified		26.5			1.9	2.23
OREAS 922 Measured		25.4			1.8	2.2
OREAS 922 Certified		26.5			1.9	2.23
OREAS 922 Measured						2.2
OREAS 922 Certified						2.23

Analyte Symbol	Li	Mg	Mn	Mo	Nb	Pb
Unit Symbol	ppm	%	ppm	ppm	ppm	ppm
Detection Limit	3	0.01	3	1	2.4	0.8
Analysis Method	FUS-MS	FUS-MS	FUS-MS	FUS-MS	FUS-MS	FUS-MS
GXR-1 Measured		0.22				
GXR-1 Certified		0.217				
GXR-1 Measured		0.19				
GXR-1 Certified		0.217				
GXR-1 Measured						
GXR-1 Certified						
GXR-1 Measured						
GXR-1 Certified						
GXR-1 Measured						
GXR-1 Certified						
GXR-1 Measured						
GXR-1 Certified						
GXR-1 Measured						
GXR-1 Certified						
OREAS 922 Measured	30	1.67	794		18	76.7
OREAS 922 Certified	29	1.61	880		15.2	64
OREAS 922 Measured	35	1.64	868		15.1	61.6
OREAS 922 Certified	29	1.61	880		15.2	64
OREAS 922 Measured	32	1.7	823		14.2	59.5
OREAS 922 Certified	29	1.61	880		15.2	64
OREAS 922 Measured		0.53	588	14	10.4	13000
OREAS 922 Certified		0.516	554	14	10.4	13300
OREAS 922 Measured		0.51	571	15	9.8	12900
OREAS 922 Certified		0.516	554	14	10.4	13300
OREAS 922 Measured		0.5				
OREAS 922 Certified		0.516				

Analyte Symbol	Pr	Rb	S	Si	Sn	Sr
Unit Symbol	ppm	ppm	%	%	ppm	ppm
Detection Limit	0.1	0.4	0.01	0.01	0.5	3
Analysis Method	FUS-MS	FUS-MS	FUS-MS	FUS-MS	FUS-MS	FUS-MS
GXR-1 Measured			0.26			
GXR-1 Certified			0.257			
GXR-1 Measured			0.33			
GXR-1 Certified			0.257			
GXR-1 Measured						
GXR-1 Certified						
GXR-1 Measured						
GXR-1 Certified						
GXR-1 Measured						
GXR-1 Certified						
GXR-1 Measured						
GXR-1 Certified						
GXR-1 Measured						
GXR-1 Certified						
OREAS 922 Measured	8.7	164	0.35	30.6	9.8	64
OREAS 922 Certified	10.6	167	0.389	30.51	10	58
OREAS 922 Measured	9.2	171	0.44	30.7	10.4	67
OREAS 922 Certified	10.6	167	0.389	30.51	10	58
OREAS 922 Measured	9.6	168	0.38	30.7	10.5	73
OREAS 922 Certified	10.6	167	0.389	30.51	10	58
OREAS 922 Measured	5.9	90.6	4.6	28.4		113
OREAS 922 Certified	6.64	89	4.51	28.1		101
OREAS 922 Measured	5.4	90	4.54	27.9		105
OREAS 922 Certified	6.64	89	4.51	28.1		101
OREAS 922 Measured			4.53	28		
OREAS 922 Certified			4.51	28.1		

Analyte Symbol	Ti	Tl	Tm	V	Y
Unit Symbol	%	ppm	ppm	ppm	ppm
Detection Limit	0.01	0.1	0.1	5	0.1
Analysis Method	FUS-MS	FUS-MS	FUS-MS	FUS-MS	FUS-MS
GXR-1 Measured	0.03				
GXR-1 Certified	0.036				
GXR-1 Measured	0.03				
GXR-1 Certified	0.036				
GXR-1 Measured					
GXR-1 Certified					
GXR-1 Measured					
GXR-1 Certified					
GXR-1 Measured					
GXR-1 Certified					
GXR-1 Measured					
GXR-1 Certified					
GXR-1 Measured					
GXR-1 Certified					
OREAS 922 Measured	0.44	0.8	0.5	86	29.9
OREAS 922 Certified	0.439	0.9	0.51	92	31.1
OREAS 922 Measured	0.45	0.8	0.4	107	28.3
OREAS 922 Certified	0.439	0.9	0.51	92	31.1
OREAS 922 Measured	0.45	0.8	0.5	103	29.1
OREAS 922 Certified	0.439	0.9	0.51	92	31.1
OREAS 922 Measured	0.19	2.1		36	13
OREAS 922 Certified	0.181	2		36.3	13.9
OREAS 922 Measured	0.18	2		37	12.5
OREAS 922 Certified	0.181	2		36.3	13.9
OREAS 922 Measured	0.18				
OREAS 922 Certified	0.181				

APPENDIX D – Porosity estimates.

The following includes porosity estimates of sample thin sections.

Sample ID	Minimum Porosity %	Maximum Porosity %	Average Porosity %
D1918-R1	20	50	35
D1918-R2	5	30	17.5
D1918-R3	5	30	17.5
D1918-R4	5	30	17.5
D1918-R5	40	40	40
D1918-R6	30	40	35
D1918-R7	30	30	30
D1918-R8	30	40	35
D1918-R9	40	45	42.5
D1918-R10	40	40	40
D1918-R11	30	40	35
D1918-R12	40	50	45
D1918-R13	40	50	45
D1919-R1	50	60	55
D1919-R2 A	30	60	45
D1919-R2 B	30	60	45
D1919-R2 C	30	60	45
D1919-R3 TOP A	50	60	55
D1919-R3 TRUNK 2	40	40	40
D1919-R4	30	40	35
D1919-R5	30	40	35
D1919-R6A	50	60	55
D1919-R6B	30	40	35
D1920-R2	40	50	45
D1920-R3	25	30	27.5
D1920-R5	20	25	22.5
D1920-R7	25	30	27.5
D1920-R8	30	40	35
D1920-R9	60	60	60
D1920-R10	60	70	65
D1920-R11	40	40	40
D1920-R12	40	40	40
D1920-R15	20	30	25
AVERAGE	**32.9**	**43.9**	**38.4**